

## INFORMATION TO USERS

This manuscript has been reproduced from the microfilm master. UMI films the text directly from the original or copy submitted. Thus, some thesis and dissertation copies are in typewriter face, while others may be from any type of computer printer.

**The quality of this reproduction is dependent upon the quality of the copy submitted.** Broken or indistinct print, colored or poor quality illustrations and photographs, print bleedthrough, substandard margins, and improper alignment can adversely affect reproduction.

In the unlikely event that the author did not send UMI a complete manuscript and there are missing pages, these will be noted. Also, if unauthorized copyright material had to be removed, a note will indicate the deletion.

Oversize materials (e.g., maps, drawings, charts) are reproduced by sectioning the original, beginning at the upper left-hand corner and continuing from left to right in equal sections with small overlaps. Each original is also photographed in one exposure and is included in reduced form at the back of the book.

Photographs included in the original manuscript have been reproduced xerographically in this copy. Higher quality 6" x 9" black and white photographic prints are available for any photographs or illustrations appearing in this copy for an additional charge. Contact UMI directly to order.

# UMI

A Bell & Howell Information Company  
300 North Zeeb Road, Ann Arbor MI 48106-1346 USA  
313/761-4700 800/521-0600



**SiC-REINFORCED  $\text{Al}_2\text{O}_3$ /METAL  
COMPOSITES BY DIRECTED  
METAL OXIDATION**

by

**MOHAMED GUERMAZI**

*Department of Mining and Metallurgical Engineering*

McGill University, Montreal

November 1996

A Thesis submitted to the  
Faculty of Graduate Studies and Research  
in partial fulfillment of the  
requirements of the degree of  
Doctor of Philosophy

© Mohamed Guermazi, 1996



National Library  
of Canada

Acquisitions and  
Bibliographic Services

395 Wellington Street  
Ottawa ON K1A 0N4  
Canada

Bibliothèque nationale  
du Canada

Acquisitions et  
services bibliographiques

395, rue Wellington  
Ottawa ON K1A 0N4  
Canada

*Your file* *Votre référence*

*Our file* *Notre référence*

The author has granted a non-exclusive licence allowing the National Library of Canada to reproduce, loan, distribute or sell copies of this thesis in microform, paper or electronic formats.

The author retains ownership of the copyright in this thesis. Neither the thesis nor substantial extracts from it may be printed or otherwise reproduced without the author's permission.

L'auteur a accordé une licence non exclusive permettant à la Bibliothèque nationale du Canada de reproduire, prêter, distribuer ou vendre des copies de cette thèse sous la forme de microfiche/film, de reproduction sur papier ou sur format électronique.

L'auteur conserve la propriété du droit d'auteur qui protège cette thèse. Ni la thèse ni des extraits substantiels de celle-ci ne doivent être imprimés ou autrement reproduits sans son autorisation.

0-612-29952-X

*to my parents...*

# ABSTRACT

A new process, the DIMOX™ Process, for making ceramic matrix and metal matrix composites was developed and commercialized by Lanxide Corporation. This technology is based on the use of a unique directed-metal oxidation process to grow ceramic matrices around pre-placed composite fillers or reinforcements. This thesis attempts to offer a good understanding of the mechanism of the process, as well as the effects of the processing parameters on the process, especially in the presence of a reinforcing material. Metal-ceramic matrix composites were grown into four different SiC powders by the directed oxidation of aluminum alloys in air at various temperatures. Microstructure, microstructural evolution, and growth kinetic studies were performed on these composites as a function of alloy compositions, processing temperature, and preform size. The results are then compared to those of composites processed without SiC-reinforcing particles.

The microstructure of the resulting composites consists of three phases: the SiC preform, a continuous  $\alpha$ -Al<sub>2</sub>O<sub>3</sub> matrix, and a network of unoxidized metal. The microstructural evolution for composites without SiC starts with an incubation period of variable length. The incubation time decreases with increase in the processing temperature and with increase in the alloy silicon content. The addition of silicon in the alloy decrease the viscosity of the melt and therefore increases the rate of metal supply

to the reaction front. However increasing the magnesium content resulted only in a slight decrease of the length of the incubation period.

For composites processed with SiC particles, the growth started immediately after introducing the alloy into the hot zone of the furnace. The incubation time was very short and was not sensitive to changes in either temperatures or alloy composition. The preform does not show any evidence of degradation by the molten alloy, however the growth front tends to climb up the surface of the particles. The composite growth rate increased with decreasing in the preform particle size.

The oxidative formation of  $\text{Al}_2\text{O}_3$  matrix composites using Al-Mg and Al-Mg-Si alloys exhibits a linear type of kinetics in both the presence and absence of SiC preforms with an activation energy of 224 kJ/mol.

# RÉSUMÉ

Un nouveau procédé, nommé DIMOX<sup>TM</sup>, pour la fabrication des composites céramiques et métalliques a été développé par la compagnie *Lanxide Corporation*. Cette nouvelle technologie est basée sur une simple méthode d'oxydation d'un métal à fin de développer des matrices céramiques au tour des renforcements. Cette thèse tente d'offrir une compréhension du mécanisme du procédé, ainsi que l'influence des divers paramètres sur le développement des composites, surtout en présence de renforcements. Des composites  $Al_2O_3/Al$  renforcés par quatre particules de SiC différents ont été fabriquées par oxydation de divers alliages d'aluminium content du silicium (Si) et du magnésium (Mg) à des températures qui varient entre 1150°C et 1300°C en air. La microstructure, l'évolution des composites, et la cinétique du procédé ont été évalués en fonction de la température, la composition des alliages d'aluminium, et la taille des particules de SiC. Les résultats ont été comparés avec celles des composites fabriquées en absence de renforcement.

La microstructure de ces composites consiste de silice de carbone (SiC), d'alumine ( $Al_2O_3$ ), de silicium (Si), et d'aluminium (Al). L'alumine et les métaux résiduels sont liés en 3-D. L'évolution des composites en absence de renforcement débute avec une période d'incubation de variable longueur. La durée de cette période diminue avec l'augmentation de la température et avec l'augmentation de la teneur de l'alliage en silicium. L'addition du silicium à l'alliage diminue la viscosité du liquide et en conséquence augmente le taux d'infiltration du métal au front de la réaction.

Cependant, l'augmentation de la teneur en magnésium a résulté en une diminution minime de la durée d'incubation.

Pour les composites renforcées avec du SiC, la croissance a débuté immédiatement après l'introduction de l'échantillon dans la zone chaude du four. La période d'incubation été très brève et n'été pas sensible aux changements de la température ni de la composition de l'alliage. Les particules de SiC sont intactes et il n'y a aucune évidence de dégradation ou de réaction avec les alliages. Le front de croissance a une tendance à gravir les particules de SiC, ce qui augmente la surface d'oxydation et en conséquence augmente le taux de croissance des composites.

La formation d'alumine par oxydation des alliages Al-Mg-Si fait preuve de cinétiques linéaires en absence et en présence du SiC avec une énergie d'activation de 224 kJ/mol.

# ACKNOWLEDGMENTS

I would like to express my sincere gratitude to Prof. R.A.L. Drew for his supervision and guidance during the entire project, and for playing a key role in my professional development throughout the duration of my time spent at McGill.

I would like to thank Dr. D. Muscat for his willingness to discuss numerous questions regarding not only the aspects of the current thesis, but anything that might have interested him. I am also thankful to Dr. H. Vali for his help with sample preparation for TEM using an advanced Pt/C replication technique.

Special thanks go to my colleagues, both past and present, who were always ready to assist me in the continued progress of my thesis, and who have constantly provided a pleasant working environment. In particular I would like to mention: Dr. E. Martinelli, Dr. Y. Baik, Miss T. Brzezinski, Dr. A. Hadian, Dr. M. Allahverdi, Miss L. Gavoret, Mr. S. Debouzy, Mr. S. Grenier, Mr. T. Lebeau, Mr. M. Entezarian, Mr. L. Ederer, and Miss P. Wanjara.

I would like to extend my thanks to the technical personnel of the department, especially Mr. C. Edovas, Ms. H. Campbell and Ms. M. Riendeau, as well as Mr. Kneopfel and all machine shop personnel, for providing me with all the required tools and suggestions.

To my wife Olfa, my love and respect for her help, support, and especially her patience.

# TABLE OF CONTENTS

ABSTRACT .....	iii
RÉSUMÉ .....	v
ACKNOWLEDGMENTS .....	vii
TABLE OF CONTENTS .....	viii
LIST OF FIGURES .....	xiii
LIST OF TABLES .....	xxi
NOMENCLATURE .....	xxiii
1. INTRODUCTION .....	1
2. LITERATURE REVIEW .....	3
2.1 PROCESSING OF METAL/CERAMIC COMPOSITES .....	4
2.1.1 Cold Pressing and Sintering .....	5
2.1.2 Hot Pressing .....	5
2.1.3 Reaction Bonding .....	8
2.1.4 Infiltration .....	9
2.1.5 DIMOX™ Process .....	12
2.2 PROPERTIES OF COMPOSITES .....	15
2.2.1 Fiber-Reinforced Composites .....	15
2.2.1.1 Effect of Fiber Length .....	17
2.2.1.2 Effect of Interfacial Bonding .....	17

2.2.1.3 Silicon Carbide Fiber Composites.....	17
2.2.2 Particle-Reinforced Composites.....	18
2.2.2.1 SiC Particle-Reinforced Composites.....	19
2.2.3 Lanxide™ Composites .....	20
2.3 OXIDATION OF ALUMINUM ALLOYS.....	24
2.3.1 Oxidation Behavior of Pure Aluminum .....	27
2.3.2 Oxidation Behavior of Aluminum Alloys.....	31
2.4 INFILTRATION OF POWDER BEDS .....	41
2.4.1 Capillary Phenomena .....	42
2.4.1.1 Infiltration Kinetics .....	45
2.4.2 Wetting Phenomena .....	46
2.4.2.1 Wetting of SiC by Aluminum Alloys.....	48
2.4.2.2 Wetting of Al <sub>2</sub> O <sub>3</sub> by Aluminum Alloys.....	51
3. OBJECTIVES.....	53
4. EXPERIMENTAL PROCEDURE .....	55
4.1 RAW MATERIALS.....	55
4.1.1 Aluminum Alloys.....	55
4.1.2 Melting and Alloying.....	56
4.1.3 Casting.....	57
4.1.4 SiC Powder Characterization.....	57
4.1.4.1 Specific Surface Area .....	60
4.1.4.2 Particle Size Analysis .....	62

4.1.5 Crucible Fabrication .....	63
4.2 COMPOSITE FABRICATION .....	64
4.2.1 Interrupted Test Experiments .....	66
4.2.2 Kinetics Experiments.....	67
4.3 CHEMICAL AND PHASE ANALYSIS .....	70
4.3.1 Emission Spectroscopy.....	70
4.3.2 X-Ray Diffraction (XRD).....	70
4.4 MICROSCOPY.....	71
4.4.1 Optical Microscopy .....	71
4.4.2 Scanning Electron Microscopy (SEM).....	71
4.4.3 Transmission Electron Microscopy (TEM) .....	74
4.4.4 TEM Replication Technique.....	74
5. RESULTS .....	76
5.1 MICROSTRUCTURE OF LANXIDE™ COMPOSITES .....	76
5.1.1 Unreinforced Composites .....	77
5.1.2 SiC-Reinforced Composites.....	80
5.1.3 Effect of Alloying Elements.....	84
5.1.4 Effect of Processing Temperature.....	86
5.1.5 Effect of SiC Powder Size.....	89
5.2 MICROSTRUCTURAL EVOLUTION OF THE COMPOSITES .....	91
5.2.1 Initial Oxidation and Incubation Period.....	92
5.2.1.1 Unreinforced Composites.....	93

5.2.1.2 SiC-Reinforced Composites .....	105
5.2.2 Bulk Oxidation: Composite Growth .....	110
5.2.2.1 Growth of Unreinforced Composites .....	110
5.2.2.2 Growth of SiC-Reinforced Composites .....	120
5.2.3 Porosity in the Composites .....	124
5.3 KINETICS OF THE DIMOX™ PROCESS .....	130
5.3.1 Oxidation of Pure Aluminum .....	130
5.3.2 Oxidation Kinetics of Aluminum Alloys into SiC Preforms.....	133
5.3.2.1 Initial Oxidation and Incubation Period.....	135
5.3.2.2 Effects of SiO <sub>2</sub> on Incubation .....	137
5.3.2.3 Al <sub>2</sub> O <sub>3</sub> Composite Growth.....	142
5.3.3 Effect of Alloying Elements .....	147
5.3.3.1 Effect of Magnesium .....	147
5.3.3.2 Effect of Silicon .....	151
5.3.4 Effect of SiC Powder Size .....	156
6. DISCUSSION .....	159
6.1 MICROSTRUCTURAL EVOLUTION.....	159
6.1.1 Unreinforced Composites .....	159
6.1.1.1 Effects of Si .....	163
6.1.2 SiC Reinforced Composites .....	169
6.1.2.1 Incubation Period .....	169
6.1.2.2 Composite Formation.....	174

6.2 GROWTH KINETICS .....	175
6.2.1 Effects of the SiO <sub>2</sub> Layer .....	177
6.2.2 Effects of Alloying Elements .....	180
6.2.3 Effects of Preform Size .....	183
7. CONCLUSIONS AND RECOMMENDATIONS .....	185
7.1 CONCLUSIONS .....	185
7.2 RECOMMENDATIONS FOR FURTHER WORK .....	187
8. CONTRIBUTIONS TO ORIGINAL KNOWLEDGE .....	188
APPENDIX I .....	189
APPENDIX II .....	191
REFERENCES .....	194

# LIST OF FIGURES

Fig. 2.1: Schematic of the slurry infiltration process of making fiber-reinforced glass and glass-ceramic composite .....	6
Fig. 2.2: Schematic of the melt infiltration process. ....	9
Fig. 2.3: Schematic of the Squeeze Casting process. ....	11
Fig. 2.4: DIMOX™ directed metal oxidation process.....	13
Fig. 2.5: Weight gain data for the initial period of oxidation at 454°C.....	28
Fig. 2.6: Schematic representation of the various stages of a model for nonprotective oxidation of Al-Mg alloy at high temperatures. ....	33
Fig. 2.7: Capillary pressure across an interface. ....	43
Fig. 2.8: The contact angle for a (A) non-wetting and (B) wetting case. ....	47
Fig. 4.1: Scanning electron micrographs of the as-received SiC powders: (a) 600-, (b) 400-, (c) 320-, and (d) 240-grit powder.....	59
Fig. 4.2: Morphology of the SiO <sub>2</sub> layer that develops on the SiC surface after oxidation. ....	60
Fig. 4.3: Measured particle size distributions of the four SiC powders by Sedigraph.....	62
Fig. 4.4: Schematic illustration of the drain-casting process, (a) fill mold with slip, (b) mold extracts liquid, forms compact along walls, (c) excess slip drained, and (d) casting removed after partial drying .....	64
Fig. 4.5: Experimental setup for composite fabrication using a filler material. ....	65
Fig. 4.6: Schematic of the furnace used for the interrupted experiments.....	66

Fig. 4.7: Experimental set-up to measure the composite growth rate.....	68
Fig. 4.8: The principal steps of image analysis.....	74
Fig. 4.9: Dimpling a sample for TEM analysis.....	74
Fig. 5.1: Microstructure of a composite grown from a (7/3) alloy at 1200°C without SiC.....	78
Fig. 5.2: Microstructure of a composite grown from a (0/3) alloy at 1200°C without SiC (normal to the growth direction).....	79
Fig. 5.3: Microstructure of a composite grown from a (7/3) alloy at 1200°C (no SiC) showing the intersection of two or more Al <sub>2</sub> O <sub>3</sub> columns.....	79
Fig. 5.4: TEM replica showing the interconnectivity of the metal channels.....	80
Fig. 5.5: Microstructures of composites grown from a (7/3) alloy at 1200°C with a 240- grit SiC reinforcing material at different magnifications.....	81
Fig. 5.6: XRD plot for the composite fabricated at 1200°C using a (7/3) alloy.....	82
Fig. 5.7: TEM micrograph showing the Al <sub>2</sub> O <sub>3</sub> /SiC interface.....	83
Fig. 5.8: Microstructure of composites grown at 1200°C with 240-grit SiC particles from (a) (3.5/3) and (b) (0/3) alloys.....	85
Fig. 5.9: Microstructure of composites grown from a (3.5/3) alloy at (a) 1200°C, (b) 1300°C, and (c) 1350°C. The arrows point to the metal channels.....	88
Fig. 5.10: Plot of metal and Al <sub>2</sub> O <sub>3</sub> volume percent as a function of processing temperature using a (7/1.5) alloy.....	88
Fig. 5.11: Plot of the metal channel average size as a function of processing temperature using a (7/1.5) alloy.....	89

Fig. 5.12: Microstructure of composites processed at 1250°C using a (7/3) alloy and reinforced by (a) 600-grit and (b) 240-grit SiC particles.....	90
Fig. 5.13: Typical oxidation behavior for Al-containing Mg alloys in air or oxygen at temperatures in the range of 1100-1300°C.....	92
Fig. 5.14: Formation of voids along the metal grain boundaries. (a) 30 seconds and (b) 1 minute exposure of (0/3) alloy to 1150°C. ....	94
Fig. 5.15: Formation of a duplex MgO/MgAl <sub>2</sub> O <sub>4</sub> layer on the surface of the alloy.....	95
Fig. 5.16: Cross-section of the alloy showing the formation of surface oxides on a (0/3) alloy (15 hours).....	96
Fig. 5.17: Top views of the MgO oxide on the (0/3) alloy held at 1150°C for (a) 15 minutes, (b) 3 hours, and (c) 10 hours. ....	98
Fig. 5.18: Top view of the MgO oxide on the (0/3) alloy held at 1150°C for 23 hours (length of the incubation period for this alloy).....	99
Fig. 5.19: Variation in the average thickness of MgO and MgAl <sub>2</sub> O <sub>4</sub> layers with time at 1150°C for (0/3) and (7/3) alloys. ....	100
Fig. 5.20: Nodule formation during growth on the surface of the (7/3) alloy at 1150°C after 5 hours.....	102
Fig. 5.21: Top views of the MgO oxide on the (7/3) alloy held at 1150°C for various times (a) 30 seconds, (b) 45 seconds, (c) 60 seconds, and (d) 75 seconds. ....	104
Fig. 5.22: Top views of the surface oxides on the (0/3) alloy with SiC held at 1150°C for (a) 2 minutes, (b) 5 minutes, (c) 7 minutes, (d) 10 minutes, (e) 15 minutes and (f) 30 minutes. ....	108

Fig. 5.23: Cross section of the (0/3) alloy surface after 5 minutes of oxidation.....	109
Fig. 5.24: Top views of the surface of the (0/3) alloy with SiC held at 1150°C for 30 minutes. ....	109
Fig. 5.25: Top views of the surface of the (7/3) alloy held at 1150°C for (a) 5 hours, (b) 10 hours, and (c) 15 hours, showing the progressive evolution of the composite....	112
Fig. 5.26: Cross sectional views showing the spinel/composite interface. ....	113
Fig. 5.27: Cross section of Al <sub>2</sub> O <sub>3</sub> nodules covered by MgO on the outer composite/air surface. ....	114
Fig. 5.28: Top views of the surface of the (7/3) alloy held at 1175°C for 20 hours (a) coarse and (b) fine scale. ....	115
Fig. 5.29: Top views of the surface of the (7/3) alloy held at 1175°C for (a) 10 hours, (b) 12 hours, and (c) 15 hours. ....	117
Fig. 5.30: TEM micrograph showing an Al <sub>2</sub> O <sub>3</sub> /Al <sub>2</sub> O <sub>3</sub> low angle grain boundary. ....	118
Fig. 5.31: External surface layers of the composite. (a) Optical micrograph of a cross section and (b) a BEI micrograph showing a fractured surface of the composite/air interface. ....	119
Fig. 5.32: Top view of a SiC reinforced composite. ....	121
Fig. 5.33: Optical micrograph showing a cross-section of the top of the composite. ....	121
Fig. 5.34: Nucleation of composite nodules on the exposed surface of the SiC particles. ....	123
Fig. 5.35: Cross section of a composite nodule.....	123

Fig. 5.36: Optical micrographs showing (a) microporosity, (b) macroporosity, and (c) voids within the SiC preform. ....	126
Fig. 5.37: Microstructure of various composites grown from a (7/3) alloy and subjected to processing at 1250°C after all of the alloy has been consumed. (a)-(b) contain SiC, and (c)-(d) no SiC. ....	128
Fig. 5.38: Binary phase diagram for the Al-Si system. ....	129
Fig. 5.39: Weight gain vs. time curves for oxidation of pure aluminum under flowing air. ....	131
Fig. 5.40: Parabolic plots of oxidation data for pure aluminum. ....	132
Fig. 5.41: Arrhenius plot of parabolic rate constant for pure aluminum. ....	133
Fig. 5.42: Weight gain vs. time curve for the (7/3) alloy at 1150°C using 240-grit SiC particles. ....	134
Fig. 5.43: Early stages of the composite growth process indicating the change in length of incubation period with change in process temperature. ....	136
Fig. 5.44: Arrhenius plot of the weight gain rates associated with the incubation period for the (7/3) alloy in air using 240-grit SiC preform. ....	136
Fig. 5.45: Microstructure of SiC powder bed infiltrated by pure aluminum under argon for 4 hours at 1250°C. ....	139
Fig. 5.46: Microstructure of SiC/SiO <sub>2</sub> powder bed infiltrated by pure aluminum under argon for 4 hours at 1250°C. ....	140
Fig. 5.47: Microstructure of a composite grown into a SiC/SiO <sub>2</sub> powder bed mixture using a (0/3) alloy at 1250°C. ....	141

Fig. 5.48: Weight gain vs. time curves for oxidation of the (7/3) alloy in air using 240-grit SiC powder at four different temperatures. ....	143
Fig. 5.49: Arrhenius plot of the weight gain rates for the (7/3) alloy in air using 240-grit SiC preform. ....	144
Fig. 5.50: Weight gain vs. time curve for the (3.5/2) alloy with changing the processing temperature. 240-grit SiC powder was used. ....	145
Fig. 5.51: Arrhenius plot of the rate of weight gain for a (7/3) alloy in air using 240-grit SiC preform. ....	146
Fig. 5.52: Weight gain vs. time curves showing the effect of presence of Mg in the parent alloy. The growth temperature was 1250°C and 240-grit SiC powder was used. ....	148
Fig. 5.53: Weight gain vs. time curves showing the effect of changing the Mg content on the growth rate (1350°C, no SiC). ....	149
Fig. 5.54: Weight gain vs. time curves showing the effect of changing the Mg content on the growth rate (1350°C, 240-grit SiC). ....	149
Fig. 5.55: Variation of the incubation period as a function of Mg content at 1350°C. ....	150
Fig. 5.56: Variation of the growth rate as a function of Mg content at 1350°C. ....	150
Fig. 5.57: Arrhenius plot of weight gain rates for alloys having different Mg contents (240-grit SiC). ....	151
Fig. 5.58: Weight gain vs. time curves showing the effect of presence of Si in the parent alloy (1100°C, no SiC) ....	152
Fig. 5.59: Weight gain vs. time curves showing the effect of changing the Si content on the growth rate (1350°C, SiC). ....	153

Fig. 5.60: Weight gain vs. time curves showing the effect of changing the Si content on the growth rate (1350°C, 240-grit SiC).....	153
Fig. 5.61: Variation of the incubation period as a function of Si content in the alloy. ....	154
Fig. 5.62: Variation of the growth rate as a function of Si content in the alloy. ....	155
Fig. 5.63: Arrhenius plot of weight gain rates for alloys having different Mg contents using 240-grit SiC preform.....	155
Fig. 5.64: Normalized weight gain vs. time curves for the (0/1.5) alloy showing the effect of SiC powder size. The processing temperature was 1150°C. ....	156
Fig. 5.65: Normalized weight gain vs. time curves for the (3.5/2) alloy showing the effect of SiC powder size. The processing temperature was 1200°C. ....	157
Fig. 5.66: Normalized weight gain vs. time curves for the (7/3) alloy showing the effect of the presence of SiC. The processing temperature was 1250°C.....	157
Fig. 5.67: Normalized growth rate vs. SiC particle size curve for the (3.5/2.0) alloy at 1150 and 1200°C.....	158
Fig. 6.1: Schematic of the mechanism leading to composite growth.....	161
Fig. 6.2: Effect of Si on the MgO and Al <sub>2</sub> O <sub>3</sub> solubilities and hence the oxygen gradient for Al-rich alloys .....	166
Fig. 6.3: Isothermal section of the Al-Mg-O phase diagram at 1100°C.....	167
Fig. 6.4: Calculated Mg concentrations for the relevant three-phase equilibria C <sub>LAS</sub> and C <sub>LSM</sub> as a function of temperature. Also shown are the liquidus (T <sub>L</sub> ) and solidus (T <sub>S</sub> ) lines for alloys within this composition range.....	168
Fig. 6.5: Schematic of the evaporation and redeposition after oxidation of Mg/Al. ....	171

Fig. 6.6: Effect of temperature on the relative oxide solubilities, hence  $\Delta[\text{O}]$  and the  $\text{Al}_2\text{O}_3$  formation rate. .... 176

Fig. 6.7: Primary oxidation surface for liquid (Al,Mg,Si) at 1300°C..... 180

Fig. AII.1: Parabolic plots of oxidation data for pure aluminum..... 191

Fig. AII.2: Arrhenius plot of parabolic rate constant for pure aluminum. .... 193

# LIST OF TABLES

Table 2.1: Summary of Mechanical Property Data for Monolithic Mullite and Mullite-Silicon Carbide Composite .....	18
Table 2.2: Examples of Particulate-Reinforced Ceramics .....	19
Table 2.3: Density and Mechanical Properties of Si <sub>3</sub> N <sub>4</sub> -SiC Composite System .....	20
Table 2.4: Physical and Mechanical Properties of Different Lanxide™ Composites.....	22
Table 2.5: Physical and Mechanical Properties for SiC <sub>p</sub> - and 2-D Nicalon™-Al <sub>2</sub> O <sub>3</sub> /Metal Composites .....	23
Table 2.6: Diffusion Rates in MgO and Al <sub>2</sub> O <sub>3</sub> .....	32
Table 2.7: Wetting Angle Data for Selected Ceramic/Metal Systems .....	52
Table 4.1: Specifications of the Starting Metals .....	55
Table 4.2: Typical Chemical and Physical Analysis of the Green Silicon Carbide Particles .....	60
Table 5.1: Composition (in Weight %) of the Various Aluminum Alloys Used .....	76
Table 5.2: Parabolic Rate Constants and Activation Energy for the Oxidation of Pure Liquid Aluminum .....	132
Table 5.3: Parabolic Rate Constants and the Activation Energy for the Oxidation of the (7/3) Alloy in Air Using 240-Grit SiC Powder (Different Runs).....	145
Table 5.4: Parabolic Rate Constants and the Activation Energy for the Oxidation of the (7/3) Alloy in Air Using 240-Grit SiC Powder (Single Run).....	146

Table 5.5: Growth Rates and Incubation Times for Alloys Containing 3.5 wt.% Si and Different Mg Contents for Composites Processed with and without SiC Reinforcing Particles at 1350°C .....	148
Table 5.6: Growth Rates and Incubation Times for Alloys Containing 1.5 wt.% Mg and Different Si Contents for Composites Processed with and without SiC Reinforcing Particles at 1350°C .....	154
Table AI.1: Calculated Pore Volume Fraction for the Four Different SiC Powders .....	190
Table AII.1: Computed Values from the Graph in Fig. AII.1 .....	192

# NOMENCLATURE

$\theta$ = contact angle	$g$ = gravitational constant
$\rho$ = density	$K$ = parabolic constant
$\xi$ = film thickness	$l$ = length of infiltration
$\eta$ = viscosity	$m$ = mass
$\phi$ = volume fraction	$M_x$ = molecular weight of component x
$\Delta G$ = Gibb's free energy	$P$ = pressure
$\Delta H$ = energy of formation	$r$ = radius of capillary
$\gamma_{lv}$ = liquid-vapor surface tension	$R$ = universal gas constant
$\Delta S$ = entropy	$Re$ = Reynolds number
$\gamma_{sl}$ = solid-liquid surface tension	$r_h$ = effective pore radius
$\gamma_{sv}$ = solid-vapor surface tension	$T$ = temperature
$A$ = surface area	$t$ = time
$A_p$ = powder surface area	$V$ = gas volume
$C_\infty$ = bulk concentration	$w$ = weight gain
$D$ = diffusion coefficient	$W_a$ = work of adhesion
$d_p$ = particle diameter	$x_i$ = concentration of element i
$E_a$ = activation energy	$Z_o$ = oxide thickness

# 1. INTRODUCTION

With the ever-increasing performance requirements of engineering materials, the properties of monolithic materials are pushed to their limits. In an effort to enhance these properties one approach that has been taken is the development of composite materials. As a result, two or more basically dissimilar materials with different mechanical and physical properties are combined to achieve a product whose final properties are superior to the individual constituents. For instance, ceramic materials having high strength suffer from brittleness and low toughness values. On the other hand, metals exhibit toughness but often lower strength. Thus, when a ceramic and a metal are combined together, the composite should exhibit the desirable properties of the two components: that is high strength, obtained from the high-strength and elastic modulus of the ceramic, and toughness, derived from the plastic deformation of the metal.<sup>1</sup> Hull<sup>2</sup> classified composite materials into seven different groups, according to the size, shape and distribution of two or more phases in the composite: (1) continuous fibers in a matrix, where the fibers are aligned in a random fashion, (2) short fibres or whiskers in a matrix, where the whiskers are aligned in a random fashion, (3) particulates in a matrix, where the particulates could be spheres, plates, ellipsoids, irregular shape, hollow or solid, (4) dispersion strengthened, as for the latter case (3), with particle size  $< 10\text{nm}$ , (5) lamellar structures, (6) skeletal or interpenetrating networks, and (7) multicomponent fibres, particles, etc.

There are also other ways to classify composite materials, i.e. by the type of matrix and the type of reinforcement. When the composite consists of an obvious type of matrix, it is termed either Ceramic-Matrix-Composite (CMC), Metal-Matrix-Composite (MMC) or Polymer-Matrix-Composite (PMC). However, when the composite is classified according to the type of reinforcement, it is termed either fibre-reinforced, whisker-reinforced, or particulate-reinforced composite.

There are several methods available for processing of ceramic matrix composites (CMC's). Sintering, hot pressing, injection moulding, and tape casting are conventional methods that suffer from some critical disadvantages such as difficulties to fully densify the composites in the presence of reinforcements, residual porosity which acts as stress concentrators and shrinkage associated with sintering. Shrinkage problems are very specific to ceramics and can cause problems with dimensional control, cracking and distortion, especially for large components. In the last ten years, a new ceramic matrix composite technology has been developed. This technology offers the potential of overcoming many of the limitations usually associated with traditional composite processing. This new technology, known as the DIMOX<sup>TM</sup> process, is the subject of this research which has concentrated on achieving a better understanding of this new process and the mechanism of formation of this composite.

## 2. LITERATURE REVIEW

Ceramic materials have properties that make them ideal candidates for many elevated temperature applications such as heat exchangers and turbine engine components. Due to the refractory nature of ceramics, they are, at times, the only choice for a material that can potentially satisfy the most demanding requirements particularly at high temperatures. In addition to offering high melting or decomposition temperatures, many ceramics possess other attractive features such as low density, high temperature strength and resistance to creep deformation, thermochemical stability and lack of reactivity in contact with other materials and various atmospheres, and, last, but not least, high wear resistance.

Probably the single most important disadvantage of ceramic materials is their relatively low fracture toughness, that is their resistance to the propagation of even a very small crack. This lack of toughness translates for design engineers into a low damage tolerance, or an unacceptably high potential for catastrophic, brittle failure. In addition, traditional ceramic processing methods place limitations on the shapes and sizes of components that can be made conveniently.

It has been established in the last decade that the fracture toughness of a ceramic material can be improved by several techniques,<sup>3</sup> (e.g. modulus transfer, crack bridging, crack deflection, etc.) The introduction of ceramic whiskers,<sup>4</sup> e.g., SiC, into

a ceramic matrix has resulted in moderate improvements in toughness, from 3-4 MPa·m<sup>1/2</sup> for conventional structural ceramics to as high as 8-12 MPa·m<sup>1/2</sup>.

## **2.1 PROCESSING OF METAL/CERAMIC COMPOSITES**

Reinforced ceramic composites present some of the most difficult processing problems known for ceramics. The combination of the requirements for optimized mechanical properties for matrix-reinforcement interfaces, and the relative instability of many reinforcements with respect to temperature, atmosphere, and chemical reaction with the matrix, place stringent limitations on processing temperatures and times. These concerns are reflected in increasing attention to coatings that can protect the reinforcements and preserve interfacial properties. Furthermore, composite systems are inherently difficult to densify without pressure because of two distinct physical effects.<sup>5</sup> One such effect is the reduced sintering stress, resulting from the internal hydrostatic tensile stress, which lowers matrix shrinkage in the presence of nondensifying inclusions. The second physical effect is the ultimate limit to densification presented by the bridging of inclusions or fibers at the percolation limit.<sup>5</sup>

The field of composite processing, either metal-matrix or ceramic-matrix composites, in itself is wide and covers a large number of methods of fabrication. Ceramic matrix composites (CMCs) can be made by either conventional powder processing techniques used for making polycrystalline ceramics or by some new and rather unconventional techniques. Some of the techniques, novel or otherwise, are no

more than variants on the processing of monolithic ceramics. As for the Lanxide™ composites, the matrix is a ceramic that contains a minor metal phase. Since Lanxide™ composites are classified as CMCs, the discussion will be limited to processing of ceramic-matrix composites.

### 2.1.1 Cold Pressing and Sintering

Cold pressing of the matrix powder and fiber followed by sintering is a carry over from conventional processing of ceramics.<sup>6</sup> This technique requires the incorporation of the ceramic powder in an organic binder. Clearly, complete removal of the organic binder must occur before a fully sintered body with a near-theoretical density can be obtained. During sintering, the matrix shrinks considerably and the resulting composite has many cracks. Depending on the difference in thermal expansion coefficients of the matrix and the reinforcement, a hydrostatic tensile stress may develop in the matrix on cooling.<sup>7,8</sup> The densification rate may be retarded in crystalline matrices in the presence of reinforcements as low as 3 vol.%.<sup>9</sup> In glass matrix composites sintering is retarded at reinforcements greater than about 15 vol.%.<sup>10</sup>

### 2.1.2 Hot Pressing

Some form of hot pressing is frequently employed in the consolidation stage of CMCs. This is because simultaneous application of pressure and high temperature can accelerate the rate of densification and a pore-free and fine-grained compact can be obtained. A common variant, called the *slurry infiltration* process, is perhaps the most important technique used to produce continuous fiber reinforced glass and glass-

ceramic composites.<sup>11,12,13</sup> The slurry infiltration process involves the incorporation of a reinforcing phase into an unconsolidated matrix followed by matrix consolidation by hot pressing. Fig. 2.1 shows a schematic of this process. In addition to incorporation of the reinforcing phase, the first stage also involves some kind of fiber alignment. A fiber preform is impregnated with a matrix-containing slurry by passing it through a slurry tank. The impregnated fiber preform sheets are called preregs, a term commonly used in the polymer matrix composites. The slurry consists of the matrix powder, a carrier liquid (water or alcohol) and an organic binder. The organic binder is burned out prior to consolidation. Wetting agents may be added to facilitate the infiltration of the fiber preform. The impregnated prepreg is wound on a drum and dried. This is followed by cutting and stacking of the preregs, and consolidation by hot pressing. The process has the advantage that the preregs can be arranged in a

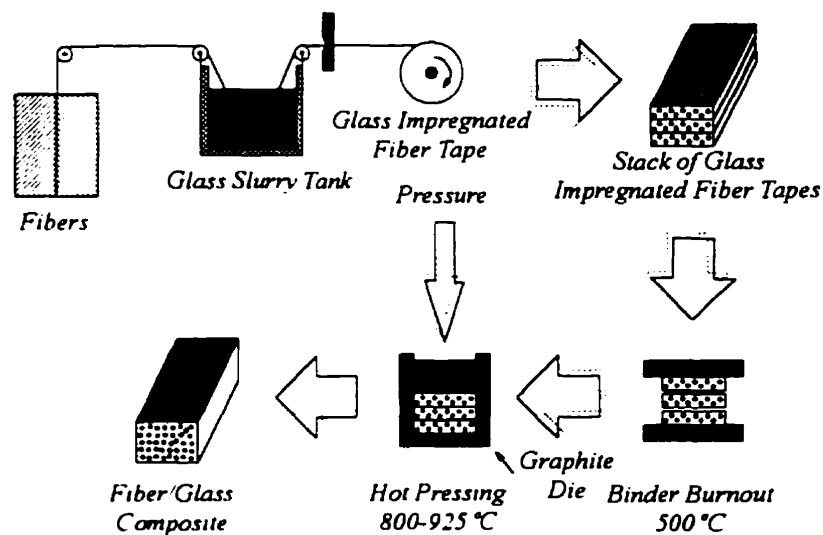


Fig. 2.1: Schematic of the slurry infiltration process of making fiber-reinforced glass and glass-ceramic composite.

variety of stacking sequences, for example unidirectional, cross-plyed ( $0^\circ/90^\circ/0^\circ/90^\circ$ , etc.), or angle-plyed ( $+\theta/-\theta/+ \theta/-\theta$ , etc.).

The slurry infiltration process is well suited for glass or glass-ceramic matrix composites, mainly because the processing temperatures for these materials are lower than those used for crystalline matrix materials. Any hot pressing process has certain limitations on producing complex shapes. Besides this basic limitation, there are certain other items that need to be considered when fabricating composites by the slurry infiltration method:

1. The fibers must be handled very carefully during all operations to avoid damaging the fiber surface.
2. The amount of tension applied determines the ability of the slurry to penetrate the tow. Too high a tension, however, can result in fiber fracture.
3. The fibers should suffer little or no damage during handling. Application of a very high pressure can easily damage fibers. The reinforcement can also suffer damage from reaction with the matrix at very high processing temperatures.
4. The slurry composition is obviously of great importance, i.e., parameters such as the powder content, particle size distribution, type and amount of binder, carrier medium, etc., will have a significant impact on the character of the final product.

The matrix should have as little porosity as possible in the final product as porosity in a structural ceramic material is highly undesirable.

In summary, the slurry infiltration process generally results in a fairly uniform fiber distribution, low porosity, and high strength values. The main

disadvantage of this process is that one is restricted to relatively low melting or low softening point matrix materials.

### **2.1.3 Reaction Bonding**

Reaction-forming methods have been successfully applied to both ceramic monolithics and composites. Excellent and often unique properties can be achieved with such materials because of their microstructural features. Major advantages of the reaction forming include net-shape fabrication, high purity, and the absence of sintering aids. Particle and reinforcement rearrangements can occur during densification without these sintering aids, thus eliminating shrinkage. The absence of such additives also allows retention of properties to high temperatures. Another advantage is that the reaction bonding temperatures for most systems are generally lower than the sintering temperatures. One great disadvantage of this process is that high porosity is hard to avoid. The reaction  $\text{Al} \rightarrow \text{Al}_2\text{O}_3$  to produce reaction-bonded  $\text{Al}_2\text{O}_3$  (RBAO) that can be infiltrated with liquid Al, Si, intermetallic phases, or superalloys, is currently available. However, silicon carbide (RBSC) and silicon nitride (RBSN) are the most commonly encountered matrices by reaction bonding. SiC powders are used to reinforce RBSN. For example, laser-synthesized submicron powders of silicon and carbon-rich SiC derived from  $\text{SiH}_4$  are dispersed in methanol or octanol, then ultrasonified, before being colloidally pressed at 17 MPa.<sup>14</sup> A drying step (20°C/h to 100°C/h) must be completed before nitriding at temperatures ranging from 1250°C to 1400°C. Depending on the nitriding temperature and material composition, composites are produced that

are 95% to 99% nitrified. Shrinkage ranges from 0.13% to 0.9%; therefore, net-shape fabrication is feasible.<sup>14</sup> However, the porosity levels are not given in this reference.

### 2.1.4 Infiltration

Infiltration of preforms made of a reinforcement can be done with a matrix material in solid, liquid or gaseous form. The infiltration technique is very similar to liquid polymer or metal infiltration (Fig. 2.2). It consists of eliminating the gases within a porous body and replacing them by a low viscosity liquid melt. Proper control of fluidity of the liquid matrix is, of course, the key to this technique because it yields a high-density matrix. Almost any reinforcement geometry can be used to produce a

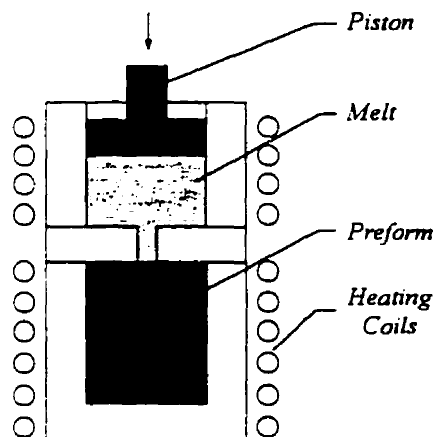


Fig. 2.2: Schematic of the melt infiltration process.

virtually flaw-free composite. The temperatures involved, however, are much higher than those encountered in polymer or metal processing. Processing at such high temperatures can lead to deleterious chemical reactions between the reinforcement and

the matrix. Viscosity of ceramic melts is generally very high, which makes the infiltration of preforms rather difficult. Wettability of the reinforcement by the molten ceramic is another item to be considered.

Muscat<sup>15</sup> has fabricated TiC/Al composites by spontaneous infiltration of aluminum into pre-sintered TiC preforms at various temperatures. He found that at temperatures as low as 860°C, infiltration of aluminum will occur.

Shanker *et al.*<sup>16</sup> have produced TaC-based metal-matrix composites by infiltration using both Al and Cu under Argon (0.1 MPa) at temperatures ranging from 1300 to 1900°C. They found that the two composites have different microstructures. While infiltration by Cu resulted in a composite with two continuous matrices, one ductile and one brittle, infiltration by Al resulted in breakdown of the interconnected TaC network and the composites consisted of discrete TaC particles in a continuous Al matrix. At elevated temperatures, Al reacted with the TaC particles and resulted in the formation of Al<sub>4</sub>C<sub>3</sub> and consequently the tensile strength and ductility are decreased.

Hillig<sup>17</sup> has discussed the melt infiltration processing of ceramic matrix composites with regard to chemical reactivity, melt viscosity and wetting of the reinforcement by the melt. A preform made of a reinforcement in any form (fiber, whisker, particle) having a network of pores can be infiltrated by a ceramic melt by using capillary pressure. Application of pressure or processing in a vacuum can aid the infiltration process. The most important of such processes is *squeeze casting* (Fig. 2.3). This process is a variant of a pre-existing process employing pressure to enhance casting quality.<sup>18</sup> The basic principle is to forge a liquid metal into a closed die and the

liquid metal then solidifies rapidly under high pressure (70 to 100 MPa). For metal matrix composites, a preheated porous preform is inserted into the die. Molten metal is then poured in, and a ram is inserted to apply pressure. The advantages of this process include simplicity, speed of operation, and high pressures that can be easily maintained throughout solidification to feed shrinkage. A major limitation is the size of parts that may be cast because of the high pressure requirements. Another limitation lies in the range of shapes that can be cast. The variety of material combinations is extensive.

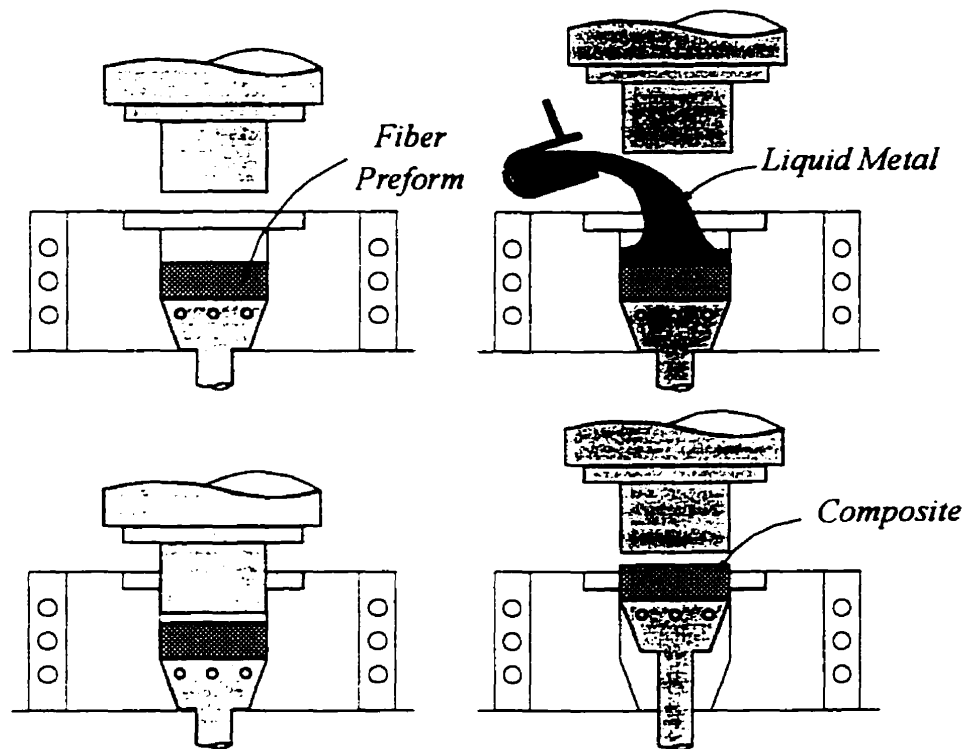


Fig. 2.3: Schematic of the Squeeze Casting process.

Naturally, Al is the most popular metal due to its low melting temperature. Ceramic preforms of all types and varieties have been infiltrated with this metal, including

particulate, whisker, and fiber preforms of SiC,<sup>19,20,21</sup> Al<sub>2</sub>O<sub>3</sub>,<sup>22,23</sup> Si<sub>3</sub>N<sub>4</sub>,<sup>24</sup> and even glass.<sup>25</sup>

### 2.1.5 DIMOX™ Process

Another version of liquid infiltration is the directed oxidation process or the Lanxide™ process. This technology was recently developed and patented<sup>26</sup> by the Lanxide Corporation\* which has kept specific details of this process confidential. One of the Lanxide™ processes is called DIMOX™, which stands for the Directed Metal OXidation process. This process involves formation of ceramic/metal composites by the directed oxidation of molten metal.<sup>27,28</sup> The ceramic-metal matrix is formed by the partial oxidation reaction of the molten metal with an oxidant. A schematic of the DIMOX™ process is shown in Fig. 2.4. Different metals can be used: aluminum, zirconium, titanium, etc., whereas both oxygen and nitrogen can be used as oxidants. The DIMOX™ process differs from the usual reaction of metals to form ceramic bodies, an example of which is the nitridation of a silicon powder compact to form reaction-bonded silicon nitride.<sup>29</sup>

The DIMOX™ process involves the oxidation of a bulk molten metal by a gas to form a solid ceramic body using a directed growth process. The reaction product forms, initially, on the exposed surface of a molten metal pool and then grows outward. The oxidation process is fed by the transport of additional metal through the

---

\*Lanxide Corporation, Tralce Industrial Park, Newark, Delaware 19711.

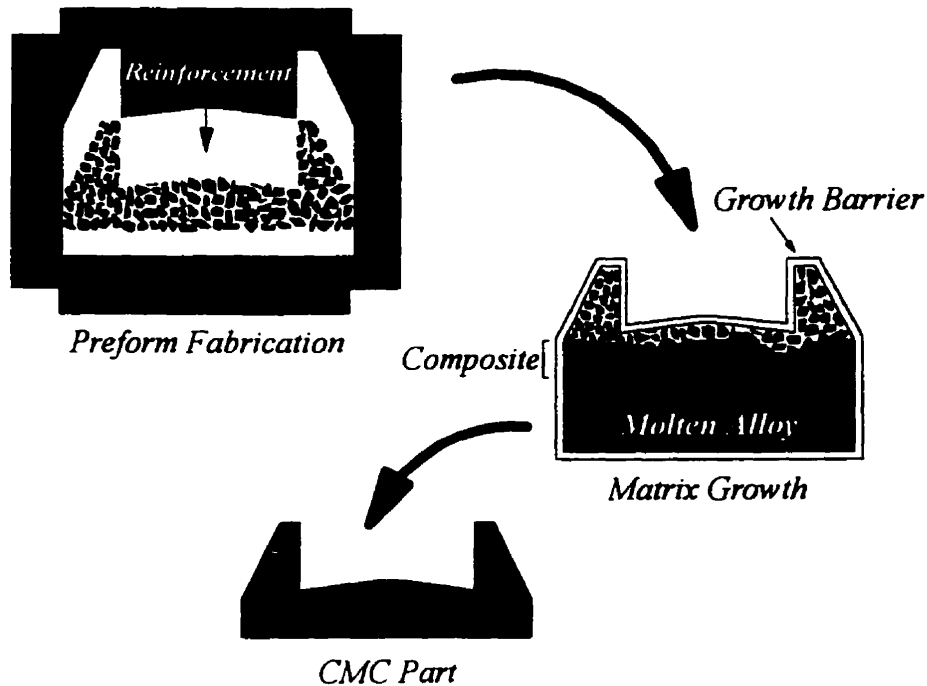


Fig. 2.4: DIMOX™ directed metal oxidation process.

ceramic product of the oxidation reaction between the parent metal and the gas phase oxidant. The amount of residual metal in the ceramic body therefore depends on the processing conditions and the starting material. Alternatively, particulate-reinforced or fiber-reinforced composites can be produced by the DIMOX™ process. In such cases, the reaction product grows into the filler material (particulates, fibers) to form the composite. The matrix of Lanxide™ composites consists of three-dimensionally interconnected ceramic material and interconnected metal channels supplying the metal to the surface during the reaction. The filler material is placed on top of the metal (in the direction of the oxidation growth process). The filler material could be in the form

of particulates, platelets, whiskers, or fibers. It is usually not displaced or disturbed during the matrix formation reaction.<sup>28</sup>

Some examples of filler materials are  $\text{Al}_2\text{O}_3$ , SiC,  $\text{BaTiO}_3$ , AlN,  $\text{B}_4\text{C}$ ,  $\text{TiB}_2$ , ZrN,  $\text{ZrB}_2$ , TiN. The choice of the filler is restricted by its compatibility with the oxidant atmosphere and with the molten metal. The  $\text{Al}_2\text{O}_3/\text{Al}$  system illustrates several features of the matrix formation process.<sup>27</sup> The desired rapid oxidation process requires minor amounts of other constituents or dopants. For example, the binary combination up to few wt. % of Mg and a group 14 element (Si, Ge, Sn, or Pb) could be introduced as constituents of the parent aluminum alloy. Alternatively, either or both doping elements could be introduced externally in the form of elemental or oxide powders that also promote rapid oxidation.<sup>30</sup> Temperatures within a limited process envelope, typically in the range of  $900^\circ$  to  $1350^\circ\text{C}$ , depending on the dopant materials used, are also necessary for practical reaction kinetics.<sup>28</sup> When the appropriate process conditions are achieved, matrix growth in the  $\text{Al}_2\text{O}_3/\text{Al}$  system typically occurs at a constant rate (linear kinetics). It has been observed that the microstructure and properties of the matrix can be strongly influenced by the nature and amount of dopants present and the process temperature and time. For instance, processing at a lower temperature tends to produce a matrix with a lower ceramic/metal phase ratio than matrices processed at higher temperatures. Once started under appropriate conditions, the DIMOX<sup>TM</sup> process appears to grow a composite of uniform microstructure as long as (i) molten metal and oxidant are available to sustain the process, and (ii) the process temperature is maintained.<sup>27</sup> Similarly, the formation of unreinforced AlN/Al ceramic composite

bodies by the directed oxidation of molten Al alloys in nitrogen has been presented,<sup>31,32,33,34</sup> and shows similarities with the  $\text{Al}_2\text{O}_3/\text{Al}$  system.

## 2.2 PROPERTIES OF COMPOSITES

When a new material is designed and fabricated, its mechanical behavior is usually the first property to be evaluated. In fact, this would be the proof of its superiority, at least when dealing with structural components. Because of this, mechanical property data has been generated from the conception of these materials and the quantity of available information is very abundant. In this section, selected materials will be reviewed, and these will be sub-divided under two categories; the first concerning *continuous fiber-reinforced-composites*, and the second *particulate-reinforced composites*. Another section will deal exclusively with *Lanxide™ composites*, since it is of special interest to this work.

### 2.2.1 Fiber-Reinforced Composites

Unidirectional fibers provide toughening and strengthening only in the direction parallel to the fibers. Such composites are referred to as having one-dimensional architecture. Strengthening and toughening in the other directions are no better than for the matrix. Such composites often fail in interlaminar shear rather than in tension. To increase the resistance to shear failure, fibers are built into the composite in additional directions.<sup>35</sup> Multidirectional architectures result in a decreased number of fibers in any single direction, so that the strength in the strongest direction is not as high as for unidirectional fibers. However, the strength in the minimum direction is

increased for three-dimensional composites to yield improved resistance to failure by the interlaminar shear fracture.

Ceramic fibers are generally available as continuous strands wound onto a spool and have an appearance similar to textile fibers. The fiber can consist of a single strand (monofilament) or multifilament strand (tow). The fiber strands are very smooth. Glass fibers were the first to be produced in large commercial volume. However, glass fibers have low elastic modulus and are not suitable for reinforcing most ceramic materials. The first high-modulus fibers produced in quantity were carbon and graphite. These have been produced with a wide range of properties, i.e., densities from less than  $1.7 \text{ g/cm}^3$  to greater than  $2.0 \text{ g/cm}^3$ , elastic moduli from 200 to over 500 GPa, and tensile strengths from under 1500 to over 5000 MPa. SiC fibers have much higher temperature capability than carbon and have been the subject of extensive development since the mid-1970's. The most widely evaluated SiC fiber has been Nicalon.<sup>\*</sup> Other Si-C-N multifilament fibers have been produced by polymer pyrolysis: Ube Tyranno, Textron 6 to 10  $\mu\text{m}$ , and several Dow Corning/Celanese compositions. All of these appear to be limited to use at less than about  $1400^\circ\text{C}$ . Textron has available monofilament fibers approximately 140  $\mu\text{m}$  in diameter. Oxide-based fibers (e.g. Nextel, Saffil, etc.) have better oxidation resistance than nonoxide fibers, but also have a greater tendency to react or bond to most matrix materials and exhibit poorer creep resistance.

---

<sup>\*</sup>Nicalon is a registered trademark of Space.

### ***2.2.1.1 Effect of Fiber Length***

Fiber length affects the toughening and strengthening of fibers in a composite. Modulus transfer can occur with short “chopped” fibers, but achieving a controlled architecture or distribution of chopped fibers is difficult. The minimum length of fiber that will yield stress transfer depends on the relative moduli of the fiber and matrix and on the degree of bonding between the fiber and the matrix. Some studies have indicated that stress transfer can occur down to an aspect ratio of about 8:1 (length of fiber:diameter of fiber).<sup>36</sup>

### ***2.2.1.2 Effect of Interfacial Bonding***

As the term stress transfer implies, the stress applied to the composite must be transferred from the matrix to the fibers. This transfer requires a reasonable level of bonding between the fibers and the matrix. Too-weak a bond can result in shear at the fiber-matrix interface and reduce the amount of stress transfer. To obtain “graceful” failure it is generally accepted that a weak interface is required for CMC and coatings are generally applied to the fibers.

### ***2.2.1.3 Silicon Carbide Fiber Composites***

Silicon carbide fibers have been incorporated in glass, mullite and  $\text{Si}_3\text{N}_4$  matrices. Singh and Gaddipati<sup>37</sup> have evaluated the mechanical properties of uniaxially reinforced mullite-SiC composites. Table 2.1 shows physical and mechanical properties of various SiC fiber-reinforced mullite.

Table 2.1: Summary of Mechanical Property Data for Monolithic Mullite and Mullite-Silicon Carbide Composite<sup>37</sup>

Monolith or Composite	Density (g/cm <sup>3</sup> )	Open Porosity (%)	Fiber Content (vol%)	Interface Type	Properties at Maximum Load		
					Stress (MPa)	Fract. Strain (%)	Elastic Mod. (GPa)
M	3.13	0	0	N	271	0.18	153
M	3.13	0	0	N	202	0.16	125
C	3.08	0.72	25	A/R	694	0.96	95
C	3.09	0.31	25	A/R	780	0.98	84
C	3.10	0.04	25	A/R	709	1.20	82
C	3.09	0.02	25	A/R	777	1.21	81
C	3.09	0.01	25	A/R	855	1.02	96
C	3.09	0.00	25	A/R	646	0.90	57

N=None

A/R= As-Received

## 2.2.2 Particle-Reinforced Composites

Fracture toughness largely depends on the microstructure of a ceramic and on the path followed by a crack when it propagates through the material. A crack passing through a material reinforced with second phase particles does not follow a smooth planar path. This is enhanced by the addition of a dispersion of particles to a matrix. The crack then follows the boundaries around some second phase particles and fractures other particles. The total new surface generated as the crack propagates is greater than was the case for the matrix alone. This results in greater fracture surface energy and greater fracture toughness. However, it is important that the particles do not react with the matrix material. If the particles are irregular in shape or much larger in grain size than the matrix, some bridging can occur. If the particles are significantly different in

thermal expansion coefficient than the matrix, some toughening by microcrack formation can occur. Table 2.2 shows some examples of particulate-reinforced ceramics.<sup>36</sup>

Table 2.2: Examples of Particulate-Reinforced Ceramics<sup>36</sup>

Material	Flexural Strength (MPa)	Fracture Toughness (MPa·m <sup>1/2</sup> )
Baseline Hot-Pressed AY6 Si <sub>3</sub> N <sub>4</sub>	773	4.6
AY6 + 10 vol. % 8 μm SiC	950	5.0
AY6 + 20 vol. % 8 μm SiC	763	4.8
AY6 + 30 vol. % 8 μm SiC	885	4.9
Baseline Hot-Pressed Si <sub>3</sub> N <sub>4</sub>	760	4.2
Si <sub>3</sub> N <sub>4</sub> + 30 vol. % 12 μm SiC	520	6.7
Baseline Al <sub>2</sub> O <sub>3</sub>	420	4.0
Al <sub>2</sub> O <sub>3</sub> -5 vol. % TiB <sub>2</sub>	650	6.5
Sintered Al <sub>2</sub> O <sub>3</sub> -30 wt % TiC	480	4.4
Hot-Pressed Al <sub>2</sub> O <sub>3</sub> -30 wt % TiC	583	4.5
Baseline SiC	360	≈3
Sintered SiC-16 vol. % TiB <sub>2</sub>	478	6.8-8.9

### 2.2.2.1 SiC Particle-Reinforced Composites

Lange<sup>38</sup> studied the effect of microstructure on the strength of Si<sub>3</sub>N<sub>4</sub>-SiC composites fabricated by hot-pressing. Some of the experimental results are presented in Table 2.3. He investigated this system to better understand the relations between the microstructure and the factors that control the strength of a brittle material, such as fracture energy, elastic modulus, and crack size. He used three SiC particle sizes: 5, 9, and 32 μm. Lange concluded that the difference in size between the matrix grains and the particles in the 5- and 9-μm composites was too small to allow the interaction of the

crack front with the second-phase dispersion. Thus, in the 32- $\mu\text{m}$  composites fracture energy increased, whereas in the 5- and 9- $\mu\text{m}$  composites the fracture energy decreased from that of the matrix. Finally, Lange concluded that the 5- $\mu\text{m}$   $\text{Si}_3\text{N}_4$ -SiC composites are superior in two aspects to the hot-pressed  $\text{Si}_3\text{N}_4$  matrix material. Despite their slightly lower strength at room temperature, these composites are twice as strong as the matrix at 1400°C. Also their thermal conductivity is greater than that of the matrix and was found to increase 13% for every 0.10 volume fraction SiC added to the matrix.

Table 2.3: Density and Mechanical Properties of  $\text{Si}_3\text{N}_4$ -SiC Composite System

Material	Vol. Fraction	Density (g/cm <sup>3</sup> )	Elastic Modulus (GPa)	Flexural Strength (MPa)		
				25°C	1300°C	1400°C
$\text{Si}_3\text{N}_4$ (matrix)	-	3.20	306.8	654±41%	187.5	119.9
5- $\mu\text{m}$ SiC Composite	0.10	3.21	317.8	577±55%	-	246.2
	0.20	3.20	329.6	593±48%	380.6	273.7
	0.30	3.15	341.3	584±34%	-	237.2
9- $\mu\text{m}$ SiC Composite	0.10	3.21	317.8	520±82%	-	206.8
	0.20	3.21	329.6	482±62%	-	209.6
	0.30	3.21	341.3	393±69%	-	194.4

### 2.2.3 Lanxide™ Composites

Lanxide™ composites fabricated without a filler material have a columnar grain structure. The  $\text{Al}_2\text{O}_3$  grains are oriented with the c-axis aligned with the growth direction.<sup>39</sup> The presence of a filler material, such as fibers and particulates, largely disrupts this preferred orientation. This is likely due to a tortuous oxidation path and random nucleation sites generated by the reinforcement phase.<sup>39</sup>

The presence of a metal phase in the particulate reinforced composites enhances the composite toughness at low temperatures by bridging any cracks with ductile metal ligaments formed by plastic deformation of the metal. The fiber reinforced composites have the metal phase removed by a secondary processing step and thus exhibit enhanced fracture toughness due to crack tip bridging by fiber pull-out. Andersson and Aghajanian<sup>40</sup> used a two-dimensional strain energy analysis to model the mechanisms of toughening in the Lanxide™ composites. They concluded that the increased fracture toughness of ceramic matrix composites with adherent ductile phases can be attributed to clamping forces applied by metal ligaments that bridge the crack faces behind the crack front. These clamping forces retard the crack from opening as an external stress is applied. The two authors calculated the fracture toughness values of several systems using their model, and found that the calculated critical stress intensity factors adequately predict experimental values for these materials.

The directed oxidation of metals for the production of ceramic matrix composites offers the potential to overcome many of the limitations of other ceramic technologies. The fabrication of reinforced ceramic composites by this process offers many advantages compared to conventional ceramic technologies. It allows the engineering of specific material properties through the selection of composite constituents and the control of composite microstructure. In the case of fiber reinforced composites, the growth process does not exert any forces on the fibers in the preform, and therefore the fiber architecture in a lay-up is not disturbed during growth. Fibers strategically placed in a preform remain in the same place in the fabricated composite.

Since matrix formation occurs by a growth process, there is no densification shrinkage; thus, the control of dimensional tolerances and the fabrication of very large components are facilitated. Parts with even relatively complex geometries can often be fabricated without difficulty. The growth process produces a matrix with grain boundaries free of impurity phases, which is favorable for high temperature properties, and the process temperatures are low enough to not thermally damage the fibers. In addition, the cost projections for components made with this technology are quite promising, depending on the specific component to be made and its performance requirements.

Table 2.4: Physical and Mechanical Properties of Different Lanxide™ Composites

Property	Material A	Material B(i)	Material B(ii)	Material B(iii)	Material D
Al <sub>2</sub> O <sub>3</sub> Content (Vol. %)	83	81	74	72	82
Al Content (Vol. %)	17	3	3	1	13
Porosity (Vol. %)	0	16	23	27	5
Density (g/cm <sup>3</sup> )	3.53	3.31	3.04	2.89	3.61
Thermal Expansion (10 <sup>-6</sup> K <sup>-1</sup> )	11.0	N/A	9.5	9.3	9.8
Thermal Conductivity (W/m·K)	39.6	11.8	N/A	N/A	29.3
Young's Modulus (GPa)	231	121	96	88	304
Shear Modulus (GPa)	88	51	41	39	123
Poisson's Ratio	0.312	0.19	0.184	0.137	0.24
Vickers Hardness (GPa)	5.09	1.82	16.9	1.41	14.4
Compressive Strength (MPa)	984	414	N/A	N/A	1910

Lanxide™ composites are reported to have superior wear characteristics compared to monolithic ceramics and metals.<sup>41</sup> The effect of processing conditions on the physical and mechanical properties of composites processed without filler materials has been reviewed.<sup>42</sup> Some mechanical and physical properties of Lanxide™ Al/Al<sub>2</sub>O<sub>3</sub> ceramic composites without filler materials are presented in Table 2.4.

Table 2.5: Physical and Mechanical Properties for SiC<sub>p</sub>- and 2-D Nicalon™-Al<sub>2</sub>O<sub>3</sub>/Metal Composites

	SiC <sub>p</sub> /Al <sub>2</sub> O <sub>3</sub> /Metal Composites	2-D Nicalon/Al <sub>2</sub> O <sub>3</sub> /Metal Composites
Bulk Density.(g/cm <sup>3</sup> )	3.35	2.9
Young's Modulus.(GPa)	320	140
Shear Modulus.(GPa)	125	-
Four Point Flexural Strength.(MPa)		
25°C	-	461±28
1200°C	-	488±22
1300°C	-	400±12
1400°C	-	340±11
Fracture Toughness.(MPa·m <sup>1/2</sup> )		
25°C	5.6	27.8±4.6
1200°C	-	23.3±2.7
1300°C	-	19.2±2.8
1400°C	-	15.6±3.7
Poisson's Ratio	0.27	-
CTE 25-1400°C.(ppm/°C)	8.0	5.8
Thermal Conductivity.....(W/m·K)		
25°C	70	8.7
500°C	34	
1000°C	20	5.7
Silicon Carbide Loading...(vol. %)	48	35
Residual Metal.....(vol. %)	13	-

Nagelberg *et al.*<sup>43</sup> reported advantageous properties for SiC/Al<sub>2</sub>O<sub>3</sub> Lanxide™ composites at low and high temperatures by reinforcing the matrix with 6-μm SiC particulates and 2-D Nicalon™ fibers. These properties are summarized in Table 2.5. The matrix of the grown composite is ceramic with some residual metal, most of which is in the form of interconnected channels. The residual metal phase consists primarily of aluminum. When these composites are used for elevated temperature applications, the presence of residual aluminum, which could become molten, can be disadvantageous. Hence, an aluminum metal removal process is used to reduce the residual aluminum content from 6-7 wt% to 1-2 wt%.<sup>44</sup>

## 2.3 OXIDATION OF ALUMINUM ALLOYS

This section of the literature review will focus on the oxidation behavior and kinetics of pure aluminum and aluminum alloys in both solid and liquid states. However, the review of the related work on the DIMOX™ process will be left for the results and discussion sections and will be used for comparison with the results of this work.

Immediately after exposure of a pure metal to some gaseous atmosphere, absorption takes place. Depending on the affinity of the metal for the gas, the temperature and the pressure, further atomic layers will be added and a film will grow. Any process that deprives the metal of electrons may be termed "oxidation". The oxide films that form in the first stages of contact at ordinary temperatures are of the order of tens, or possibly hundreds, of Angstroms. What is usually measured is the change in

weight per unit area with time. It is then assumed that the film grows uniformly and the weight increase is converted into thickness ( $\xi$ ). A number of relationships, thickness versus time, have been observed experimentally for thin and thick film growth, such as linear, parabolic, cubic, logarithmic and inverse logarithmic growth, represented by the following equations:<sup>45</sup>

$$\text{Linear} \quad \xi = k_l \cdot t \quad (2.1)$$

$$\text{Parabolic} \quad \xi^2 = k_p \cdot t \quad (2.2)$$

$$\text{Cubic} \quad \xi^3 = k_c \cdot t \quad (2.3)$$

$$\text{Logarithmic} \quad \xi = k_e \cdot \log(a \cdot t + t_0) \quad (2.4)$$

$$\text{Inverse Logarithmic} \quad \frac{1}{\xi} = A - k_i \cdot \log t \quad (2.5)$$

where  $\xi$  is thickness,  $t$  is time, and  $k$ ,  $a$ , and  $A$ , are constants. For the film to grow, it must be penetrated by electrons and ions, either cations or anions or both. It has been the aim of various theories to find the rate-determining step. Use is made of the "volume ratio" representing the ratio of the molecular volume of a compound to the atomic volume of its metal, where both volumes refer to equivalent amounts of metal. Coherent oxidation layers are generally formed only when this ratio is between one and two. When it is less than unity (alkali metals, magnesium, etc.) the metal surface tends not to be fully covered by the oxide which is therefore not protective, and linear oxidation prevails. When the volume ratio is greater than two, strong compressive stresses develop near the interface, in particular when initial exchange of matter is by

oxygen diffusion, and this then breaks up into fragments, often a powdery mass. The rate law is again linear, mostly after an initial parabolic rate (paralinear).<sup>45</sup>

The linear relationship,

$$\Delta m = k_1 \cdot t \quad (2.6)$$

is the simplest form that was found to express experimental data. Equation (2.6) can also be expressed in terms of thickness ( $\xi$ ) of the surface oxide or decrease in pressure ( $\Delta P$ ) of the gas in place of increase in weight per unit surface area ( $\Delta m$ ). As a rule, one may convert these quantities from one to the other. If the gas volume ( $V$ ) and the composition of the oxide layer are accurately known, the decrease in pressure is calculated from the increase in weight by the ideal gas law:

$$\Delta P = \Delta m \cdot A \cdot R \cdot T / M \cdot V \quad (2.7)$$

where  $A$  is the surface area in  $\text{cm}^2$  of the metal specimen and  $M$  the molecular weight of the absorbed gas. The thickness of the surface layer can be obtained from the increase in weight by means of:

$$\xi = \Delta m \cdot M_{AX} / M_x \cdot \rho \quad (2.8)$$

where  $M_{AX}$  and  $\rho$  are the molecular weight and density of the surface compound, respectively, and  $M_x$  the weight of negative component per molecule of surface compound. This relationship must be applied with great caution as the density of a surface layer need not necessarily agree with that of the bulk material. Layers may either be porous or in a compressed state.

### 2.3.1 Oxidation Behavior of Pure Aluminum

This section reviews the oxidation behavior of aluminum, including amorphous film growth and the effects of alloying elements on the kinetics of oxidation. Aluminum is an extremely reactive metal and its usefulness as an engineering material is partly due to the tough, thin, highly protective, self-healing surface oxide film that readily forms when freshly created surfaces are exposed to the environment. At relatively low temperatures (i.e.,  $\leq 300^\circ\text{C}$ ), the surface oxide can be thought of in terms of a continuous amorphous film that thickens as a function of temperature.

The oxidation of pure solid aluminum has been studied previously and there are significant amounts of data available on the kinetics of oxidation of aluminum.<sup>46,47,48,49</sup> Dignam *et al.*<sup>50</sup> reported that the kinetics of oxidation of aluminum in dry oxygen at  $454^\circ\text{C}$  change at about 10.5 hours, as seen in Fig. 2.5. In the initial period, the rate of weight gain steadily decreases with time, whereas in the second period it begins to increase slowly. The first or initial period represents the growth of a protective oxide film and corresponds to the thickening of the initially present amorphous film. The inflection point is related to the onset of appreciable growth of crystalline oxide. Doherty and Davis<sup>48</sup> observed that crystallites of  $\gamma\text{-Al}_2\text{O}_3$  were nucleated at the surface between the metal and the amorphous oxide in air, and grew down into the metal by diffusion of oxygen from the oxide-oxygen interface. Thus the onset of this process should be accompanied by an increase in the rate of oxidation over

that due to the growth of the amorphous film alone. Above 530°C, the growth of the crystalline oxide was reported to start at essentially time zero.<sup>50</sup> Stucki *et al.*<sup>51</sup> used EELS (Electron Energy Loss Spectroscopy) to estimate the oxide coverage on surfaces of pure solid and pure liquid aluminum. In their experiments, intensity variations of the plasmon oscillations in EELS show that for solid Al, only electrons from the surface region take part in bonding to oxygen. In the case of liquid Al, after a compact oxide layer on the liquid surface is formed, the oxidation rate decreases drastically, and further oxidation is controlled by the diffusion of Al (not oxygen, which requires a much higher thermal activation energy) through the solid oxide layer.<sup>51</sup>

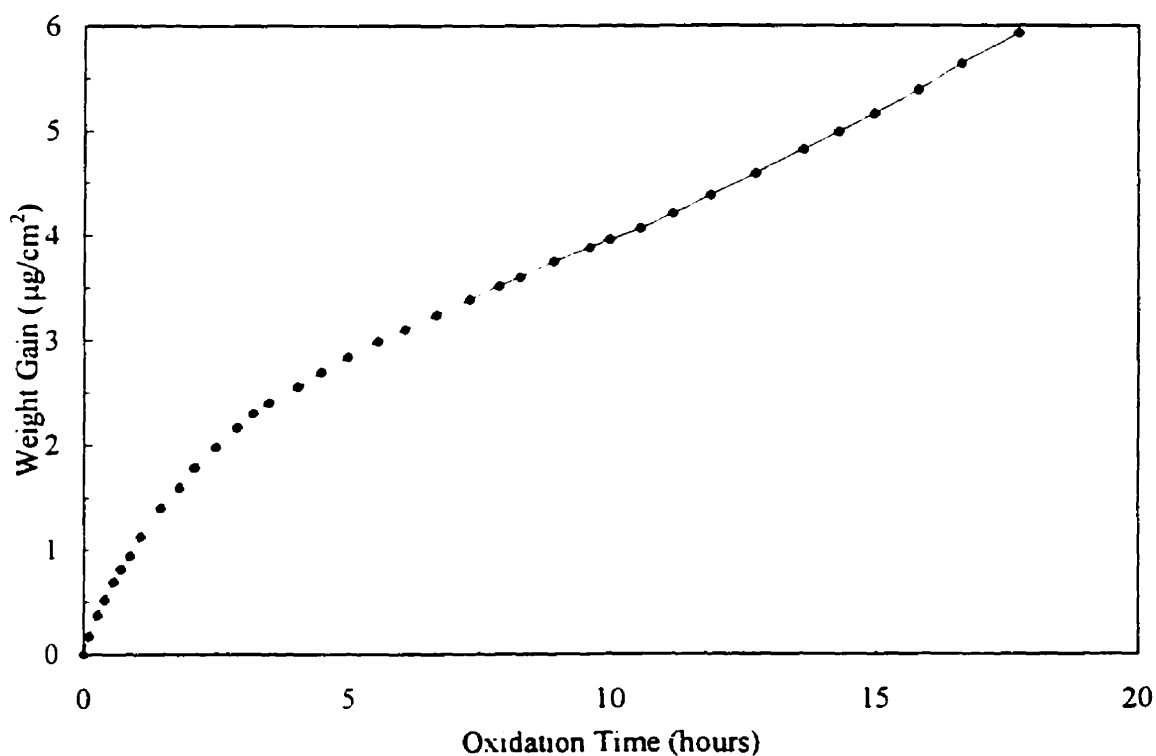


Fig. 2.5: Weight gain data for the initial period of oxidation at 454°C.<sup>50</sup>

Dignam and Fawcett<sup>50</sup> suggested a model for the mechanism of oxidation of superpurity aluminum in dry oxygen based, in large measure, on the results reported by Doherty and Davis,<sup>48</sup> and are summarized below.

1. The crystallites grow down into the metal rather than protrude from the surface and do not extend to the surface.
2. The crystallites grow as a result of transport of oxygen species, rather than metal species, through the amorphous film.
3. The crystallites form over a short period of time relative to their period of growth, in that the number density of crystallites, once formed, is independent of oxidation time within the limits of observation. It is also independent of oxidation temperature in the range 450°-600°C.
4. The local number density of crystallites varies somewhat within the boundaries of a single metal grain and very significantly from grain to grain.
5. As far as it is possible to tell by examination of the micrographs, the breadth of a crystallite increases approximately linearly with time, until coalescence occurs. The variation in shape of crystallites from one metal grain to another, however, makes size comparison difficult.
6. The amorphous film lying between the crystallites continues to grow. Thus contact between the amorphous film and the metal in these regions is maintained.
7. The amorphous film lying on top of the crystallites does not continue to grow.

Smeltzer<sup>52</sup> has studied the surface oxidation kinetics of metallographically polished high purity aluminum in the temperature range 400°-600°C using a vacuum

microbalance technique. He reported that at all temperatures there was an initial rapid rate of oxidation that was followed by an approximately constant rate of film growth for a period dependent on temperature. After this period, the rate of oxidation decreased with time to a negligible value. The concept of diffusion-controlled parabolic oxidation was employed in his analysis, which was borne out first by Cabrera and Mott<sup>53</sup> who postulated that the surface film on aluminum consists of a metal-excess oxide and that the film growth occurs by diffusion of metallic ions through lattice interstitial positions. In their view, the kinetics of gaseous oxidation of aluminum should be governed by a parabolic law in the temperature range 400°-600°C.

The equation for the parabolic law of oxidation is:

$$x^2 = Kt + C \quad (2.9)$$

where  $x$  is the film thickness,  $t$  is the time,  $K$  is the parabolic rate constant, and  $C$  is a constant representing the initial film thickness.

Cabrera and Mott<sup>53</sup> showed that this law is applicable to the growth of both thin and thick films. The parabolic rate constant for a thin film is:

$$K = \frac{V\Omega q_i \gamma}{a_i kT} \exp\left(-\frac{W_i}{kT}\right) \quad (2.10)$$

and for a thick film:

$$K = 2\Omega(N_i N_o)^{1/2} a_i \gamma \exp\left\{-\frac{1}{2}(W_i + \phi) - U/kT\right\} \quad (2.11)$$

Here  $W$  and  $\phi$  are the potential energy barriers at the metal/oxide interface against ion and electron diffusion, respectively.  $W_i$  and  $U$  are the potential energy barriers between ion diffusion states from metal to oxide and between interstitial positions in the oxide,

respectively,  $N_i$  and  $N_c$  are the concentrations of interstitial positions in the oxide per metal ion,  $q_i$  is the electrical charge of the metallic ion,  $\gamma$  is the frequency of vibration of the oxide lattice,  $a_i$  is the half-width of the potential barrier against ion diffusion,  $k$  is Boltzmann's constant, and  $T$  is the absolute temperature.

Parabolic oxidation rate constants are expressed in Arrhenius form:

$$\ln K = A - E/RT \quad (2.12)$$

where  $A$  is the frequency factor and  $E$  is the activation energy. Values of 37.9 and 41.0 kcal/mole (158.7 and 171.7 kJ/mol) were determined for the activation energy of reaction in the thin film range for specimens vacuum annealed at 500°C and 600°C, respectively.<sup>52</sup>

### 2.3.2 Oxidation Behavior of Aluminum Alloys

The temperature dependence of reaction rates is governed by an exponential relation known as the Arrhenius equation. Corresponding to this equation, the temperature dependence of diffusion rates is generally written in the form:

$$D = D_o \cdot \exp\left(-\frac{Q}{RT}\right) \quad (2.13)$$

where  $D_o$  and  $Q$  are constants. The values of these two constants for MgO and Al<sub>2</sub>O<sub>3</sub> are shown in Table 2.6.<sup>54</sup>

Table 2.6: Diffusion Rates in MgO and Al<sub>2</sub>O<sub>3</sub>

Compound	Diffusing Ion	Temp. Range (°C)	$D_o$ (cm <sup>2</sup> /sec)	$Q$ (kJ/mol)
MgO	Mg <sup>2+</sup>	1400-1600	0.25	330.8
	O <sup>2-</sup>	1300-1750	$2.5 \times 10^{-6}$	261.3
Al <sub>2</sub> O <sub>3</sub>	O <sup>2-</sup>	1200-1600	$6.3 \times 10^{-8}$	241.2

Magnesium additions to aluminum form a technologically important alloy system having good mechanical and physical properties in conjunction with excellent aqueous corrosion resistance. However, these alloys oxidize rapidly both when molten and during high temperature heat treatment of solid product forms, giving rise to thick surface films of magnesium oxide which may be accompanied by severe metal blistering in moist environments. Before further processing can take place, the surface films must be removed which results in an expensive loss of metal, and can make processes such as scrap recycling commercially uneconomical. Methods of controlling the rapid oxidation of Al-Mg alloys have been established, such as by trace-alloying additions, with the most effective additive being toxic Be. The surfaces of aluminum and aluminum alloys are covered by a layer of oxide which is very stable under a variety of conditions. The composition, thickness and morphology of the oxide layer are determined by the composition of the alloy and the conditions under which the oxide was formed. Magnesium-containing aluminum alloys are of interest because it may be possible to produce high integrity castings from them by using hot isostatic pressure treatment to close and heal internal porosity. However, if pore surfaces are

oxidized, the ability of these surfaces to diffusion bond after closure will depend on the composition and thickness of the oxide.

The oxidation of pure magnesium has been studied by Gregg and Jepson,<sup>55</sup> who found that a protective film was always formed initially, but that above 400°C a “breakaway” process occurred (Fig. 2.6) and the oxidation became linear. Above 550°C

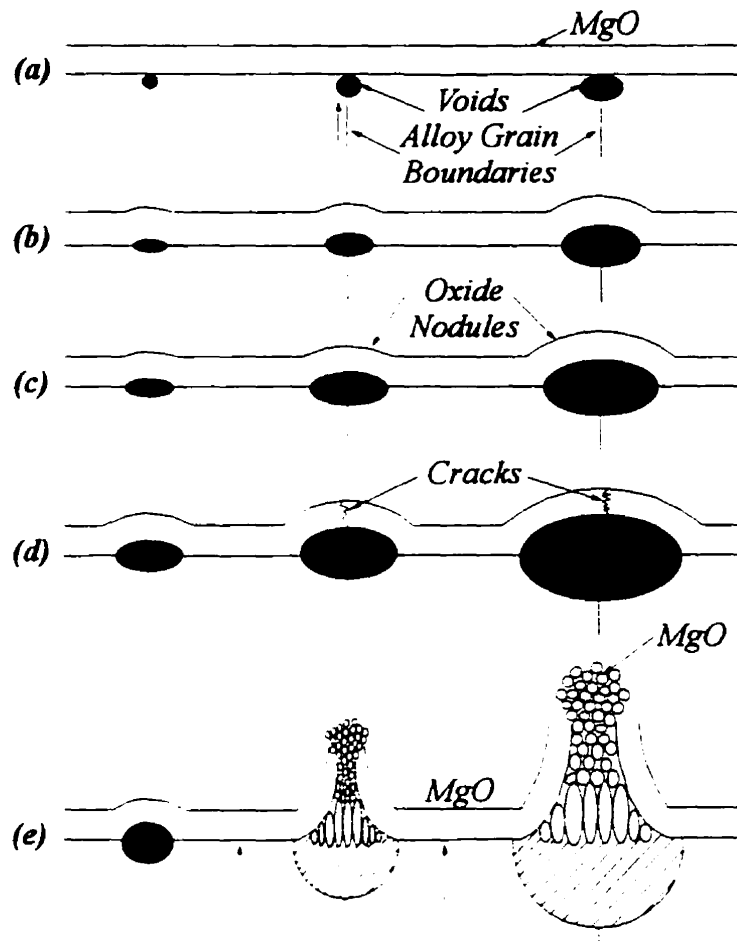


Fig. 2.6: Schematic representation of the various stages of a model for nonprotective oxidation of Al-Mg alloy at high temperatures.

a second breakaway to a more rapid linear oxidation was observed. It was postulated that at the first breakaway ruptures appeared in the protective film, but the ruptures did not extend right down to the metal surface; at the second breakaway the cracks penetrated to the underlying metal, and the oxidation rate then became proportional to the area of metal exposed.

The heat of formation of  $\text{Al}_2\text{O}_3$  is 1,113.6 kJ/mol at 298K while that of MgO is 1202.2 kJ/mol.<sup>56</sup> These figures indicate that both metals have a very high affinity for oxygen with magnesium being the higher of the two. If aluminum and magnesium atoms are equally available at the metal surface, then the oxide layer would be expected to be predominantly MgO. However, the formation of oxides on metals is not controlled only by the thermodynamic equilibrium. The rate of growth is determined by diffusion rates of the metal cations and/or oxygen anions through the oxide. At high temperatures, where ions and vacancies are highly mobile in the oxide lattice, a chemical potential gradient between the outer oxide surface and the oxide/metal interface causes migration of the mobile species through the oxide. During low-temperature oxidation (which includes room-temperature oxidation for most metals) the metal and oxide species are much less mobile in the oxide lattice and the chemical potential gradient is too small to drive the mobile species through the oxide film. The driving force for migration in this case is a large electric field ( $10^5$ - $10^6$  V/m) which is set up across the oxide.<sup>57</sup> The electric field enhances the flux of cations through the oxide layer.

The mechanism of oxidation of aluminum-magnesium alloys is of theoretical interest, since the two pure metals follow different oxidation rate laws. There are also important practical aspects that arise from the high rate of oxidation of the alloys and lead to undesirable effects during fabrication. For example, dark surface films are produced when the alloys are heat-treated; compared with magnesium-free alloys, more tool wear takes place when they are processed; and frequently the adhesion of applied organic films is poor.<sup>58</sup> The different oxidation characteristics shown by aluminum and magnesium are largely a result of the fact that aluminum forms an oxide of volume ratio  $> 1$ , while magnesium oxide has a volume ratio  $< 1$ . Therefore aluminum should form a continuous protective oxide film, whereas magnesium should form a porous one.<sup>59</sup>

The oxidation characteristics of aluminum-magnesium alloys would be expected to depend on the relative rates of diffusion of the ions of the metals, the rate being higher for magnesium than aluminum. De Brouckère<sup>60</sup> studied the oxidation of aluminum containing up to 8% magnesium by means of electron diffraction and showed that the film had a duplex structure. The inner film was thin and continuous and consisted of alumina ( $\text{Al}_2\text{O}_3$ ) or magnesium aluminate ( $\text{MgAl}_2\text{O}_4$ ), while the thick outer layer was porous and consisted largely of magnesia ( $\text{MgO}$ ). Smeltzer<sup>61</sup> studied the oxidation of pure aluminum-3% magnesium alloy in dry oxygen between 200 and 550°C. He found that the oxidation kinetics were complex, but approximated his results for temperatures above 350°C to a parabolic-linear mode of oxidation.

Field *et al.*<sup>69</sup> studied the high temperature oxidation of Al-4.2 wt. % Mg alloy in dry and wet oxygen environment between 400 and 575°C. They reported that the high temperature oxide films that develop on this particular alloy are essentially microcrystalline MgO and consist of two types of MgO, termed primary and secondary oxides, depending on the mechanism of formation. Primary oxidation is the direct reaction between magnesium from the alloy substrate with oxygen to form MgO and this occurs at the oxide/metal interface. Secondary oxidation is the solid-state reduction of the original air formed film of amorphous  $\gamma$ -Al<sub>2</sub>O<sub>3</sub> by Mg from the alloy substrate to form MgO, according to:



The oxidation weight gain curves were explained in terms of microstructural model based on disruption of a protective amorphous overlayer by penetrative primary MgO and subsequent development of a corrugated oxide/metal interface.

Zayan *et al.*<sup>62</sup> have studied the oxidation behavior of two high-purity Al-Mg (0.4 and 2.0 wt. % Mg) alloys in dry air at 550°C for 18 and 90 hours. They reported the following observations.

1. The oxidation of the alloys showed a strong tendency for Mg to diffuse from the base alloys. The magnesium has appeared in the oxide layer as MgO and spinel (MgAl<sub>2</sub>O<sub>4</sub>). The major constituent was MgO. The molar concentration of MgO decreased with increasing depth, while that of spinel increased.
2. The rate-controlling mechanism for the growth of the oxide layer in the Al-0.4% Mg alloy was the solid-state diffusion of Mg in the MgO-spinel constituents.

3. For alloys of higher magnesium content, the high outward diffusion rate of Mg atoms through local paths of easy diffusion in the alloy surface has resulted in the participation of Mg vapor locally in the growth of the oxide layer. The growth of the oxide layer would therefore be controlled by solid-state diffusion of Mg through the adherent protective oxide areas by the transport of Mg vapor across voids formed between the alloy metal and oxide layer.

Zayan *et al.*<sup>62</sup> established some kinetic mechanisms for the oxidation of solid Al-Mg alloys at 550°C. They concluded that MgO does not usually form a continuous layer, and therefore the adjacent matrix would be depleted in magnesium, inducing the formation of the thermodynamically favored spinel phase.<sup>63</sup> The spinel phase could also be formed by the reduction of the amorphous Al<sub>2</sub>O<sub>3</sub> layer,<sup>62</sup> which constitutes the alloy surface before the oxidation treatment. The overall growth rate of the oxide layer would therefore be controlled by solid-state diffusion of Mg in MgO and spinel constituents, since the inward diffusion of oxygen in the oxide is negligible.<sup>64</sup> Assuming that the concentration gradient of Mg through the oxide layer is linear, the solution to Fick's law for the Mg flux would be given by:<sup>65</sup>

$$Z_o^2 C_s = 2DC_x t \quad (2.15)$$

where  $Z_o$  is the oxide thickness,  $t$  is the oxidation time,  $D$  is diffusion coefficient of Mg through the oxide layer,  $C_x$  is the bulk concentration of Mg in the alloy, and  $C_s$  is the concentration of Mg at the oxide surface. Taking  $Z_o$  as the mean depth at which the aluminum signal had risen to 50 at. %, the diffusion coefficient of Mg in the growing mixed oxide layer was estimated as  $2.5 \times 10^{-17} \text{ m}^2/\text{sec}$  at 550°C. This value is lower than

the diffusion coefficient of Mg in MgO alone, being  $3.02 \times 10^{-16} \text{ m}^2/\text{sec}$  at  $550^\circ\text{C}$ .<sup>65</sup> The presence of dispersed spinel particles can serve as diffusion barriers<sup>66</sup> and decreases the total cross-sectional area available for the transport of Mg through the growing oxide layer.<sup>62</sup> Also, since the diffusion coefficient of Mg in the alloy is  $\sim 3 \times 10^{-13} \text{ m}^2/\text{sec}$  at  $550^\circ\text{C}$ , the growth rate of the oxide layer could not be controlled by the diffusion of Mg in the alloy metal.<sup>62</sup> Therefore, it can be concluded that the rate-controlling mechanism for the growth of the oxide layer in the 0.4% Mg alloy is the solid-state diffusion of Mg in the MgO-spinel constituents. Bishop and Fletcher<sup>67</sup> found that the effect of higher Mg concentration on the oxidation of the alloy is that the surface was covered with an adherent uniform oxide layer interspersed by oxide nodules or blisters. Zayan<sup>68</sup> later showed that increasing the oxidation time to 90 hours resulted in the breaking of these blisters into a cauliflower morphology. The rate of growth of the new MgO with this morphology should depend on the rate of Mg evaporation beneath the cracked ridges and nodules. The rate of evaporation of Mg from the alloy surface at a given temperature is given by:<sup>68</sup>

$$R = 2.64 \times 10^{24} P / (W \cdot T)^{1/2} \quad \text{atoms} \cdot \text{m}^{-2} \cdot \text{sec}^{-1} \quad (2.16)$$

where  $P$  is the equilibrium vapor pressure of a solute (expressed in Pa) and  $W$  is the atomic weight of the solute.  $P$ , in turn is related to the vapor pressure of pure solute, in an approximate way according to Raoult's law by:

$$P = P_o \cdot N \quad (2.17)$$

where  $N$  is the mole fraction. He suggested that the model of nonprotective oxidation of Al-Mg alloys indicates that an outward diffusion process is occurring. During the

growth of the MgO layer, voids are formed at the oxide/metal interface by condensation of vacancies. These vacancies are the result of the outward diffusion of Mg.

Goldstein and Dresner<sup>64</sup> studied the growth of MgO films with high secondary electron emission on ultra-pure Al with Mg concentrations from 0.1% to 3%. They reported that it is essential that there be an initial layer of Al<sub>2</sub>O<sub>3</sub> on the Al-Mg alloy; without it, MgO will not form at oxygen pressures less than about  $5 \times 10^{-4}$  Torr. Upon heating to 450°C, Mg accumulates in the Al<sub>2</sub>O<sub>3</sub> to a level 20 to 30 times its initial concentration. The evaporation of Mg increases significantly, and part of the Al<sub>2</sub>O<sub>3</sub> is converted to MgO. The MgO film formed upon heating in oxygen is localized on the outer surface, because the Al<sub>2</sub>O<sub>3</sub> is, in addition, relatively impermeable to oxygen. If the Al<sub>2</sub>O<sub>3</sub> is amorphous (grown at  $T < 350^\circ\text{C}$ ), the growth of MgO is rapid. If the Al<sub>2</sub>O<sub>3</sub> is crystalline (grown at 450 to 500°C), the MgO growth rate is slower by more than one order of magnitude; however, the rate can be increased by increasing the O<sub>2</sub> pressure. And finally, as the MgO film grows, the evaporation of Mg decreases.

The oxide films that form on most aluminum alloys during the majority of metal-processing operations are of little consequence; however, there are many instances where the oxide film is of technological importance, e.g., powder metallurgy, brazing, scrap recycling, and all high-temperature metal-processing operations, where alloys containing magnesium and, more recently, lithium are concerned.

The oxidation behavior of aluminum alloys has mainly been studied at low temperatures, primarily for foundry applications. Oxidation of solid aluminum alloys

has been well documented<sup>69,70</sup> and the various mechanisms can be extended to higher temperatures where the alloy is liquid.

Melts of pure aluminum and commercial aluminum alloys, nominally free of magnesium, and if undisturbed, oxidize slowly at normal melt processing temperatures because a protective aluminum oxide film forms.<sup>71</sup> In contrast, aluminum-magnesium melts under the same conditions can oxidize much more rapidly with the formation of magnesium oxide (MgO) and magnesium aluminate ( $\text{MgAl}_2\text{O}_4$ ) films. This rapid oxidation necessitates special practices to prevent: 1) severe melt losses, 2) alloy compositional changes from preferential oxidation of magnesium, 3) gassing of the melt when water is in the atmosphere, and 4) formation of oxide inclusions that cause difficulties in fabricating fine products such as screen wire and foil. Cochran *et al.*<sup>72</sup> have studied the oxidation rates of aluminum-magnesium melts in various oxidizing atmospheres at temperatures ranging from 600 to 1100°C with the aid of an automatic recording balance. They reported for most conditions, a protective amorphous film on the melt surface initially kept the oxidation rate low. After an interval that was shortened by increasing the temperature or the magnesium content, the film crystallized to magnesium oxide (MgO) and magnesium aluminate ( $\text{MgAl}_2\text{O}_4$ ), accompanied by a sudden increase in oxidation rate. They reported that breakaway oxidation could be promoted by adding crystalline magnesium oxide or magnesium aluminate seed to melts protected with amorphous  $\text{Al}_2\text{O}_3$ .

## 2.4 INFILTRATION OF POWDER BEDS

Recently, considerable work has been done on melt infiltration of ceramic preforms by vacuum casting, squeeze casting and their various modifications.<sup>73,74,75,76</sup> By contrast, relatively few studies have focused attention on melt infiltration of ceramic particulates such as silicon carbide,<sup>77</sup> although the literature on infiltration of porous sintered metal bodies by metals in wettable systems is abundant.<sup>78</sup> The melt infiltration of ceramic particulates affords an opportunity to study such fundamental materials phenomena as dynamic wetting, and nucleation and growth in constrained environments, besides making available a processing route to reinforce metal matrices with relatively large (up to 50 vol% or more) volume fractions of a discontinuous ceramic phase that cannot be accomplished using conventional stir casting techniques.

The liquid metal infiltration process for fabricating Metal Matrix Composites consists of the injection and subsequent solidification of liquid metal within the interstitial spaces of a preform. Fluid flow aspects of the infiltration process can be treated readily following the extensive literature on flow of fluids through porous media, an important topic in soil science and chemical engineering. The important parameters in the melt infiltration process include the size and morphology of the pores that make up the preform, and the physical characteristics of the infiltrant (melt).

Melt infiltration of powder beds can be accomplished by either the action of capillary force and/or the assistance of an external pressure. In the first method, the rate of the infiltration is the most important factor which determines the process

parameters. However, in the case where an external pressure is applied, the magnitude of the force is more important. The literature review of this section will be limited only to the capillarity infiltration.

### 2.4.1 Capillary Phenomena

The pressure change,  $\Delta P$ , across the liquid/vapor interface was first related to the surface tension by Young<sup>100</sup> using a mechanistic argument and then later by Gibbs<sup>79</sup> using a thermodynamic approach. The equation is:

$$\Delta P = \gamma_{lv} \left\{ \frac{1}{R_1} + \frac{1}{R_2} \right\} \quad (2.18)$$

where  $R_1$  and  $R_2$  are the principle radii of curvature of the interface, as shown in Fig.

2.7. The equilibrium height,  $\Delta h$ , of a liquid in a circular capillary of radius  $r$ , can be determined by relating the hydrostatic pressure of the fluid,  $\Delta P = \rho g \Delta h$ , to the pressure across the interface. The result is:

$$\Delta h = \frac{2\gamma_{lv}}{r \rho g} \quad (2.19)$$

A powder bed, however, is not composed of regular capillaries. Several methods have been proposed to calculate an average or characteristic radius of a porous bed from easily measured properties of the powder.<sup>80,81</sup> Each method gives an equation of the form:

$$r \propto \frac{(1 - \phi)}{S \rho \phi} \quad (2.20)$$

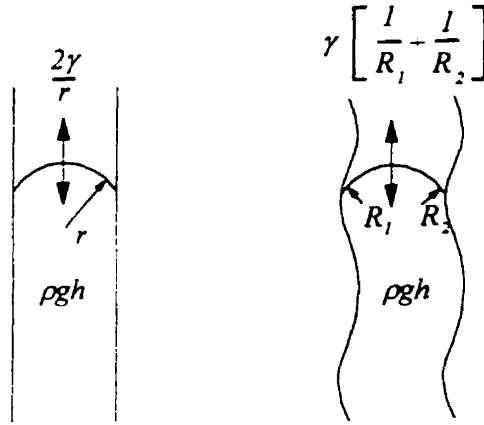


Fig. 2.7: Capillary pressure across an interface.

where  $\rho$  is the density,  $S$  is the surface area per gram of powder, and  $\phi$  is the volume fraction of solid in the bed. The proportionality constant is dependent on the method of derivation of the equation. Using the concept of hydraulic radius, the constant is equal to unity.<sup>80</sup>

In systems of capillary flow into packed beds, meniscus effects are important. From equation (2.19), the smaller the radius of the capillary, the higher the column of the fluid. For a distribution of radii, then the fluid will move higher in the smaller capillaries. Furthermore, the capillaries, being irregular, have regions of high curvature (or small radii). Where these small angles are formed by the particles, the edge of the meniscus will show a large rise over the bottom of the meniscus. This is known as the “meniscus effect” and can be explained in terms of the pressure increase

due to the increased curvature of the interface as indicated in equation (2.18). The higher the pressure difference, the greater the driving force for capillary flow, which results in these narrower regions being filled first.

The study of the capillarity infiltration at room temperature dates back to 1872 when Decharme<sup>82</sup> investigated the motion of a liquid in a capillary. Later, modifications to his model emerged as it became less convincing due to the numerous assumptions he made. Washburn<sup>83</sup> studied the infiltration of liquids into cylindrical capillaries and porous bodies, assuming the porous body consists of very fine cylindrical capillaries where the flow followed Poiseuille's law:<sup>84</sup>

$$\frac{dV}{dt} = \frac{\pi r^4 dp}{8\eta l} \quad (2.21)$$

where  $dV$  is the volume of liquid which in time  $dt$  flows through a length  $l$ , of a capillary having radius  $r$ ,  $\eta$  is the viscosity of the liquid and  $dp$  is the total effective pressure acting to force the liquid along the capillary. If

$$dV = \pi r^2 dl \quad (2.22)$$

and according to Kelvin's<sup>85</sup> law

$$dp = \frac{2\gamma_{lv} \cos\theta}{r} \quad (2.23)$$

$\gamma_{lv}$  being the surface tension and  $\theta$  the wetting angle, the expression can be rewritten as:

$$\frac{dl}{dt} = \frac{r\gamma_{lv} \cos\theta}{4\eta l} \quad (2.24)$$

After integration, the expression becomes a distance of infiltration as a function of time, where the air resistance and gravity effects are neglected:

$$l^2 = \frac{r\gamma_N \cos\theta}{2\eta} t \quad (2.25)$$

Washburn used mercury, water and other liquids to show the validity of this equation and it is still in use today in commercial porosimetry equipment.

It should be noted that the assumptions proposed in the Washburn model are subject to extensive criticism. In reality, the pore channels that were assumed to be represented by parallel capillaries, are more complex and present a tortuous path for the advance of liquid through them.<sup>86</sup> Once the liquid is in the channels of the preform, it has to overcome three different forces in order to advance and move through them: i) the friction associated with flow of a viscous Newtonian fluid, ii) frictional effects due to the non-uniformity of the capillarie pore, and iii) contact angle hysteresis, resulting from mechanical and/or chemical heterogeneities on the solid surface.

#### 2.4.1.1 Infiltration Kinetics

Much of the experimental work done on the infiltration of liquid metals through preforms consists of interrupted tests, where samples were rapidly removed from the hot-zone of a furnace during infiltration, thus freezing the position of the moving infiltrating front. The samples were then cut in order to measure the length of infiltration after some predetermined time.<sup>87,88,89,90</sup> Variations on this method include measuring the weight gain of the sample,<sup>91</sup> or using an electric-sensing technique.<sup>92</sup>

As expected from theory, the infiltration kinetics of a viscous melt follow a parabolic behavior (i.e.  $h^2 \propto t$ ). This has been confirmed experimentally by several authors.<sup>74,87,93</sup> Muscat and Drew<sup>94</sup> have measured the pressureless infiltration rates of

pure Al into TiC preforms using a thermogravimetric analyzer system. The system monitored the weight increase due to the penetration of the liquid metal within the preform pores. This was then translated into an infiltration distance as a function of time. At high temperatures, they reported a parabolic infiltration profile. The rate of infiltration was obtained by evaluating the gradient of the distance vs. time curve at 50% infiltration. The 50% value was selected on the basis that the system had reached an equilibrium infiltration rate.

## 2.4.2 Wetting Phenomena

The most important limitation to the fabrication of MMC's by liquid-phase processes relates to the compatibility between the reinforcement and the matrix.<sup>95</sup> This compatibility is particularly important in the case of aluminum-based composites, because Al is usually covered with a thin oxide layer that prevents wetting,<sup>96</sup> and when uncovered, readily reacts with most ceramics to form intermetallics. In particular, liquid aluminum reacts with SiC to produce aluminum carbide and free silicon. Wettability and reactivity determine the quality of the bond between the two materials and, therefore, greatly influence the final properties of the composite. Several methods are being investigated to improve the compatibility between the two materials, among which are the addition of alloying elements<sup>97</sup> or wetting agents<sup>98</sup> to the melt and the coating of the ceramic reinforcement prior to mixing.<sup>99</sup>

Wettability is measured from the contact angle between the metal and ceramic, as shown in Fig. 2.8.

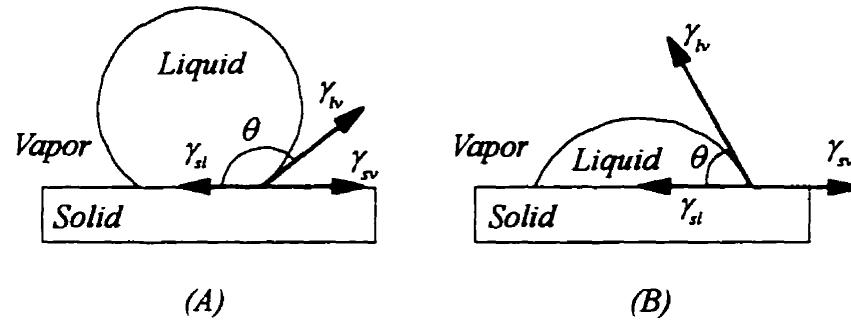


Fig. 2.8: The contact angle for a (A) non-wetting and (B) wetting case.

This angle,  $\theta$ , is related to the three surface tensions, i.e. the solid-vapor interface,  $\gamma_{sv}$ , the solid-liquid interface,  $\gamma_{sl}$ , and the liquid-vapor interface,  $\gamma_{lv}$ , by the relation:

$$\gamma_{lv} \cos \theta = \gamma_{sv} - \gamma_{sl} \quad (2.26)$$

Wetting occurs when  $\theta < 90^\circ$ . This relationship is known as the Young's equation.<sup>100</sup> The Young's equation may be interpreted by considering the work of adhesion,  $W_a$ , which is defined by Dupré<sup>101</sup> as:

$$W_a = \gamma_{sv} + \gamma_{lv} - \gamma_{sl} \quad (2.27)$$

and is a measure of the strength of binding of the liquid and the solid surfaces.

Equation (2.27) can be rewritten as:

$$\gamma_{sl} = \gamma_{sv} + \gamma_{lv} - W_a \quad (2.28)$$

If equations (2.26) and (2.27) are combined together, then:

$$W_a = \gamma_{lv}(1 + \cos\theta) \quad (2.29)$$

where both  $\gamma_{lv}$  and  $\theta$  are measurable quantities.

#### 2.4.2.1 Wetting of SiC by Aluminum Alloys

The silica layer grown naturally or artificially on the surface of SiC fibers or particles used in aluminum-based matrix composites is supposed to have two functions: protection of the SiC from aluminum attack and improvement of the wettability of SiC by aluminum which could result from the reaction between aluminum and SiO<sub>2</sub>. Laurent *et al.*<sup>102</sup> have used the sessile drop method and the immersion-emersion tensiometric technique to measure the contact angles of aluminum on SiO<sub>2</sub> and oxidized SiC. They concluded that their experiments could not be treated as a study of reactive wetting because the SiO<sub>2</sub> reduction reaction by aluminum did not take place during the spreading of aluminum on SiO<sub>2</sub>, but before. The SiO<sub>2</sub> coating of SiC fibers or particles would be interesting to induce wetting, and therefore promotes the incorporation or infiltration, because of the strong driving force of the silica reduction reaction by aluminum. However, experimentally this energy is dissipated before the two phases are in contact and the reaction product does not favor the promotion of wetting. In the Al-SiO<sub>2</sub> system, the "non-real contact stage" is much longer than in the Al-Al<sub>2</sub>O<sub>3</sub> system because the evaporation-reduction of the alumina film by liquid aluminum, that is the reaction:



is slowed down by the reaction of the reduction of silica:



which imposes a higher oxygen potential around the drop. The aluminum is then in direct contact with SiC and wetting becomes truly representative of the Al-SiC system. The role of the SiO<sub>2</sub> layer in this case is to delay the wetting of aluminum on SiC.

Alonso *et al.*<sup>93</sup> have studied the wettability of SiC particles by different aluminum alloys with pressure infiltration. Their results indicated that the changes in threshold pressure promoted by alloying (Si and Mg) are essentially due to the corresponding changes in the surface tension of aluminum, and the effect of wetting seemed to be less important. Goicoechea *et al.*<sup>103</sup> have measured the surface tension of Al-Si-Mg alloys as a function of Si and Mg contents. They found that the surface tension in the Al-Si alloy varied linearly with the silicon content (wt. %),  $x_{\text{Si}}$ , (below the eutectic point). At  $T=973\text{K}$ , their data were satisfactorily fitted by:

$$\gamma_{\text{Al-Si}} = (869 - 1.6x_{\text{Si}}) \text{ mJ/m}^2 \quad (2.32)$$

In the case of magnesium the surface tension shows a logarithmic dependence with the Mg content,  $x_{\text{Mg}}$ . At  $T=973\text{K}$ , the fitted function is:

$$\gamma_{\text{Al-Mg}} = \left\{ 869 - 72 \ln(1 + 0.3x_{\text{Mg}}) \right\} \text{ mJ/m}^2 \quad (2.33)$$

Goicoechea *et al.*<sup>103</sup> reported that for a ternary alloy at a constant temperature, the surface tension of the alloy is described by the following equation:

$$\gamma_{\text{Al-Si-Mg}} = \gamma_{\text{Al}} + \Delta\gamma_{\text{Al-Si}} + \Delta\gamma_{\text{Al-Mg}} \quad (2.34)$$

where  $\Delta\gamma_{Al-Si}$  and  $\Delta\gamma_{Al-Mg}$  are the changes in the surface tension of aluminum,  $\gamma_{Al}$ , induced by the Si and Mg additions, respectively.

Laurent *et al.*<sup>96</sup> investigated the wettability of SiC single crystals by aluminum and Al-Si alloys in the temperature range 973-1173K under various experimental conditions (low total pressure, low oxygen pressure, fresh metallic surfaces). Their study allowed an actual molten metal-substrate interface to develop upon reaching the melting point of the alloys. In all cases (pure aluminum or Al-Si alloys), the common reaction occurring at the interface:



leads to changing contact angle for about 30 to 120 minutes depending on the temperature. In the case of the Al/SiC system, spreading of the aluminum drop is observed to occur concurrently for both  $Al_4C_3$  development and the SiC/Al dissolution reaction. The “non-wetting-wetting” transition temperature decreases with increasing holding time and for comparatively long times ( $\cong 2h$ ), no transition exists at all: aluminum wets SiC even in the vicinity of its melting point ( $\theta \cong 75^\circ$  at  $T = 950K$ ). Additions of silicon to aluminum avoid the formation of  $Al_4C_3$ , but do not affect wettability.

Choh and Oki<sup>104</sup> have measured the wettability of SiC by liquid aluminum and the effects of alloying elements on it by the dip coverage method where SiC was dipped into liquid metal. It was found that the wetting process of SiC by aluminum or aluminum alloys initially shows an incubation period ( $\tau$ ) which decreases by about 10-

20% through the addition of silicon, manganese, or iron to aluminum and that there was no compound detected at the SiC/aluminum alloy interface.

#### 2.4.2.2 Wetting of $Al_2O_3$ by Aluminum Alloys

Table 2.7 shows the wetting angle,  $\theta$ , for a variety of materials. The wetting behavior of molten aluminum on aluminum oxide has been studied by several authors.<sup>105,106,107</sup> Carnahan *et al.*<sup>105</sup> studied the wetting of single-crystal and polycrystalline  $Al_2O_3$  by molten aluminum at temperatures near 1200°C. They found a significant difference in spreading behavior on the two substrates: in the case of aluminum on recrystallized  $Al_2O_3$ , the contact angle attained a steady value, whereas on sapphire the drop was observed to spread and contract repeatedly. Wolf *et al.*<sup>106</sup> studied the wetting of aluminum on sapphire ( $\alpha-Al_2O_3$ ) over a temperature range 700 to 1150°C. Above about 925°C, these authors found that the sapphire was partially dissolved by the aluminum and even below this temperature they found some evidence of attack. Champion *et al.*<sup>107</sup> studied the wetting of aluminum, copper, and gold on sapphire, ruby and recrystallized  $Al_2O_3$  over the temperature range 800 to 1500°C. At temperatures below 950°C, sessile drops of aluminum reached equilibrium only after a period of time which increased with decrease in temperature and could be in excess of one hour. A rapid increase in contact area occurred around 900°C. Above 1150°C drops of aluminum were observed to spread and contract repeatedly. Contractions were observed with both polycrystalline and single-crystal  $Al_2O_3$ , although they were much

more pronounced with the latter, and were associated with the formation of a series of reaction rings on the plaque. Ruby and sapphire behaved similarly.

Table 2.7: Wetting Angle Data for Selected Ceramic/Metal Systems<sup>108</sup>

Metal	Ceramic	Temperature (°C)	Wetting Angle (degrees)
Al	TiC	700	118
Al	WC	900	135
Al	Silica	900	126
Al	Alumina	700	167
		900	120
Al-12Si	Alumina	700	138
Al-6Mg	Alumina	700	116
Al	TiB <sub>2</sub>	700	92
Al	TiB <sub>2</sub>	900	37
Al	SiC	700	120
Al	SiC	770	70
Si	Alumina	1450	95
Si	Graphite	1450	0
Cu	Graphite	1100	157
Cu	SiC	1100	140
Si	SiC	1450	35
Ni	SiC	1460	36

### 3. OBJECTIVES

The current interest in ceramic-matrix composites produced by directed melt oxidation (DIMOX™) of aluminum alloys have been a subject of recent interest in the studies of interactions between gases and molten metals. Particular emphasis has been placed on the oxidation of suitably doped Al alloys, which generates a product consisting of interpenetrating networks of Al<sub>2</sub>O<sub>3</sub> and residual metal. However, the fundamental mechanisms involved in the composite growth process are not yet well understood and there are different theories on the mechanism behind this process. At McGill University, work was directed at investigating the fundamentals of the DIMOX™ process and to provide a better understanding of the mechanism, as well as the effects of the various parameters on the composite formation process. This has led to the initiation of this thesis work.

The main objective was to study the various parameters that affect the growth process to make SiC-reinforced composites by the directed melt oxidation of aluminum alloys. This involved establishing a suitable range of fabrication conditions, defined by temperature and time, and their influence on variables such as alloy composition and SiC particle size. This was done with the aid of intensive microstructural examination, as well as kinetic studies of the process.

The kinetics of oxidation are important in such a process. This can serve to establish the composite growth parameters of temperature and time. All of the previous studies have focused on the kinetics of the process in the absence of a reinforcing

material. Our investigation included SiC particles to reinforce the composites and to study the kinetics of the process. This was done using a continuous measuring technique and the results were compared to existing data on composites not containing a reinforcing phase.

# 4. EXPERIMENTAL PROCEDURE

## 4.1 RAW MATERIALS

To ensure purity of the system being investigated, it is important to start with high purity raw materials. All the metals used to prepare the alloys as well as the silicon carbide powders were of controlled purity and composition.

### 4.1.1 Aluminum Alloys

The aluminum alloys used in this work were prepared in house starting with pure metals with the specifications given in Table 4.1. A series of alloys of binary Al-

Table 4.1: Specifications of the Starting Metals

Elements Content (Wt. %)	Material		
	Aluminum (As-Received)	Aluminum (After Melting and Casting)	Magnesium (As-Received)
Al	Balance	Balance	0.003
Si	0.003	0.003	0.002
Fe	0.003	0.005	0.001
Cu	-	0.003	-
Mn	-	0.002	0.002
Mg	-	-	Balance
Cr	-	0.001	-
Ni	-	0.001	-
Zn	0.002	0.003	0.005
Sr	-	-	-
Ti	-	-	-
Sn	-	-	0.002

Si, Al-Mg, and ternary Al-Si-Mg were prepared. The aluminum<sup>\*</sup> used to cast the alloys was in the form of shots with an average size of 5 mm and was 99.99% pure. The silicon was in the form of 1 cm x 2 cm lumps and was semiconductor grade with a purity of 99.9999%. The magnesium was cut from a 16 kg-ingot and was 99.98% pure.

### 4.1.2 Melting and Alloying

Melting of the alloys was carried out using a *Tocco MeltMaster* induction furnace which was a 38kW, 30kVAR unit operating at 440V and 68A. The crucibles for melting were machined from a high purity graphite block<sup>‡</sup> which was baked at 800°C to remove volatiles. The alloys were induction melted in 500g batches in the baked crucible. Initially, Si pieces were placed at the bottom of the crucible and then Al shot was loaded on top. The melt temperature was brought up to 740°C and then maintained within  $\pm 2^\circ\text{C}$  of this value for 15 minutes. The melt temperature was monitored using a chromel-alumel K-type thermocouple placed directly in the melt. Once the aluminum and silicon were molten and mixed, the temperature of the induction furnace was lowered to about 650°C. The magnesium pieces, wrapped in aluminum foil (high purity aluminum), were then added to the melt to minimize the loss of magnesium by oxidation. Once the magnesium had dissolved in the alloy, the

---

<sup>\*</sup>Belmont Metals Inc., Brooklyn New York.

<sup>†</sup>Johnson Matthey AESAR Group, Brampton, Ontario.

<sup>‡</sup>Timminco Metals, Toronto, Ontario

<sup>§</sup>Speer Canada Inc., St. Laurent, Quebec.

temperature was raised back to 740°C to ensure complete mixing. The temperature was reduced to about 720°C prior to casting.

### 4.1.3 Casting

The molten alloys were cast into a cylindrical graphite mold, having an outer diameter of 60mm and a height of 230mm, which was preheated to 150°C to remove any humidity and water vapor. After filling the mold, the remaining melt was cast into a small copper mold to obtain samples for spectrochemical analysis.

A control sample of pure aluminum was also produced in exactly the same manner in order to determine the degree of contamination during melting and casting. The chemical analysis of this sample, given in Table 4.1, revealed that the alloys did not suffer any appreciable decrease in purity. The cast ingots were 200 mm in length and 25.0 mm in diameter. These ingots were sectioned into discs 5-6 mm in thickness.

### 4.1.4 SiC Powder Characterization

Four  $\alpha$ -SiC powders were used: 240-, 320-, 400-, and 600-grit. The four SiC powders\* were of a high purity grade (green silicon carbide). The manufacturer's specifications of the powders are given in Table 4.2. Each powder was oxidized in air for a period of 48 hours at 1400°C prior to composite fabrication. Scanning electron micrographs of each powder before oxidation are shown in Fig. 4.1 (a)-(d). The morphology of the silica layer resulting from the oxidation of the SiC powders is shown in Fig. 4.2.

---

\*Norton Company, Worcester, Massachusetts.



(a)



(b)



(c)



(d)

Fig. 4.1: Scanning electron micrographs of the as-received SiC powders: (a) 600-, (b) 400-, (c) 320-, and (d) 240-grit powder.



Fig. 4.2: Morphology of the SiO<sub>2</sub> layer that develops on the SiC surface after oxidation.

Table 4.2: Typical Chemical and Physical Analysis of the Green Silicon Carbide Particles

Grit Size	240	320	400	600
% SiC	99.7	99.7	99.7	99.7
% Free C	0.10	0.10	0.10	0.10
% Free SiO <sub>2</sub>	0.10	0.10	0.10	0.10
% Free Si	0.05	0.05	0.05	0.05
% Free Fe <sub>2</sub> O <sub>3</sub>	0.02	0.02	0.02	0.02
D <sub>50</sub> % (μm)	44.5±2.0	29.2±1.5	17.3±1.0	9.3±1.0
Tap Particle Density (g/ml)	1.84	1.78	1.76	1.67

#### 4.1.4.1 Specific Surface Area

The specific surface areas of the powders were measured by the single point Brunauer, Emmett and Teller (BET) method, using a Quantachrome system

(Quantasorb Sorption). The SiC powders (0.5-1 g of each) were loaded into a pyrex glass sample holder (U-shaped tube), and then heated to 300°C for 30 minutes to remove adsorbed water. After heating, N<sub>2</sub>/He gas flows through the sample holder and then the powder is cooled down by liquid nitrogen. The volume of N<sub>2</sub> adsorbed is a function of the specific surface area of the powder. The process of adsorption and desorption are monitored by measuring the change in the thermal conductivity of the gas mixture. All tests were performed three times to assure repeatability. The drop in the nitrogen partial pressure is then directly related to the specific surface area using the BET equation:<sup>109</sup>

$$S_t = \left(1 - \frac{P}{P_o}\right) \left(\frac{A}{A_c}\right) V_c \frac{N \cdot A_{cs} \cdot P_a}{R \cdot T} \quad (\text{m}^2) \quad (4.1)$$

where  $P$  is the partial pressure of the adsorbate,  $P_o$  is the saturated pressure of the adsorbate,  $V_c$  is the calibration volume,  $A$  is the signal area,  $A_c$  is the area of calibration,  $N$  is the Avogadro's number,  $R$  is the gas constant,  $P_a$  is the ambient pressure,  $A_{cs}$  is the cross sectional area of the adsorbate molecule, and  $T$  is the temperature of calibration volume. For N<sub>2</sub> as an adsorbate at  $T=295$  K and  $P_a=1$  atm., equation (4.1) reduces to:

$$S_t = 4.03 \times \left(1 - \frac{P}{P_o}\right) \frac{A}{A_c} \cdot V_c \quad (\text{m}^2) \quad (4.2)$$

where  $A/A_c$  represents the weight of the sample.  $P$  is defined as:

$$P = \frac{F_s}{F_a + F_c} \times P_a \quad (4.3)$$

where  $F_a$  is the adsorbate flow rate and  $F_c$  is the carrier flow rate. Then the surface area of the powder can be calculated by dividing  $S_r$  by the weight of the sample.

#### 4.1.4.2 Particle Size Analysis

The particle size distributions of the four powders were analyzed using a Sedigraph 5000D<sup>\*</sup> particle size analyzer. First, about 4-5 grams of SiC powder were placed into 40 ml of distilled water and stirred for about 30 seconds with a magnetic stirrer in the Sedigraph. Then the powder dispersed in water was injected into the instrument and the 100% line is calibrated. The particle size distribution is plotted on a

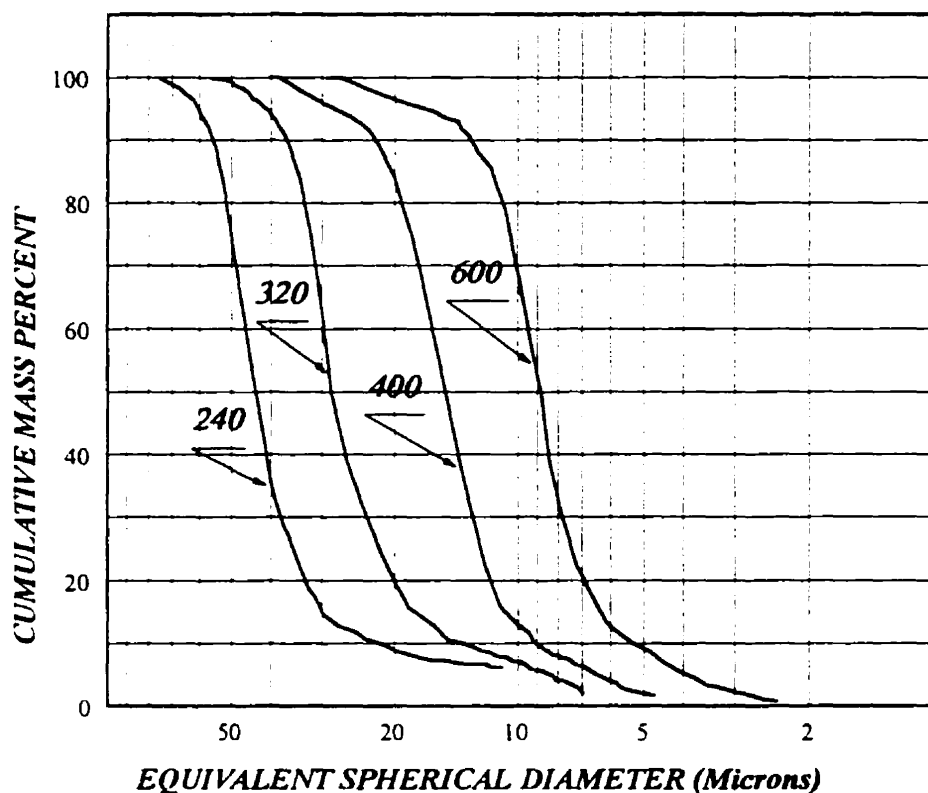


Fig. 4.3: Measured particle size distributions of the four SiC powders by Sedigraph.

<sup>\*</sup>Micromeritics Instrument Corporation, Norcross, Georgia

log-scaled graph paper as the sample is running through the instrument. The measured particle size distributions are shown in Fig. 4.3. Each powder was run through the Sedigraph three times to assure repeatability.

#### **4.1.5 Crucible Fabrication**

The crucibles used in this work to grow the ceramic composites were manufactured in house from an A-17 alumina powder.<sup>\*</sup> A slip was prepared with a weight ratio of 70:30 alumina to water. Darvan 821A was used as the deflocculant in a proportion of 0.18-0.20 wt. % of the Al<sub>2</sub>O<sub>3</sub> solid content. The slip was then ball-milled for three hours using alumina media. The Darvan 821A dispersant was used instead of HCl acid since it provides better stability with time (no change of pH) and does not degrade the slip casting molds. The mold used for slip casting was made from Plaster of Paris with a ratio of 70:30 plaster to water. The crucibles were then drain cast to a wall thickness of 2-3 mm (Fig. 4.4). The crucibles were air dried at room temperature for a period of 10 hours and then partially sintered in air at 1200°C for about three hours. They were machined to remove any sharp angles and to smooth the surface of the crucibles. They were then fully sintered in air at 1550°C for a period of four hours. The final dimensions of the crucibles were 28.5 mm outside diameter, 24.5 mm inner diameter, and 36 mm high.

---

<sup>\*</sup>Aluminum Company of America, Pittsburg, Pennsylvania.

<sup>†</sup>R.T. Vanderbilt Company, Inc., Norwalk, Connecticut.

<sup>‡</sup>J.E. Tremblay Ltd., Montreal, Quebec.

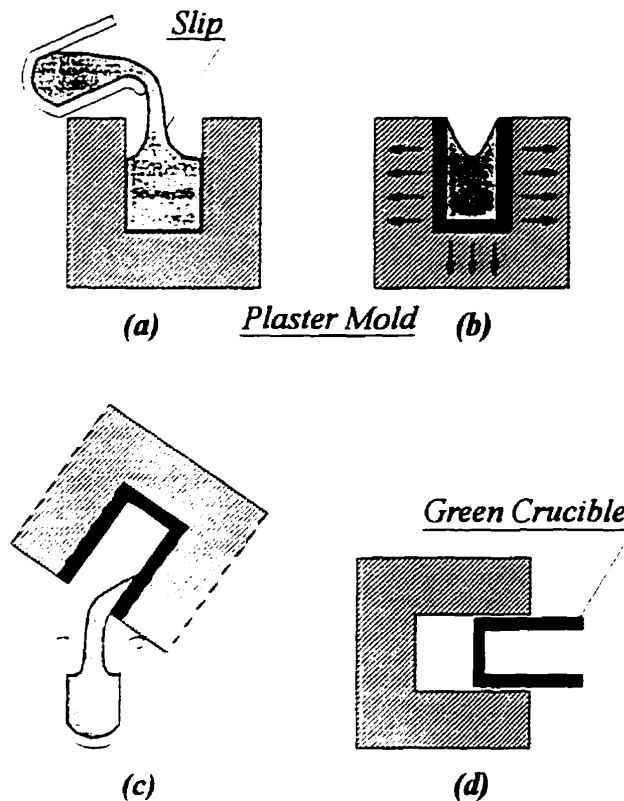


Fig. 4.4: Schematic illustration of the drain-casting process, (a) fill mold with slip, (b) mold extracts liquid, forms compact along walls, (c) excess slip drained, and (d) casting removed after partial drying.

## 4.2 COMPOSITE FABRICATION

For composites grown without a filler material (SiC), cylindrical alloy specimens approximately 25.0 mm in diameter and 5 mm high were cut from the castings, degreased and placed in an  $\text{Al}_2\text{O}_3$  crucible. The weight of the crucible and the alloy were noted prior to composite fabrication. In some instances, the top surface of

the alloy was coated with a thin layer of  $\text{SiO}_2^*$  powder to accelerate the growth of the composite. When a filler material was used to grow the composites, SiC powder was placed on top of the alloy in the  $\text{Al}_2\text{O}_3$  crucible and tapped level using a vibrating table to ensure reproducible tap densities, as shown in Fig. 4.5. The weight of the crucible, alloy and SiC powder were noted prior to composite fabrication. The growth of the molten Al-Mg-Si alloys in air was studied by two types of experiments: (1) interruption of the growth process at intermediate times during the isothermal soak and (2) TGA measurement of the composite growth rate.

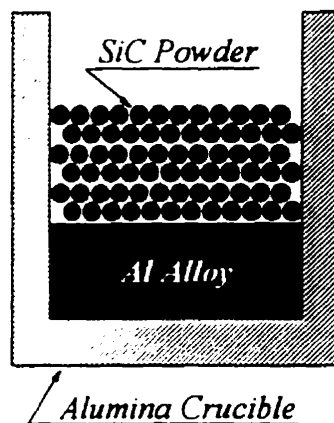


Fig. 4.5: Experimental setup for composite fabrication using a filler material.

---

\*SIGMA Chemical Company, St. Louis, Missouri.

### 4.2.1 Interrupted Test Experiments

The crucible containing the alloy and the SiC powder was placed in a SiC-element air furnace (Fig. 4.6) and heated to an isothermal soak temperature ranging from 1100 to 1350°C. Samples were removed and air-cooled after being held for various desired soak times (up to 24 hours). The length of time required for the alloy to reach the molten state is not very important since all of the alloys undergo the same procedure. When the furnace reaches the desired temperature, the furnace door is opened and the sample is quickly positioned under the thermocouple. From the point the furnace door is closed, the timing starts, and after the desired soak time has elapsed,

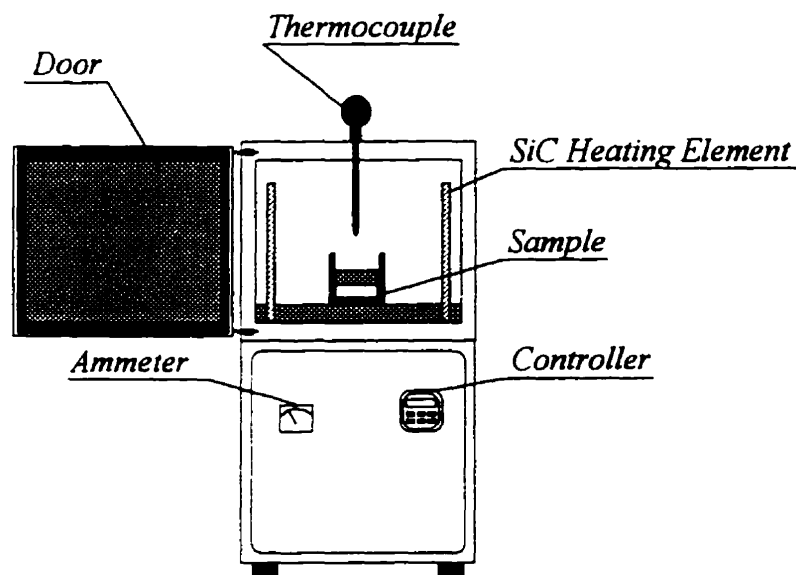


Fig. 4.6: Schematic of the furnace used for the interrupted experiments.

the furnace is opened and the sample is removed and placed outside at ambient temperature.

### **4.2.2 Kinetics Experiments**

From the literature cited, the most commonly used method to measure the oxidation rates is the interrupted test technique. However, this method is liable to produce many inconsistencies in the gathering of data. A continuous technique would be preferable, since it will give one profile for each sample, thus eliminating a lot of possible errors due to variations in the preforms and/or the furnace conditions under which the tests are performed.

The method for measuring oxidation rates used in this work allows continuous monitoring of the sample weight gain. However, the actual weight being registered by the balance is not solely that of the "Lanxide" reaction. There are two other factors that have to be considered: the first, which is applicable to the oxidation of the alloys in the presence of SiC preform, is the weight gain associated with the oxidation of SiC at the test temperature. The other is the weight gain due to the oxidation of the refractory wire suspending the sample in the hot zone of the furnace. Even though these two factors have little contribution to the total weight gain, they were taken into consideration when analyzing the oxidation curves. This was done as follows: First an empty  $\text{Al}_2\text{O}_3$  crucible suspended using a refractory wire was placed in the furnace and an experiment was run in which the microbalance was monitoring the weight gain due to oxidation of the wire. Second, an  $\text{Al}_2\text{O}_3$  crucible containing only

SiC powder of certain weight was placed in the microbalance. This second step can be eliminated by oxidizing the SiC powder prior to processing the composite. This procedure was done at the different temperatures, and after each run, the weight change due to the oxidation of the wire and/or the SiC particles was subtracted from the recorded weight gain.

For the kinetic studies, a TGA set-up shown in Fig. 4.7 was used. A custom-built 6cm-diameter vertical dense mullite tube furnace, was fitted with a vacuum system on the bottom end. The top end was attached to a glass tube of a similar

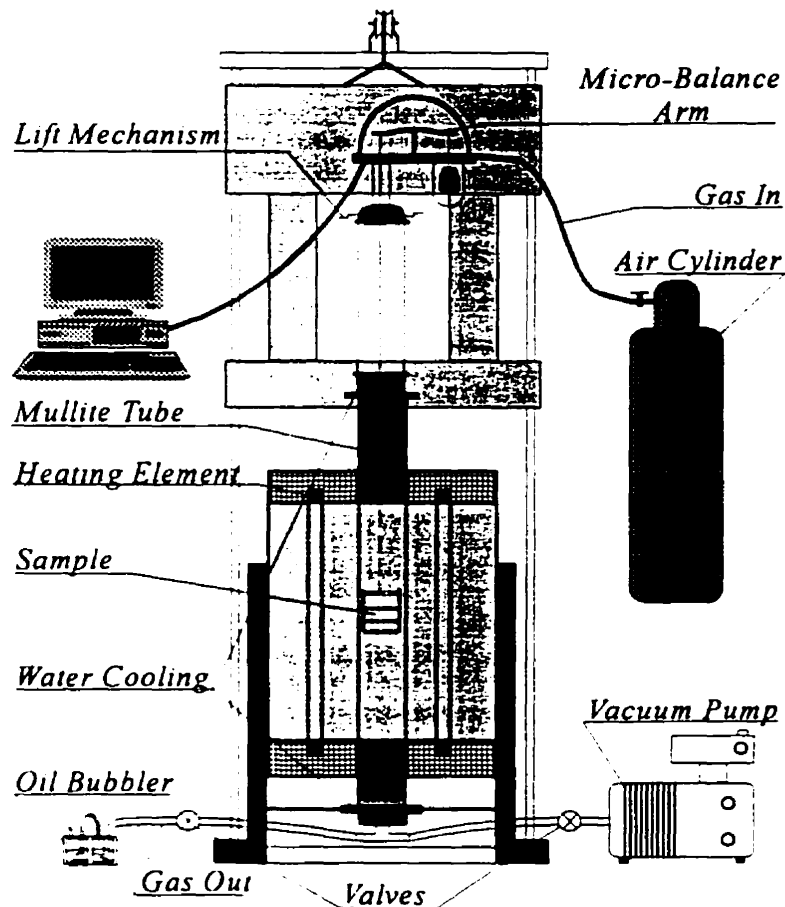


Fig. 4.7: Experimental set-up to measure the composite growth rate.

diameter, leading to a Thermo-Gravimetric Analyzer, or TGA (Cahn D-100). The glass tube and the TGA were mounted onto a framework such that they could be moved in the vertical direction, parallel to the mullite tube. This allowed for sample preparation prior to the start of the test. The whole system was gas tight, and reached a vacuum of  $<20\text{mTorr}$ . Gas flow was controlled through an inlet in the TGA frame, and an outlet in the vacuum tubing at the bottom. The gas line was also fitted with a flowmeter to control the gas flow rate.

The furnace had a B-type (Pt-6%Rh vs. Pt-30%Rh) thermocouple, with an accuracy of  $\pm 1\%$  and was connected to a Gultan West 2050 temperature controller. The furnace was calibrated using another B-type thermocouple, in air placed inside the mullite muffle-tube at the point where the sample is to be placed. The readings of the two thermocouples were compared for different set-point temperatures, and a plot of the deviation with temperature was created. It was noticed that the deviation increased with increasing temperature from about  $70^\circ\text{C}$  at  $800^\circ\text{C}$  to  $130^\circ\text{C}$  at  $1400^\circ\text{C}$ . This was possibly due to stronger convection currents within the hot-zone, despite the fact that the tube was closed from both ends.

While the furnace was still open, an  $\text{Al}_2\text{O}_3$  crucible containing the alloy and the SiC powder was suspended from the TGA arm, using a refractory metal wire long enough to reach into the hot-zone. After making sure that the crucible was centered with respect to the mullite tube, the TGA was tared. The furnace was then closed and evacuated to a vacuum of less than  $20\text{ mTorr}$ . The crucible was retracted away from the hot-zone using a lift mechanism and, while still under vacuum, the furnace was

heated to about 700°C. The chamber was then back-filled with dry-air<sup>\*</sup> up to atmospheric pressure. When the desired temperature was reached, the crucible was lowered slowly and introduced into the hot-zone. The weight change experienced by the sample as the aluminum alloy oxidized was monitored through the TGA, which collected weight readings every five minutes and stored them in a PC. Growth rate curves were thus obtained for the four different SiC powders, with different alloy compositions, and at temperatures from 1100°C to 1350°C.

## **4.3 CHEMICAL AND PHASE ANALYSIS**

### **4.3.1 Emission Spectroscopy**

The chemical composition of the different cast alloys was quantified using an emission spectroscope Spectovac 1000 equipped with an MC20 data processing system. Each sample obtained from the copper mold, 4cm in diameter by 2 cm high, was ground to provide a flat surface free of visual pores. SiC grinding paper was used up to 400 grit size. The spectrometer required calibration before analyzing the samples. This was done using Al alloy standards provided with the equipment.

### **4.3.2 X-Ray Diffraction (XRD)**

X-Ray Diffraction (XRD) was used to determine the phases present in the bulk samples. A section of the each sample was crushed using a cast iron vibratory mill, so as to produce enough powder to fill the sample holder. This was then scanned

---

<sup>\*</sup>MEGS Inc., St. Laurent, Quebec.

<sup>†</sup>Baird Corporation, Boston, Massachusetts.

at a rate of 0.1°/s with filtered Cu-K $\alpha$  radiation, at an accelerating voltage of 40kV ( $\pm 0.1\%$ ) and a beam current of 20mA ( $\pm 0.1\%$ ), using a Philips APD 1700 diffractometer. The range of  $2\theta$  was from 15 to 70°. The data were acquired and stored on the computer system. The phases identified were later verified using Energy Dispersion Spectroscopy (EDS) elemental analysis and X-ray mapping, on the Scanning Electron Microscope (SEM), as will be explained below.

## **4.4 MICROSCOPY**

### **4.4.1 Optical Microscopy**

Samples were first cut to approximately 2cm<sup>3</sup> pieces and mounted in a cold setting epoxy resin. They were then ground using two diamond "ultra-prep" grinding discs of 45 $\mu$ m followed by 15 $\mu$ m. The samples were later polished with a diamond paste and an ethylene glycol lubricant, using a diamond grit of 6 $\mu$ m down to a 1 $\mu$ m finish. Ultrasonic cleaning was carried out after each polishing step. Optical micrographs were taken on a Zeiss Neophot 21, fitted with an oil immersion lens ( $\times 2000$ ). Photomicrographs of representative areas of the samples were taken using Polaroid film.

### **4.4.2 Scanning Electron Microscopy (SEM)**

Both fractured and polished surfaces were examined using the SEM. The polished samples were prepared as explained above. Occasionally the specimens were sputter coated with a very thin Au-Pd coating, to enhance electron conductivity on the

surface. The microscope used was a Jeol JSM-840A, which is equipped with an ultra-thin window (Al, 0.1 $\mu$ m thick) installed, to allow detection of very light elements (C to Na). A Tracor Northern TN-96-606E3/513 system was used to carry out (a) chemical analysis using Energy Dispersive Spectroscopy (EDS), (b) X-ray mapping, and (c) image analysis using a compatible software package.

### Image Analysis

In order to develop a more consistent and less subjective evaluation of the microstructure of the composites, quantitative metallography was employed using image analysis by scanning electron microscopy. Image analysis was carried out on coated samples that were polished down to a 1 $\mu$ m finish, as described earlier. It was conducted with Tracor Northern TN-5700 image analyzer, interfaced with the SEM through the IPA 57 program. The main steps of the image analysis are image acquisition, segmentation, object detection, measuring, and analysis (see Fig. 4.8).

### X-Ray Mapping

X-ray mapping was performed using the TN-8500 Advanced Imaging System, run by the OS-9<sup>TM</sup> operating system, and a TN-5500 X-Ray Analysis system, linked together through one switchable operator's console to provide integrated EDS and imaging functions. X-ray mapping was also performed on polished samples.

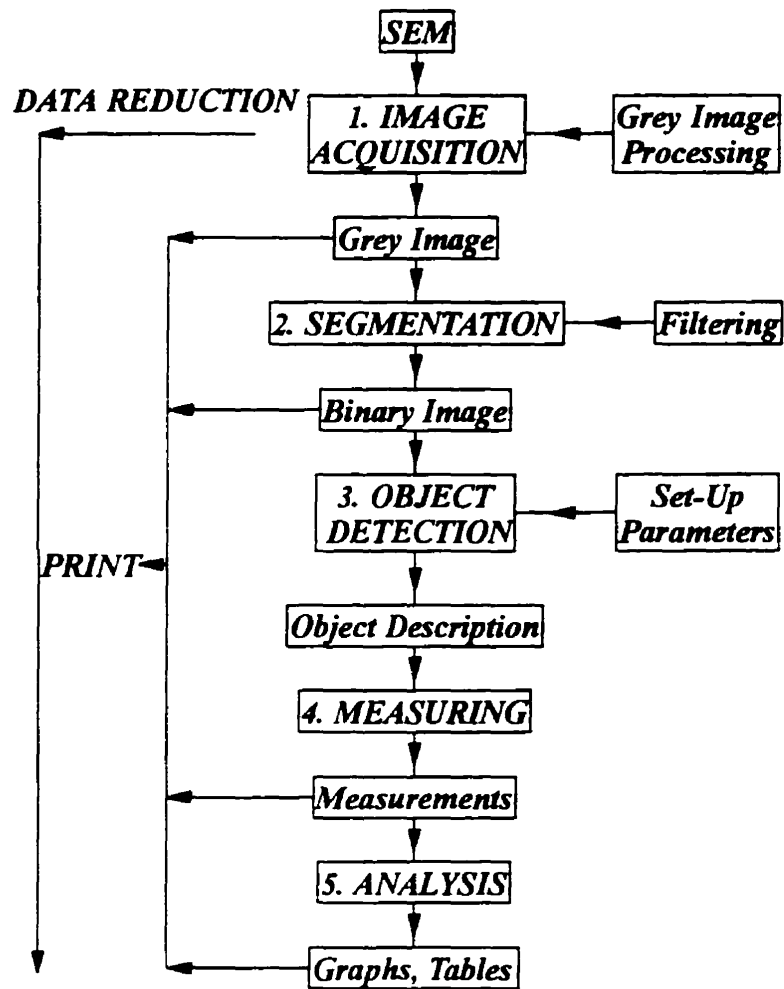


Fig. 4.8: The principal steps of image analysis.

#### 4.4.3 Transmission Electron Microscopy (TEM)

Some samples were also examined using TEM in order to closely observe the nature of the interface of the composite material. Samples were first cut to a thickness of  $\sim 1\text{mm}$  and were subsequently thinned from both sides to a thickness of  $\sim 100\mu\text{m}$ , finishing with a  $15\mu\text{m}$  impregnated diamond disc. One side was then polished with  $1\mu\text{m}$  diamond paste and the other side was dimpled to a thickness of  $\sim 30\mu\text{m}$  (see Fig.

4.9). The foils were mounted on copper grids and each specimen was ion-beam milled with Ar at a voltage of 4kV. The beam angle was set at  $12^\circ$  and milling time ranged from 6 to 10 hours. The specimens were then viewed in a TEM (Philips CM20) having an accelerating voltage of 200kV, which was equipped with an EDAX system for micro-chemical analysis.

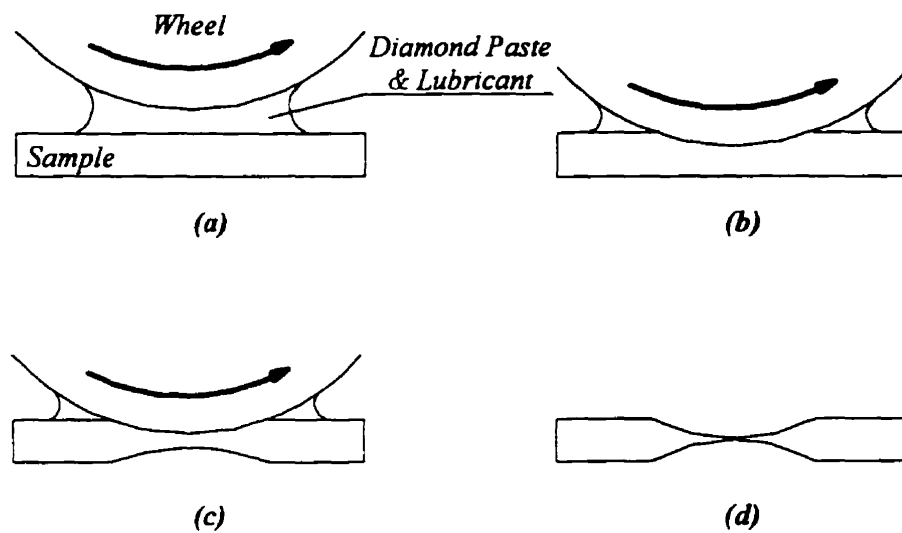


Fig. 4.9: Dimpling a sample for TEM analysis.

#### 4.4.4 TEM Replication Technique

The surface microtopography of the composites was examined on high-resolution replicas by TEM. The replicas consisted of a thin platinum/carbon (Pt/C) film (95Pt/5C wt. % and 1-2 nm thick) and a supporting carbon film (15-20 nm thick). Polished cross sections of the composites were mounted on a flat substrate using

double-sided adhesive tape, with the surface of interest parallel to the substrate. The shadowing and replication procedure was performed in a freeze-etch unit (Balzer 400) under high vacuum ( $1.333 \times 10^{-4}$  Pa) and at room temperature. An extremely fine granular Pt/C film was condensed on the crystal surface by an electron beam evaporation gun as a point source at an angle of  $30^\circ$  and a distance of 15 cm. Instrumental conditions (i.e. acceleration potential and emission current) allowed a Pt/C deposition rate of 0.25 nm/s.

A supporting carbon film was immediately condensed on the Pt/C coating by a vertical electron beam gun at  $90^\circ$  at 12 cm distance away from the surface of the specimen for 6 seconds. Under the optimal operational conditions and a deposition rate of 2.5 nm/s, a total thickness of  $\approx 15$  nm carbon film was produced. The replica was cleaned by dissolving the composite adhering to the replica using a 10% HF solution, rinsed with deionized water and transferred onto a 200 mesh TEM grid.

## 5. RESULTS

### 5.1 MICROSTRUCTURE OF LANXIDE™ COMPOSITES

The purpose of this first set of experiments was to determine a good temperature/alloy combination in order to achieve good growth characteristics and a consistent microstructure. Good growth characteristics implied a uniform growth across the powder bed moving outward from the metal reservoir. The experiments were performed at five different temperatures: 1100°C, 1150°C, 1200°C, 1250°C, and 1300°C. The oxidation time was set to 24 hours. The spectrochemical analysis of different alloy compositions are presented in Table 5.1.

Table 5.1: Composition (in Weight %) of the Various Aluminum Alloys Used

Alloy	Si (wt. %)	Mg (wt. %)	Al (wt. %)
(0/1.5)	-	1.20	98.80
(3.5/1.5)	3.71	1.32	94.97
(7/1.5)	7.27	1.45	91.28
(10/1.5)	10.63	1.57	87.80
(3.5/0)	3.85	-	96.15
(3.5/0.5)	3.38	0.38	96.24
(3.5/1)	3.63	0.83	95.54
(3.5/2)	3.96	1.97	94.07
(0/3)	-	2.39	97.61
(7/3)	6.11	1.94	91.95
(3.5/3)	3.58	2.98	93.44
(3.5/2)	3.61	2.05	94.34
(3.5/2.5)	3.39	2.37	94.24
(0/1.5)	-	1.43	98.57
(7/1)	7.21	0.72	92.07
(12/1.5)	12.32	1.34	86.34
(7/4)	7.88	4.05	88.07

In order to distinguish the growth front, an insufficient amount of the alloy was used to completely infiltrate the powder. For simplicity, and throughout the remaining text, the following notation will be used to describe the alloys: (a/b), where a and b are the weight % of Si and Mg in the alloy, respectively. For example, an Al-10 wt.% Si-3 wt.% Mg will be denoted as a (10/3) alloy. Whereas (0/3) alloy denotes an Al-3 wt.% Mg alloy.

### 5.1.1 Unreinforced Composites

To better understand the effect of the SiC reinforcing particles on the microstructure of the composites, it is important to compare the microstructure of composites processed with and without SiC preforms. The microstructure of a composite processed without a filler material is shown in Fig. 5.1. The composite consists of two different phases: the dark phase being the newly formed  $\text{Al}_2\text{O}_3$  matrix and the bright phase is the metal channels remaining in the composite after oxidation. The resulting matrix material is typically a ceramic/metal composite comprising a three-dimensionally interconnected ceramic reaction product and usually some interconnected metal. The matrix material consists of long continuous columnar regions containing predominantly low-angle  $\text{Al}_2\text{O}_3/\text{Al}_2\text{O}_3$  boundaries which are devoid of any grain boundary phase. The metallic component of the composite is present as both interconnected tortuous channels within and between the alumina columns and isolated small pockets. The  $\text{Al}_2\text{O}_3$  columns are aligned parallel to the growth direction of the composite. Fig. 5.2 shows the microstructure of a composite processed without a

reinforcing material in a direction normal to the growth direction. This figure shows that both the metal channels and the alumina grains are three-dimensionally interconnected, however, the preferred orientation of the  $\text{Al}_2\text{O}_3$  columns is not present along this direction. Fig. 5.3 shows the intersection of two or more  $\text{Al}_2\text{O}_3$  columns as represented by the change in the direction of alignment of the metal channels, in agreement with the findings of previous workers.<sup>27,43,110</sup> Fig. 5.4 is a TEM replica showing the interconnectivity of the metal channels that was not detected by either the optical microscope or the SEM. This figure shows two metal channels interconnected via a very fine metal film running along the grain boundary of two adjacent  $\text{Al}_2\text{O}_3$  grains.

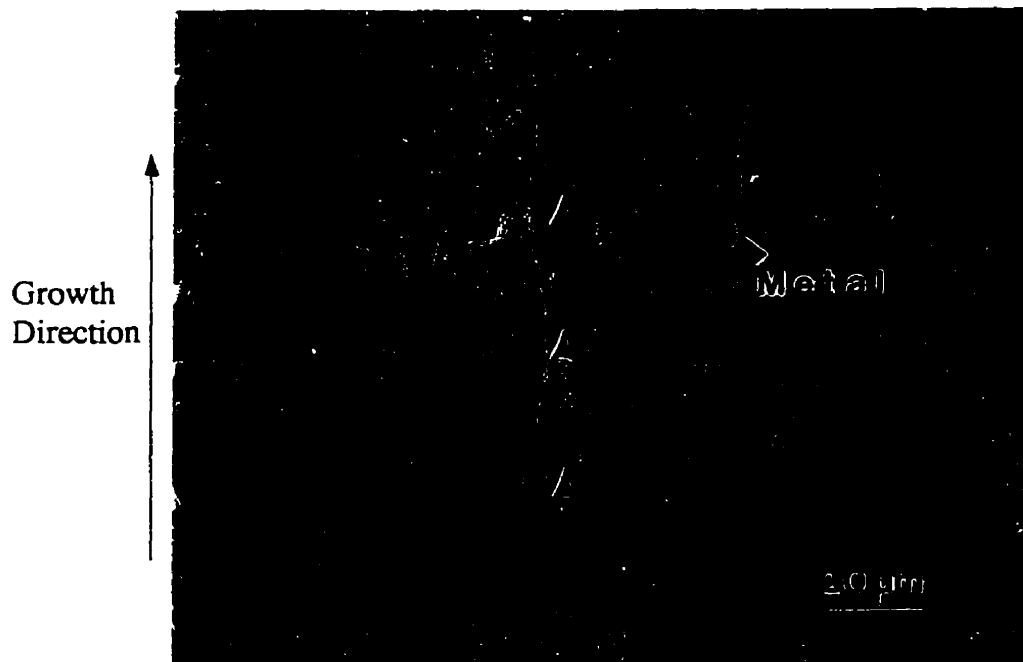


Fig. 5.1: Microstructure of a composite grown from a (7/3) alloy at 1200°C without SiC.

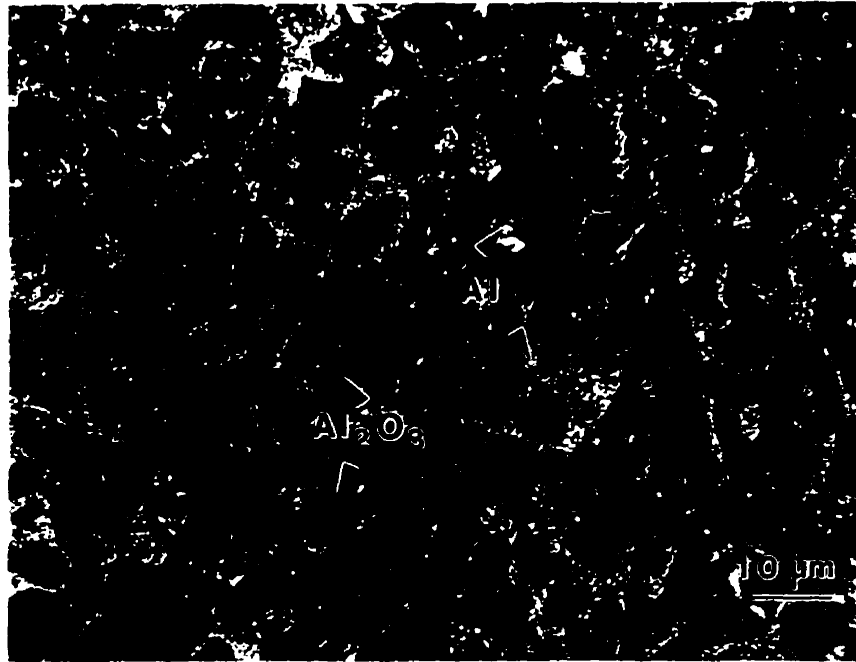


Fig. 5.2: Microstructure of a composite grown from a (0/3) alloy at 1200°C without SiC (normal to the growth direction).

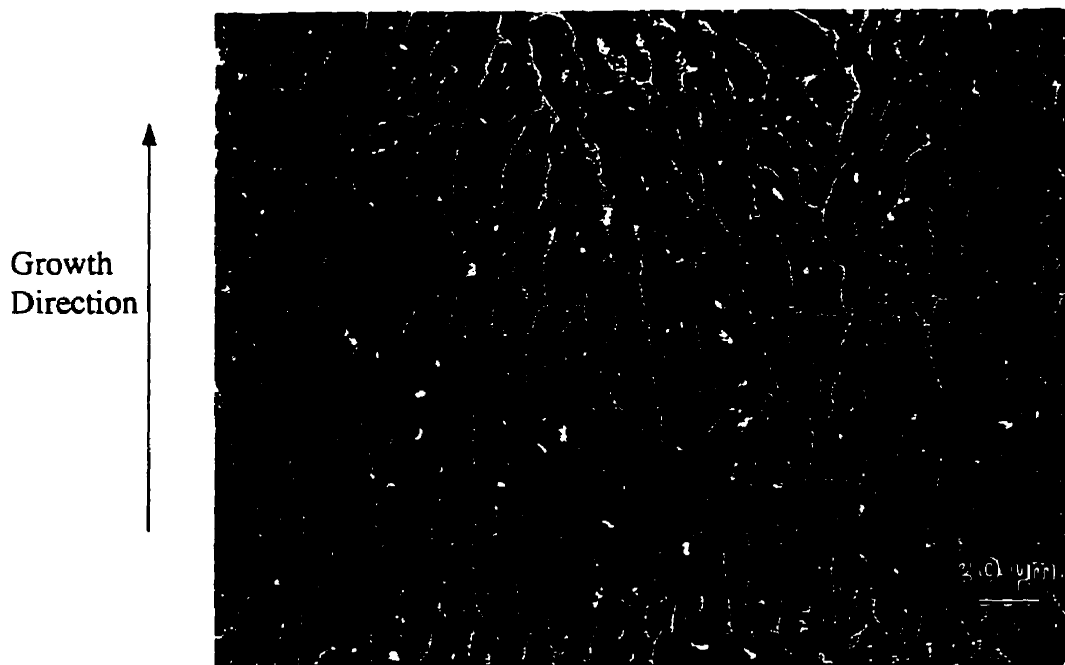


Fig. 5.3: Microstructure of a composite grown from a (7/3) alloy at 1200°C (no SiC) showing the intersection of two or more Al<sub>2</sub>O<sub>3</sub> columns.

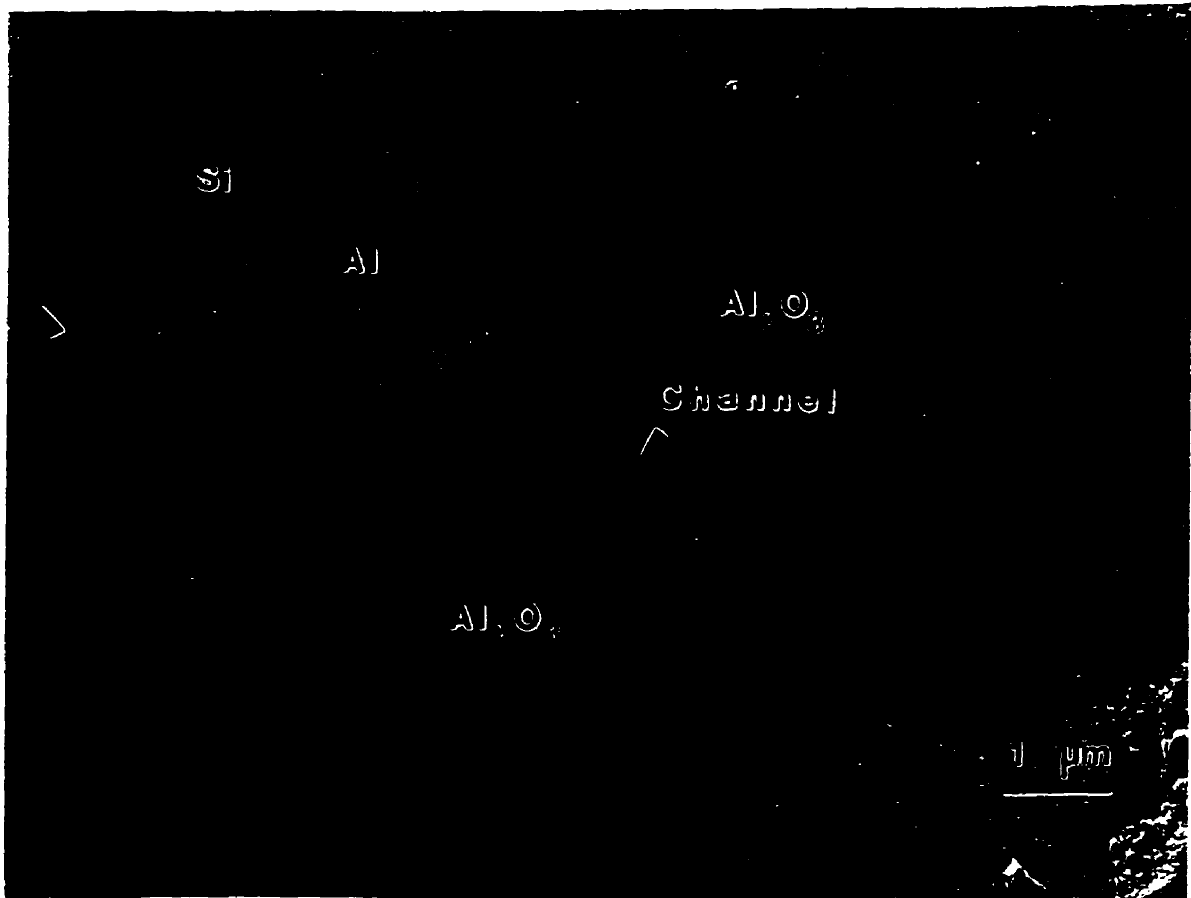
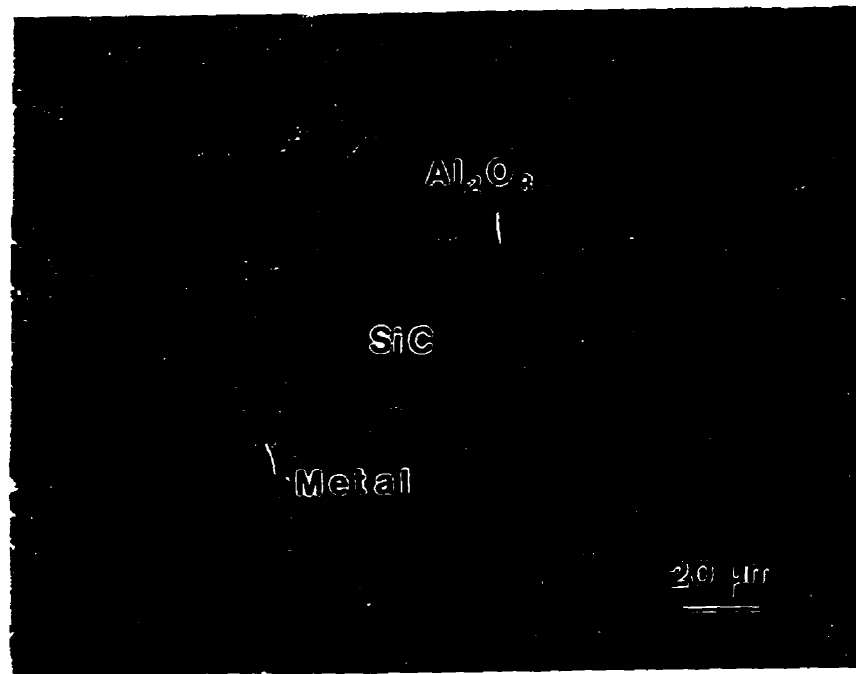


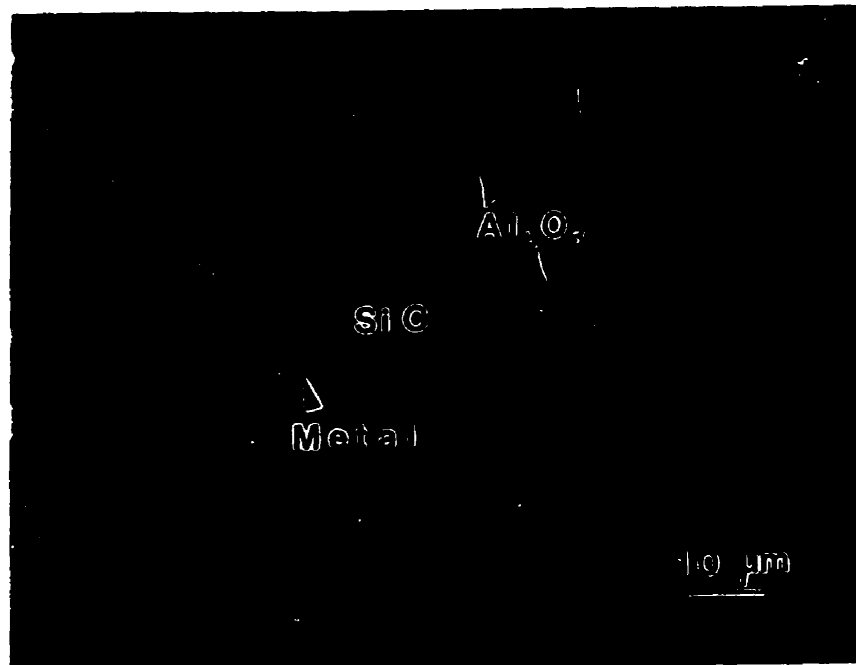
Fig. 5.4: TEM replica showing the interconnectivity of the metal channels.

### 5.1.2 SiC-Reinforced Composites

Typical microstructures of composites grown at 1200°C using a 240-grit SiC reinforcing material are depicted in Fig. 5.5. The composite consists of three distinct phases: the gray phase is the SiC particles, the dark phase is the newly formed Al<sub>2</sub>O<sub>3</sub> matrix, and the bright phase represents the metal channels remaining in the composite after oxidation. The connectivity of the ceramic and metallic phases is quite evident. The majority of the metal phase was contained in microchannels 1-5 μm thick, with spacing in the 4-6 μm range, although areas with smaller and seemingly discrete metal



(a)



(b)

Fig. 5.5: Microstructures of composites grown from a (7/3) alloy at 1200°C with a 240-grit SiC reinforcing material at different magnifications.

pockets were commonly observed (Fig. 5.5(b)). It should be noted that the columnar growth of the  $\text{Al}_2\text{O}_3$  matrix has been disturbed by the presence of the SiC reinforcing particles and there is no preferential growth direction of the  $\text{Al}_2\text{O}_3$  grains.

The incorporation of the SiC filler material into the ceramic matrix produces a refinement of the matrix; i.e. both the ceramic ligament and the metal channel sizes decreased. The distribution of the SiC particles is quite uniform, and the volume fraction is essentially the same as that of the loosely packed SiC preform prior to composite processing.

Upon processing, there was no apparent reaction between the Al alloy and the SiC powder. XRD analysis for the as-fabricated material, crushed into a powder, shows only peaks for  $\text{Al}_2\text{O}_3$ , SiC, Al, and Si metals, as can be seen in Fig. 5.6, which

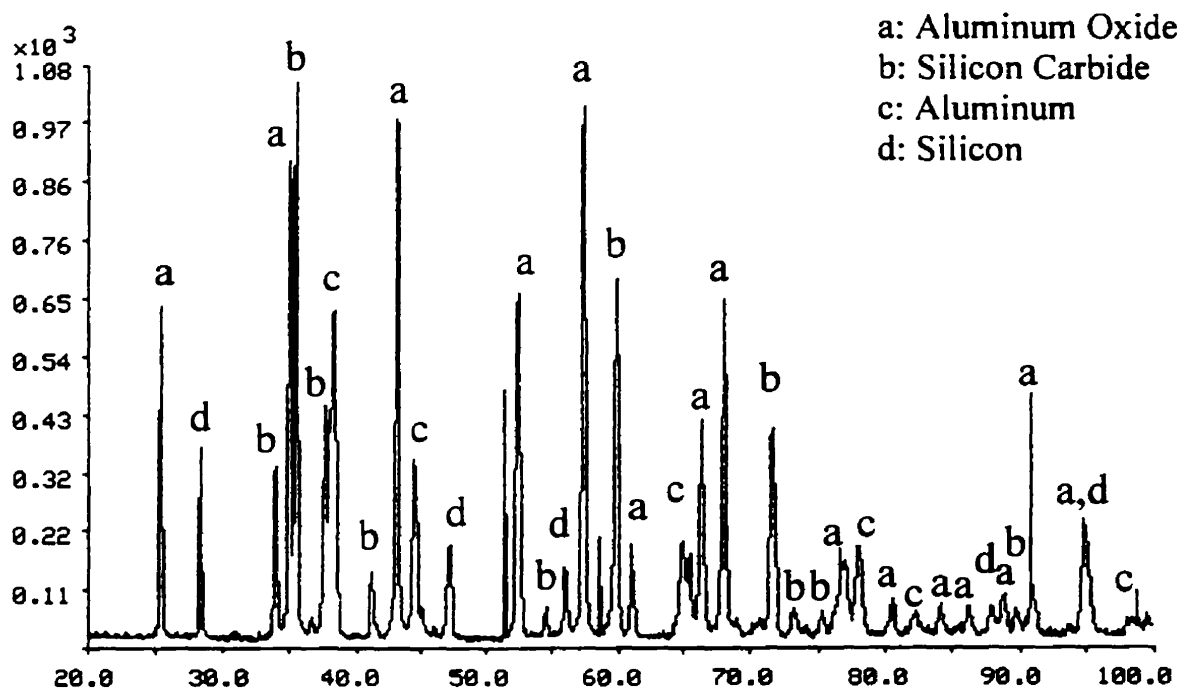


Fig. 5.6: XRD plot for the composite fabricated at 1200°C using a (7/3) alloy.

is the plot for the composite fabricated at 1200°C using a (7/3) alloy. Similar peaks were obtained for the other processing temperatures and using different alloy compositions. Results from x-ray powder diffraction show that the  $\text{Al}_2\text{O}_3$  formed is corundum ( $\alpha\text{-Al}_2\text{O}_3$ ).

Preliminary TEM analysis revealed only SiC,  $\text{Al}_2\text{O}_3$ , and the metallic alloy constituents at the preform/matrix interfaces. No  $\text{SiO}_2$  oxidation layer on the SiC was detected, suggesting that the former had been reduced by the melt. TEM analysis of the interface between the SiC particles and the residual metal also revealed the absence of  $\text{Al}_4\text{C}_3$  or any of the ternary carbides reported for this system,<sup>111</sup> as seen in Fig. 5.7.

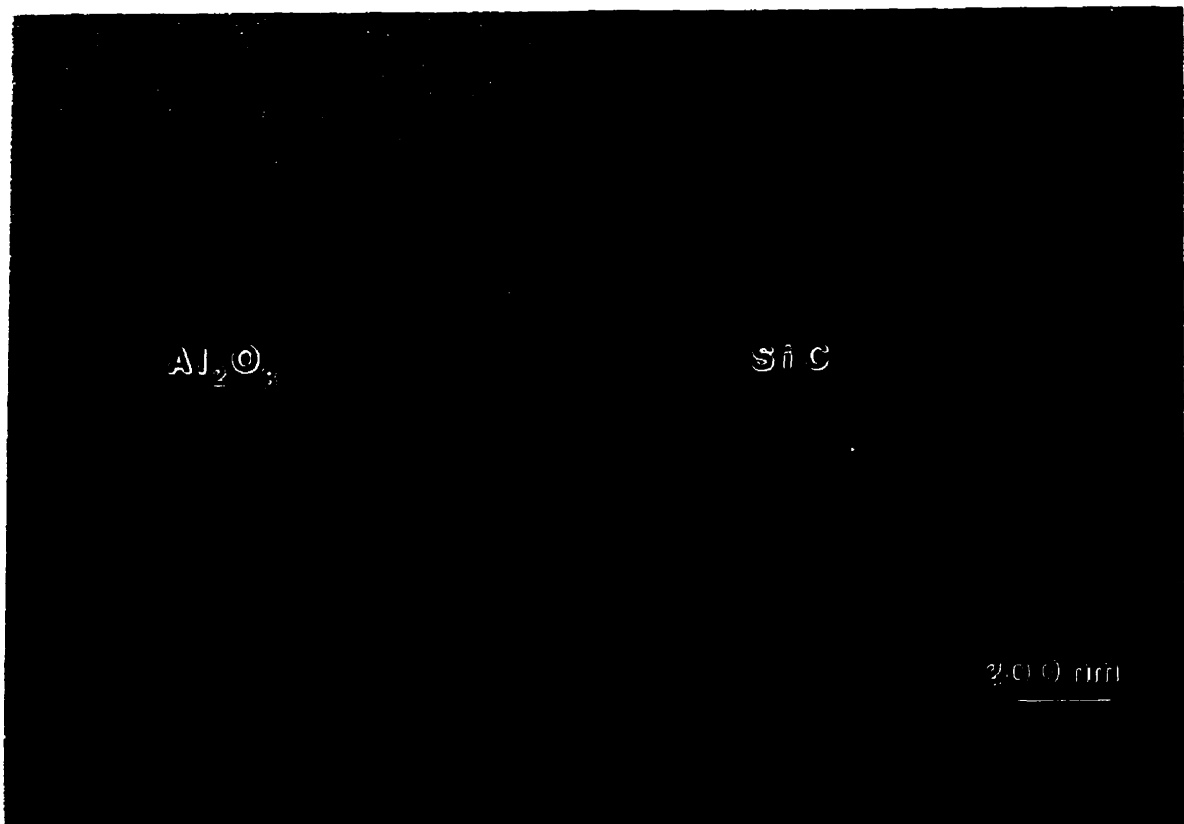


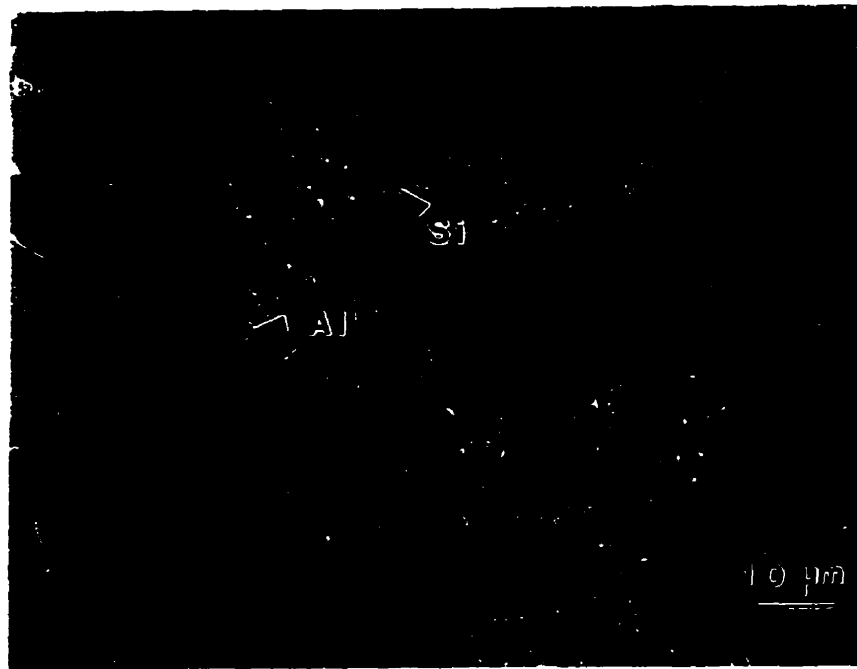
Fig. 5.7: TEM micrograph showing the  $\text{Al}_2\text{O}_3/\text{SiC}$  interface.

Aluminum carbide can be particularly deleterious, since it may react with moisture in the environment and cause the structural disintegration of the composite. Available information on the Al-Si-C phase diagram<sup>111</sup> indicates that the formation of  $\text{Al}_4\text{C}_3$  is precluded by the high Si content of the alloy, which renders the SiC/melt interface thermodynamically stable.

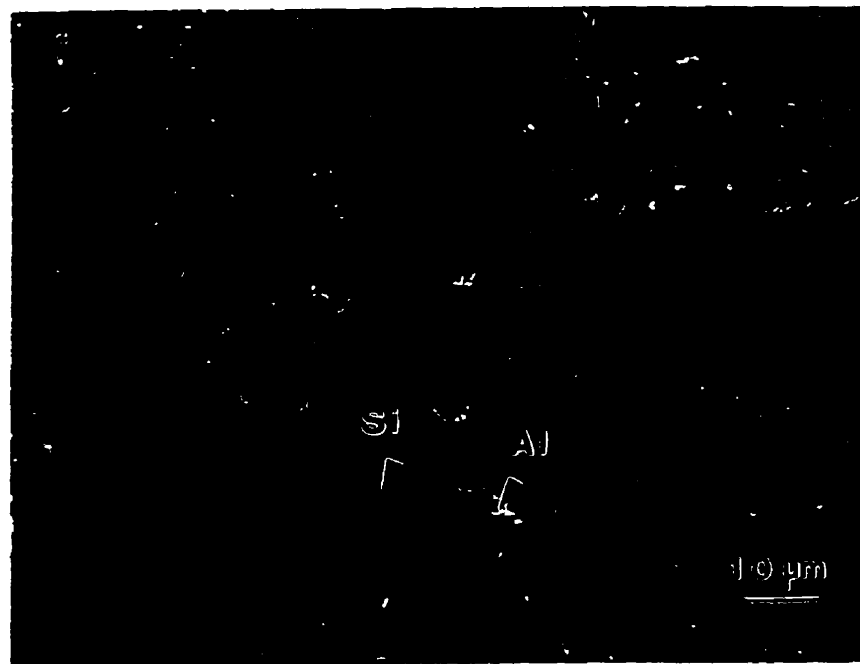
### 5.1.3 Effect of Alloying Elements

Fig. 5.8(a) and (b) show the microstructure of two composites processed at  $1200^\circ\text{C}$  using two different alloy compositions: (3.5/3) and (0/3) alloy, respectively. It is clear that the microstructure retained its typical features, i.e. interconnected  $\text{Al}_2\text{O}_3$  phases surrounding the SiC particles and containing interconnected metal channels. One should expect that the composite processed from an alloy containing only Mg would contain only Al in the metal channels. On the other hand, a composite processed from an alloy containing both Si and Mg should contain both Si and Al metals. However, it is observed that both these composites contain Si and Al in the metal channels, as shown in Fig. 5.8(a) and (b). This is explained as follows: during the reaction, the  $\text{SiO}_2$  passivating film which is present on the surface of the SiC particles is reduced to metallic Si and alloys by the aluminum, as described by:





(a)



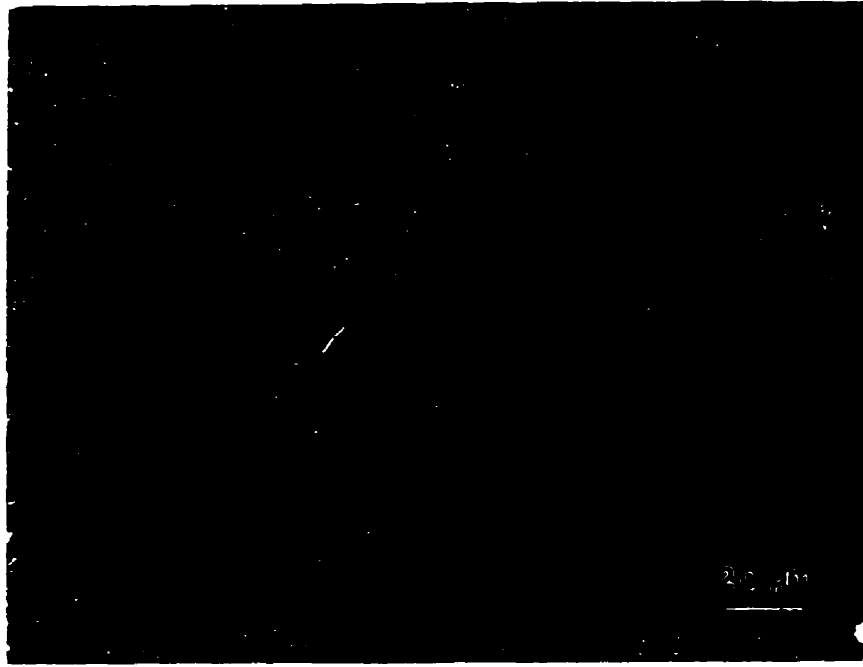
(b)

Fig. 5.8: Microstructure of composites grown at 1200°C with 240-grit SiC particles from (a) (3.5/3) and (b) (0/3) alloys.

By contrast, when processing a composite in the absence of SiC but using the same alloys, the one processed from an Al-Mg alloy contained only Al in the metal channels, whereas that processed from an Al-Si-Mg alloy contained both Al and Si (refer to Fig. 5.1 and Fig. 5.2).

#### 5.1.4 Effect of Processing Temperature

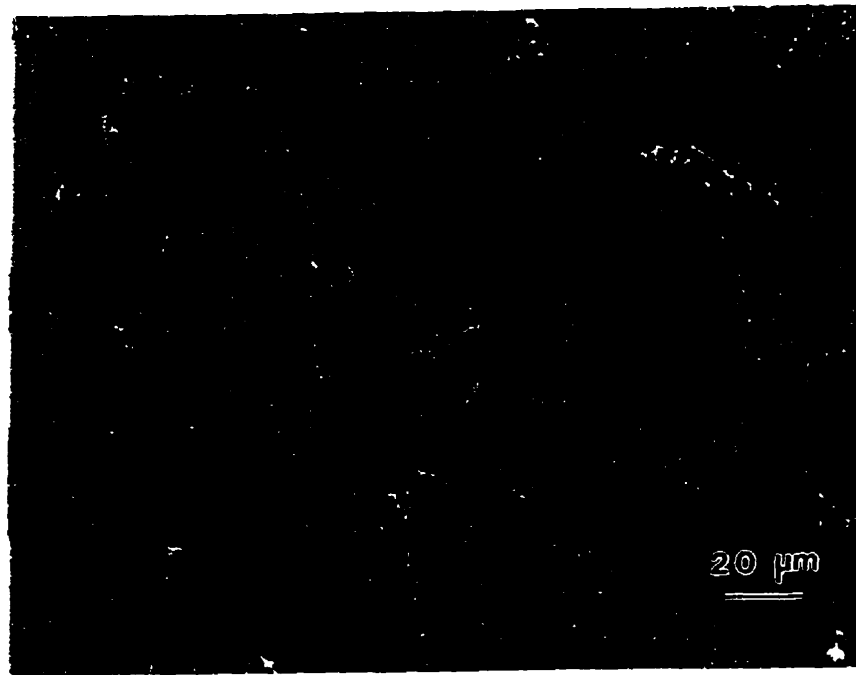
Fig. 5.9(a), (b), and (c) show the microstructures of three composites processed at different temperatures using a (3.5/3) alloy. It is clear that the microstructure consists of a 3-D interconnected  $\text{Al}_2\text{O}_3$  phase surrounding the SiC particles and containing metallic channels. However, the composite processed at lower temperature contained a higher volume fraction of metal and consequently a lower amount of  $\text{Al}_2\text{O}_3$ . Fig. 5.10 shows a plot of the volume fraction of both the metal and  $\text{Al}_2\text{O}_3$  phases in the composite as a function of processing temperature as determined by image analysis. Also Fig. 5.11 shows the size of the metal channels in the composite as a function of temperature. At low processing temperatures, the average size of the metal channels is larger than those of a composite processed at higher temperatures. Both of the previous plots were obtained using image analysis of polished sections of the composites. The values shown are averages taken over twenty different locations or fields within the samples.



(a)



(b)



(c)

Fig. 5.9: Microstructure of composites grown from a (3.5/3) alloy at (a) 1200°C, (b) 1300°C, and (c) 1350°C. The arrows point to the metal channels.

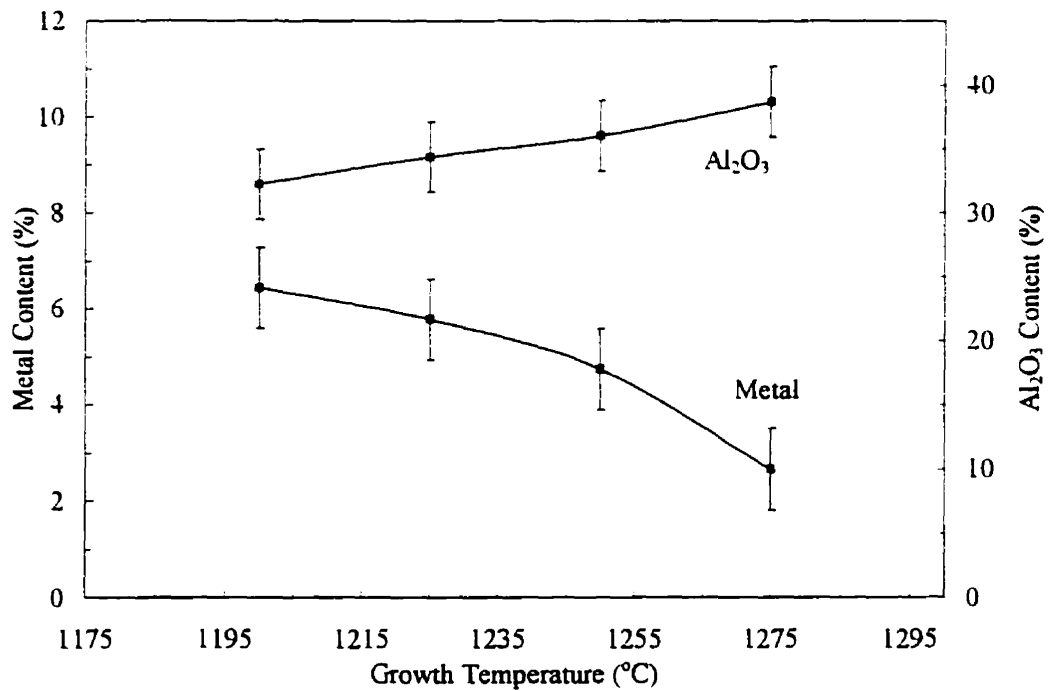


Fig. 5.10: Plot of metal and Al<sub>2</sub>O<sub>3</sub> volume percent as a function of processing temperature using a (7/1.5) alloy.

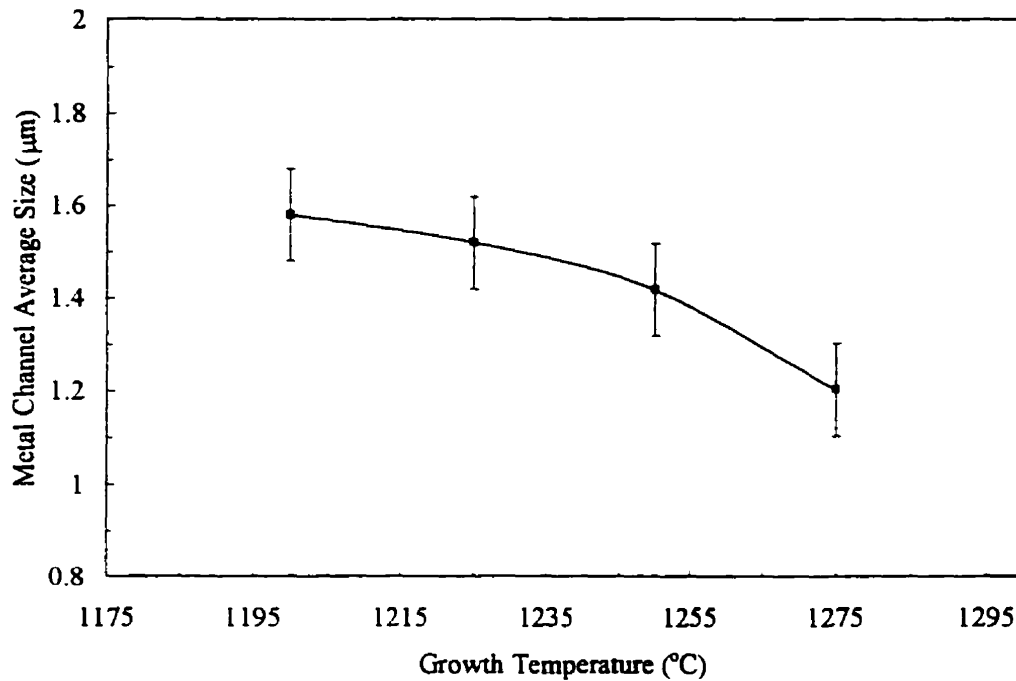
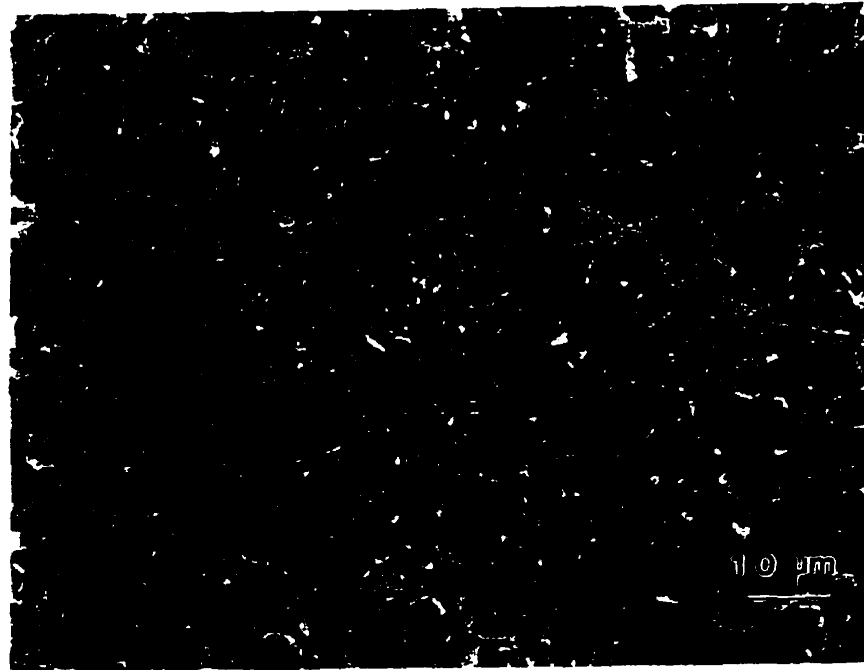


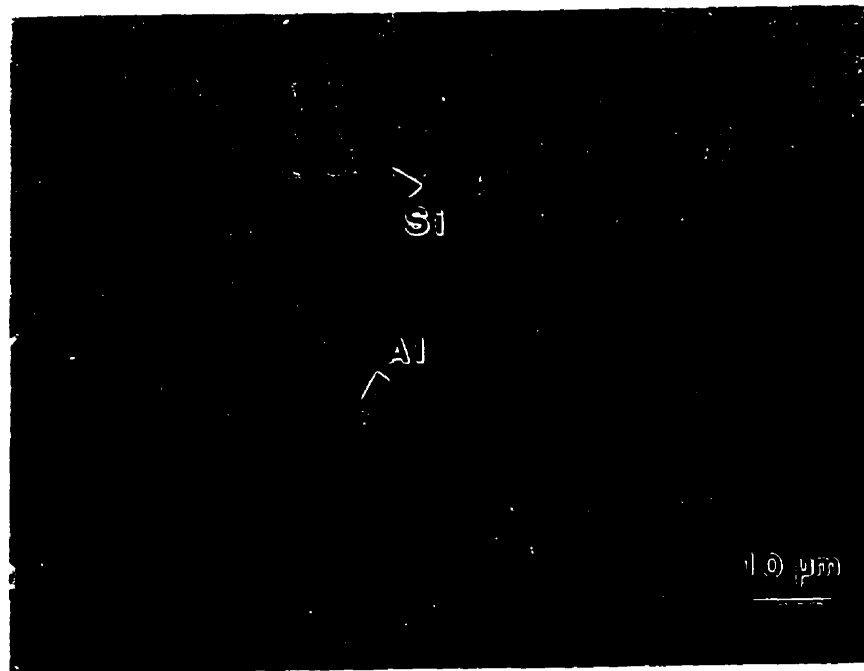
Fig. 5.11: Plot of the metal channel average size as a function of processing temperature using a (7/1.5) alloy.

### 5.1.5 Effect of SiC Powder Size

Fig. 5.12(a) and (b) show the microstructure of composites processed at 1250°C using a (7/3) alloy and reinforced by different SiC powders. It is clear that the microstructure retained its typical features. The introduction of a filler into the composite results in several additional effects on the matrix growth and microstructure. While acting as a structure upon which the composite matrix growth process can proceed, the filler particles also may limit the ingress of  $O_2$  to the growth surface and result in a more tortuous path for the metal wicking to that surface. Even though the filler effectively disrupts the matrix  $Al_2O_3$  columnar structure, it is believed that the



(a)



(b)

Fig. 5.12: Microstructure of composites processed at 1250°C using a (7/3) alloy and reinforced by (a) 600-grit and (b) 240-grit SiC particles.

same basic ceramic growth process is occurring as in the absence of the filler, as will be explained later.

## 5.2 MICROSTRUCTURAL EVOLUTION OF THE COMPOSITES

This investigation examines the nucleation and growth mechanisms responsible for the formation of  $\text{Al}_2\text{O}_3/\text{Al}$  alloy composites by oxidation of (0/3) and (7/3) alloys. These two compositions were chosen because they offer uniform composite growth behavior until completion of the process. One composition contains both alloying elements used for this study, while the other contains only Mg, thus allowing some conclusions to be drawn on the role of Si in the microstructural development (Mg is essential to the formation of these composites without it, no reaction occurs). All composites in this investigation were reinforced with 240-grit SiC particles and composites produced without preforms were used for comparison reasons. The present experiments were conducted at relatively low temperature ( $1150^\circ\text{C}$ ) to facilitate the study of the early stages of the process. The approach includes extensive microstructural characterization of oxidation reaction products. Mechanisms are proposed based on these observations that explain the high temperature nucleation and growth phenomena leading to the conversion of the majority of the bulk Al into  $\text{Al}_2\text{O}_3$ .

The typical oxidation behavior of these alloys in the temperature range where composites can be grown may be conveniently represented by the TGA curve shown in Fig. 5.13.<sup>113</sup> A limited weight gain occurs initially representing the incubation period with variable length depending on several parameters, as will be discussed in section

5.3. After this incubation period, the bulk  $\text{Al}_2\text{O}_3$ -matrix composite forms. The growth ends rather abruptly, although some further oxidation of the alloy continues at an exceedingly slow rate. It is anticipated that the sudden drop in growth rate corresponds to the exhaustion of the bulk metal reservoir, with the additional slow weight gain resulting from the oxidation of residual metal in the microchannels of the composite. However, TGA evidence indicates that in some cases composite growth may cease long before the bulk metal is totally consumed.

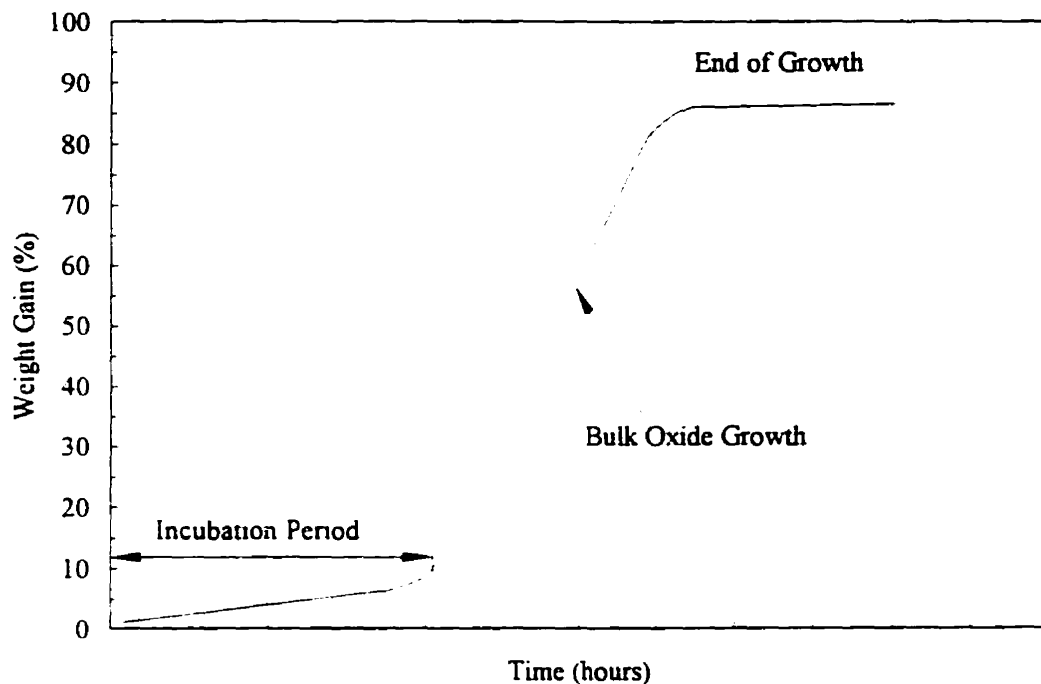


Fig. 5.13: Typical oxidation behavior for Al-containing Mg alloys in air or oxygen at temperatures in the range of 1100-1300°C.<sup>113</sup>

### 5.2.1 Initial Oxidation and Incubation Period

This section presents the microstructural changes that accompany the incubation period of limited oxide growth. The general features are similar for both the

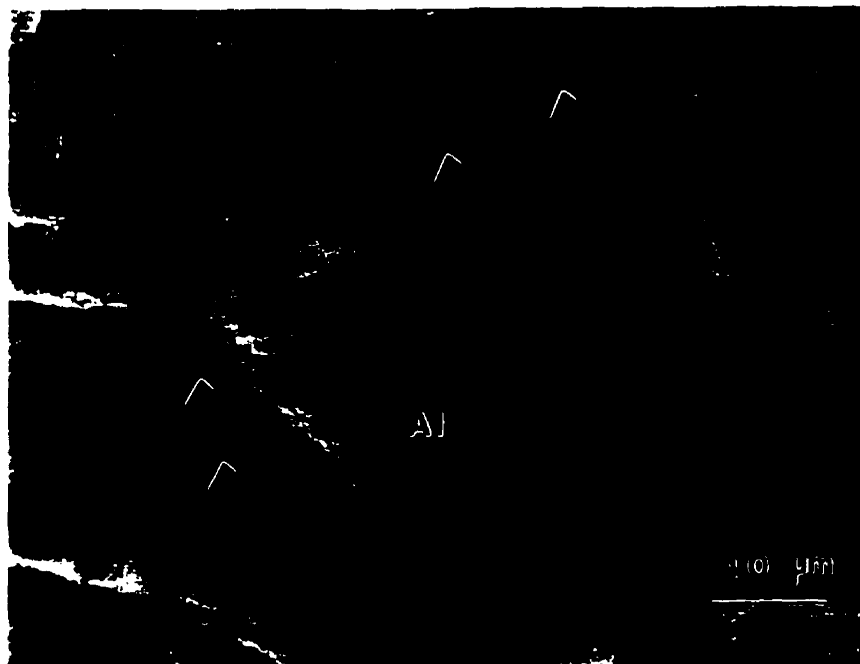
(0/3) and (7/3) alloys, although the duration of the incubation period is considerably shorter for the latter alloy.

### ***5.2.1.1 Unreinforced Composites***

Samples withdrawn 10 seconds after being exposed to 1150°C in the furnace were covered by a thin continuous (~2 μm) layer of fine-grained MgAl<sub>2</sub>O<sub>4</sub>. Immediately after exposure of the alloy at 1150°C (after 20 seconds), the shiny surface of the alloy oxidizes almost immediately into a light gray film even though the bulk alloy is still not molten. After 30 seconds of exposure at 1150°C, the surface of the alloy starts to soften, and voids along the metal grain boundaries are observed, typical of “breakaway” oxidation. These voids, which are the result of some evaporation of Mg from the metal, are shown in Fig. 5.14 (a). Complete melting of the alloy takes place after about 45 seconds of exposure at 1150°C, at which point the liquid melt surface is covered by a continuous dull gray film with many folds and splits (Fig. 5.14 (b)). After 1 minute at 1150°C, the continuous spinel layer thickens to ~3-5 μm and is covered by a very fine white powder typically ≤0.3 μm, which was identified by XRD as MgO. This powder is loose and can be removed by simply tapping the crucible and turning it upside down.



(a)



(b)

Fig. 5.14: Formation of voids along the metal grain boundaries. (a) 30 seconds and (b) 1 minute exposure of (0/3) alloy to 1150°C.

This white MgO powder is the result of the oxidation of Mg vapor which subsequently deposits on the sample surface.

After 5 minutes, the spinel layer grows to a measured thickness of ~8-10  $\mu\text{m}$  and is covered by a continuous ~1  $\mu\text{m}$  MgO layer. This MgO layer is quite different in appearance from the white MgO powder that formed on top of the spinel during initial heating in air. The spinel layer starts to become porous. Occasionally, the spinel is observed to extend to the free surface, but is subsequently covered by MgO. After one hour, the two oxide layers (MgAl<sub>2</sub>O<sub>4</sub> layer between the MgO layer and the alloy) have grown in thickness to ~10-15  $\mu\text{m}$  and ~3  $\mu\text{m}$ , respectively. The two oxides persist with little change macroscopically. Fig. 5.15 shows an SEM view of the top surface after 2

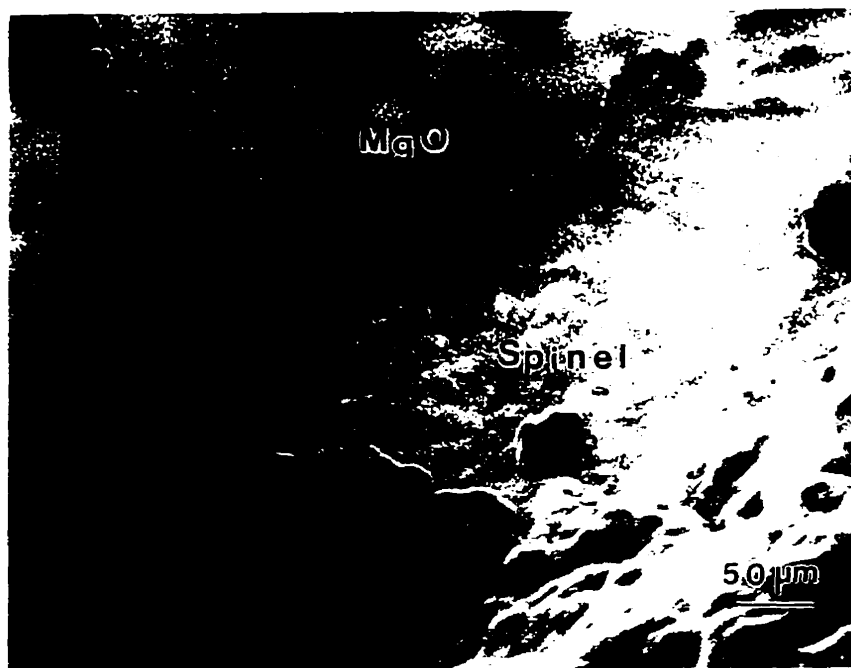


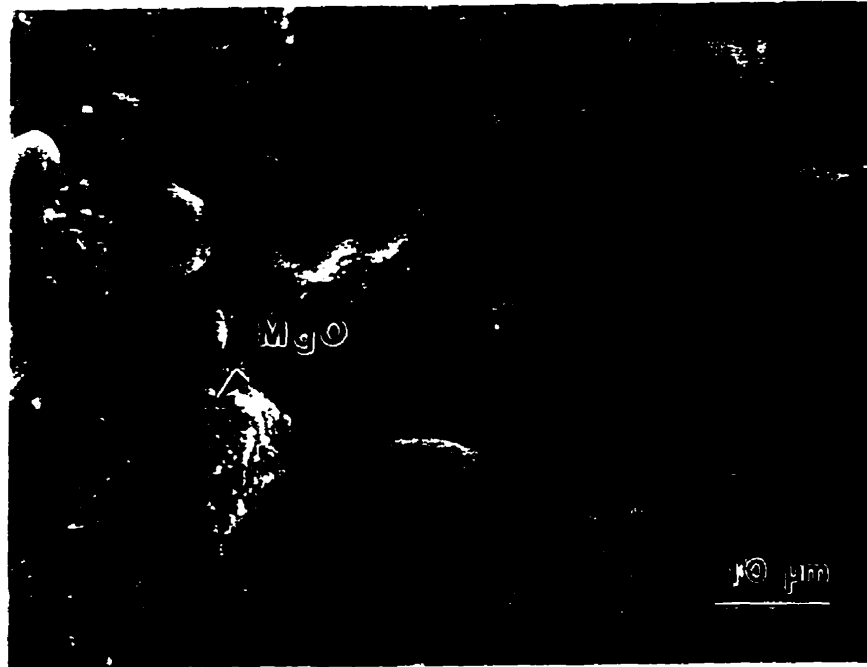
Fig. 5.15: Formation of a duplex MgO/MgAl<sub>2</sub>O<sub>4</sub> layer on the surface of the alloy.

hours of exposure at 1150°C. The top MgO surface layer was flaked away to reveal the underlying oxide, which was identified as having the elemental composition of  $\text{MgAl}_2\text{O}_4$  by EDS. Still no evidence of  $\text{Al}_2\text{O}_3$  formation was detected at this point.

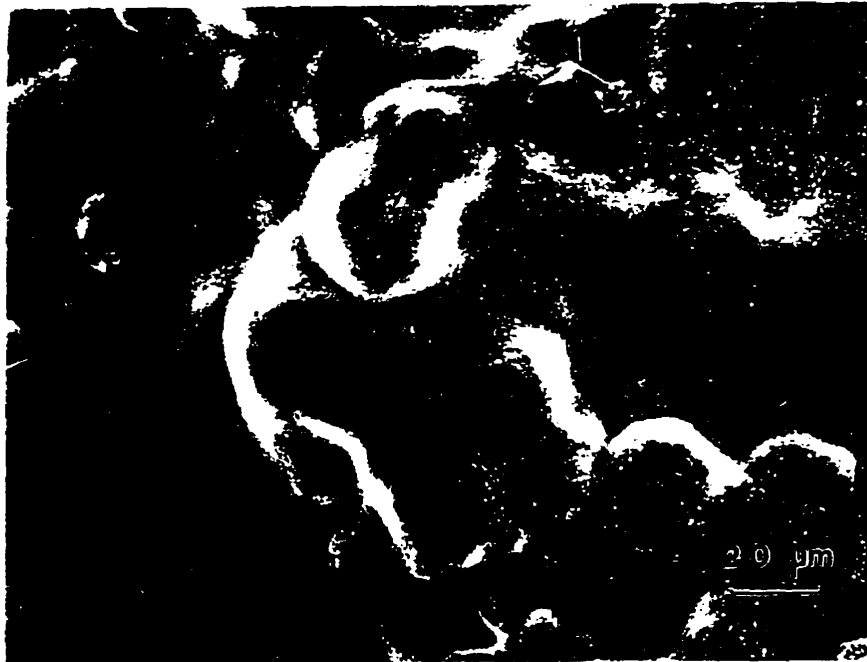
Examination of cross sections of alloys from the bulk oxidation experiments revealed additional information regarding the behavior during the incubation period. For example, Fig. 5.16 shows the surface oxides on a (0/3) alloy heated to 1150°C and held for 15 hours, wherein three distinct zones may be noted. First is a region of spinel containing metal microchannels developing from the bottom, which become progressively finer away from the alloy/spinel interface. Based on the volume fraction



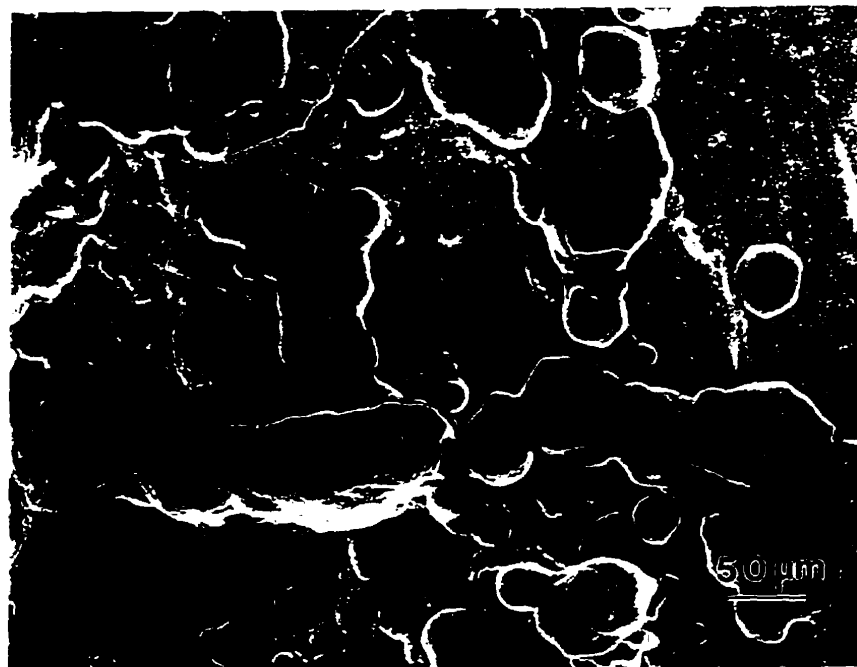
Fig. 5.16: Cross-section of the alloy showing the formation of surface oxides on a (0/3) alloy (15 hours).



(a)



(b)



(c)

Fig. 5.17: Top views of the MgO oxide on the (0/3) alloy held at 1150°C for (a) 15 minutes, (b) 3 hours, and (c) 10 hours.

of metal in this spinel layer (~10-15%), it is likely that the microchannels are interconnected in a 3-D network, even though they may appear as discrete pockets in a 2-D section. Isolated metal pockets, however, may also be present.

The surface morphology of the MgO layer changes continuously during the incubation period leading to the onset of the bulk oxide growth. Fig. 5.17 shows top views of the MgO on the (0/3) alloy held at 1150°C for various times. In Fig. 5.17(a), after 15 minutes of oxidation, the surface has a rough appearance with asperities spread ~20 μm apart. On the fine scale, ~1 μm faceted crystallites of MgO are observed. After 3 hours of exposure at 1150°C, the spinel layer grew to 20-30 μm and the MgO layer

has now a thickness ranging from 5 to 10  $\mu\text{m}$ . After 10 hours, the surface morphology is drastically different. The initial asperities appear to have coarsened into smoother hills and valleys of approximately 75  $\mu\text{m}$  spacing, as shown in Fig. 5.17(c).

In the final stages of incubation for this alloy, after 23 hours at 1150°C, further coarsening results on a relatively flat and dense surface. Simultaneously, new and different perturbations appear which are associated with the arrival of the metal microchannels near the surface and the reduction in the MgO layer thickness. This event is followed by the initiation of the bulk oxidation, which takes place by formation and growth of  $\text{Al}_2\text{O}_3$  nodules, as the one shown in Fig. 5.18.

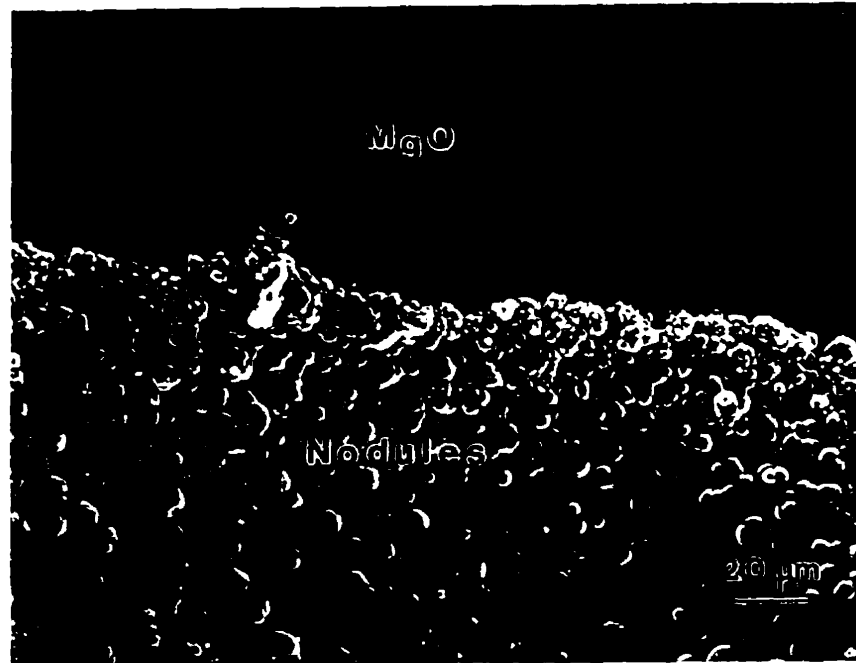


Fig. 5.18: Top view of the MgO oxide on the (0/3) alloy held at 1150°C for 23 hours (length of the incubation period for this alloy).

The microstructure and extent of these three regions change as a function of time. The MgO layer thickens and densifies for the first 10 hours and then becomes thinner. Furthermore, as time progresses, the metal microchannels coarsen and appear to advance through the thickening spinel toward the outer surface.

While the initiation of the bulk oxidation and formation of  $\text{Al}_2\text{O}_3$  nodules start after 24-25 hours for the (0/3) alloy, it took only 4-5 hours for the (7/3) alloy to initiate the formation of  $\text{Al}_2\text{O}_3$  nodules, but the evolution of the surface morphology is similar to that of the former alloy. Fig. 5.19 shows the changes in average thickness of the MgO and  $\text{MgAl}_2\text{O}_4$  layers with time for the (0/3) and (7/3) alloys. The values in this figure are averages measured on different locations (8-14 locations) of the sample using the SEM.

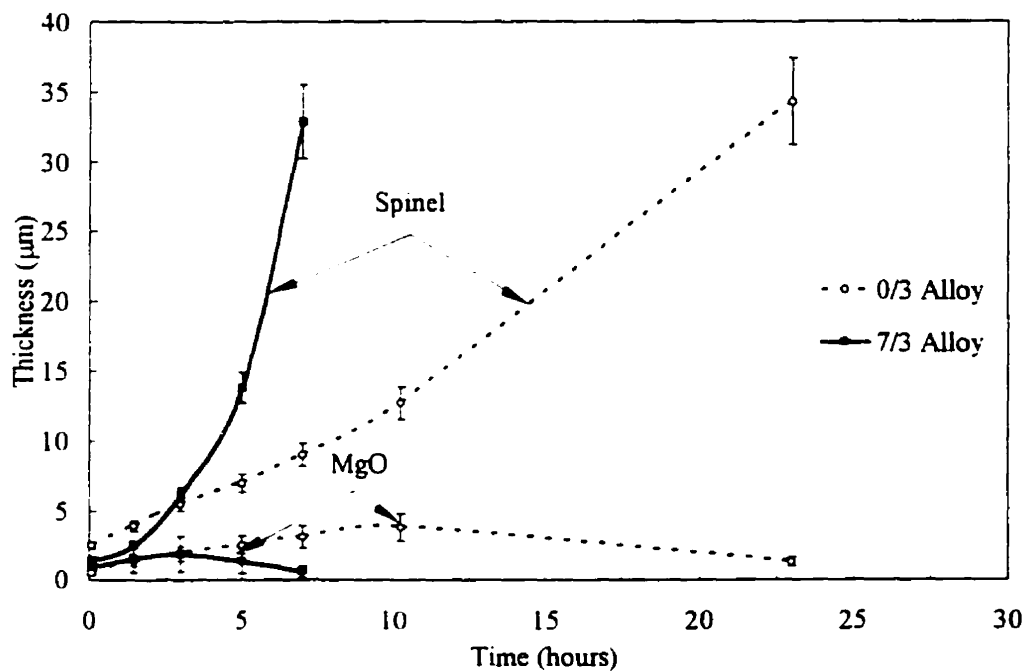


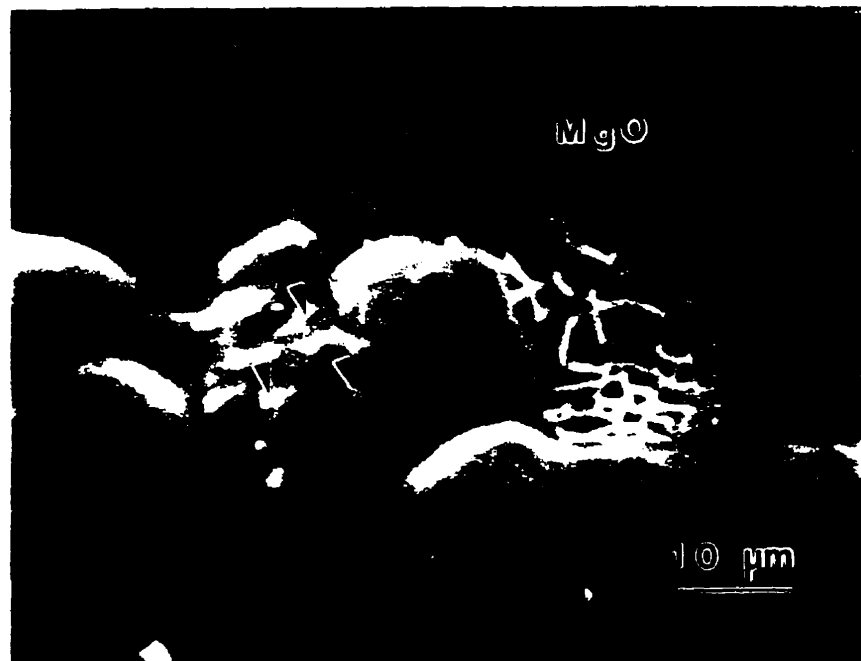
Fig. 5.19: Variation in the average thickness of MgO and  $\text{MgAl}_2\text{O}_4$  layers with time at  $1150^\circ\text{C}$  for (0/3) and (7/3) alloys.

Fig. 5.20 shows a more advanced stage of nodule formation on the surface of the (7/3) alloy. It is evident that the nodules evolve on the undulated region of the MgO surface. Fig. 5.20 (a) shows the dissociation of the MgO layer which becomes porous and opens to expose the underlying metal channels to the oxidizing atmosphere. Mg vapor oxidizes when in contact with oxygen and MgO crystals are formed (indicated by the arrows) and are deposited on the outer surface. Fig. 5.20 (b) shows both the dissociation of the MgO layer (right-hand side) and the nucleation of  $\text{Al}_2\text{O}_3$  nodules (left-hand side).

For the Si containing alloy (7/3), the sequence of microstructural evolution during the incubation period is shown Fig. 5.21. After 30 seconds of exposure, spinel starts forming along the Al grains. Shortly afterwards, the spinel grows outwards and covers the top surface of the alloys by coalescence of the spinel grains from different growth sites. The surface of spinel smoothes out and MgO crystals ( $\sim 2\text{-}3\ \mu\text{m}$ ) start appearing after 75 seconds and spread all over the outer surface (Fig. 5.21(d)).

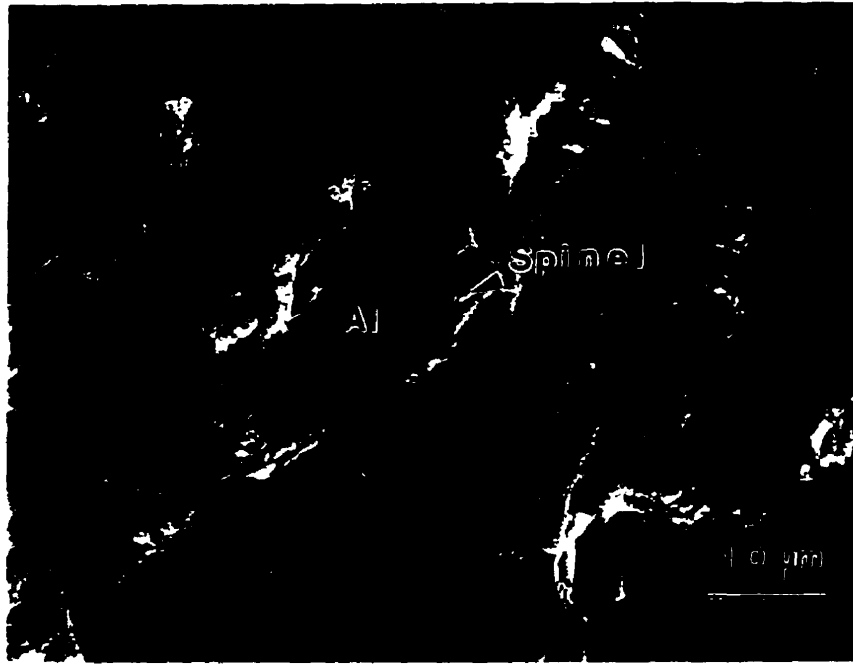


(a)



(b)

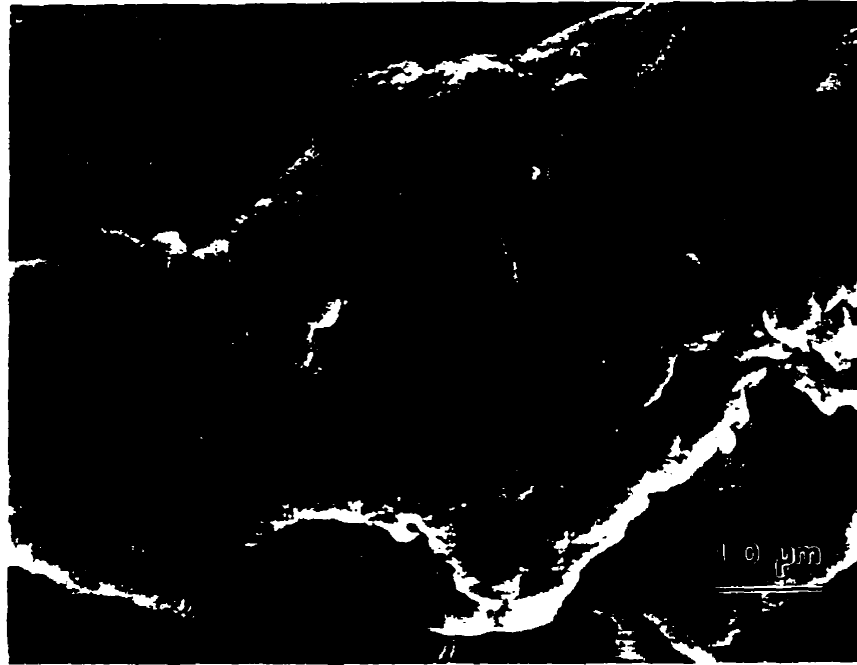
Fig. 5.20: Nodule formation during growth on the surface of the (7/3) alloy at 1150°C after 5 hours.



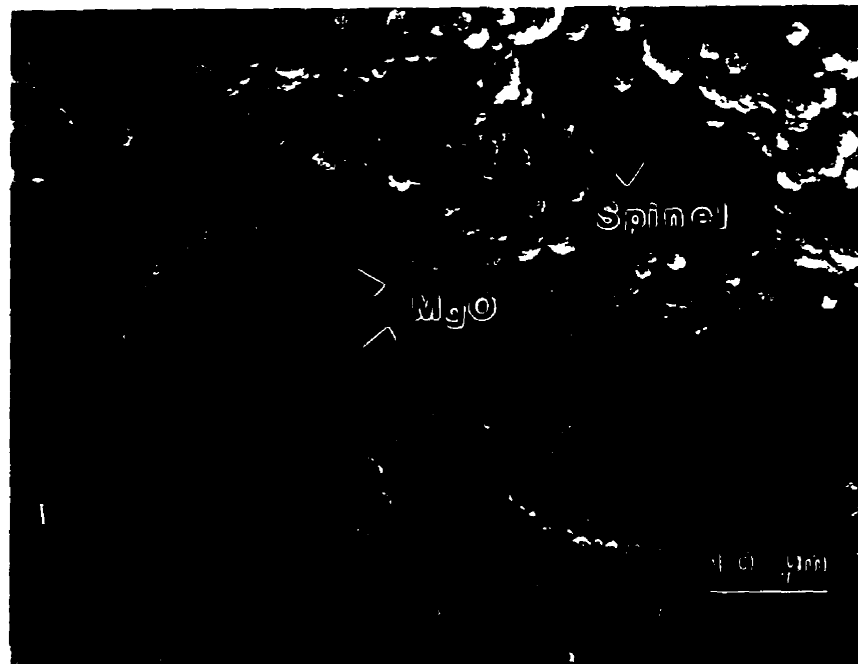
(a)



(b)



(c)

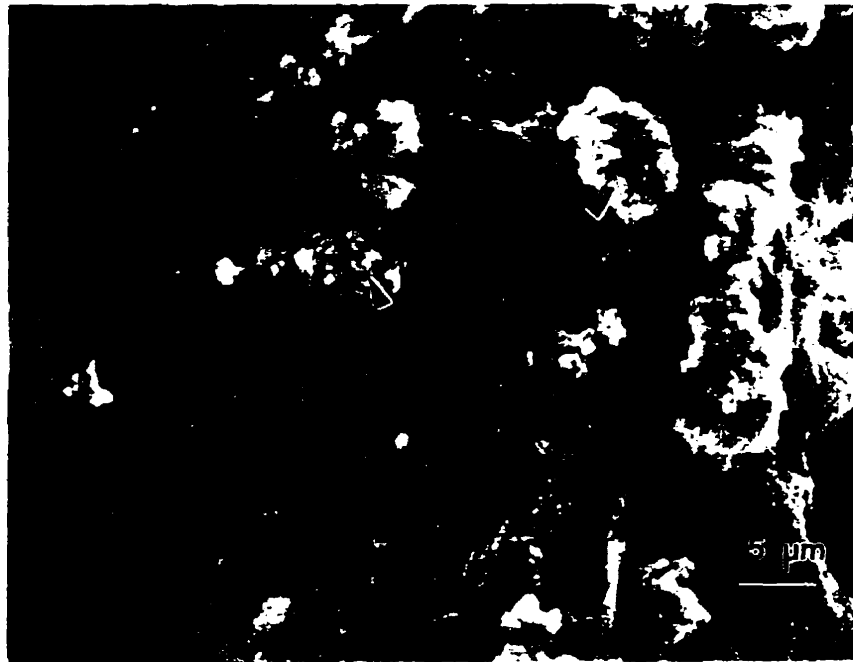


(d)

Fig. 5.21: Top views of the MgO oxide on the (7/3) alloy held at 1150°C for various times (a) 30 seconds, (b) 45 seconds, (c) 60 seconds, and (d) 75 seconds.

### 5.2.1.2 SiC-Reinforced Composites

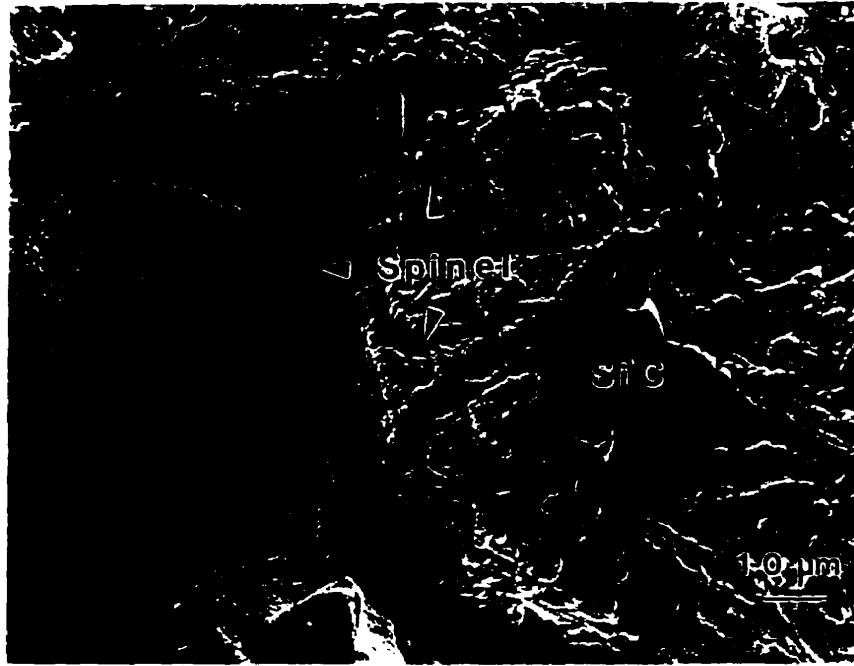
The initial oxidation of the alloys in the presence of SiC particles is similar to that of the unreinforced composites, except that the incubation period is much shorter and sometimes not observed at all. After 2 minutes of exposure at 1150°C, the exposed surface of the alloy becomes porous and spinel rings appear around the surface pores, as shown in Fig. 5.22(a). Cross sections of the samples do not reveal any traces of either spinel or MgO. This is due to the fact that the spinel rings are small (1-5  $\mu\text{m}$ ) and it is difficult to intercept them during sectioning of the samples. After 5 minutes, the exposed surface is completely covered by a continuous dense spinel layer but contains metal channels (Fig. 5.23). New MgO crystallites start nucleating on the outer spinel surface with an average grain size of 3-4  $\mu\text{m}$  and grow favorably along the SiC particles, as shown in Fig. 5.22(d). The MgO crystallites quickly cover the spinel surface and form a locally continuous layer between the SiC particles shown in Fig. 5.22 (e). The MgO then starts to dissociate upon arrival of the metal to the spinel/MgO interface and composite nodules start forming on the exposed surface as seen in Fig. 5.22(f). The composite nodules nucleate between the SiC particles, and can actually nucleate on the surface of the SiC, as shown in Fig. 5.24.



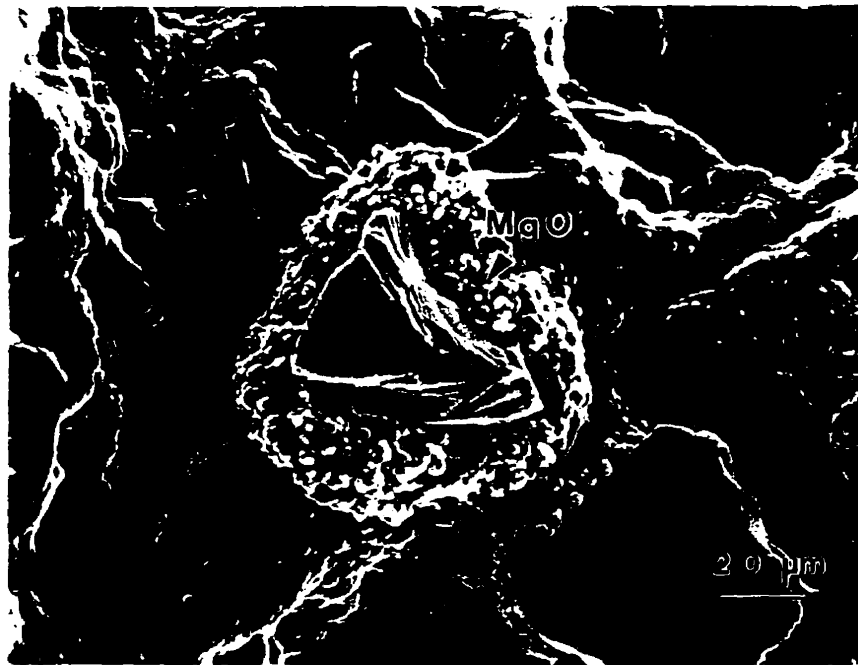
(a)



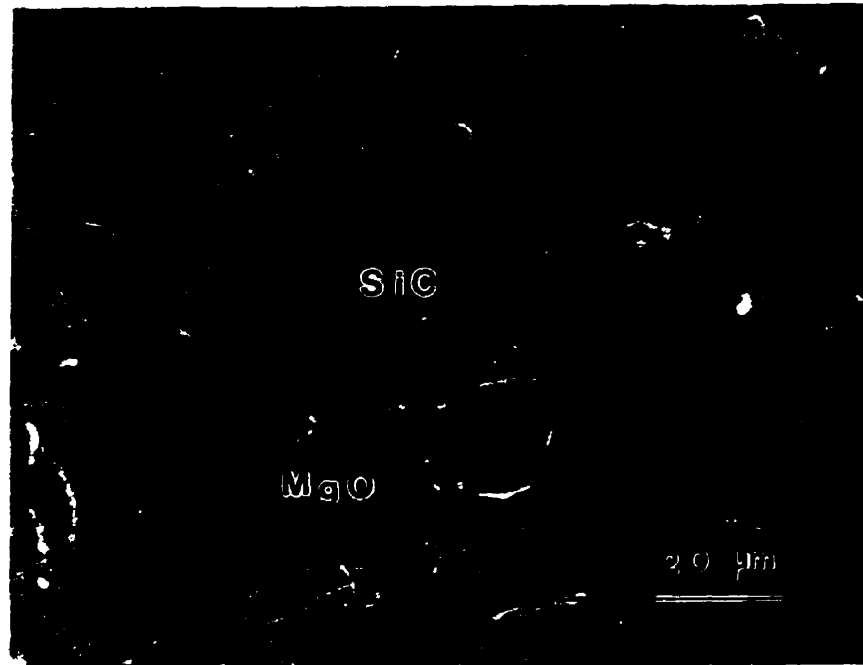
(b)



(c)



(d)



(e)



(f)

Fig. 5.22: Top views of the surface oxides on the (0/3) alloy with SiC held at 1150°C for (a) 2 minutes, (b) 5 minutes, (c) 7 minutes, (d) 10 minutes, (e) 15 minutes and (f) 30 minutes.

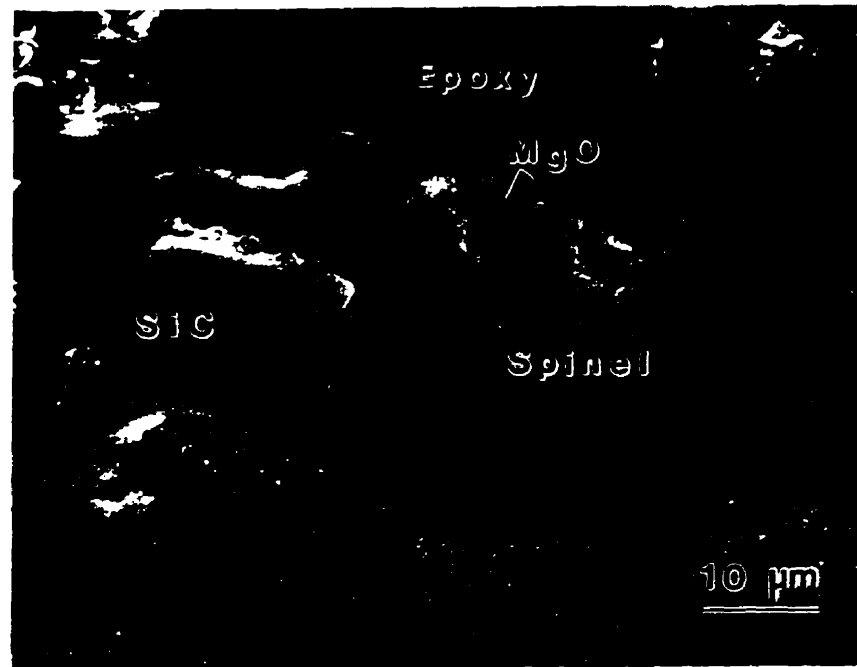


Fig. 5.23: Cross section of the (0/3) alloy surface after 5 minutes of oxidation.

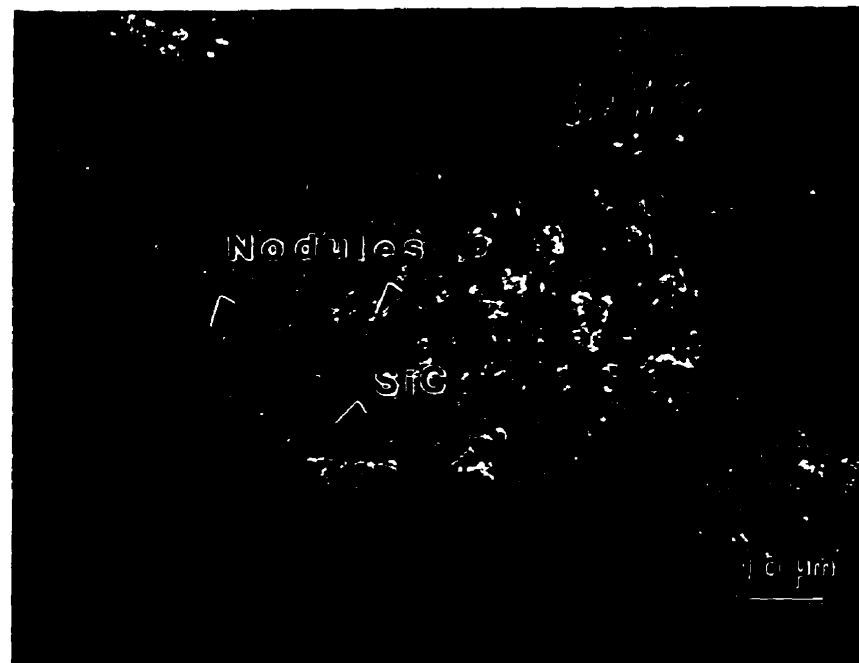


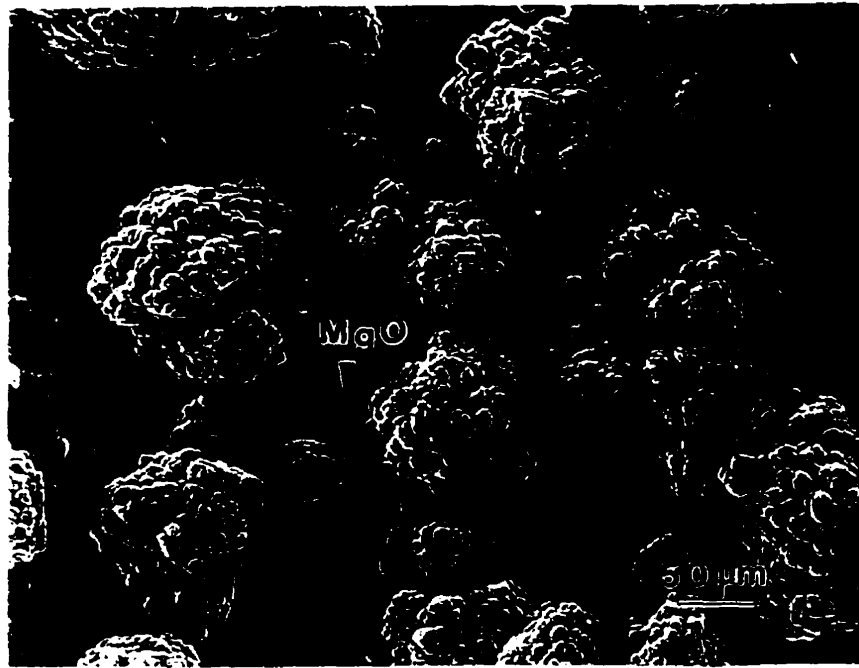
Fig. 5.24: Top views of the surface of the (0/3) alloy with SiC held at 1150°C for 30 minutes.

## 5.2.2 Bulk Oxidation: Composite Growth

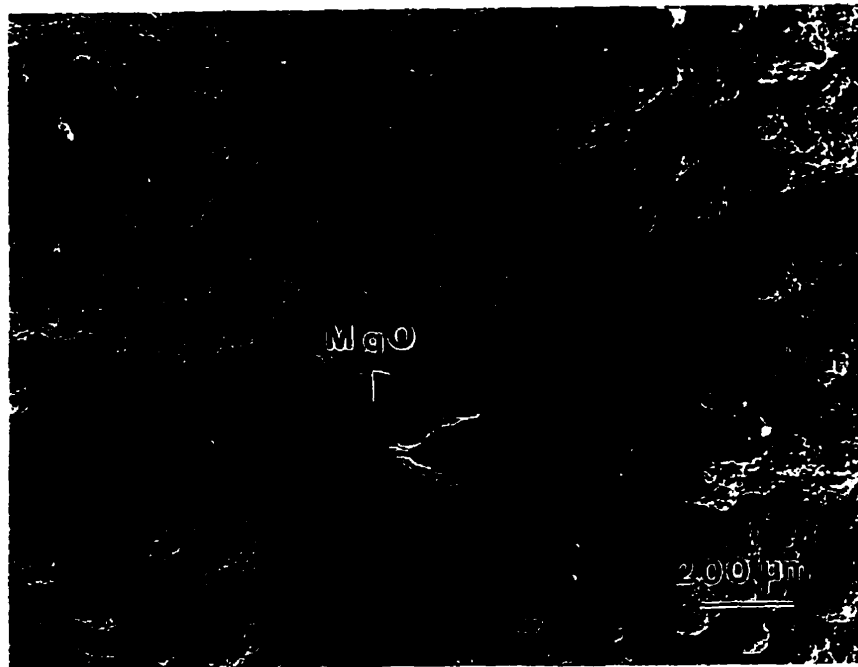
### 5.2.2.1 Growth of Unreinforced Composites

The surface appearance changes throughout the incubation period and eventually leads to the formation of clearly distinguishable composite nodules, as illustrated in Fig. 5.25(a). At this stage, the alloy/atmosphere interface consists of: (i) the spinel/metal mixture (in the form of channels and/or isolated pockets) produced by the initial rapid oxidation and (ii) the MgO layer which forms by the preferential diffusion of Mg (relative to Al) toward the higher O potential. Nodules at this stage are sometimes seen to contain two distinct morphologies, one more convoluted and finer in scale growing on top of another with coarser features but a smoother surface.

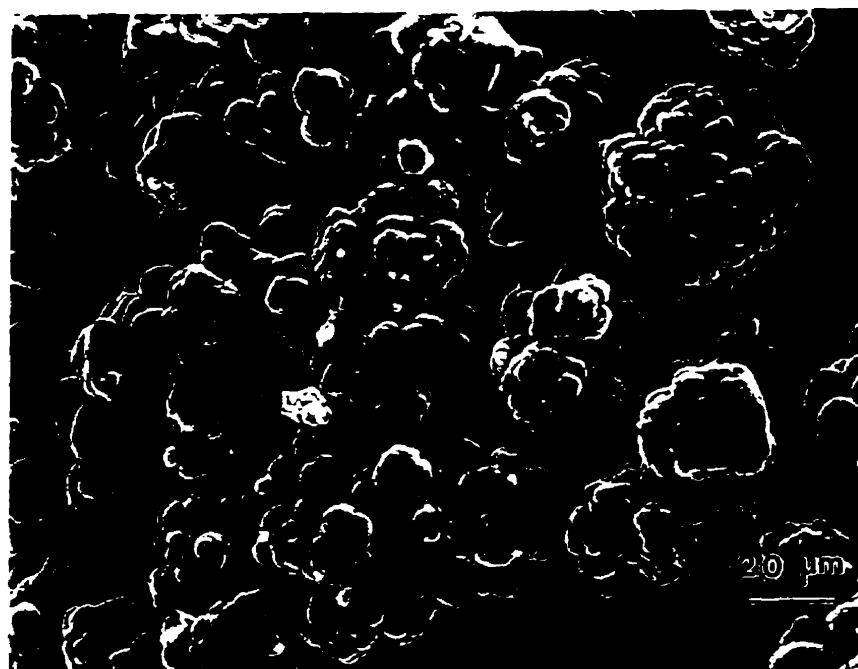
Cross-sectional views of several nodules from the early stages are shown in Fig. 5.26. Small nodules ( $\leq 100 \mu\text{m}$ ) typically contain spinel and metal covered by a surface MgO layer. Larger nodules consist predominantly of  $\text{Al}_2\text{O}_3$ , and are covered by MgO, such as the one shown in Fig. 5.27, although some spinel is often noticeable at their base. These observations lead to the conclusion that growth of the  $\text{Al}_2\text{O}_3/\text{Al}$  composite is preceded by evolution of  $\text{MgAl}_2\text{O}_4/\text{Al}$  nodules on the surface of the metal alloy.



(a)



(b)

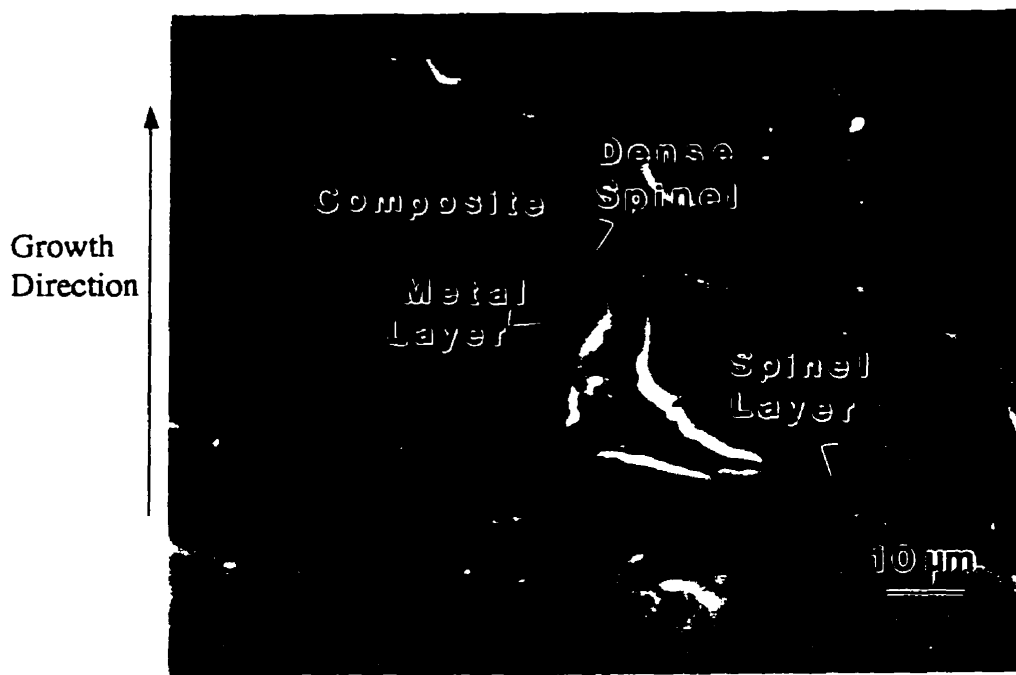


(c)

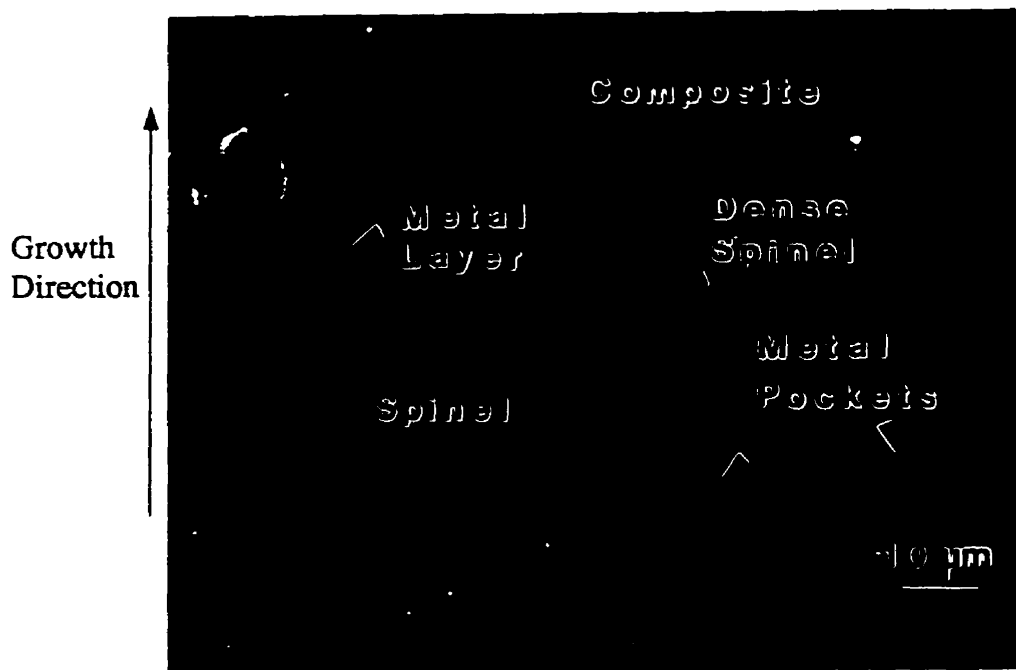
Fig. 5.25: Top views of the surface of the (7/3) alloy held at 1150°C for (a) 5 hours, (b) 10 hours, and (c) 15 hours, showing the progressive evolution of the composite.

After the nucleation of the  $\text{Al}_2\text{O}_3/\text{Al}$  nodules, the bulk oxide growth proceeds. Adjacent to the parent alloy is the original  $\text{MgAl}_2\text{O}_4/\text{Al}$  layer, followed by the  $\text{Al}_2\text{O}_3/\text{Al}$  composite structure, extending out to the reaction surface. During growth, the top surface morphology is nodular on both the coarse ( $\sim 0.5$ -1 mm) and fine ( $\sim 50$ -100  $\mu\text{m}$ ) scales, Fig. 5.28(a) and Fig. 5.28(b), respectively.

Since the formation of the composite nodules is random at the surface of the alloy, there are regions where new nodules are not formed until later in the process. These regions which are contained by already formed nodules, have the two-layer structure (i.e. spinel/ metal mixture and MgO layer).



(a)



(b)

Fig. 5.26: Cross sectional views showing the spinel/composite interface.

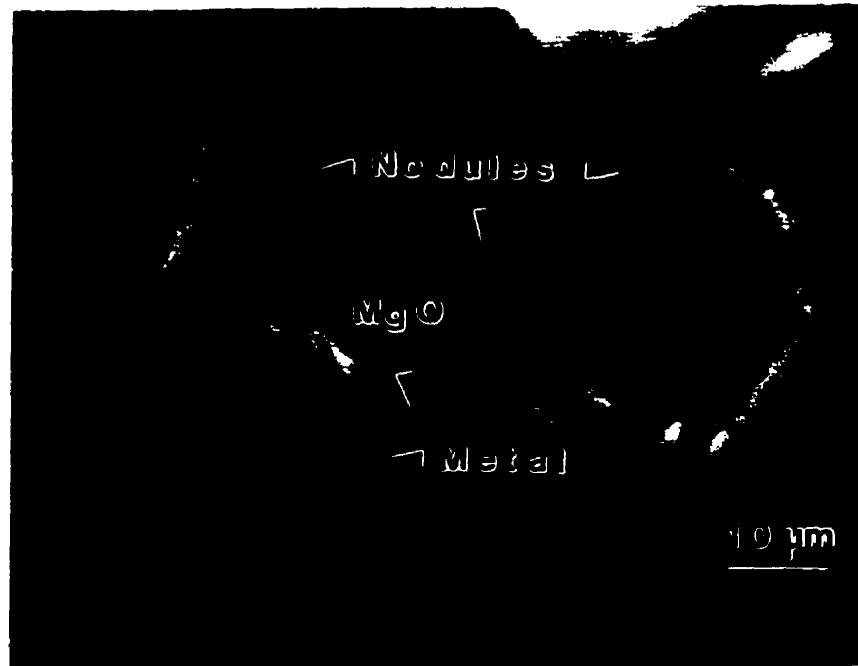
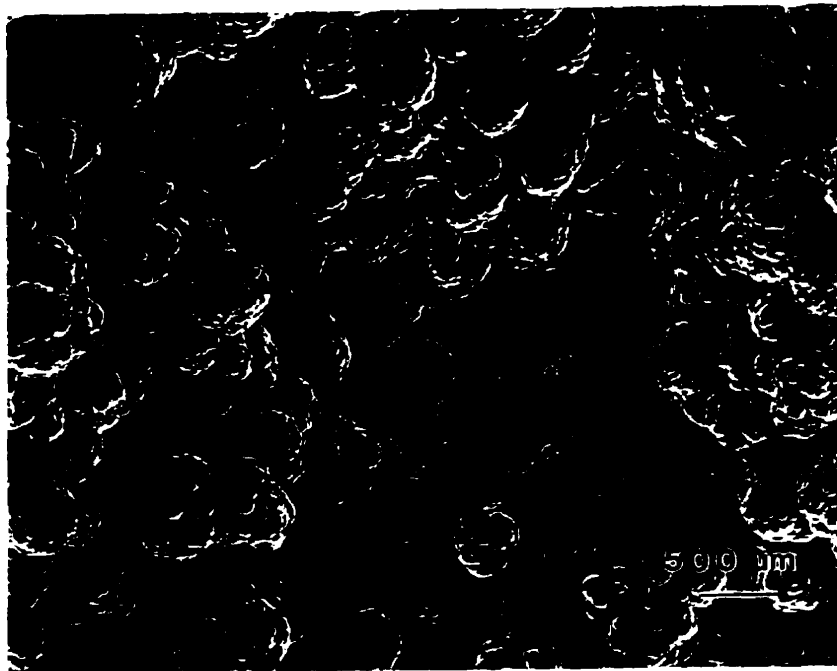


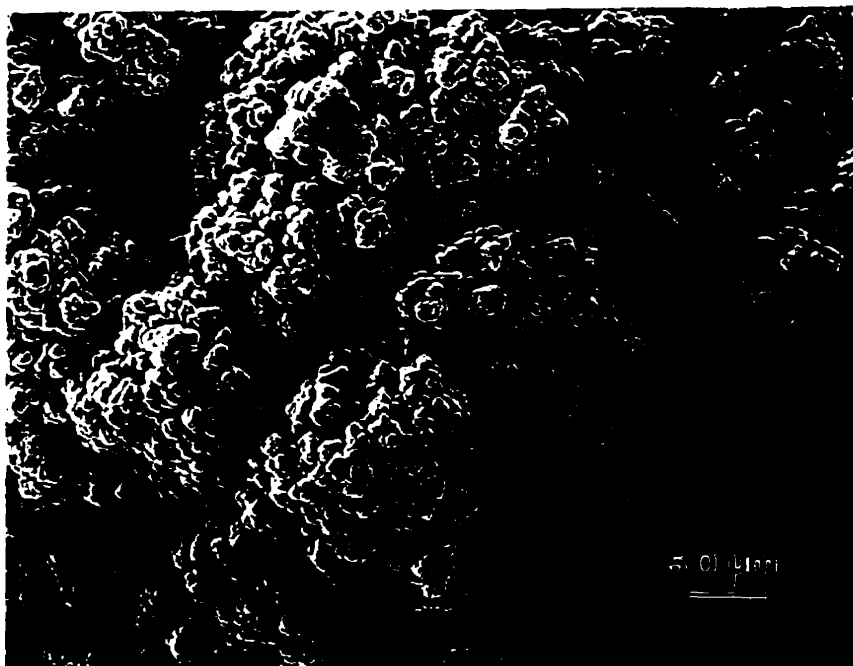
Fig. 5.27: Cross section of  $\text{Al}_2\text{O}_3$  nodules covered by MgO on the outer composite/air surface.

These regions (50-100  $\mu\text{m}$  in size) often assume a circular shape and evolve above the surface of the composite and become spheres. Eventually new composite nodules nucleate from these sites, as shown in Fig. 5.29.

The formation of nodules in this manner contributes to the undulating nature of the growth front of these composites. The cracks observed on the surface of these spheres is attributed to one or more of the following factors: (i) the large expansion of their surface layers and the underlying alloy is then exposed to the oxidizing atmosphere, (ii) the evaporation of Mg from the alloy, and (iii) the cooling from the growth temperature.

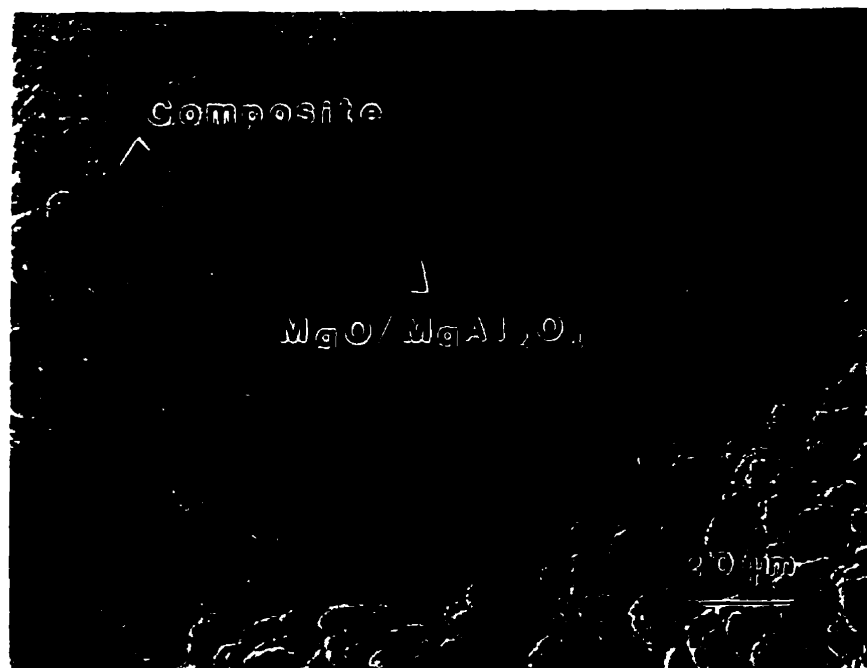


(a)



(b)

Fig. 5.28: Top views of the surface of the (7/3) alloy held at 1175°C for 20 hours (a) coarse and (b) fine scale.



(a)



(b)



(c)

Fig. 5.29: Top views of the surface of the (7/3) alloy held at 1175°C for (a) 10 hours, (b) 12 hours, and (c) 15 hours.

The metal microchannels in the composites vary in size from 1 to 10 μm. The magnesium content of the alloy in these channels is very low ( $\leq 1.2\%$  measured by EDS quantitative analysis), while the silicon concentration varies with the starting content of silicon in the original alloy. The  $Al_2O_3$  grains appear to grow over tens of microns with the same crystallographic orientation, containing from time to time low angle grain-boundaries, as seen in Fig. 5.30.

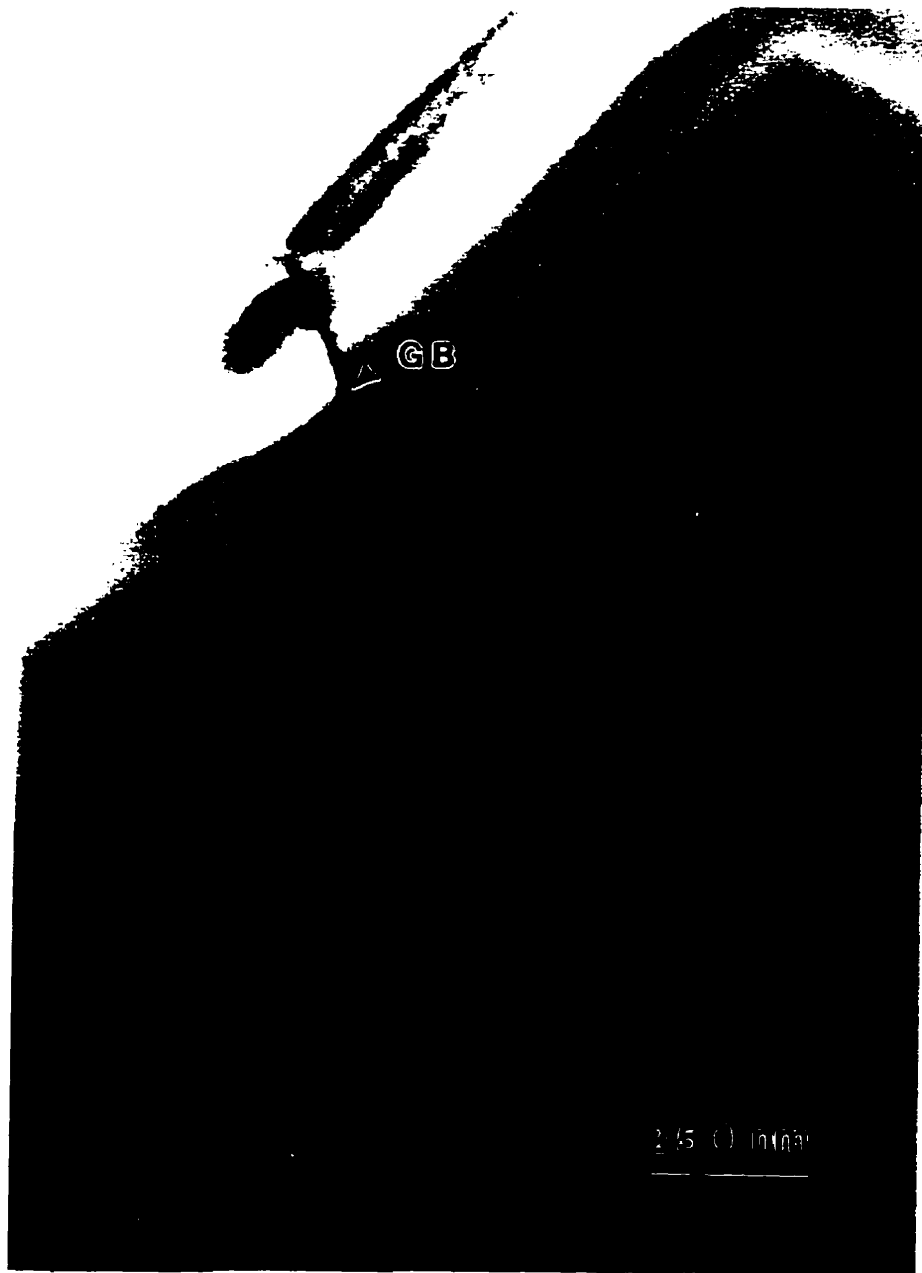
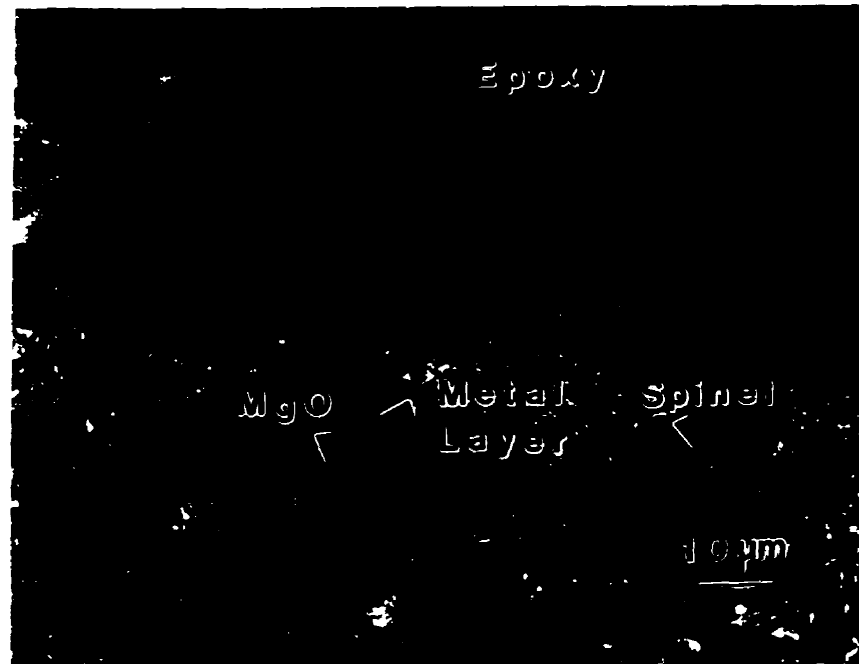
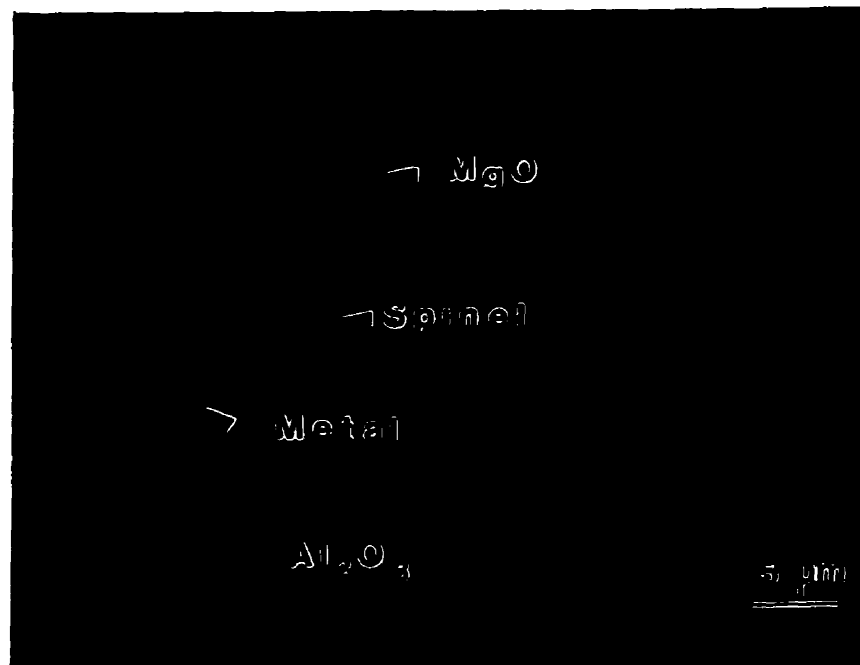


Fig. 5.30: TEM micrograph showing an Al<sub>2</sub>O<sub>3</sub>/Al<sub>2</sub>O<sub>3</sub> low angle grain boundary.



(a)



(b)

Fig. 5.31: External surface layers of the composite. (a) Optical micrograph of a cross section and (b) a BEI micrograph showing a fractured surface of the composite/air interface.

Within the bulk of the composites, the microstructure is fairly uniform, however significant variations in composition are observed close to the external growth surface. A continuous MgO layer covers the external composite surface. The thickness of this surface layer is variable and ranges from 2-5  $\mu\text{m}$ . In addition, a thin layer of metal is often found directly below the external oxide layer, as shown in Fig. 5.31.

#### 5.2.2.2 *Growth of SiC-Reinforced Composites*

Initial examination of the composite surface after careful removal of the uninfiltred portion of the preform reveals a slightly undulated front covered by a continuous MgO layer between the SiC particles, as shown in Fig. 5.32. Thus, the proposed growth mechanism involving formation and dissolution of the MgO surface layer seems to be essentially preserved within the preform. The surface roughness in Fig. 5.32 does not appear to be significantly different from that of the base alloy to justify a substantial increase in the area of the oxidation interface. However, the cross section of the same specimen in Fig. 5.33 shows that the profile of the oxidation front is much more convoluted than that suggested by the top surface view. The front is rather porous and extends over a scale of several particle diameters with the volume fraction of the  $\text{Al}_2\text{O}_3$ /alloy reaction product increasing inward from the surface. It was also found that a layer of SiC particles immediately above the visible surface oxide remained attached to the composite when the crucible was turned upside down and tapped to remove the uninfiltred portion of the preform. These particles appeared to

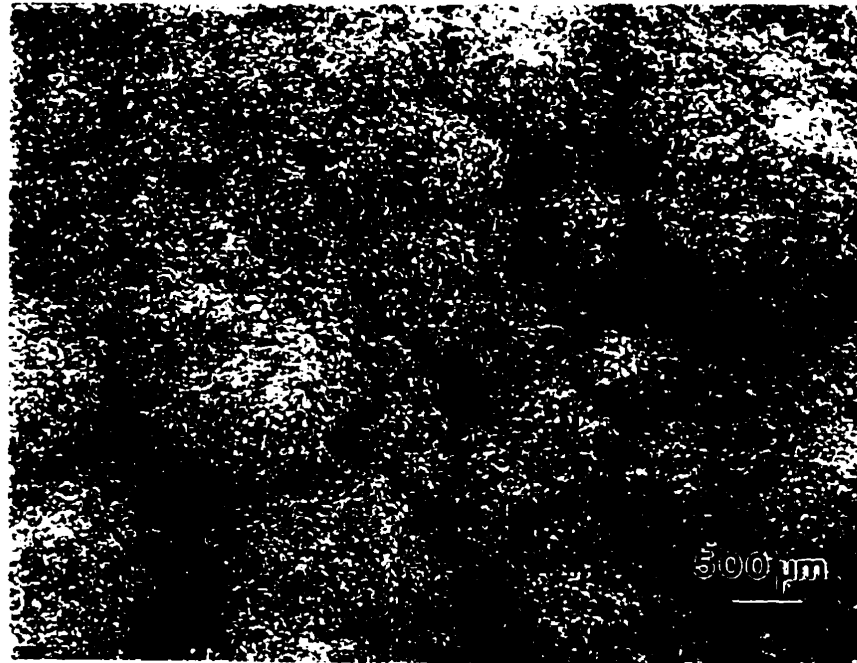


Fig. 5.32: Top view of a SiC reinforced composite.

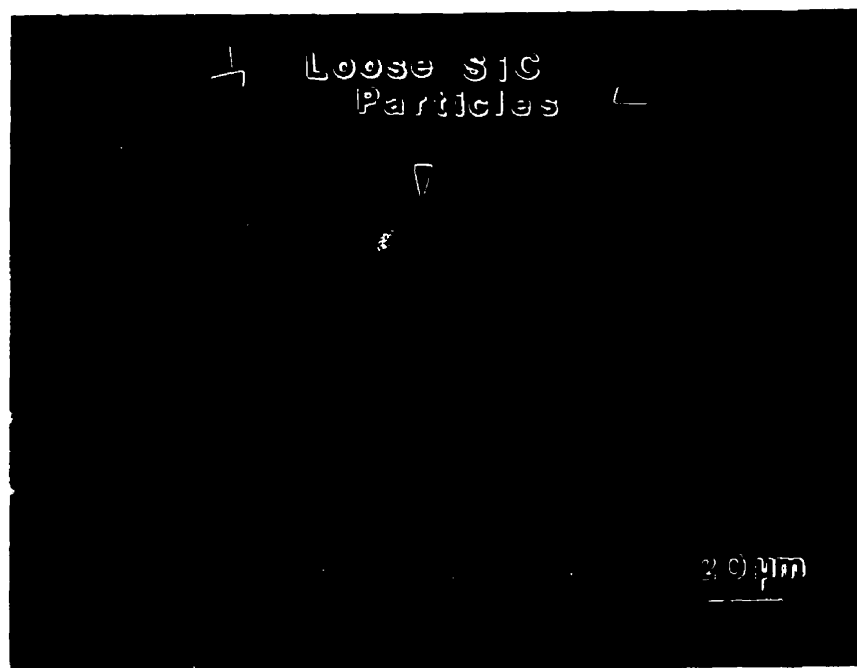
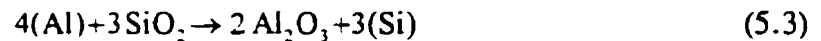


Fig. 5.33: Optical micrograph showing a cross-section of the top of the composite.

be lightly sintered, suggesting that neck formation is aided by some form of condensation (presumably MgO) from the vapor phase ahead of the oxidation front.<sup>112</sup>

The case for secondary nucleation and growth from the particles is supported by observations of the grain structure in the final composite. It is well established that oxidation in the absence of a preform leads to columnar  $\text{Al}_2\text{O}_3$  grains tens of micrometers across, growing with the same crystallographic orientation over hundreds of micrometers.<sup>27,113</sup> Composites grown from the present alloy clearly showed a preferred orientation of the alumina grains parallel to the growth direction. In contrast, grain boundaries (revealed by changes in channel pattern orientation) were often found between particles in the SiC-bearing composites, suggesting that the preform tends to refine the alumina grain size and produce a more randomly oriented microstructure.

The nucleation of  $\text{Al}_2\text{O}_3$  on the preform particles could arise from the reaction of Al in the spreading melt with the protective oxide layer typically present on SiC, especially after lengthy exposure of the preform to air at high temperature, according to:



This phenomenon is shown in Fig. 5.34, where the composite nodules are shown to be nucleating on the exposed surface of the SiC particles. Fig. 5.35 shows a composite nodule nucleating on the surface of the alloy at the early stages of the composite formation. This would tend to promote more random nucleation of the alumina grains within the microstructure.

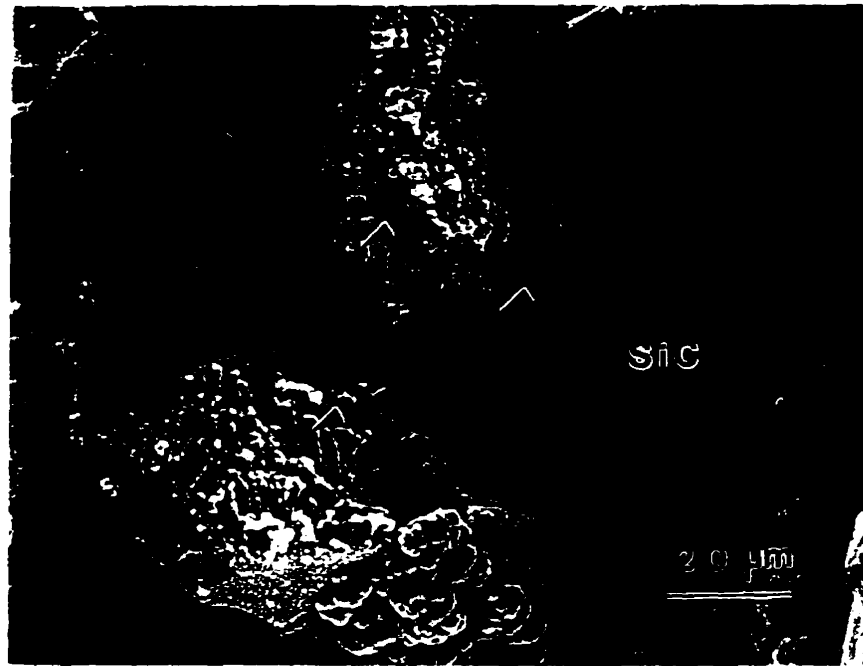


Fig. 5.34: Nucleation of composite nodules on the exposed surface of the SiC particles.

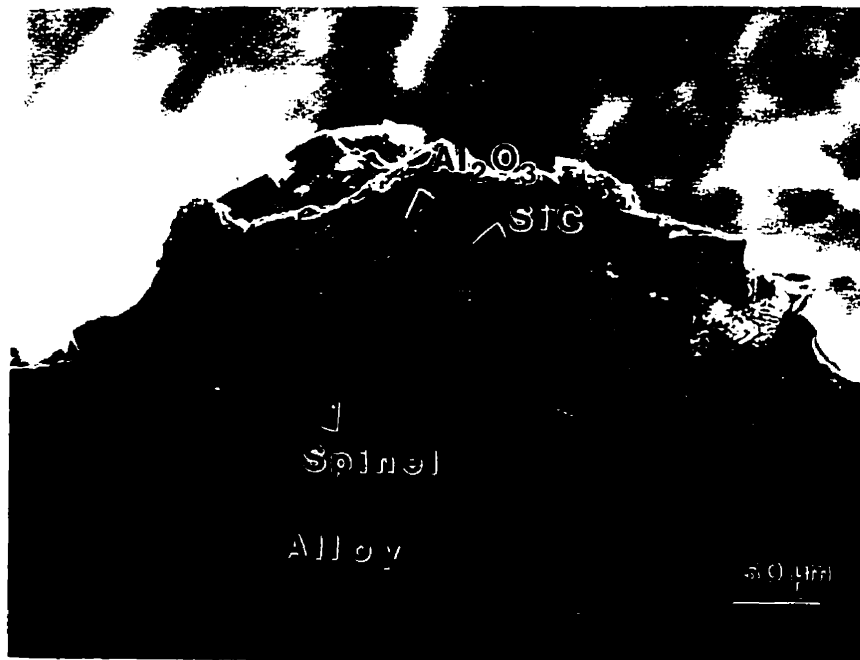


Fig. 5.35: Cross section of a composite nodule.

### 5.2.3 Porosity in the Composites

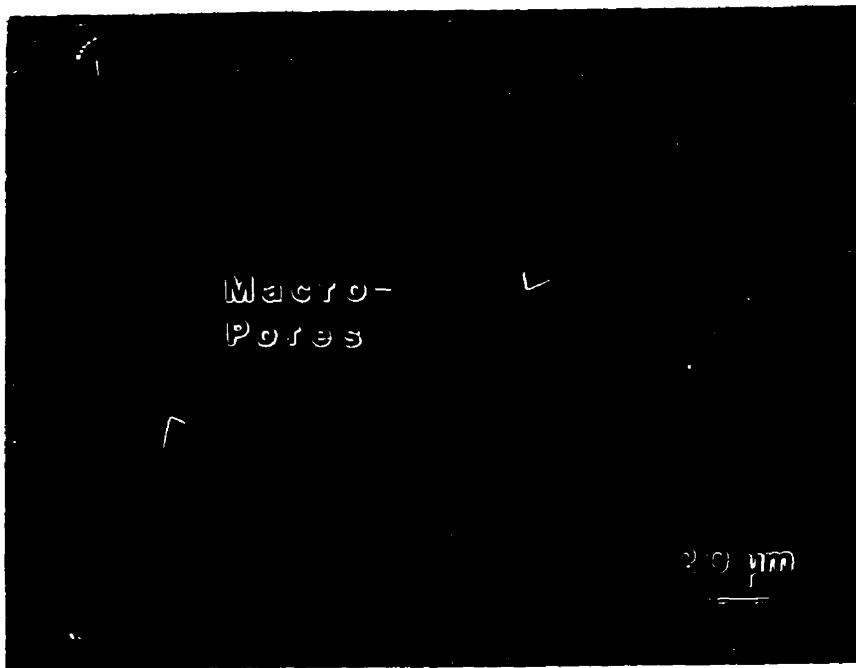
Two types of porosity denoted as micro- and macro-porosity were observed in these composites. Micropores are voids within the metal network clearly delineated by the oxide phase, as shown in Fig. 5.36(a). They originate primarily from the solidification shrinkage and they are typically associated with the last metallic constituent to evolve from the melt. Actually, the liquid alloy cannot be easily fed to the last solidifying regions, due to the blocking of the microchannels by the primary phases.

Macropores are cavities devoid of both metal and ceramic on a scale much larger than the microchannel spacing, e.g. Fig. 5.36(b). They are found in most of the composites whether with or without preforms. Their origin is likely associated with the spreading of the oxidation front, intruding into void space within the preform, as clearly seen in Fig. 5.36(c). Initially these voids are interconnected, allowing gas transport from the outer surface to maintain the oxidation process and gradually filling the space. However, one could easily visualize the spreading growth front occasionally blocking off gas access to a cavity, and consequently locally arresting the composite growth and creating a macropore.

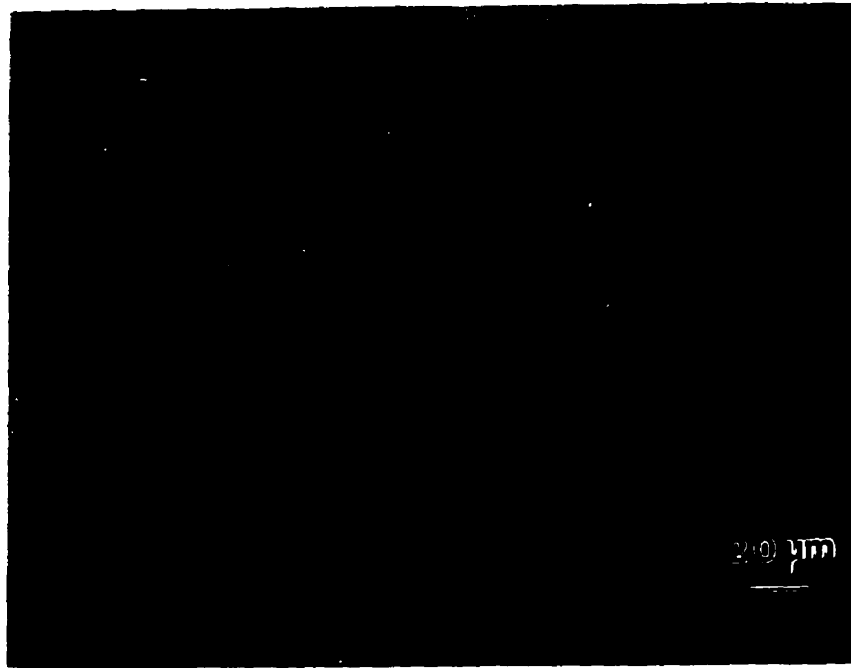
The primary advantages of the DIMOX™ process include its ability to form relatively complex, fully dense composite net shapes. From the micrographs showing the microstructure of different composites, it is clear that the composites are fully dense and contain little porosity. However, if the composite is still subjected to the processing



(a)



(b)



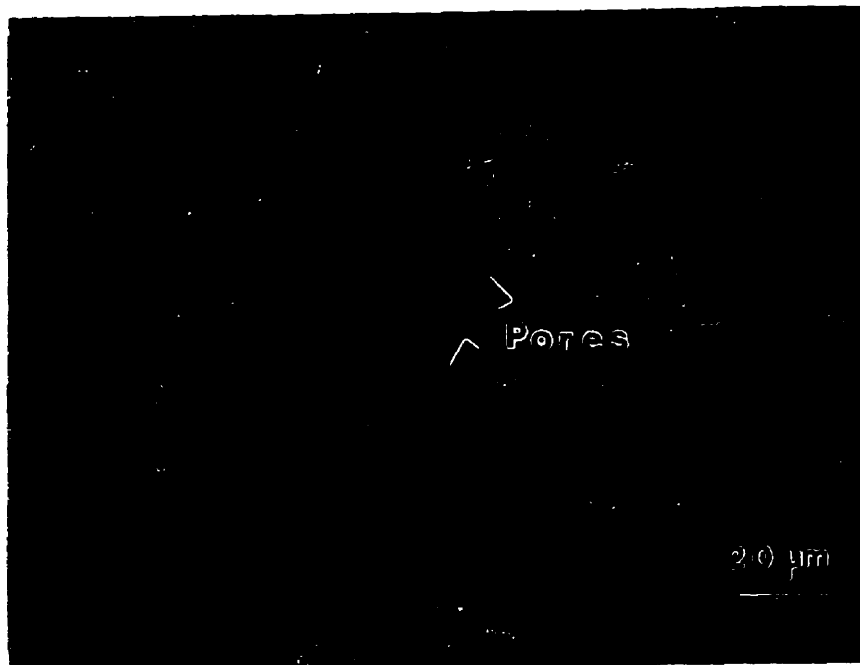
(c)

Fig. 5.36: Optical micrographs showing (a) microporosity, (b) macroporosity, and (c) voids within the SiC preform.

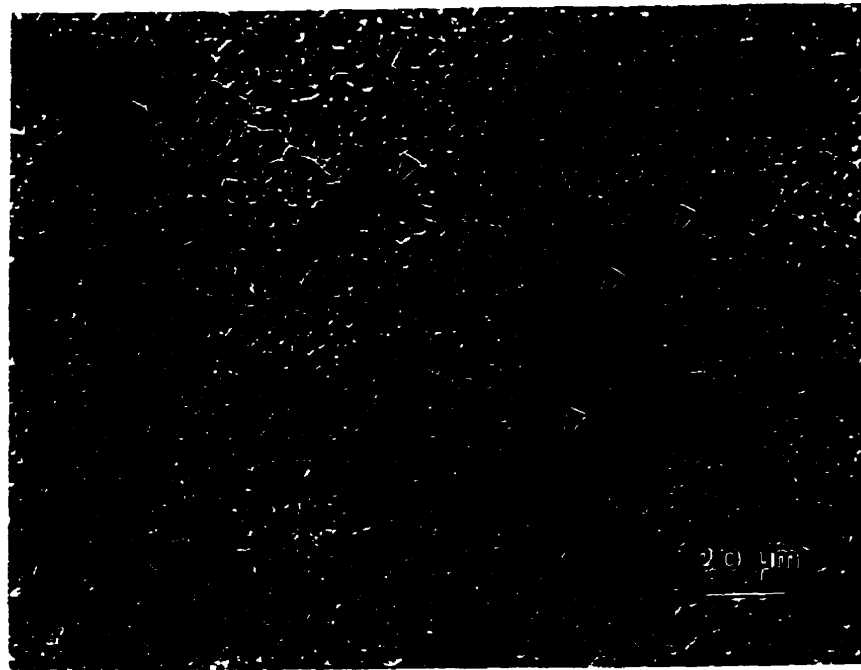
temperature after all of the alloy has been consumed, some porosity starts to develop as can be seen in Fig. 5.37, where the microstructures of composites, with and without reinforcing particles, subjected to the processing temperature well after complete consumption of the alloy are shown. In such case, after the majority of the metal from the reservoir has been oxidized to form the ceramic matrix with residual metal channels, further exposure at the oxidation temperature results in continued oxidation of the aluminum from the metal channels which consist of increasing amounts of metallic Si. The aluminum from the metal channels oxidizes preferentially and leaves behind porosity. As aluminum is consumed, the metal becomes richer in Si at the reaction temperature and crossing of the solid region of the Al-Si phase diagram



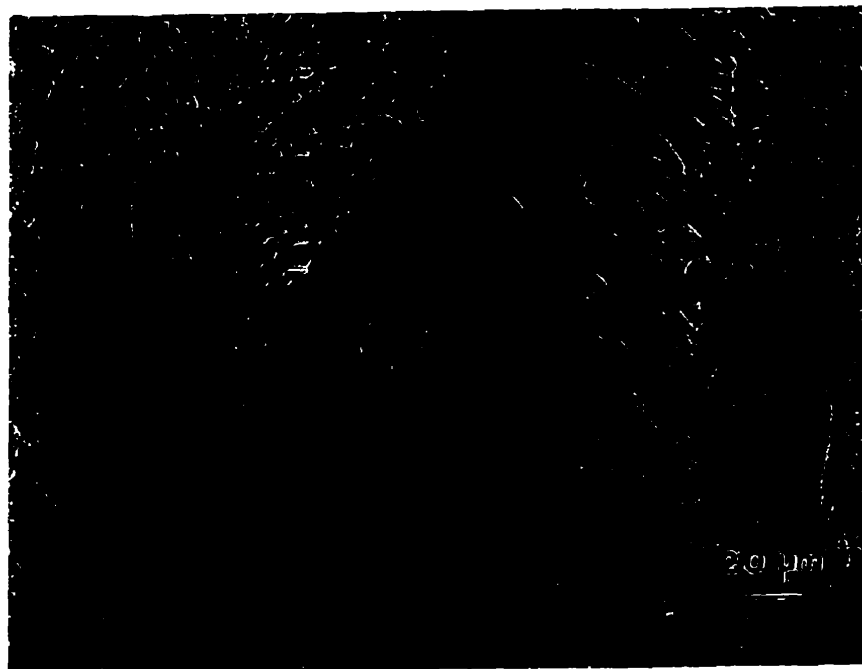
(a)



(b)



(c)



(d)

Fig. 5.37: Microstructure of various composites grown from a (7/3) alloy and subjected to processing at 1250°C after all of the alloy has been consumed. (a)-(b) contain SiC, and (c)-(d) no SiC.

occurs, as shown in Fig. 5.38. Consequently, primary Si precipitates in the channels at the reaction temperature.

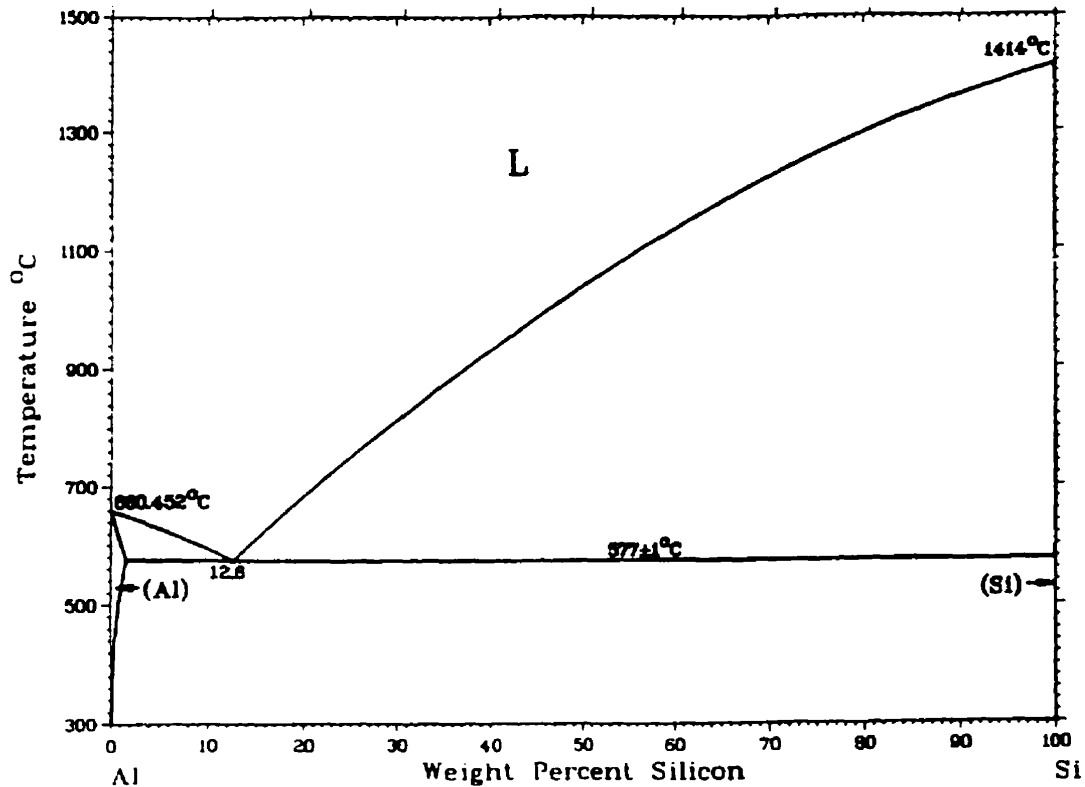


Fig. 5.38: Binary phase diagram for the Al-Si system.

The total amount of porosity was found to increase with the Mg content in the alloy, from 1.8% for 0.5 wt. % Mg to 5.2% for 3 wt. % Mg (measured by means of image analysis). A corresponding trend in the growth rate was observed: the average linear velocity of the oxidation front increased by a factor of two (especially in the case of composites without reinforcing SiC particles) when the Mg content was raised from 0.5 to 3 wt. %. However, a minimum amount of Mg is required to promote “wicking” of the alloy through the composite and ensure the continuous supply of metal to the

growth interface. The 0.5 wt. % Mg content was found to be suitable for maintaining infiltration while minimizing porosity.

Control of porosity and its scale is obviously important to the integrity and properties of the final product. Even though, it is unlikely that microporosity could be totally eliminated, owing to the inherent difficulty in feeding the solidification shrinkage through the tortuous network of microchannels. Elimination of the macroporosity is also difficult, as it involves controlling the processing temperature and particle size of the preform. A possible approach to reduce the effect of the macropores involves an isothermal hold between the oxidation temperature and the liquidus of the alloy, wherein additional metal from the reservoir could be slowly fed by capillarity to the large pores developed during growth.

## 5.3 KINETICS OF THE DIMOX™ PROCESS

### 5.3.1 Oxidation of Pure Aluminum

It is valuable to study the oxidation of pure liquid aluminum under the same high temperature conditions as for composite processing. Fig. 5.39 shows the oxidation curves obtained in the range 1150-1300°C for pure liquid aluminum. These curves appear not to have an incubation period prior to becoming a parabolic form of curve. The parabolic profile is consistent with the literature review which states that the oxidation of pure aluminum in the solid state follows a parabolic behavior. The equation for the parabolic oxidation law is:

$$w^2 = K \cdot t \quad (5.4)$$

where  $w$  is the weight gain,  $K$  is the parabolic rate constant, and  $t$  is the time.

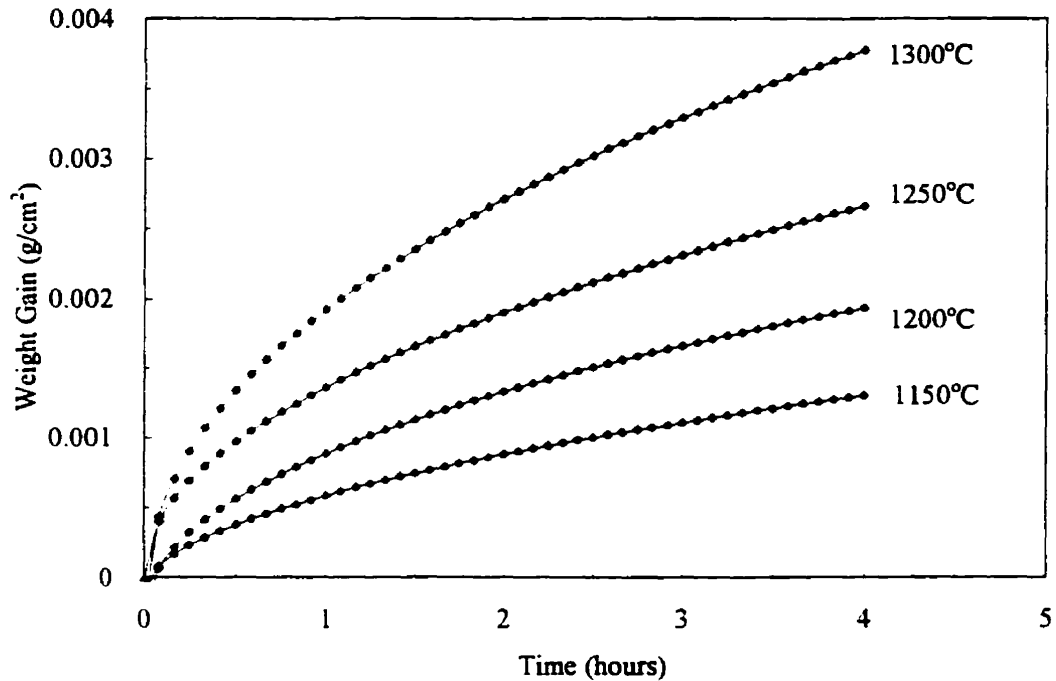


Fig. 5.39: Weight gain vs. time curves for oxidation of pure aluminum under flowing air.

Since the parabolic rate constant of oxidation of pure aluminum,  $K=w^2/t$ , increases with temperature ( $T$ ), it is possible to perform an Arrhenius analysis on these curves, hence establishing an activation energy,  $E_a$ , according to the equation:

$$K = A \cdot \exp\left(-\frac{E_a}{RT}\right) \quad (5.5)$$

where  $A$  is a constant,  $R$  is the Universal Gas constant, and  $T$  is the absolute temperature. Consequently, the plots of the square of the weight gain as a function of time were obtained (Fig. 5.40). In these plots, the parabolic rate constant,  $K$ , represents the slope of the curves. These constants for each temperature are recorded in Table 5.2. Their log was then plotted against the reciprocal of the oxidation temperature, in Kelvin. The resulting points were fitted with a straight line, giving the

Arrhenius plot shown in Fig. 5.41. The slope of this curve translates into an activation energy of 258 kJ/mol. Thus, for pure liquid aluminum, the oxidation can be represented by:

$$K \left( \text{g}^2/\text{cm}^4 \cdot \text{sec} \right) = 0.36 \cdot \exp\left(-\frac{30,015}{T}\right) \quad (5.6)$$

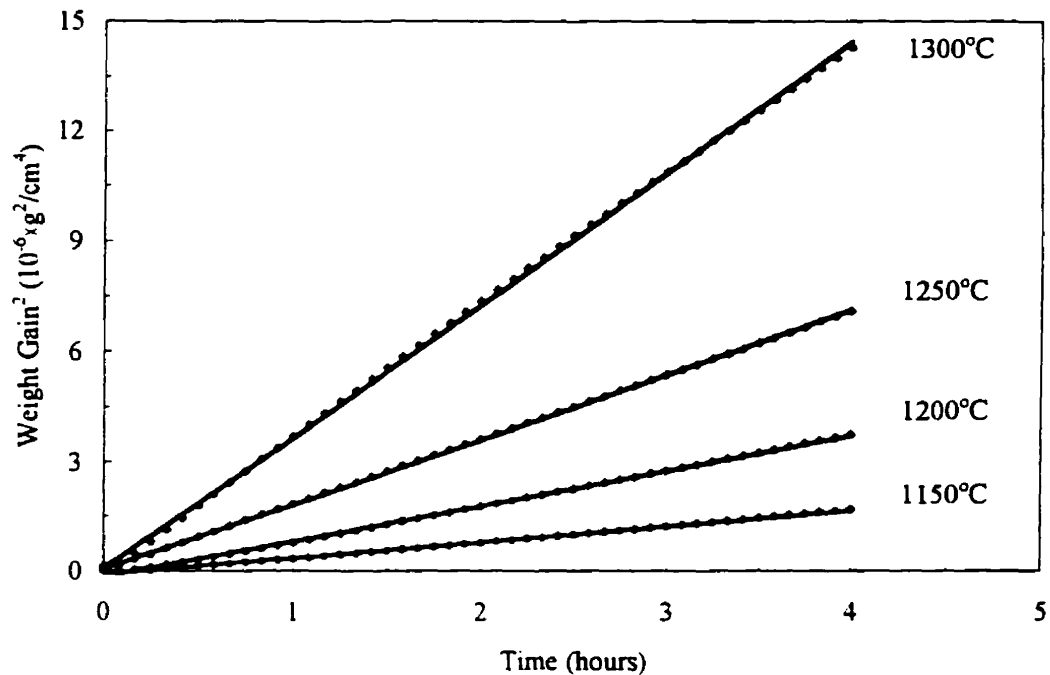


Fig. 5.40: Parabolic plots of oxidation data for pure aluminum.

Table 5.2: Parabolic Rate Constants and Activation Energy for the Oxidation of Pure Liquid Aluminum

Temp. °C	$K$ $\text{g}^2/\text{cm}^4 \cdot \text{sec}$	$A$ $\text{g}^2/\text{cm}^4 \cdot \text{sec}$	$E_a$ J/mol
1150	$1.21 \times 10^{-10}$	0.36	257,860
1200	$2.69 \times 10^{-10}$		
1250	$4.90 \times 10^{-10}$		
1300	$9.97 \times 10^{-10}$		

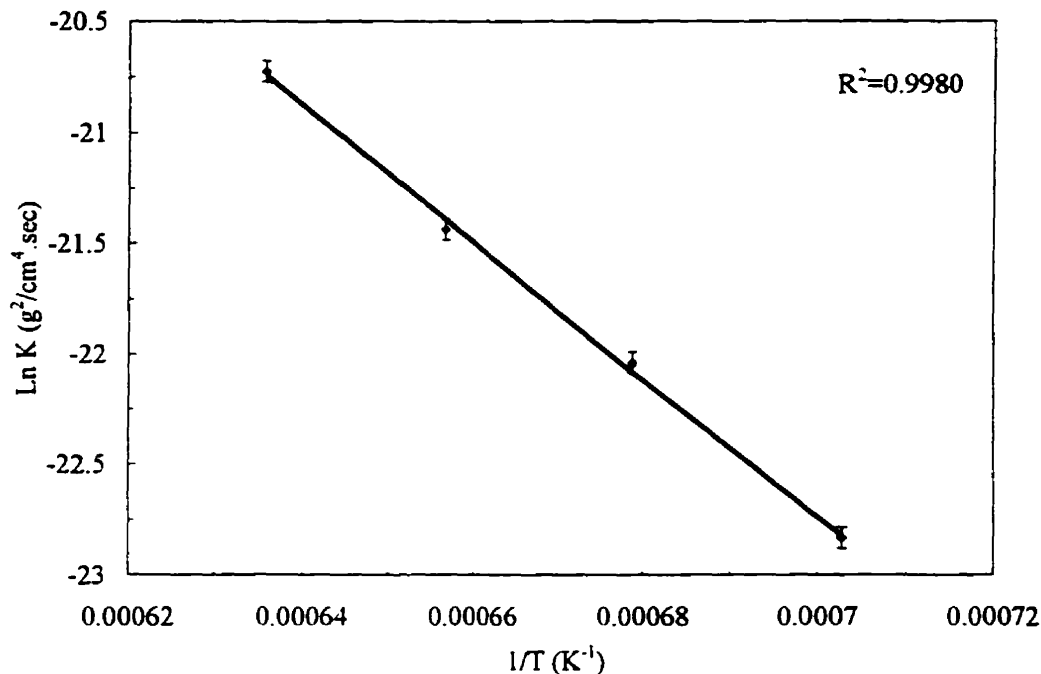


Fig. 5.41: Arrhenius plot of parabolic rate constant for pure aluminum.

### 5.3.2 Oxidation Kinetics of Aluminum Alloys into SiC Preforms

In a typical experiment, the rate of weight gain increased briefly during heating. This small weight gain was associated with the convolution of the alloy/gas surface and the subsequent rapid oxidation to form  $\text{MgAl}_2\text{O}_4$ . The growth rate then rose sharply to a maximum and then maintained an essentially constant rate, as shown in Fig. 5.42. This growth rate maximum was associated with the nucleation, growth, and impingement of  $\text{Al}_2\text{O}_3$ /metal composite nodules above the  $\text{MgAl}_2\text{O}_4$  layer. Eventually, the composite nodules impinged to form a nearly planar growth front exhibiting constant growth kinetics.

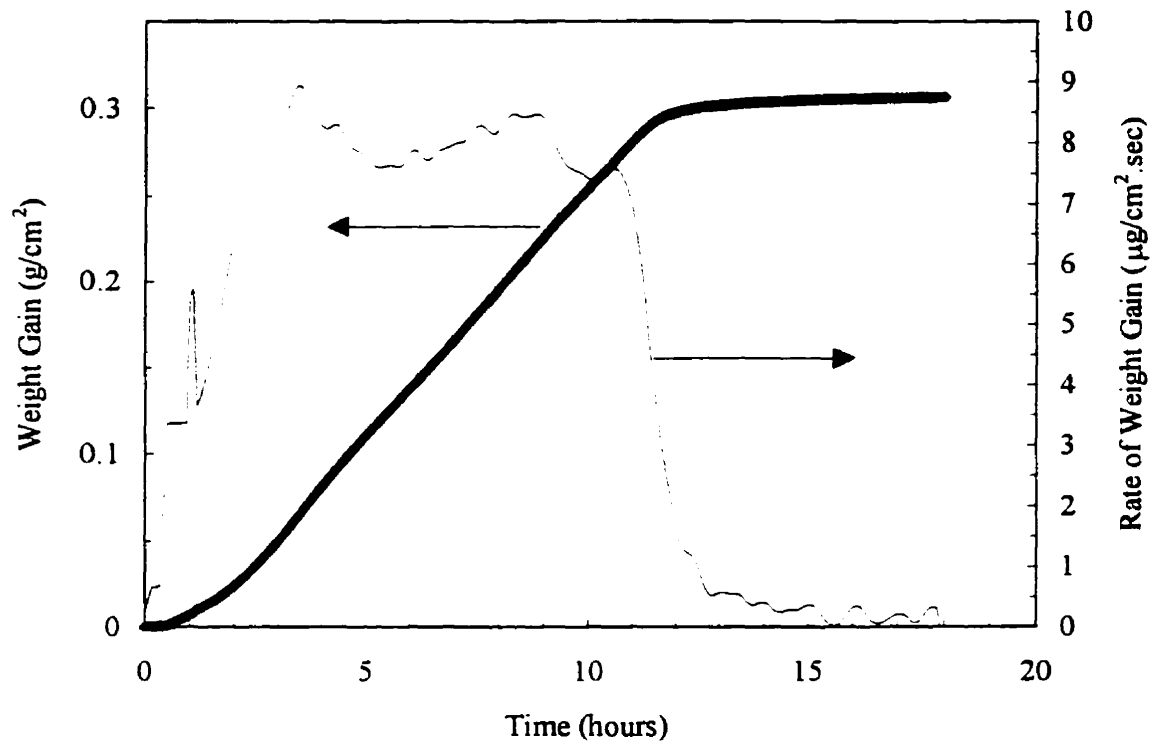
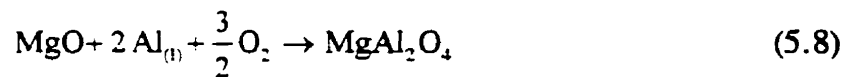


Fig. 5.42: Weight gain vs. time curve for the (7/3) alloy at 1150°C using 240-grit SiC particles.

The process starts with a slow and limited oxidation process upon introduction of the sample into the hot zone of the furnace, corresponding to the formation of  $\text{MgAl}_2\text{O}_4$  and/or  $\text{MgO}$  layer on the alloy surface. This leads to an incubation period of varying duration, depending on the temperature and alloy composition, and with minimal weight gain. The onset of the bulk growth is marked by a substantial increase in the oxidation rate. Composite growth typically follows a linear regime during which an extensive coverage of the alloy surface by oxide nodules occurs, as described in section 5.2.2. Once the alloy reservoir is exhausted, the curve levels off and no further weight gain is observed indicating that the process is complete.

### 5.3.2.1 Initial Oxidation and Incubation Period

The next most obvious feature in Fig. 5.42 is that it appears to have an incubation period prior to stabilizing into linear growth kinetics. This incubation period also appears to become less significant as the oxidation temperature increases. The early stages of oxidation for alloy (7/3) are shown in greater detail in Fig. 5.43. The weight gain is small. Microstructural evidence discussed in section 5.2.1 revealed a duplex layer of MgO/MgAl<sub>2</sub>O<sub>4</sub> on the sample surface during this period. The spinel layer contains multiple metal pockets and microchannels which progressively link and coarsen during incubation. Eventually, the liquid alloy reaches the MgO/MgAl<sub>2</sub>O<sub>4</sub> interface leading to accelerated spinel formation, reoxidation of the Mg released by the following reactions:<sup>114</sup>



and local depletion of Mg in the near-surface metal by the third reaction until it reaches a critical level, whereupon Al<sub>2</sub>O<sub>3</sub> can form. The weight gain rates during incubation are quite low but increase with temperature in the 1100-1300°C range, with an activation energy of ~210 kJ/mol, as derived from the Arrhenius plot shown in Fig. 5.44. This is

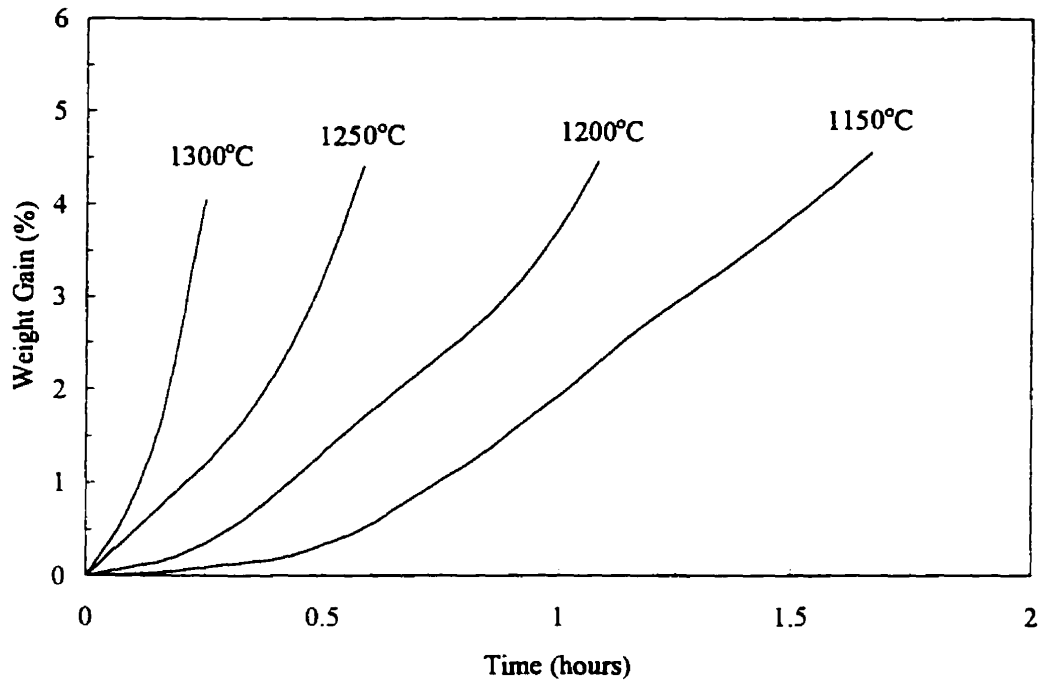


Fig. 5.43: Early stages of the composite growth process indicating the change in length of incubation period with change in process temperature.

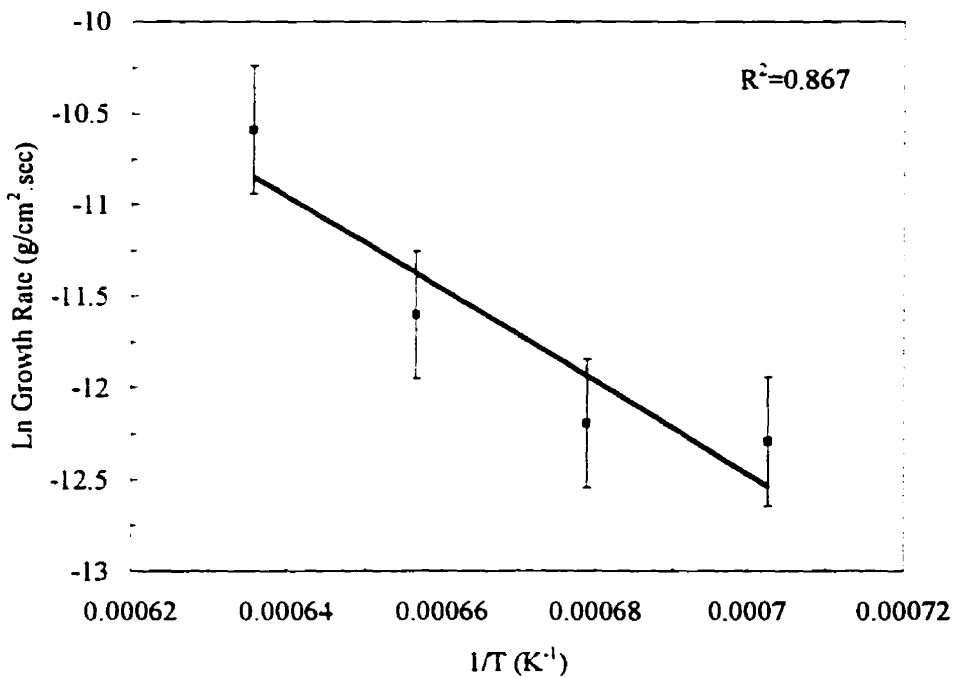


Fig. 5.44: Arrhenius plot of the weight gain rates associated with the incubation period for the (7/3) alloy in air using 240-grit SiC preform.

of the magnitude expected for rate-limiting cation diffusion through the  $\text{MgAl}_2\text{O}_4$  layer, whose thickening accounts for most of the weight gain in this period.

### 5.3.2.2 *Effects of $\text{SiO}_2$ on Incubation*

The incubation periods associated with composite growths without SiC preforms are very long (up to 24 hours) compared to those associated with composites grown into SiC preforms. Previous studies have shown that the surface application of  $\text{SiO}_2$  powder effectively minimizes the incubation time when the reaction is carried out in an oxidizing atmosphere.<sup>115</sup> The  $\text{SiO}_2$  addition also reduces the weight loss during processing, presumably by reacting with the vaporizing Mg. Indeed, in the present experiments, a similar effect was observed when using the SiC preforms. Since the SiC particles were oxidized prior to composite growth, they are covered by an  $\text{SiO}_2$  layer which resulted in a significant reduction of the incubation period. To clearly understand the beneficial effect of  $\text{SiO}_2$  on the incubation time, a set of experiments was devised for this purpose. Preoxidized SiC particles were mixed with  $\text{SiO}_2$  powder and then capillary infiltrated under argon with pure aluminum in the temperature range of the present oxidation experiments. In this manner, the source of oxygen was limited to  $\text{SiO}_2$  only. Also SiC preforms, only, were infiltrated with pure aluminum in order to observe the effect of  $\text{SiO}_2$ . Fig. 5.45(a) shows the microstructure of a SiC preform infiltrated by pure aluminum under argon for 4 hours at  $1250^\circ\text{C}$ . It is clear that aluminum has infiltrated the SiC preform and resulted in an aluminum matrix reinforced by SiC. The SiC has reacted with the aluminum as seen by the degradation

of the particles edges and resulted in the formation of  $Al_4C_3$  as confirmed by EDS analysis. In fact, the matrix contains not only the starting aluminum, but also Si as a result of the reaction between the aluminum and the SiC according to the reaction:

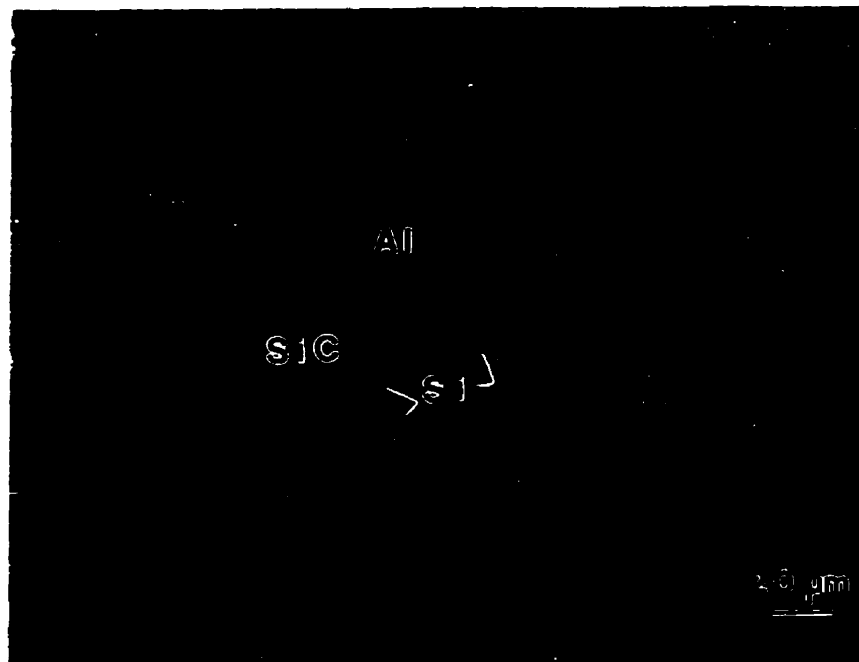


It is also interesting to note that there are regions in the composite where the Si seems to have migrated to areas where the SiC particles are almost embedded in a Si matrix, as shown in Fig. 5.45(b). The SiC particles that are not in contact with the aluminum matrix are intact and there are no signs of chemical attack on the particles in these regions. This is expected since in the Al-Si-SiC system, the extent of attack of SiC by the melt is severely diminished when the melt is saturated with Si.<sup>116</sup>

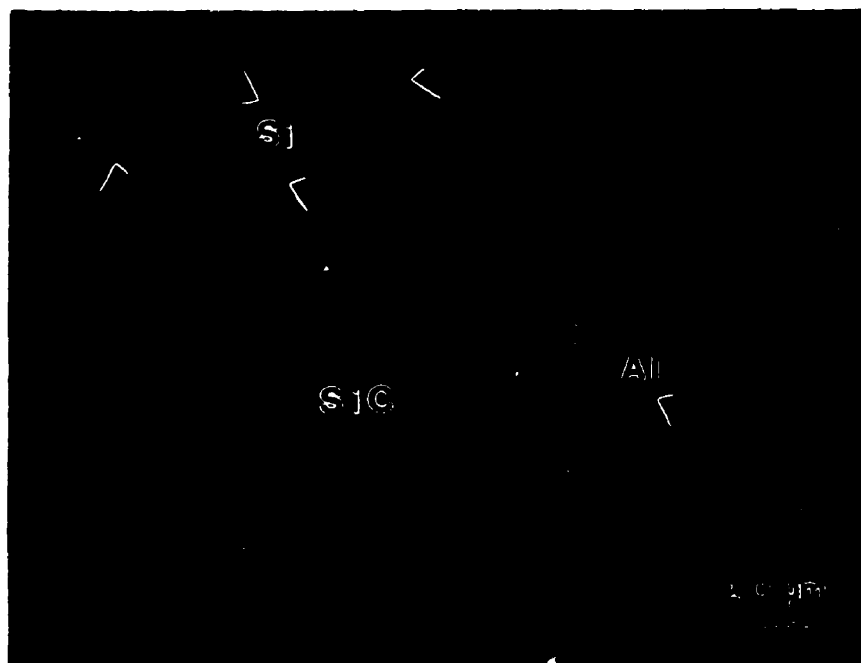
When a SiC/SiO<sub>2</sub> mixture (20 wt.% SiO<sub>2</sub>) is used, the microstructure is shown in Fig. 5.46(a). It is evident that Al<sub>2</sub>O<sub>3</sub> has nucleated and grown from the original SiO<sub>2</sub> powder by reaction of Al with the latter, as described by:



Si particles are therefore present in the Al matrix as a result of reaction (5.11). When Al is in contact with SiO<sub>2</sub>, Al diffuses inward and O<sub>2</sub> diffuses outward. The Al<sub>2</sub>O<sub>3</sub> then forms into a "donut-like" shape, i.e. with an empty core in the center, as shown in Fig. 5.46(b). Al also reacts slightly with SiC but not as much as with the SiO<sub>2</sub> since SiC does not decompose as easily. This gives rise to the brittle Al<sub>4</sub>C<sub>3</sub> phase, traces of which were detected by EDS analysis. Consequently, the SiO<sub>2</sub> film which forms on the surface of SiC at the reaction temperature will act in a similar manner to the SiO<sub>2</sub> particles. This SiO<sub>2</sub> film on the SiC functions as a very important reaction accelerator

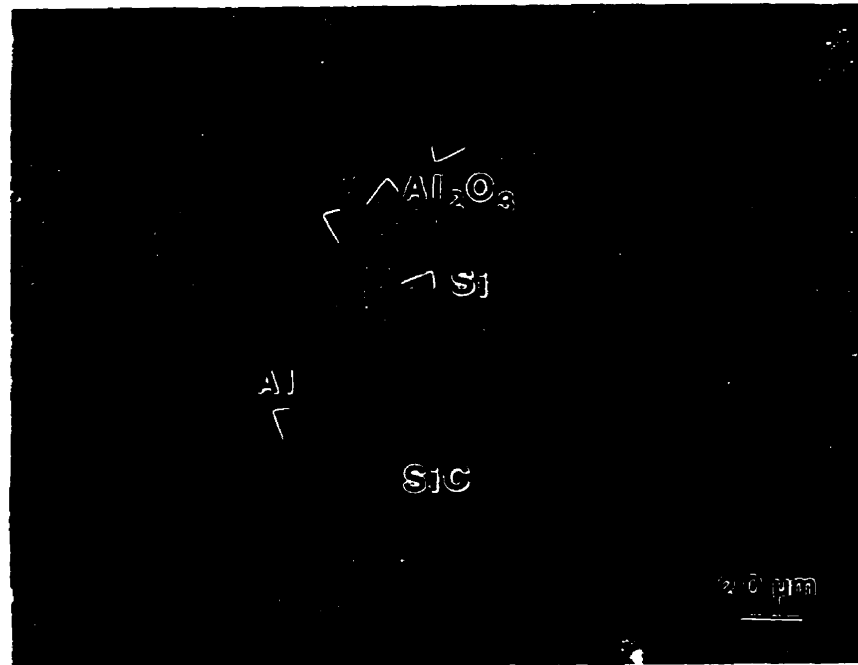


(a)

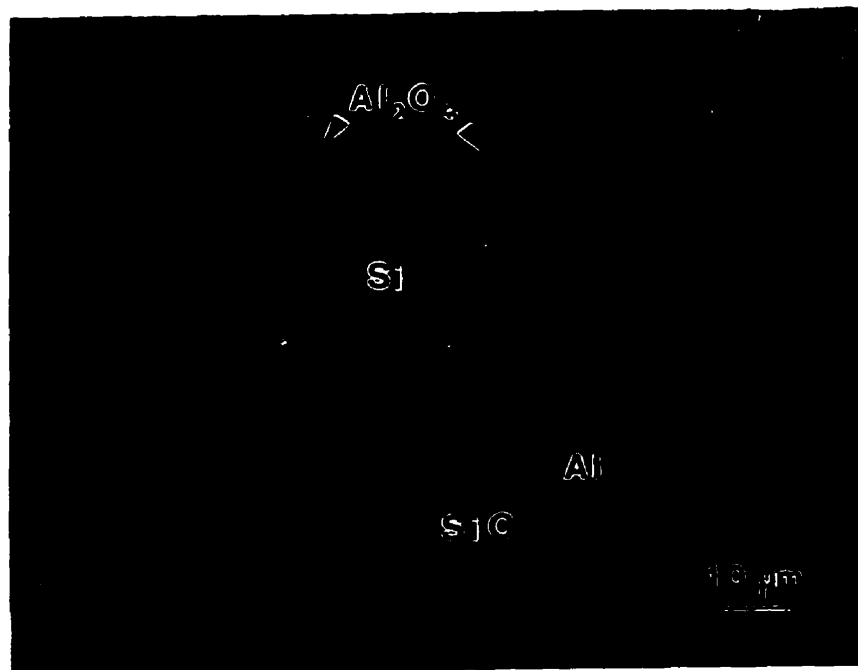


(b)

Fig. 5.45: Microstructure of SiC powder bed infiltrated by pure aluminum under argon for 4 hours at 1250°C.



(a)



(b)

Fig. 5.46: Microstructure of SiC/SiO<sub>2</sub> powder bed infiltrated by pure aluminum under argon for 4 hours at 1250°C.

during the directed oxidation of the aluminum alloy.

When the same mixture (SiC/20 wt.% SiO<sub>2</sub>) is used to grow a composite in air, the resulting microstructure is similar to that of composites described earlier, i.e. interconnected Al<sub>2</sub>O<sub>3</sub> and metal channels reinforced by SiC particles. Most of the metal channels are composed primarily of Si and aluminum is not observed as often. However, it should be pointed out that the Al<sub>2</sub>O<sub>3</sub> grains appear smaller and are not so interconnected, as indicated in Fig. 5.47. It appears that SiO<sub>2</sub> particles have reacted with the aluminum to form Al<sub>2</sub>O<sub>3</sub> grains which have later coalesced. Also each Al<sub>2</sub>O<sub>3</sub> grain contains a metal pocket or core in its center, similar to that observed in Fig. 5.46(b). Another observation is that the SiC particles did not react with the aluminum, but rather remained intact, and therefore no Al<sub>4</sub>C<sub>3</sub> phase was detected by EDS.

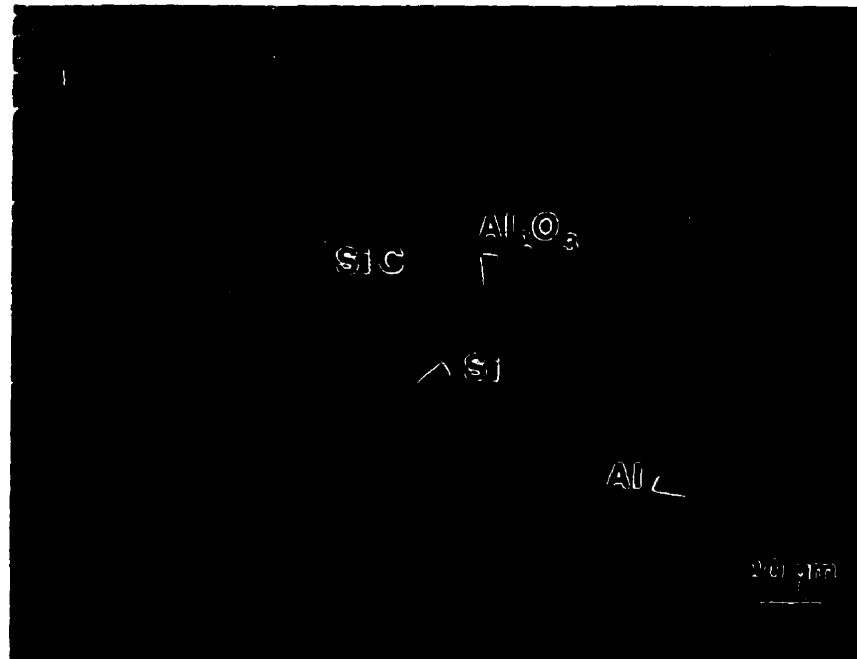
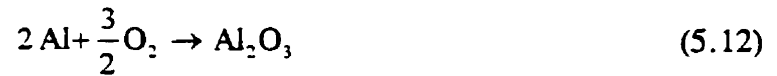


Fig. 5.47: Microstructure of a composite grown into a SiC/SiO<sub>2</sub> powder bed mixture using a (0/3) alloy at 1250°C.

### 5.3.2.3 $Al_2O_3$ Composite Growth

The incubation period is followed by bulk oxidation, which transforms a large fraction of the remaining Al into  $Al_2O_3$ . Complete oxidation of pure Al would produce a weight gain of 88.9%, according to the following reaction:



which states that 2 moles of Al would require 3 moles of O. Knowing that 2 moles of Al weigh 53.963g and 3 moles of O weigh 47.998g, then the weight gain is the ratio of the weight of O divided by the weight of Al. However, the resulting SiC/ $Al_2O_3$ /Al composites typically contain 30-40 vol. % of  $Al_2O_3$  (refer to Fig. 5.10). If we neglect the contribution from Mg oxidation to form MgO and  $MgAl_2O_4$ , and subtract the weight of silicon in the alloy, the estimated weight gain at the end of the composite growth should be ~89%, which is in good agreement with the present data for the various alloys, i.e. values ranging from 80-85%. Knowing that the SiC content in the composites is ~55 vol. %, the  $Al_2O_3$  content then should be 67-89 vol. % for the composites without a SiC preform.

Fig. 5.48 shows the oxidation rate curves obtained at different temperatures for a (7/3) alloy containing SiC powder having a 240 grit size. There are a few points that are worthwhile noting. The growth rate responded rapidly to changes in temperature. Within the growth temperature range (1100-1300°C), growth rates were constant for any given temperature. Composite growth rates varied significantly with temperature. Further information that can be deduced from Fig. 5.48 is that the high

temperature curve shows a higher weight gain than the low temperature one, as confirmed by image analysis of samples and shown in Fig. 5.10.

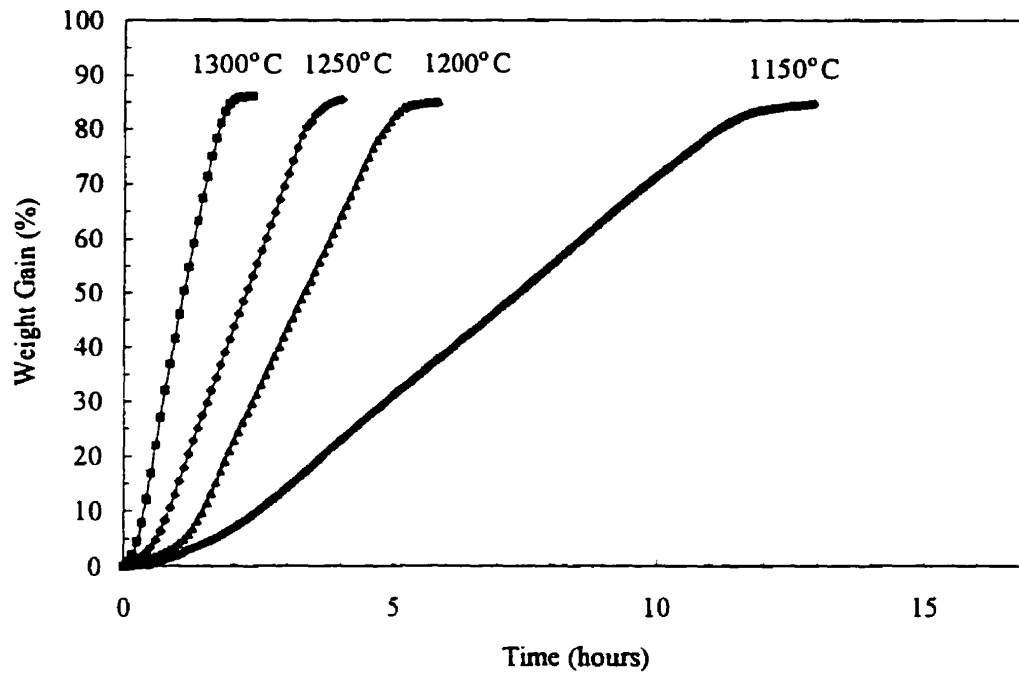


Fig. 5.48: Weight gain vs. time curves for oxidation of the (7/3) alloy in air using 240-grit SiC powder at four different temperatures.

Since the growth rate ( $dw/dt$ ), increases with temperature,  $T$ , it is possible to perform an Arrhenius analysis on these curves, hence establishing an activation energy,  $E_a$ , according to the equation:

$$\frac{dw}{dt} = A \cdot \exp\left(-\frac{E_a}{RT}\right) \quad (5.13)$$

where  $A$  is a constant and  $R$  is the Universal Gas Constant. Consequently, the bulk oxide growth regime may be characterized by a linear rate after the incubation period, defined as the weight gain divided by the corresponding time increment and the cross-sectional area of the crucible. The growth rate at any temperature is given by the slope

of the linear portion of the curve and is computed using linear regression. The resulting points were fitted with a straight line, giving the Arrhenius plot shown in Fig. 5.49. The resulting values are given in Table 5.3. The growth rates for all the alloys increased with nominal temperature in the range 1100-1300°C. It can be seen that the average activation energy is ~193 kJ/mol (compared with the value of activation of oxidation of Al ~258 kJ/mol.)

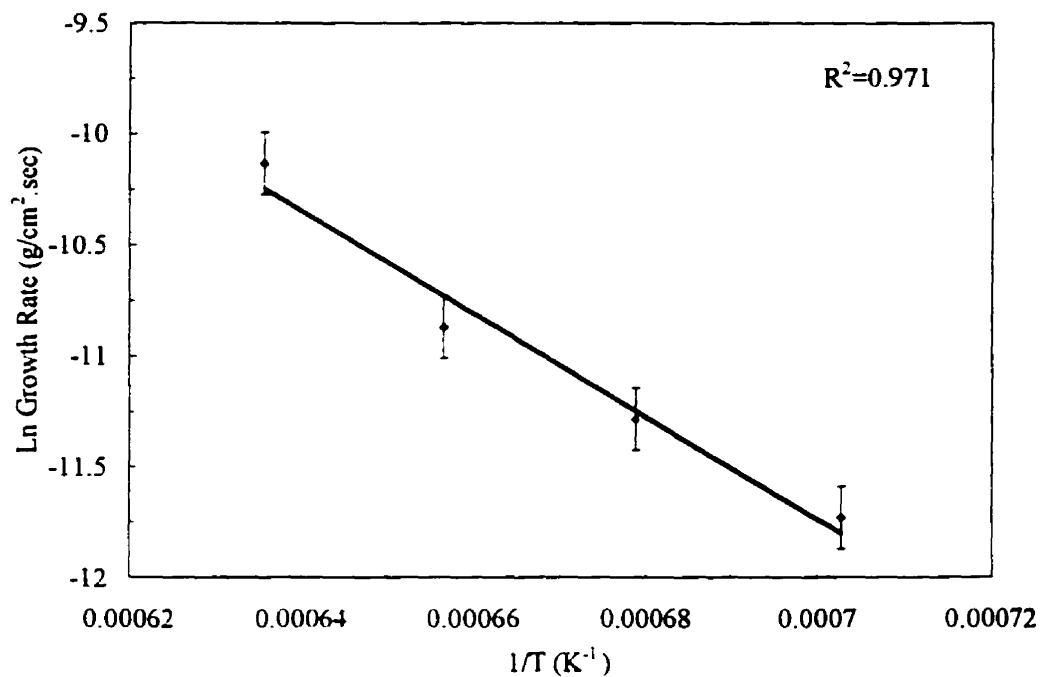


Fig. 5.49: Arrhenius plot of the weight gain rates for the (7/3) alloy in air using 240-grit SiC preform.

Table 5.3: Parabolic Rate Constants and the Activation Energy for the Oxidation of the (7/3) Alloy in Air Using 240-Grit SiC Powder (Different Runs)

Temp. °C	$dw/dt$ g/cm <sup>2</sup> .sec	$A$ g/cm <sup>2</sup> .sec	$E_a$ J/mol
1150	$8.04 \times 10^{-6}$	93.46	193,314
1200	$1.25 \times 10^{-5}$		
1250	$1.90 \times 10^{-5}$		
1300	$3.98 \times 10^{-5}$		

An alternate method for obtaining the activation energy is to start a growth experiment at a given temperature and then rapidly decrease the growth temperature in predefined steps of equal magnitude, yielding the curve shown in Fig. 5.50. This method is more accurate than the above method since the same sample is being tested at different temperatures, thus eliminating any errors due to changes in the experimental setup.

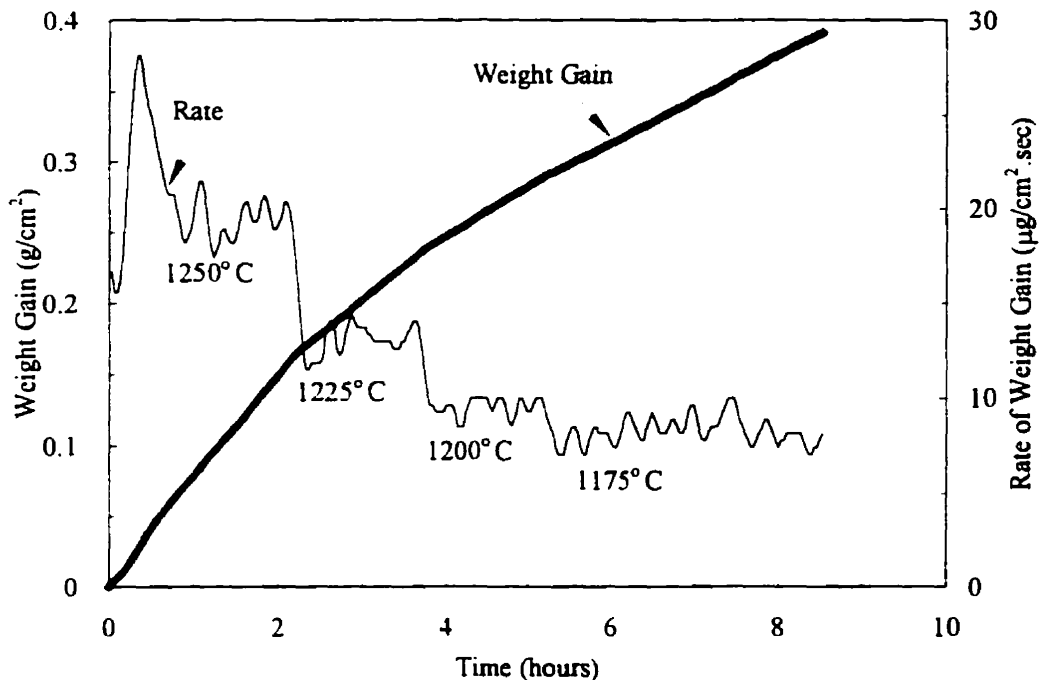


Fig. 5.50: Weight gain vs. time curve for the (3.5/2) alloy with changing the processing temperature. 240-grit SiC powder was used.

Also this method leads to significant time saving and is amenable to a furnace equipped with a programmable temperature controller. It is worth noting that decreasing the process temperature decreases the growth rate and then the growth rate of the bulk composite remains linear with time. The resulting values are given in Table 5.4 and plotted as a function of temperature in Fig. 5.51.

Table 5.4: Parabolic Rate Constants and the Activation Energy for the Oxidation of the (7/3) Alloy in Air Using 240-Grit SiC Powder (Single Run)

Temp. °C	$dw/dt$ g/cm <sup>2</sup> .sec	$A$ g/cm <sup>2</sup> .sec	$E_a$ J/mol
1175	$8.00 \times 10^{-6}$	892.06	223,823
1200	$9.60 \times 10^{-6}$		
1225	$1.33 \times 10^{-5}$		
1250	$1.99 \times 10^{-5}$		

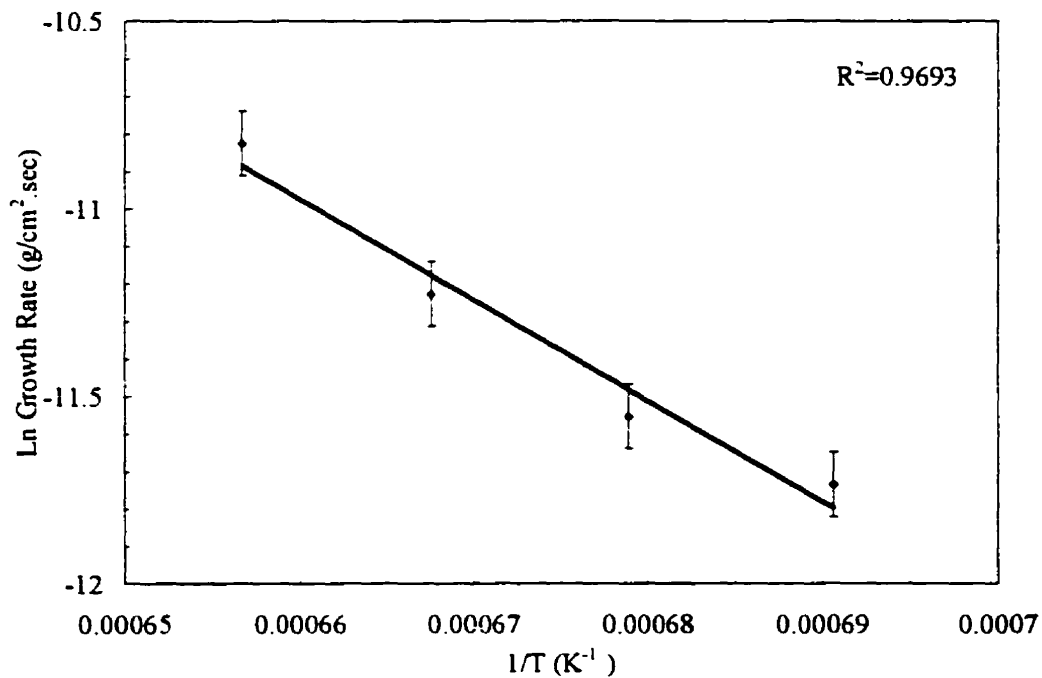


Fig. 5.51: Arrhenius plot of the rate of weight gain for a (7/3) alloy in air using 240-grit SiC preform.

The rate of growth of the composites in the linear regime may be expressed by:

$$\text{Rate (g/cm}^2 \cdot \text{sec)} = 892.06 \cdot \exp\left(-\frac{26,921}{T}\right) \quad (5.14)$$

### 5.3.3 Effect of Alloying Elements

#### 5.3.3.1 Effect of Magnesium

Fig. 5.52 shows growth curves for two different alloys: (7/3) and (7/0). It can be immediately concluded that the presence of Mg is vital to the growth and formation of the composites. Without Mg, the alloy will simply follow the parabolic oxidation behavior characteristic of pure aluminum shown in Fig. 5.39, in which the alloy is covered by a passive oxide layer that prevents it from further oxidation. When processing composites without a SiC preform, changing the Mg content in the alloy did not affect the growth kinetics of the composites significantly, with only a small decrease in the incubation time and a small increase in the growth rate as the Mg content increased, as shown in Fig. 5.53. With the presence of a SiC preform, the change in alloy content in Mg resulted in even smaller changes in the growth rate, as shown in Fig. 5.54. Table 5.5 compares the growth rates and incubation times for alloys with different Mg contents with and without a SiC preform. These results are shown graphically in Fig. 5.55 and Fig. 5.56. The Arrhenius plots for composites processed with SiC preforms are shown in Fig. 5.57, where the activation is essentially the same for the four alloys. The Arrhenius plots corresponding to (3.5/0.5), (3.5/1.0), and (3.5/2.0) alloys basically possess the same slope, indicating similar activation

energy values (within the experimental errors). The slope corresponding to (3.5/1.5) alloy is different from the other three. The reason for this is still not clear.

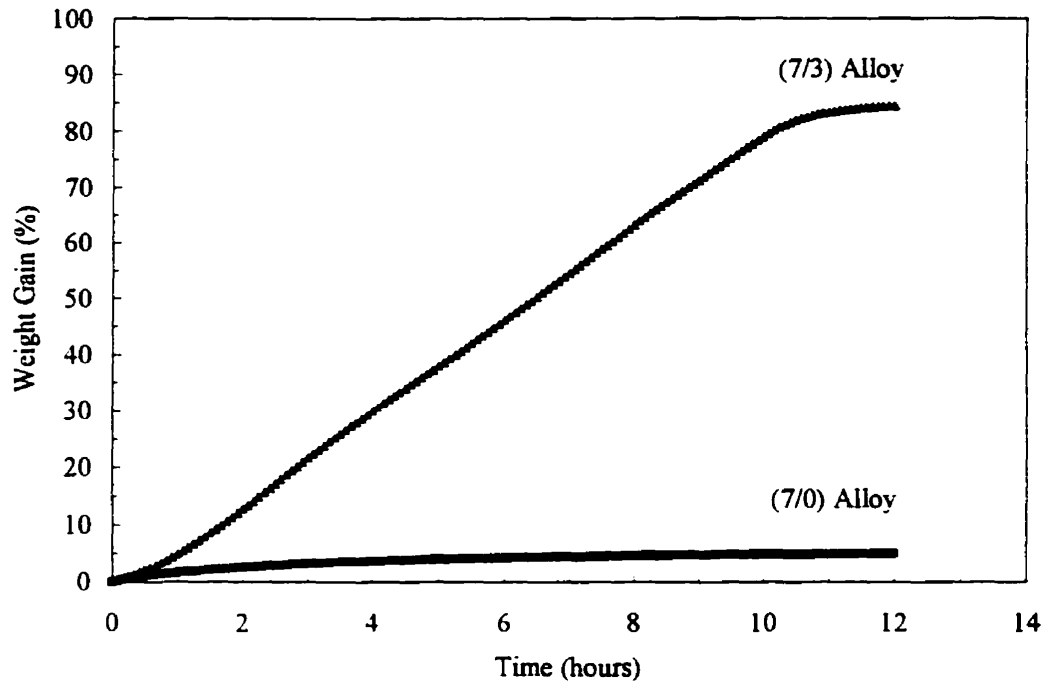


Fig. 5.52: Weight gain vs. time curves showing the effect of presence of Mg in the parent alloy. The growth temperature was 1250°C and 240-grit SiC powder was used.

Table 5.5: Growth Rates and Incubation Times for Alloys Containing 3.5 wt.% Si and Different Mg Contents for Composites Processed with and without SiC Reinforcing Particles at 1350°C

Mg (wt. %)	No SiC Particles				240 Grit-SiC Particles			
	0.5	1.0	1.5	2.0	0.5	1.0	1.5	2.0
Growth Rate ( $\times 10^{-5}$ g/cm <sup>2</sup> ·sec)	7.18	7.96	9.53	9.83	9.51	9.34	9.13	9.16
Incubation Time (ksec)	15.8	14.8	13.0	12.9	1.8	2.7	3.0	3.2
Activation Energy (kJ/mol)					332.6	322.1	213.2	346.4

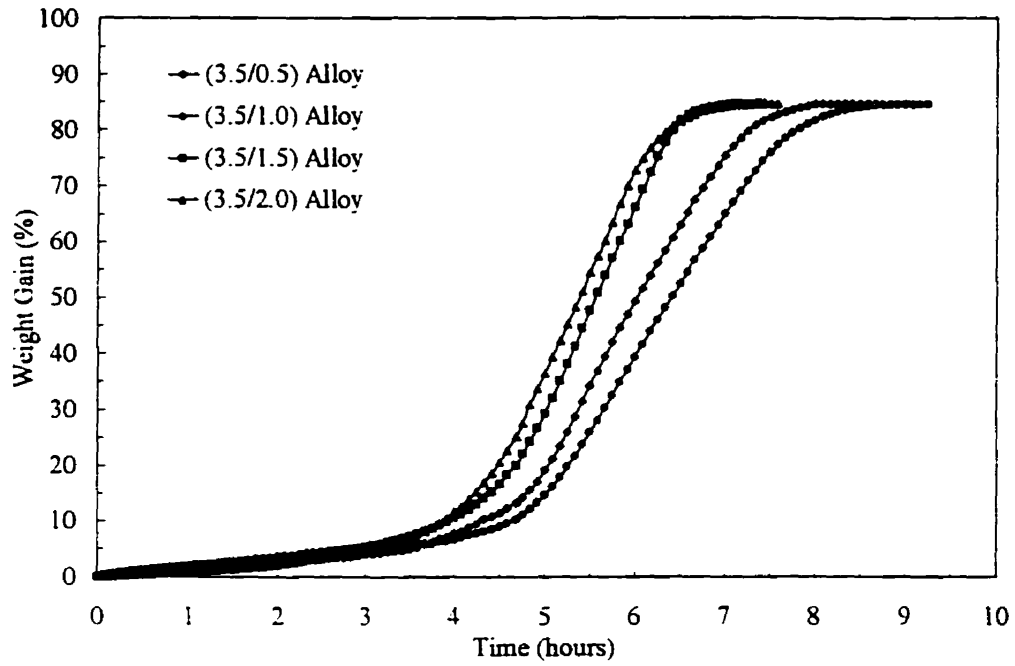


Fig. 5.53: Weight gain vs. time curves showing the effect of changing the Mg content on the growth rate (1350°C, no SiC).

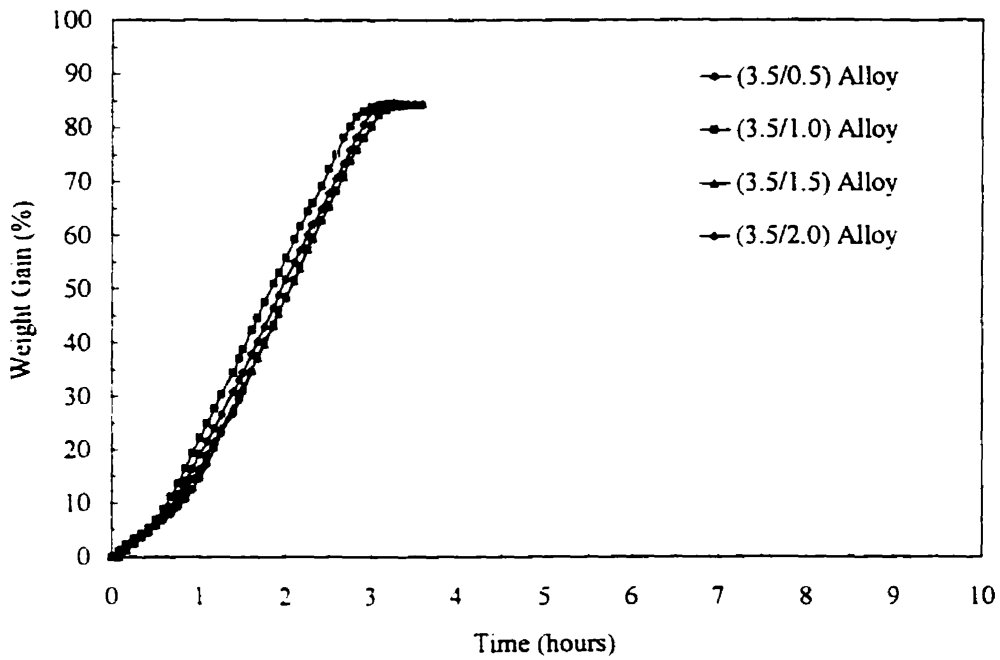


Fig. 5.54: Weight gain vs. time curves showing the effect of changing the Mg content on the growth rate (1350°C, 240-grit SiC).

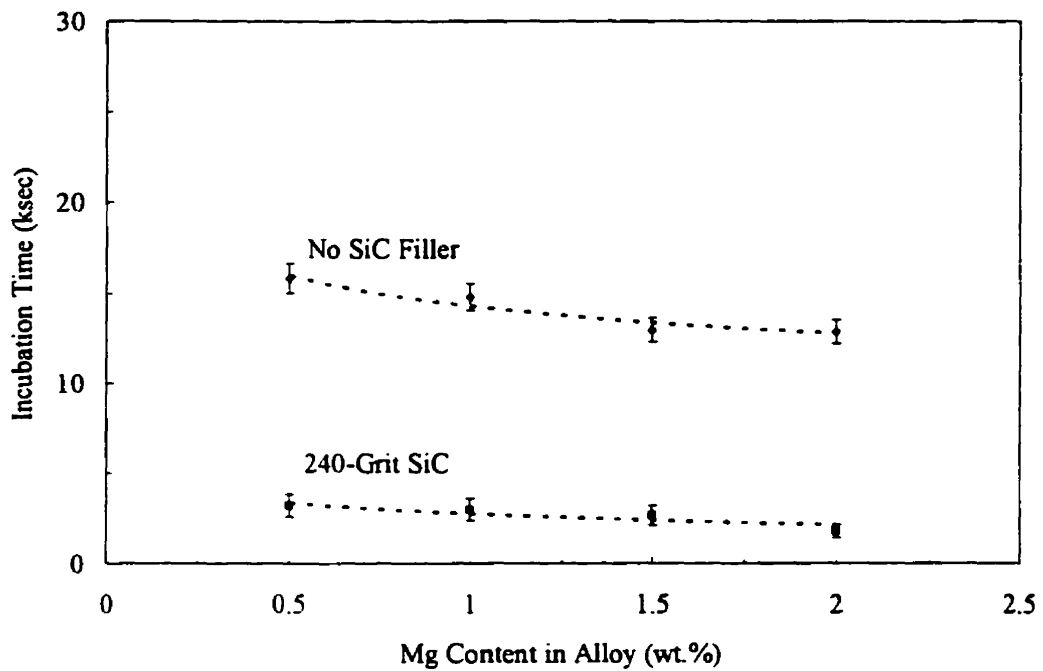


Fig. 5.55: Variation of the incubation period as a function of Mg content at 1350°C.

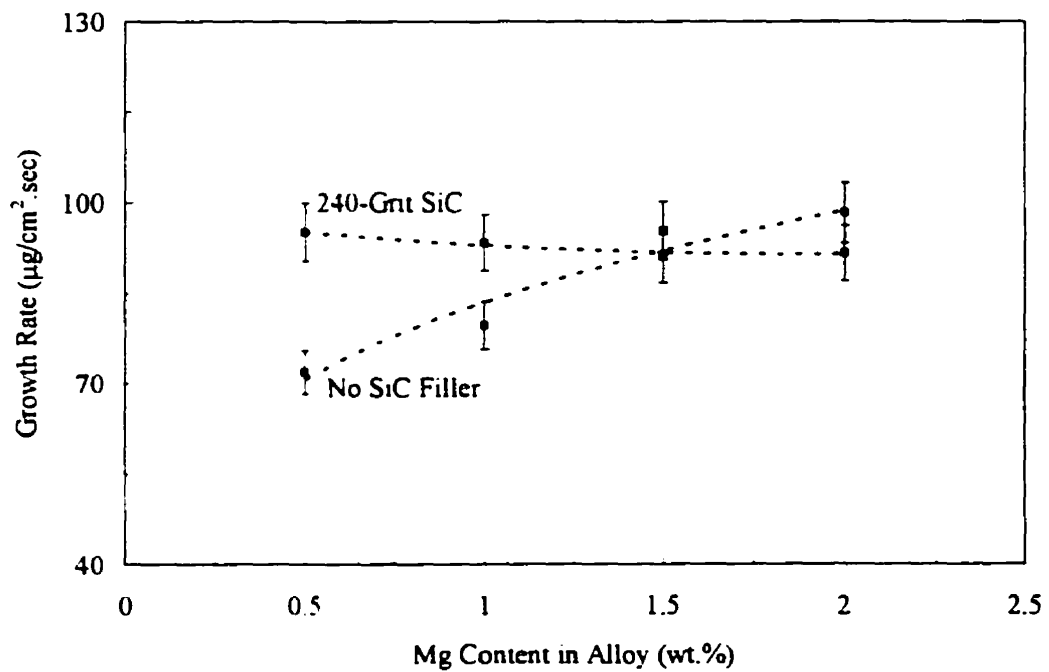


Fig. 5.56: Variation of the growth rate as a function of Mg content at 1350°C.

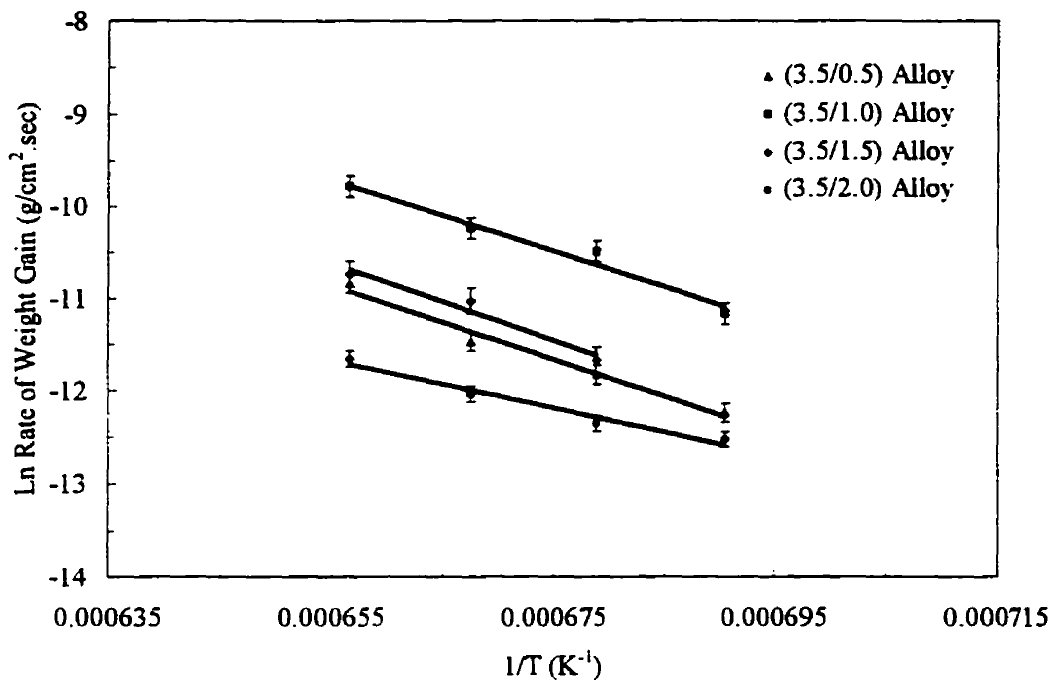


Fig. 5.57: Arrhenius plot of weight gain rates for alloys having different Mg contents (240-grit SiC).

### 5.3.3.2 Effect of Silicon

Fig. 5.58 shows the growth curves for two different alloys: (0/3) and (7/3) without SiC. It is clear that the presence of Si in the alloy drastically reduces the length of the incubation period from about 33 hours for the (0/3) alloy down to 5 hours for the (7/3) alloy at 1100°C. Fig. 5.59 shows weight gain curves for different alloys containing variable amounts of Si in the starting alloy with a Mg content of 1.5 wt. % at 1350°C. It is immediately concluded that for each ~3 wt. % Si content increase in the alloy, the length of the incubation period is reduced by about 1.75 hours. Also the rate of weight gain is slightly increased when the Si content in the alloy increases. The above results are summarized in Table 5.6. For the case of composites with SiC

preforms, Si addition did not result in significant changes. The incubation time remained essentially the same as well as the rate of weight gain, as shown in Fig. 5.60, Fig. 5.61, and Fig. 5.62. The Arrhenius plots for composites processed with SiC preforms are shown in Fig. 5.63, where the activation energies are essentially the same for the four alloys. The Arrhenius plots corresponding to the alloys with low silicon content (0 and 3.5 wt.% Si) possess very comparable slopes which indicates nearly similar activation energy values (within experimental error). The same can be said about the alloys with the high silicon contents (7 and 10 wt.% Si). There appears to be a transition in activation energy which decreases in the high range of silicon content. However, the reason for this is still not clear.

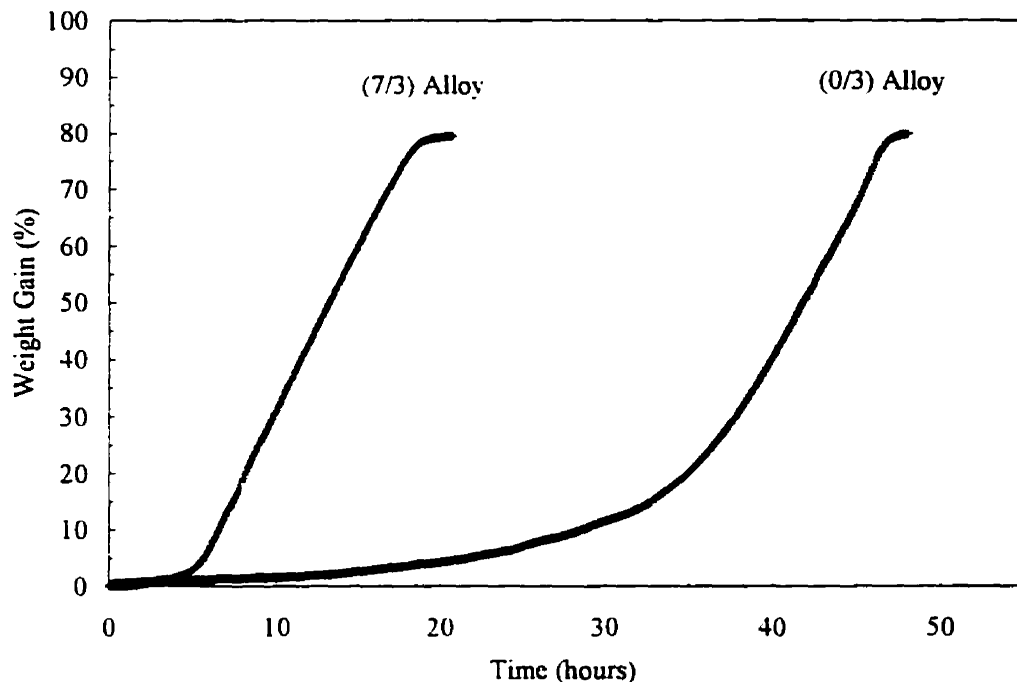


Fig. 5.58: Weight gain vs. time curves showing the effect of presence of Si in the parent alloy (1100°C, no SiC).

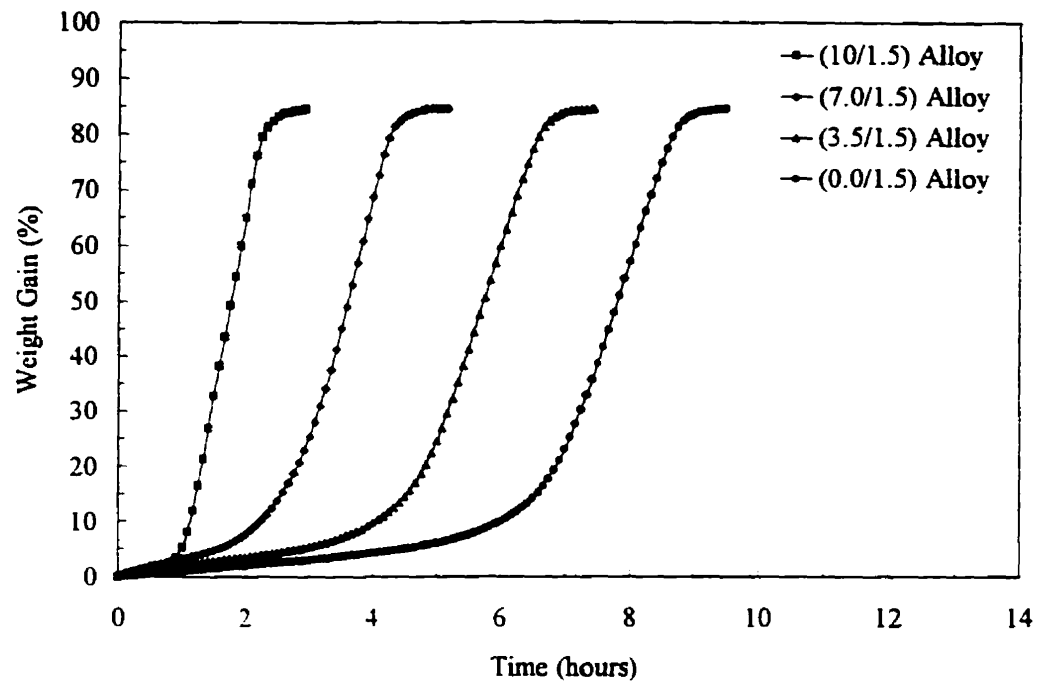


Fig. 5.59: Weight gain vs. time curves showing the effect of changing the Si content on the growth rate (1350°C, SiC).

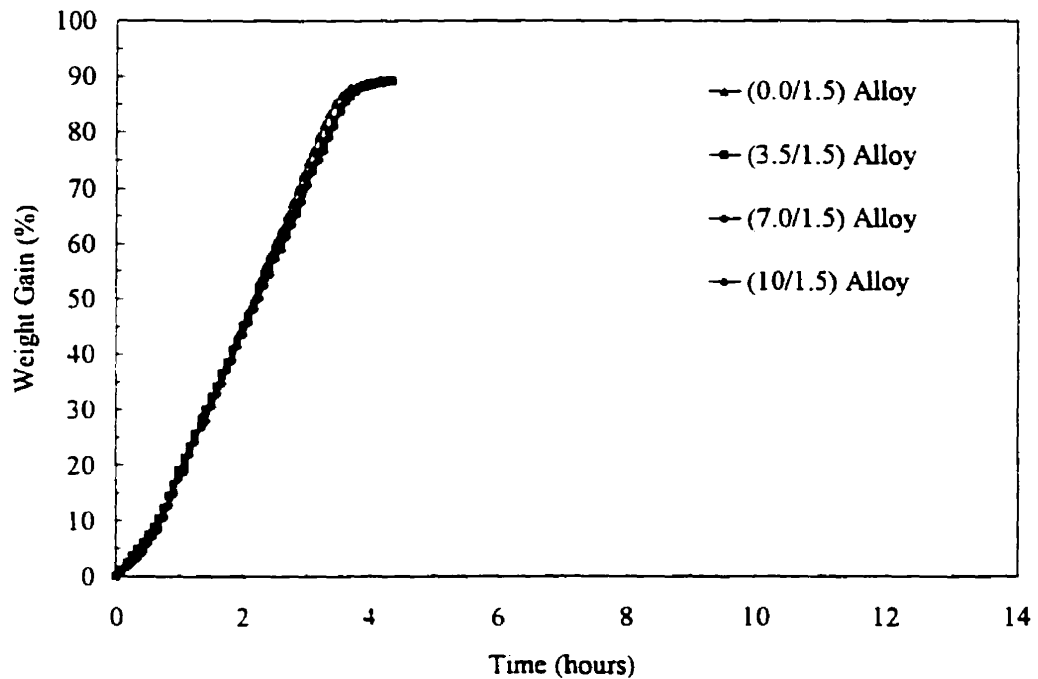


Fig. 5.60: Weight gain vs. time curves showing the effect of changing the Si content on the growth rate (1350°C, 240-grit SiC).

Table 5.6: Growth Rates and Incubation Times for Alloys Containing 1.5 wt.% Mg and Different Si Contents for Composites Processed with and without SiC Reinforcing Particles at 1350°C

Si wt. %	No SiC Particles				240 Grit-SiC Particles			
	0	3.5	7.0	10	0	3.5	7.0	10
Growth Rate ( $\times 10^{-5}$ g/cm <sup>2</sup> sec)	10.1	9.98	12.3	17.2	7.83	7.37	7.34	7.34
Incubation Time (ksec)	19.2	12.5	6.2	3.3	1.2	1.2	1.2	1.2
Activation Energy (kJ/mol)	347.5 346.4 253.9 270.3							

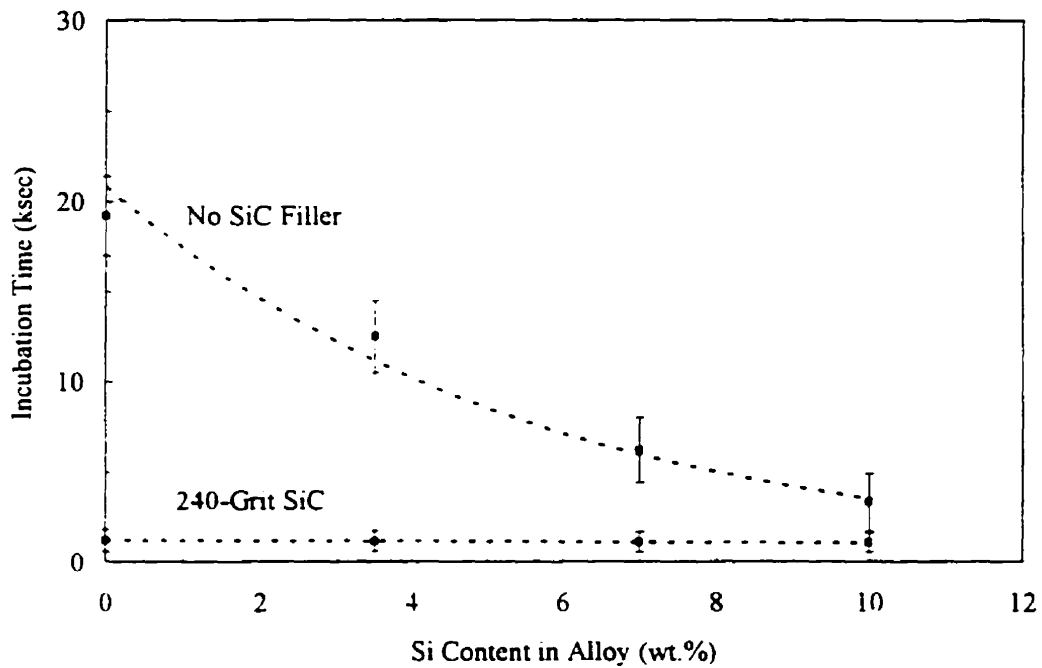


Fig. 5.61: Variation of the incubation period as a function of Si content in the alloy.

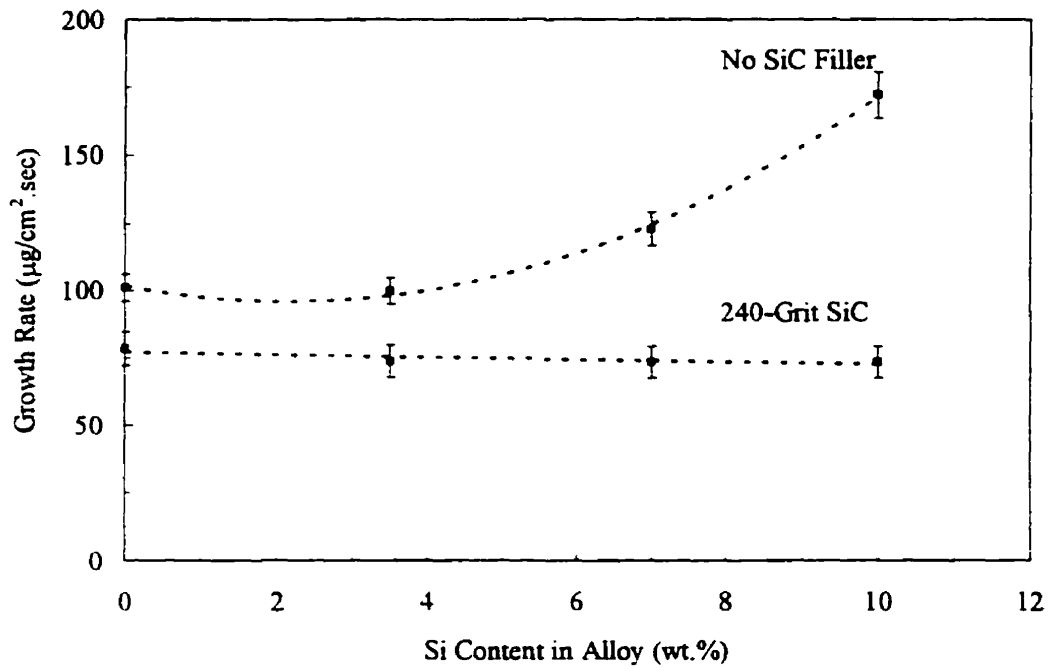


Fig. 5.62: Variation of the growth rate as a function of Si content in the alloy.

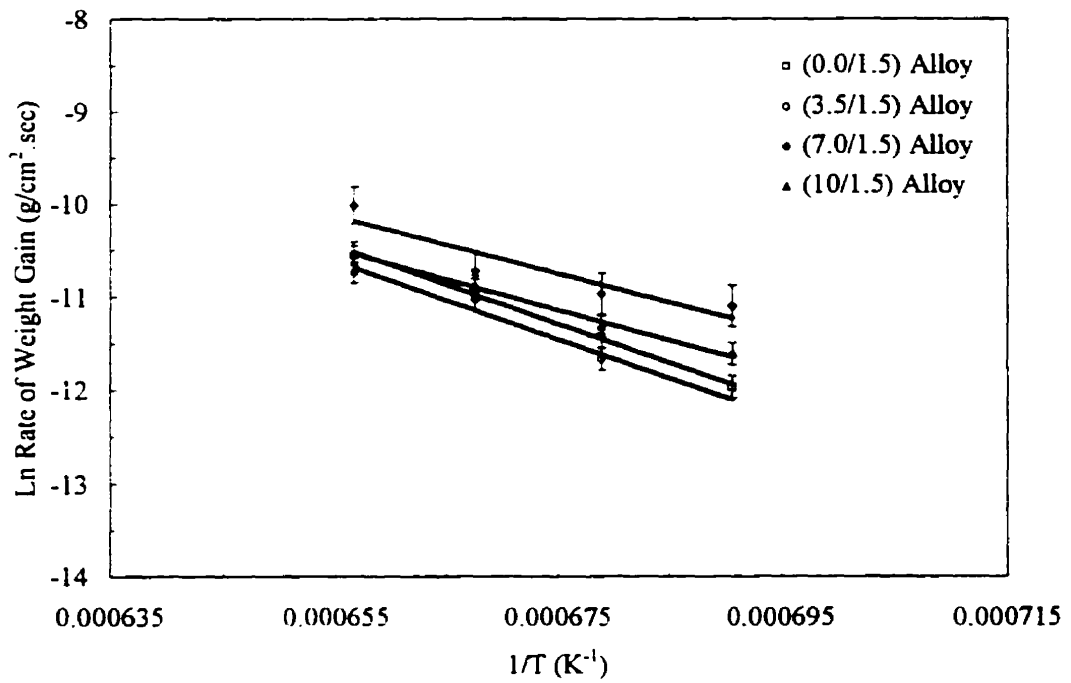


Fig. 5.63: Arrhenius plot of weight gain rates for alloys having different Mg contents using 240-grit SiC preform.

### 5.3.4 Effect of SiC Powder Size

The weight gain curves of different alloys in air at various temperatures and into SiC preforms of different particle sizes are depicted in Fig. 5.64-Fig. 5.66. In general, all curves showed an initial period of accelerating oxidation to a regime wherein the rate appeared to be nearly constant with time. The weight gains shown in Fig. 5.64 and Fig. 5.65, for the composites containing SiC preforms, were normalized with respect to the net cross-sectional area of voids normal to the macroscopic growth direction. This area was measured using the volume fraction of void space between the SiC particles, as described in APPENDIX I.

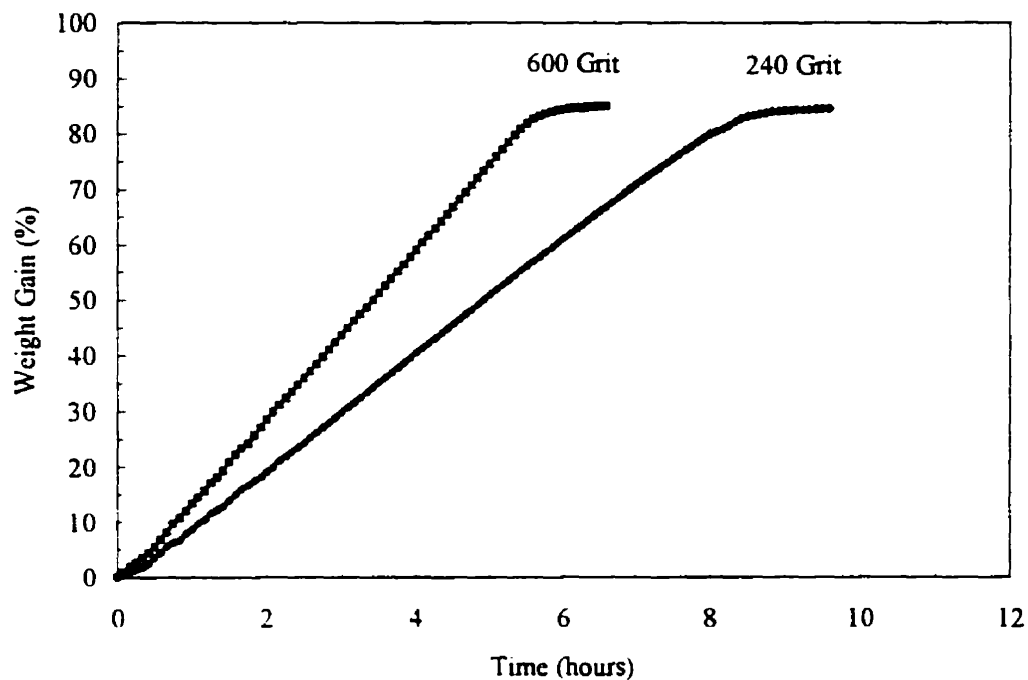


Fig. 5.64: Normalized weight gain vs. time curves for the (0/1.5) alloy showing the effect of SiC powder size. The processing temperature was 1150°C.

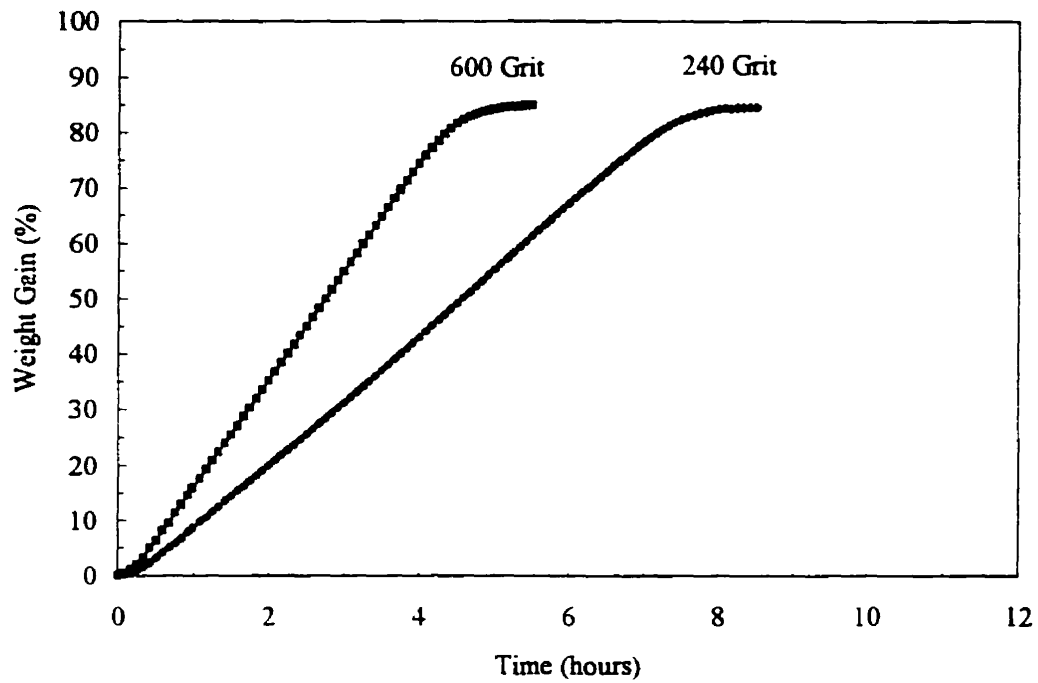


Fig. 5.65: Normalized weight gain vs. time curves for the (3.5/2) alloy showing the effect of SiC powder size. The processing temperature was 1200°C.

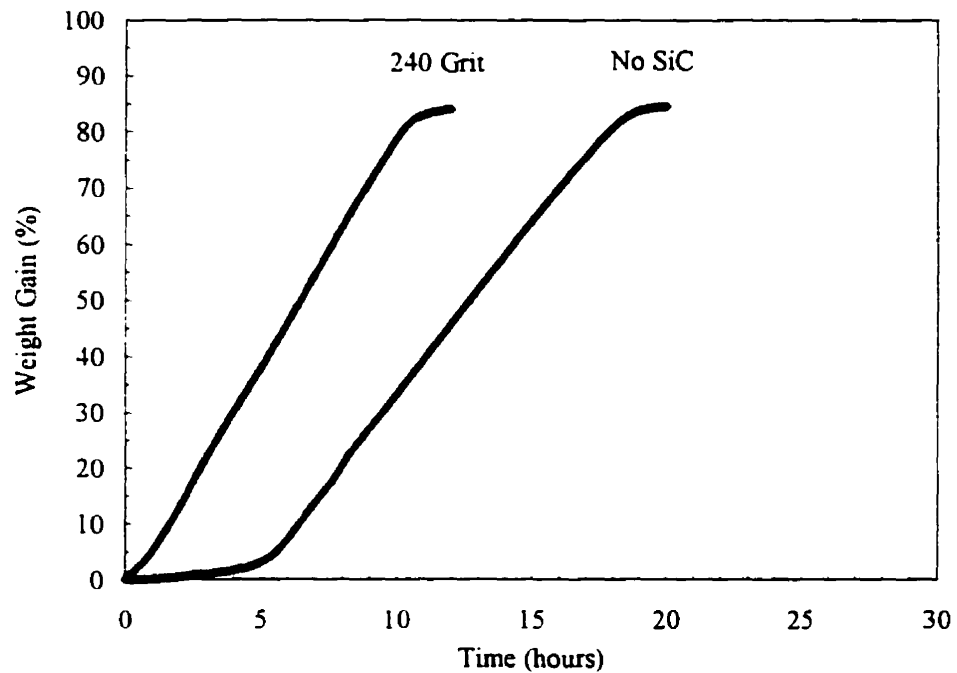


Fig. 5.66: Normalized weight gain vs. time curves for the (7/3) alloy showing the effect of the presence of SiC. The processing temperature was 1250°C.

If the preform had no effect other than to reduce the net area available for growth of the reaction product, the normalized weight gain curves should almost overlap. However, it is clear that the composites grown into SiC preforms exhibit a weight gain per unit area consistently higher than that of the base alloy alone. Their oxidation rates are higher than those of the base alloys by at least a factor or two, with a tendency to increase with decreasing particle size (Fig. 5.67).

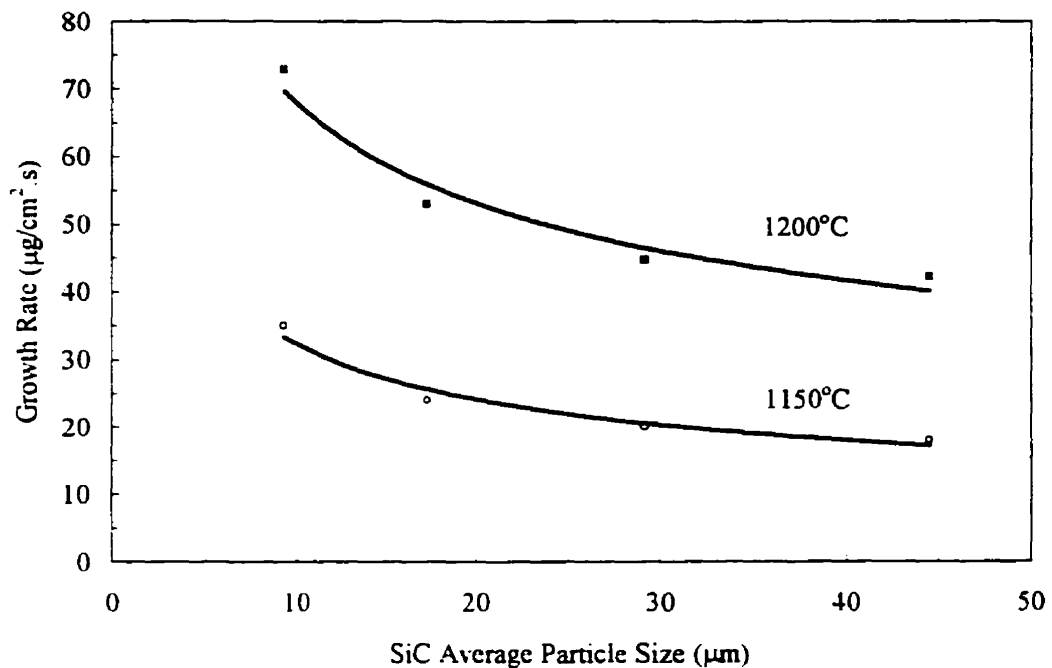


Fig. 5.67: Normalized growth rate vs. SiC particle size curve for the (3.5/2.0) alloy at 1150 and 1200°C.

## 6. DISCUSSION

### 6.1 MICROSTRUCTURAL EVOLUTION

#### 6.1.1 Unreinforced Composites

Data on the oxidation of aluminum and its alloys in the liquid state are not widely available as for the solid state, and only few workers have investigated oxidation of liquid aluminum, especially at the high temperatures of interest here.<sup>63,66,117,118,119</sup> In pure Al, the surface oxide undergoes a transition from amorphous to  $\gamma$ - $\text{Al}_2\text{O}_3$  at temperatures above  $680^\circ\text{C}$  and finally to  $\alpha$ - $\text{Al}_2\text{O}_3$  at  $\sim 1100^\circ\text{C}$ .<sup>113</sup> Binary Al-Mg alloys favor the formation of both MgO and  $\text{MgAl}_2\text{O}_4$  for magnesium concentrations above 0.02%.<sup>113</sup> The oxide formed on the surface of Al-Mg alloys is highly protective below  $350^\circ\text{C}$ .<sup>63</sup> Above this point, the oxide becomes nonprotective and the aluminum oxide initially formed on the surface is replaced by spinel ( $\text{MgAl}_2\text{O}_4$ ) after a few hours of oxidation. At intermediate times, MgO is observed followed by a mixture of MgO and  $\text{MgAl}_2\text{O}_4$ . Bulk depletion of Mg in the alloys results in the eventual conversion of nearly all the MgO to  $\text{MgAl}_2\text{O}_4$ .<sup>72</sup>

The microstructural evolution of the unreinforced composites is in good agreement with the findings of previous researchers.<sup>113,124</sup> The initial oxidation corresponds to the formation of  $\text{MgAl}_2\text{O}_4$  spinel, which is followed by evolution of MgO at the gas/oxide interface during the incubation period. Both layers thicken continuously with time, but at  $1150^\circ\text{C}$ , the MgO layer starts to thin toward the end of

the incubation period. It was reported that a dense spinel layer forms between the MgO and porous spinel layers during incubation.<sup>113</sup> However, our experiments showed no signs of any such dense spinel layer. This could be attributed to the fact that the experiments of Salas *et al.* were carried out at 1100°C instead of 1150°C. However, this is unlikely because if lower temperatures favor the formation of this layer, then other workers,<sup>27,121</sup> who studied the oxidation behavior of Al-Mg alloys at low temperatures, would have reported the presence of such a layer.

The thinning of the MgO layer after reaching a maximum thickness is an indication that some kind of mechanism is taking place to allow the initiation of the composite nodule formation. Salas *et al.*<sup>124</sup> suggested that the nodule nucleation starts when the metal microchannels created during the incubation period reach the MgAl<sub>2</sub>O<sub>4</sub>/MgO interface. Therefore the duration of the incubation period depends on the time required for a significant number of channels to penetrate the spinel layer. If growth initiation requires a number of metal channels to arrive at the MgAl<sub>2</sub>O<sub>4</sub>/MgO interface, then the metal channels start forming during the incubation period emanating from the alloy/spinel interface and progressing outward to the MgAl<sub>2</sub>O<sub>4</sub>/MgO interface. However, this is not consistent with the present experimental observations in that the spinel layer that forms during the incubation period is porous and contains metal channels from the start of incubation. Spinel rings form at the alloy surface around the voids created on the surface of the alloy from the "breakaway" and reoxidation of Mg on the surface. This explains the network configuration of the spinel layer containing 3-D interconnected metal channels. The spaces between the spinel rings are filled by

liquid metal via capillary infiltration and become interconnected channels. The liquid metal in the channels undergoes the same “breakaway” process and new spinel rings are formed on the surface. The newly formed spinel rings grow and coalesce with time and

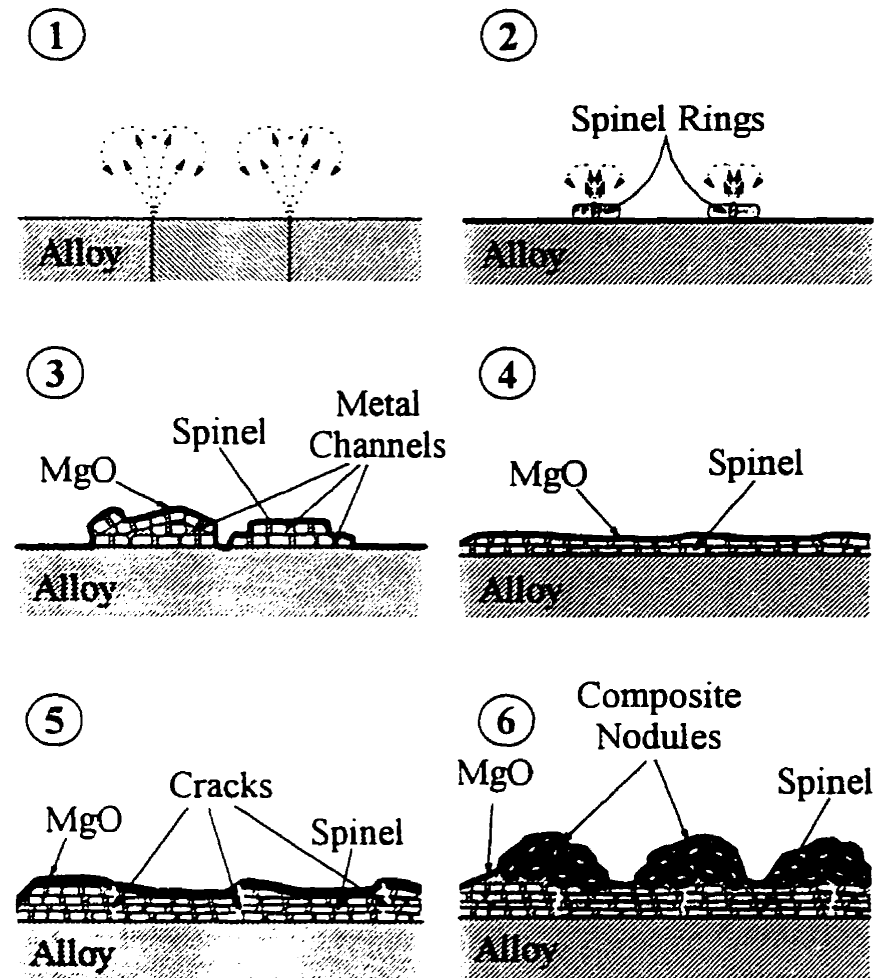


Fig. 6.1: Schematic of the mechanism leading to composite growth.

become nodules. A network of spinel then forms which becomes 3-D interconnected and containing metal channels. At the same time, excess Mg reacts with the oxygen and

forms an MgO layer which covers the spinel. This sequential process is shown schematically in Fig. 6.1.

The thinning of the MgO layer at the end of the incubation period corresponds with the arrival of the metal from the reservoir to the  $\text{MgAl}_2\text{O}_4/\text{MgO}$  interface. This metal layer is supplied by capillarity by the channels existing in the spinel layer. The metal layer reduces the MgO layer, by reacting with the oxygen, and free Mg is released. However, the metal supplied to the interface contains Mg as well as Al. Therefore the Mg concentration build-up helps in breaking the MgO layer to expose the underlying metal. This process is responsible for the nucleation of the composite nodules by reaction of Al with the oxygen from the atmosphere as well as the oxygen released from the dissolution of the MgO layer. There is also evidence that the spinel layer is vulnerable to cracking at the end of the incubation period. These cracks act as channels for extra metal supply to the  $\text{MgAl}_2\text{O}_4/\text{MgO}$  interface. Two types of cracks were observed and resulted from two different sources: (i) cracks running parallel to the growth direction across the spinel layer and formed during the reaction, as indicated by the presence of aluminum alloy in the cracks, and (ii) cracks running diagonally across the spinel layer and sometimes in a direction normal to the growth plane. These cracks develop upon cooling from the process temperature as a result of the difference in thermal expansion coefficients of the aluminum alloy and the spinel. In some cases the spinel layer is delaminated from the metal reservoir. These cracks are free of any metal.

Once the  $\text{Al}_2\text{O}_3/\text{Al}$  composite nodules form, they are covered by a thin MgO layer. Nagelberg<sup>115</sup> reported that the top layer is a continuous MgO layer and controls the oxygen uptake.<sup>120</sup> In contrast to this, the present investigation revealed a discontinuous layer. If we take into consideration that the MgO layer is thin and undergoes a dissolution-precipitation process, then it cannot be continuous since in some locations the MgO is likely to be dissolving and in others reprecipitating. Also in certain locations in the composite, a thin metal layer is maintained at the  $\text{Al}_2\text{O}_3/\text{MgO}$  interface. This represents the growth front where the melt, being supplied via the metal channels, is continuously reacting with the oxygen from either the atmosphere and/or the dissolution of the MgO layer. If the metal channels are not 3-D interconnected, then the growth of the composite cannot be maintained and stops once the metal cannot reach the growth front.

#### *6.1.1.1 Effects of Si*

It is well established that the growth of  $\text{Al}_2\text{O}_3/\text{Al}$  composites from molten Al-Mg-Si alloys requires Mg to be present.<sup>27,110,113,121</sup> The role of Mg is clear and is related to the “breakaway” oxidation behavior that occurs during the oxidation of solid Al-Mg alloys. Increasing the Mg content did not affect the incubation period nor the growth rate. However, the role of silicon is still not fully clear. This section attempts to offer a better understanding of the effect of Si on the microstructural evolution as well as on the growth rate of the composites.

The effect of silicon on the incubation period is clearly shown in Fig. 5.19, where silicon drastically decreases the length of the incubation period and therefore the  $\text{MgAl}_2\text{O}_4$  and  $\text{MgO}$  layers grow to a defined thicknesses in a shorter amount of time. Nagelberg<sup>121</sup> stated that the growth in Al-Mg alloy occurs only after mechanical disruption of the alloy surface. Our experiments showed in fact this is not the case and growth occurs in Al-Mg alloys even at low temperatures ( $1150^\circ\text{C}$ ). It should be noted, however, that at  $1150^\circ\text{C}$ , the length of the incubation time is  $\sim 23$  hours and the previous author reported the results up to only 20 hours and hence his material was still in the incubation period.

The presence of Si in the alloy, in addition to promoting the growth initiation process, appears to assist in maintaining uniform composite growth. In its absence, composite growth would frequently stop or be significantly reduced in localized regions, leading to a "pockmarked" and uneven surface.

It was mentioned earlier that the thickness of the  $\text{MgO}$  layer decreases at the end of the incubation period due to the reaction of the metal with the  $\text{MgO}$  layer. This is where the Si comes into play and is related to the capillary infiltration of the melt in the metal channels. If we consider the rate of infiltration equation:<sup>80</sup>

$$\frac{dl}{dt} = \frac{r \gamma_{lv} \cos\theta}{4 \eta l} \quad (6.1)$$

where  $r$  is the channels radius,  $\gamma_{lv}$  is the surface tension of the melt,  $\cos\theta$  is the contact angle the metal makes with the spinel,  $\eta$  is the viscosity of the metal, and  $l$  is the length infiltrated in the channel. Upon silicon addition to the melt, the two quantities that are

largely affected are  $\gamma_{lv}$  and  $\eta$ . For the rate of infiltration to increase,  $\eta$  has to decrease whereas  $\gamma_{lv}$  must increase.

Silicon additions to aluminum are known to lower the viscosity of the melt.<sup>122,123</sup> So that, if all other parameters remained unchanged, the rate of infiltration of the melt into the metal channels would increase as  $\eta$  decreases upon addition of silicon to the alloy. Goicoechea *et al.*<sup>103</sup> have measured the surface tension of Al-Si-Mg alloys as a function of Si and Mg contents. They found that the surface tension in the Al-Mg-Si alloy varies linearly with the silicon concentration,  $x_{Si}$ , according to:<sup>103</sup>

$$\gamma_{Al-Si} = (869 - 1.6x_{Si}) \text{ mJ/m}^2 \quad (6.2)$$

$$\gamma_{Al-Mg} = \left\{ 869 - 72 \ln(1 + 0.3x_{Mg}) \right\} \text{ mJ/m}^2 \quad (6.3)$$

$$\gamma_{Al-Si-Mg} = \gamma_{Al} + \Delta\gamma_{Al-Si} + \Delta\gamma_{Al-Mg} \quad (6.4)$$

where  $\Delta\gamma_{Al-Si}$  and  $\Delta\gamma_{Al-Mg}$  are the increments in the magnitude,  $\Delta\gamma_{Al}$ , induced by the Si and Mg additions, respectively. One might argue that since silicon addition to the aluminum alloy decreases the surface tension, then the infiltration rate,  $dl/dt$ , would decrease. However, the contact angle in the infiltration equation is inversely proportional to the surface tension, according to:<sup>80</sup>

$$\cos\theta = \frac{(\Delta\rho g)r}{2\gamma_{lv}} \quad (6.5)$$

where  $\Delta\rho$  is the density difference between the vapor and the liquid phase and  $g$  is the gravity. So the surface tension has no effect on the infiltration rate since the  $\gamma_{lv}$  terms in equations (6.1) and (6.5) cancel each other. So the only contribution to the change in infiltration rate comes from the viscosity term.

The third important consequence of Si additions is on the oxygen supply for  $\text{Al}_2\text{O}_3$  formation. Fig. 6.2 shows the pronounced effect of Si on the solubility limits for MgO and  $\text{Al}_2\text{O}_3$  in contact with the melt, increasing  $\Delta[\text{O}]$  and hence the rate of oxygen supply to the near-surface layer (NSA)/ $\text{Al}_2\text{O}_3$  interface.<sup>127</sup> The oxygen gradient is expected to increase with Si build-up at the NSA layer, initially offsetting the effects

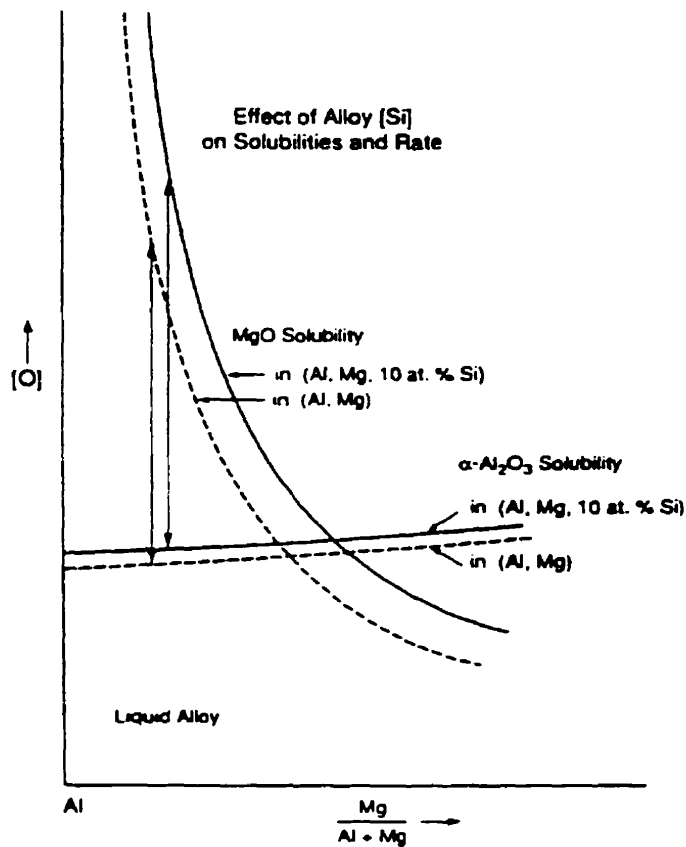


Fig. 6.2: Effect of Si on the MgO and  $\text{Al}_2\text{O}_3$  solubilities and hence the oxygen gradient for Al-rich alloys.<sup>127</sup>

of Mg enrichment and enhancing the growth rate. This is believed to be partially responsible for the initial acceleration after the onset of growth. Continued Si enrichment in the NSA layer is eventually slowed by back diffusion, but could still lead

to a significant decrease in the aluminum content, increasing the  $[Mg]/([Mg]+[Al])$  in Fig. 6.2 and consequently reducing  $\Delta[O]$ .

Salas *et al.*<sup>124</sup> concluded that Si decreases the activity of Mg in the melt and should promote the dissolution of spinel producing shorter incubation times for Al-Mg-Si alloys.

These authors calculated an isothermal section for the Al-Mg-O phase diagram at 1100°C which is shown in Fig. 6.3.<sup>124</sup> Their calculation was based on

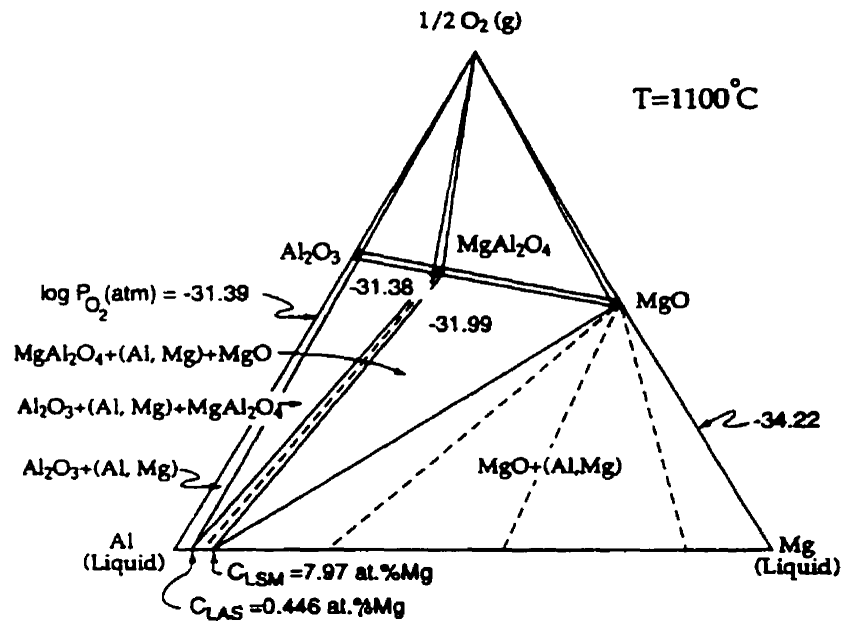


Fig. 6.3: Isothermal section of the Al-Mg-O phase diagram at 1100°C.<sup>124</sup>

thermochemical data for the relevant oxides and the Al-Mg system. The phase relationships and general features of this diagram persist through the typical temperature range for composite formation in Al-Mg alloys, i.e. ~1050°C to 1350°C.

Salas *et al.* concluded that the liquid solution emerging from the Al-Mg binary extends only very slightly into the ternary, as anticipated from the very low solubility of oxygen in molten aluminum.<sup>125</sup> The oxide phase in equilibrium with liquid (Al,Mg) changes from  $\text{Al}_2\text{O}_3$  to  $\text{MgAl}_2\text{O}_4$  and finally to  $\text{MgO}$  as the Mg content in the alloy increases. The transition points correspond to the liquid compositions for the equilibria  $\text{L}/\text{Al}_2\text{O}_3/\text{MgAl}_2\text{O}_4$  and  $\text{L}/\text{MgAl}_2\text{O}_4/\text{MgO}$ , denoted as  $C_{\text{LAS}}$  and  $C_{\text{LSM}}$ , respectively in Fig. 6.3. The calculated ternary equilibrium compositions change with temperature as depicted in Fig. 6.4, and shift to higher Mg and O contents as Si is added to the melt.<sup>124</sup>

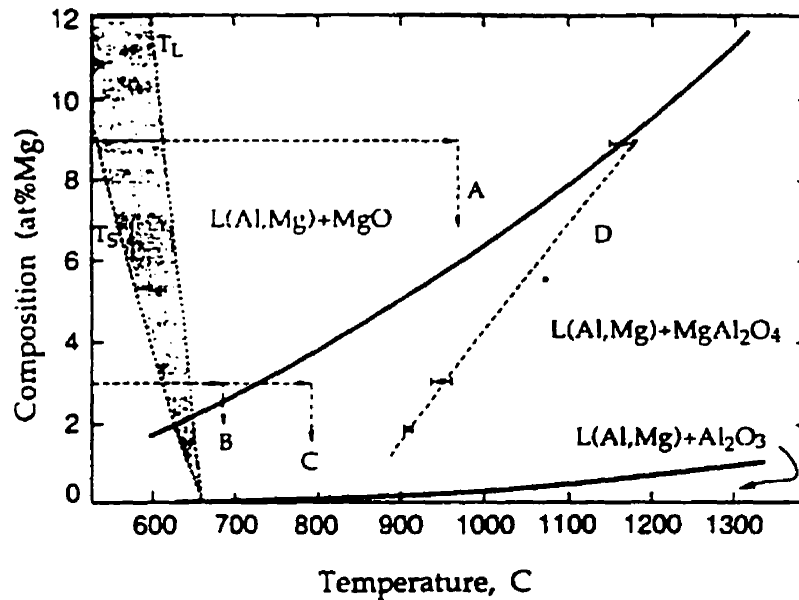


Fig. 6.4: Calculated Mg concentrations for the relevant three-phase equilibria  $C_{\text{LAS}}$  and  $C_{\text{LSM}}$  as a function of temperature. Also shown are the liquidus ( $T_L$ ) and solidus ( $T_S$ ) lines for alloys within this composition range.<sup>124</sup>

They concluded from the previous two figures that the binary alloys with 3.0, 5.4 and 8.9Mg would be expected to form  $\text{MgO}$  on the surface upon melting. In

contrast, the melting range for the Al-1.9Mg alloy is approximately 625-655°C, well within the  $\text{MgAl}_2\text{O}_4$  stability field in Fig. 6.4.<sup>124</sup> As temperature increases to 1100°C, the 3.0 and 5.4Mg alloys also move into the spinel stability field, but not the 8.9Mg alloy. They also concluded that full equilibrium cannot actually be achieved between the oxide and the melt in the presence of significant partial oxygen pressures, but that local equilibrium can be presumed as diffusion through the oxide film is much slower than the interfacial reactions.

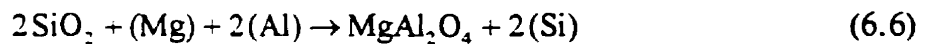
## 6.1.2 SiC Reinforced Composites

The presence of SiC preforms in the composites did not affect their microstructures which still consisted of a 3-D interconnected ceramic phase ( $\text{Al}_2\text{O}_3$ ) and 3-D interconnected residual metal channels as well as isolated metal pockets. However, the presence of SiC disrupted the columnar growth of the ceramic phase (which was aligned parallel to the growth direction when no SiC preform was used). However, between the SiC particles, there is some local orientation of the  $\text{Al}_2\text{O}_3$  phase in the direction of growth. Overall, the introduction of a SiC preform in the composite resulted in refinement of the composites, that is, the metal channels became finer than in the unreinforced composites.

### 6.1.2.1 Incubation Period

It is evident that the presence of the SiC preform in the composites affected the microstructural evolution of the composites, and resulted in much shorter incubation times (compared to composites without SiC preforms). In some composites,

the growth started immediately after introduction of the sample into the furnace. Besides the fact that the SiC preform provides a skeleton upon which the reaction product grows, the surface of the SiC particles seems to play a key role. It is well established that Al and Al-Mg alloys wet SiC at temperature  $> 1100^{\circ}\text{C}$ .<sup>93,96,103</sup> As soon as the alloy is molten and is in contact with the SiC particles, spreading of the alloy occurs over the edges of the SiC particles that are in contact with the melt. Between the SiC particles, the same process occurs as in the unreinforced composites, where the surface of the alloy is covered by  $\text{MgAl}_2\text{O}_4$  and MgO layers (see Fig. 6.5). However, on the surface of the SiC particles, and during the incubation period, nucleation of  $\text{MgAl}_2\text{O}_4$  takes place due to the evaporation of Mg accompanied by spreading of the aluminum melt. Mg and Al both react with oxygen from the atmosphere and from the dissolution of the  $\text{SiO}_2$  passivation layer surrounding the SiC particles. The new products ( $\text{MgO}$  and  $\text{MgAl}_2\text{O}_4$ ) are deposited on the outer surface of the alloy, according to:<sup>126</sup>



Therefore the SiC surface is a preferential nucleation site for the spinel and MgO layers.

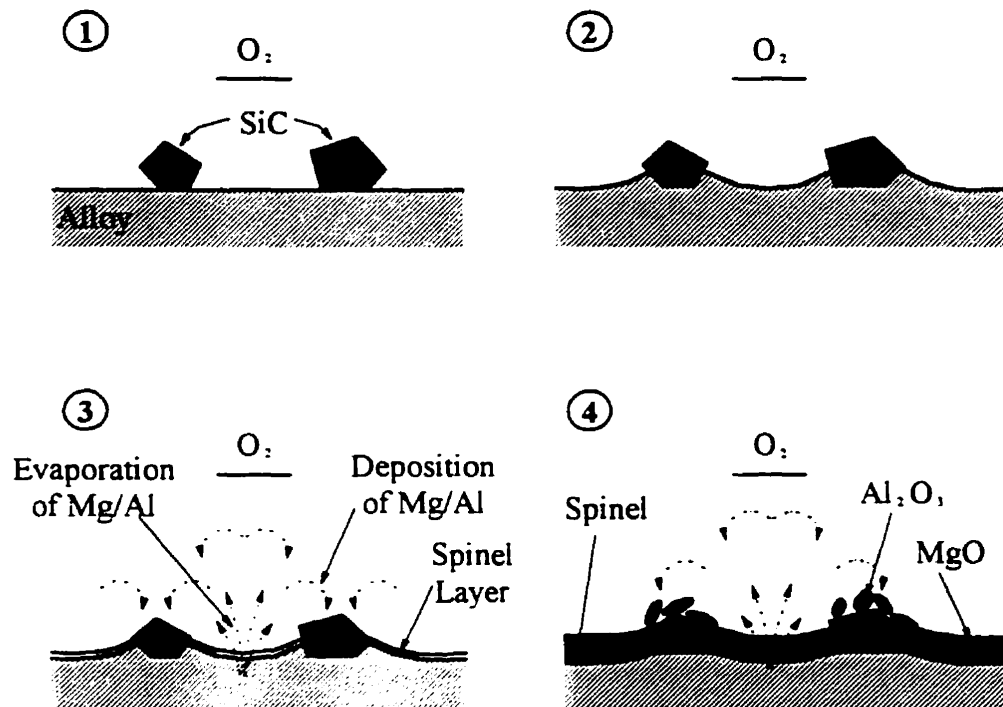


Fig. 6.5: Schematic of the evaporation and redeposition after oxidation of Mg/Al.

The present investigations helped clarify the microstructural evolution of the composites in relation to the role of the surface oxide layers ( $MgO$  and  $MgAl_2O_4$ ) in both the absence and the presence of SiC preforms. These two layers start appearing as soon as the alloy is in contact with oxygen at the processing temperature, and they persist until the growth process is completed. Therefore these two oxides are responsible for the continuous oxidation process responsible for composite formation.

From the microstructural observations of the unreinforced composites, the Al-Mg and Al-Mg-Si alloy surfaces are covered by two oxide layers:  $MgO$  and  $MgAl_2O_4$ . Salas *et al.*<sup>124</sup> have performed experiments where they covered the surface of the alloy with a thin  $SiO_2$  layer prior to oxidation. They concluded that the  $SiO_2$

shortens the incubation period by providing sites wherein the dense spinel layer, which seals off the metal channels, is prevented from forming. It is documented that the reaction between Al-Mg alloys and  $\text{SiO}_2$  involves the reduction of  $\text{SiO}_2$  to form spinel according to equation (6.6).<sup>126</sup> This transition from  $\text{SiO}_2$  to  $\text{MgAl}_2\text{O}_4$  is accompanied by a volume contraction of ~14%, which is filled by the molten metal.<sup>124</sup> Unlike Mg, however, the released Si does not get reoxidized but gradually diffuses back into the bulk melt.

Our experimental observations do not fully agree with the conclusion of Salas *et al.* that the  $\text{SiO}_2$  shortens the incubation period by providing sites which prevent the dense spinel layer from forming. If the  $\text{SiO}_2$  is the only factor responsible for the elimination of incubation, then Al-Mg-Si alloys should have no incubation period, or a very short one at the least. This is not the case since Al-Mg-Si alloys still exhibit an incubation period of up to 4.5 hours at 1350°C. On the other hand, when using a SiC preform, the incubation period remained the same and did not vary with the change in alloy content of either Mg or Si. The spinel that forms during the incubation period in the SiC-reinforced composites grows between the SiC particles and composite growth soon follows.

According to equation (6.6), free silicon is released into the melt. It was observed that in composites grown from Al-Mg alloys, silicon is present in the metal channels of the composite. If the length of the incubation period is solely dependent on the presence of Si in the alloy, then it should be expected that the length of the

incubation period in the Al-Mg alloys is of approximately the same magnitude as in the Al-Mg-Si alloys, which is in good agreement with our experimental observations.

When a SiC preform is used as a reinforcement upon which the composite grows, dissolution of the  $\text{SiO}_2$  layer surrounding the SiC particles leads to the formation of  $\text{MgAl}_2\text{O}_4$ . It should be recalled that the SiC powder was preoxidized prior to the growth process. Another important observation is that even if the SiC powder was not preoxidized, the composite growth process started immediately after a brief incubation period. This implies that the role of the SiC particles is not limited to the presence of a thick  $\text{SiO}_2$  layer, but also the fact that the particles are disrupting the formation of the two oxides on the alloy surface.  $\text{MgO}$  and  $\text{MgAl}_2\text{O}_4$  layers can be thought of as passivating layers that prevent the alloy from oxidation when in contact with air. The points or surfaces of contact between the particles and the alloy surface are actually shielded (relatively speaking) from the oxygen. Consequently the portion of the particles that is in contact with the alloy is transformed into  $\text{MgAl}_2\text{O}_4$  and the other side of the particles is in contact with oxygen and it reacts only with the evaporated Mg/Al mixture. The triple points (intersection of the SiC particles, the alloy surface and the oxygen) are sites where the alloy can be withdrawn upwards to the oxygen (by wetting of SiC).

Nagelberg<sup>121</sup> grew composites starting from Al-3 wt. % Mg and Al-3 wt. % Mg-10 wt. % Si alloys at temperatures ranging from 1100-1250°C. On some of his samples, he scratched the surface of the molten alloy during the incubation period and concluded that this resulted in the growth of  $\text{Al}_2\text{O}_3$ /metal composites along the

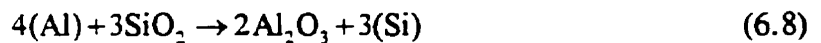
scratches. He also observed that the sizes of the nodules along the scratch were proportional to the elapsed time following surface scratching and appeared to be independent of the presence or absence of Si in the alloy. The role of the SiC preform in decreasing or nearly eliminating the incubation period is therefore attributed to the disruption of the outer passivating oxide layers (i.e. MgO/MgAl<sub>2</sub>O<sub>4</sub>). The two-layer structure still exists on the outer surface of the alloy in the presence of the SiC preform, but this layer is continuous only between the preform particles. Under the SiC particles, the layer is discontinuous which would serve as a mechanical disruption to promote growth initiation sites, as was observed in our experiments, where the growth initiation of the MgAl<sub>2</sub>O<sub>4</sub> is located at the SiC particles surfaces.

#### *6.1.2.2 Composite Formation*

Cracking of the spinel layer is a common occurrence observed in the composites. The thicker the initial oxide layer on the alloy, the more susceptible to cracking it becomes under growth stresses. Since the oxide layers grow faster in the Al-Mg-Si alloy than in the Al-Mg alloy, cracks would develop sooner in the Al-Mg-Si alloy indicating a shorter incubation period than the Al-Mg alloy. When a SiC preform is used, the spinel layer grows very thick in a significantly shorter time.

The MgO layer covering the composite nodules has a texture similar to that of a sponge, and in some locations it is not even observed. This leads to the conclusion that MgO is dissolved and then precipitated on the outer surface. The reaction starts around the SiC particles, and the product grows outward from the SiC surface. Further

reaction results in the coalescence of the  $\text{Al}_2\text{O}_3$  nodules originating from different SiC particles. The reaction on the preform surface is enhanced by the wetting of the SiC by aluminum and its alloys and is even further enhanced by the presence of the  $\text{SiO}_2$  layer around SiC. Manor *et al.*<sup>112</sup> suggested that the nucleation of the  $\text{Al}_2\text{O}_3$  on the preform particles could arise from the reaction of Al in the spreading melt with the  $\text{SiO}_2$  layer typically present on the SiC. This might occur especially after lengthy exposure of the preform to air at high temperature, according to:<sup>112</sup>



It should be noted that the process of formation of  $\text{Al}_2\text{O}_3$  nodules occurs in a similar manner to that of  $\text{MgAl}_2\text{O}_4$  and MgO layers, i.e. formation starts on the surface of the SiC particles and grows away from them.

## 6.2 GROWTH KINETICS

If the parabolic equation is applied to calculate the rate constant for the oxidation of aluminum in the liquid state, for example at  $800^\circ\text{C}$ ,  $K=1.36 \times 10^{-16}$   $\text{g}^2/\text{cm}^4 \cdot \text{sec}$ . This value is much lower than that obtained for the oxidation of solid aluminum, that is  $K=6.0 \times 10^{-13}$   $\text{g}^2/\text{cm}^4 \cdot \text{sec}$  at  $600^\circ\text{C}$ .<sup>52</sup> Also the activation energy for oxidation of liquid aluminum ( $E_a=258$  kJ/mol) is much higher than that for solid aluminum at  $450\text{-}650^\circ\text{C}$  ( $E_a=156$  kJ/mol).<sup>117</sup> This leads to the conclusion that the oxidation of pure liquid aluminum is much slower than that for pure solid aluminum. This is in agreement with the work of Stucki *et al.*<sup>51</sup> who compared the initial stages of

low-pressure oxidation of very pure solid and liquid Al using Auger electron spectroscopy (AES) and electron energy loss spectroscopy (EELS). They showed that for solid Al, only electrons from the surface region take part in bonding to oxygen. In the case of liquid Al, there exists an initial phase before the growth of a surface oxide is detectable. They concluded that after a compact oxide layer on the liquid surface is formed, the oxidation rate decreases drastically, and further oxidation is controlled by the diffusion of Al (not oxygen, which requires a much higher thermal activation energy) through the solid oxide layer.

Temperature change affects the relative solubilities of the surface oxides more significantly than it affects the transport rates of the different reactants within the liquid alloy. Vlach *et al.*<sup>127</sup> conducted thermodynamic calculations and found that increasing

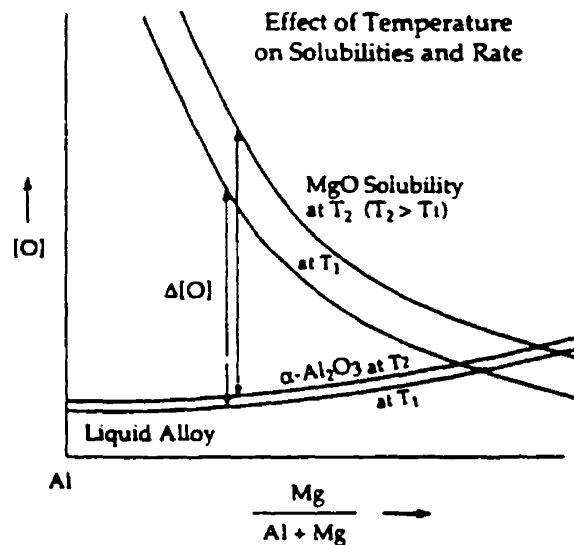


Fig. 6.6: Effect of temperature on the relative oxide solubilities, hence  $\Delta[\text{O}]$  and the  $\text{Al}_2\text{O}_3$  formation rate.<sup>127</sup>

temperature results in a much larger increase in the solubility of MgO than that of  $\text{Al}_2\text{O}_3$ . When the temperature increases, so does the  $\Delta[\text{O}]$  across the near-surface layer (NSA) layer and hence the reaction rate, as shown in Fig. 6.6.

They also found that the primary contribution to the activation energy for the reaction arises from the enthalpy of solution of MgO in the liquid alloy. While actual thermochemical data are lacking, their evaluation resulted in a value of about 240 kJ/mol, which is in reasonable agreement with the measured  $E_a$  values obtained from the current work (~223 kJ/mol).

### 6.2.1 Effects of the $\text{SiO}_2$ Layer

When a mixture (SiC/20 wt.%  $\text{SiO}_2$ ) is used to grow composites in air, the resulting microstructure is similar to that of composites described before. Most of the metal channels are composed primarily of Si and aluminum is not observed as often. It appears that  $\text{SiO}_2$  particles have reacted with the aluminum to form  $\text{Al}_2\text{O}_3$  grains which have later coalesced. It was also observed that the SiC particles did not react with the aluminum and remained intact and therefore no  $\text{Al}_4\text{C}_3$  phase was detected.

However, during infiltration of SiC by aluminum, the silicon carbide particles have reacted with the aluminum, as seen by the degradation of the particle edges, and resulted in the formation of  $\text{Al}_4\text{C}_3$ . The matrix is composed of the starting aluminum and also of Si particles resulting from the reaction between the aluminum and the SiC. However, when the SiC particles are not in contact with the aluminum (surrounded by Si), they are intact and there are no signs of chemical attack on the

particles in these regions. This is expected, since in the Al-Si-SiC system, the extent of attack of SiC by the melt is severely diminished when the melt is saturated with Si.

On the other hand, when a SiC/SiO<sub>2</sub> mixture (20 wt. % SiO<sub>2</sub>) is infiltrated by aluminum, Al<sub>2</sub>O<sub>3</sub> grains form and grow as a result of the reaction of the SiO<sub>2</sub> powder with Al. The Si particles are present in the matrix as a result of the reaction. However, Al reacts slightly with SiC but not as much as with the SiO<sub>2</sub> since SiC does not decompose as easily and traces of the brittle Al<sub>4</sub>C<sub>3</sub> phase were detected by EDS analysis. The previous observations are in agreement with other authors, who discussed the chemical stability of SiC in molten Al and its alloys.<sup>128,129,130</sup> In general, these studies have confirmed that reactions between SiC and Al can occur under suitable conditions to form aluminum carbide, which is a brittle compound, has poor corrosion resistance and is expected to degrade the composite properties. In addition, the enrichment of the metal with Si from the carbide dissolution reaction modifies the basic metallurgy of the alloy. For SiC with an oxidized surface, the nature of the chemical reactions depends on the thickness of the oxide film. With a thin native oxide film on SiC, aluminosilicates and amorphous alumina form; however, once SiO<sub>2</sub> is consumed, Al<sub>4</sub>C<sub>3</sub> starts to form. With a thick oxide layer on SiC (>5 nm), only aluminosilicates and alumina are formed.<sup>131</sup> SiO<sub>2</sub> layers on SiC protect it from attack by Al.

In the reaction of Al with SiC, the carbide product precipitates as a discontinuous layer and Si precipitates between the carbide crystals.<sup>132</sup> It has been proposed that aluminum carbide first nucleates at preferred sites on SiC, after which SiC dissolution continues where the SiC and Al are in direct contact. Finally

dissolution of SiC occurs from areas separated by the interfacial reaction products together with the enrichment of the melt with Si.<sup>108</sup> The dissolution of SiC depends upon the temperature, Si content in the melt, and the diffusion rate of Si in the melt.

The rate of the carbide dissolution reaction can be reduced by melt enrichment with free Si. Iseki *et al.* showed the formation of  $Al_4C_3$ , Si and Al layers at the interface between SiC and Al without free Si, however, no aluminum carbide forms in the case where free Si is present in the metal.<sup>133</sup> In the case of Al-Si alloys, the equilibrium Si level in the melt increases from 8.4 wt.% at 607°C to 12.8 wt.% at 827°C; so if the Si content reaches these levels at the respective temperatures, the carbide dissolution reaction will become thermodynamically unfavorable.

Vlach *et al.*<sup>127</sup> have used the Al-Mg-Si-O phase diagram in Fig. 6.7 to determine the effect of Mg and Si additions on the growth rate. An important feature of the primary oxidation surface in Fig. 6.7 is the upward curvature of the alloy compositions of the three-phase equilibria when moving away from the Al-Mg side. They concluded that the Mg concentration for the liquid alloy- $Al_2O_3$ - $MgAl_2O_4$  equilibrium increases from ~1 at.% at the Al-Mg side to ~5 at.% with 50 at.% Si content, reflecting a strong thermochemical interaction between Mg and Si in the liquid which greatly reduces the activity of the Mg in the melt. This has two important consequences. First, one should note that the continuous formation of  $Al_2O_3$  tends to shift the alloy composition directly away from the Al corner of the diagram. For binary Al-Mg alloys, the progressive enrichment of solute is likely to move the system into the  $MgAl_2O_4$  equilibrium oxide field, leading to  $MgAl_2O_4$  formation, reducing the growth

rate due to the slower dissolution rate of the surface oxide, and oscillatory growth over an extended temperature range.<sup>134</sup> In contrast, modest Si additions allow the liquid composition to stay close to the three-phase equilibrium line in Fig. 6.7, minimizing the  $\text{MgAl}_2\text{O}_4$  supersaturation and enabling growth by direct MgO dissolution over an extended period of time.

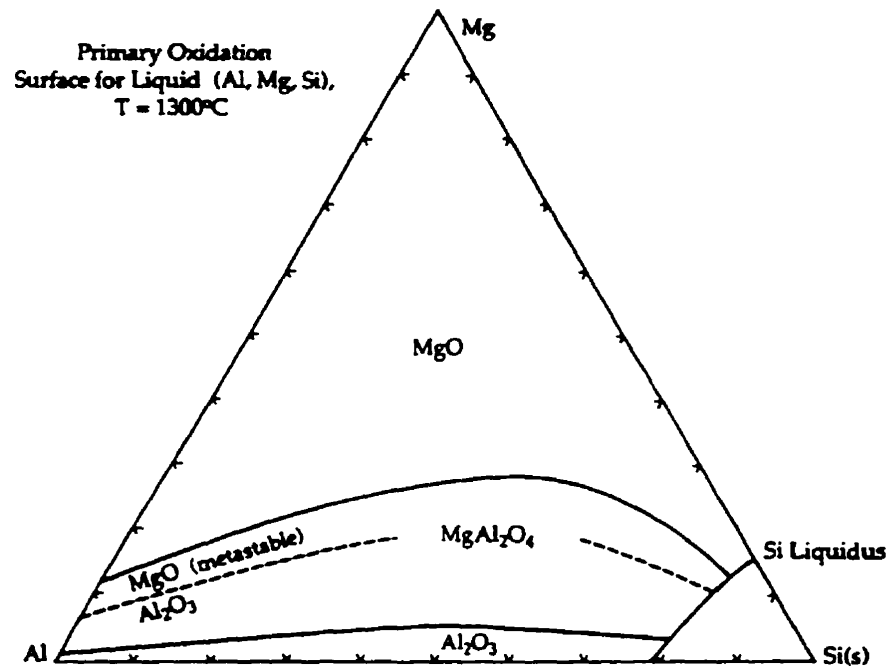


Fig. 6.7: Primary oxidation surface for liquid (Al, Mg, Si) at 1300°C.<sup>127</sup>

## 6.2.2 Effects of Alloying Elements

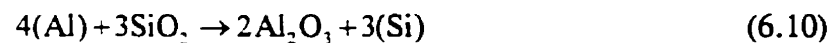
In the SiC-free composites, increasing the Mg content in the alloy from 0.5 wt.% to 2 wt.% resulted in a slight increase in the composite growth rate. This is expected since most of the Mg in the alloy is converted into MgO and  $\text{MgAl}_2\text{O}_4$ . Once these two layers reach certain thicknesses, composite growth begins. So Mg addition

will simply maintain a coherent oxide layer and minor Mg additions were able to provide a continuous growth of the composites. However, in the Al-0.5 wt.% Mg alloys, often the growth of the composites stops before the alloy has been totally consumed, especially at high temperatures (1350°C) where the rate of evaporation of Mg is high. Sufficient amounts of Mg are therefore required to form  $\text{MgAl}_2\text{O}_4$  and MgO, as well as maintaining a constant Mg concentration in the reservoir. This implies that the growth process does not solely rely on the outer MgO layer to keep providing oxygen to the reaction front by its dissolution, but rather the wicking melt through the metal channels must also contain Mg to promote the “breakaway” oxidation process. This is consistent with the observation that increasing the Mg content in the alloy did not affect the length of the incubation period, in a sense that the MgO and  $\text{MgAl}_2\text{O}_4$  layers grow to the same thicknesses in different alloys independent of the amount of Mg present in the alloy.

On the other hand, Si additions to the alloy greatly affected the length of the incubation period, and also increased the rate at which the composites grew. The effect of silicon additions on the incubation period was discussed earlier. Si in the metal channels within the composite, acts in the same manner as in the channels of the  $\text{MgAl}_2\text{O}_4$  layer, i.e. it lowers the surface tension of the alloy as well as the melt viscosity. In this manner, the liquid metal is fed to the reaction front faster which is reflected in an increase in the growth rate. However, too large an addition of silicon to the alloy would result in clogging of the metal channels, due to solidification, which in turn would decrease the rate of growth. Hence, the growth could cease before the metal

reservoir would be exhausted. There should be a compromise between a fast growth rate and optimal mechanical properties of the final composites. All the silicon in the starting composition will end up in the metal channels of the final composite. When the composite contains a large volume fraction of silicon, its mechanical properties will be degraded due to the inherent brittleness of the silicon phase.

For SiC-reinforced composites, no change was observed in either the incubation time or the growth rate as a function of the alloy (Mg or Si) content. Increasing the Mg content in the alloy is not expected to affect the length of the incubation period nor, as discussed earlier, the composite growth rate for the unreinforced composites. As for the Si content, consider the following two reactions for dissolution of the SiO<sub>2</sub> layer:



In both equations, increasing the Si concentration will tend to reverse the direction of both reactions and, hence, the rate of dissolution of the SiO<sub>2</sub> layer will decrease. In other words, the Si concentration in the metal channels will be constantly independent of the Si concentration in the starting alloy. If the alloy has a low content of Si, then the dissolution of the SiO<sub>2</sub> layer around the SiC particles is accelerated. This explains why the incubation period and the growth rate remain unchanged when increasing or altering the Si content of the SiC reinforced composites.

### 6.2.3 Effects of Preform Size

From the microstructural observations, it is clear that new  $\text{Al}_2\text{O}_3$  grains nucleate on the SiC particle surfaces and grow outward from them. Since smaller SiC particles ( $d_p=17.3\mu\text{m}$ ) have a higher surface area ( $S_o=0.386\text{ m}^2/\text{g}$ ) than larger ( $d_p=44.5\mu\text{m}$ ) particles ( $S_o=0.127\text{ m}^2/\text{g}$ ), there is a larger nucleation area on the small particles on which nucleation of  $\text{Al}_2\text{O}_3$  takes place. Therefore, at a given time, more grains nucleate which increases the weight gain per unit time. As temperature increases, the effect of the particle size on the growth rate becomes more pronounced (refer to Fig. 5.67), presumably because as temperature increases, the rate of metal supply to the reaction front increases.

Manor *et al.*<sup>112</sup> argued that the thickness of the extended oxidation interface decreases with particle size, as the interparticle spaces behind the growth front become smaller and can be filled in a shorter time by the composite growing from the particle surfaces. Thus, the volume associated with the extended interface decreases with particle size, partially counteracting the increase in surface area per unit volume. Furthermore, the particle size effects decrease with increasing time, presumably because the oxidation process becomes controlled by the transport of metal to the reaction front.<sup>112</sup> However, our experimental observations revealed that the growth rate increases with decrease in particle size. As mentioned earlier, for smaller particles the surface area increases and therefore the number of nucleation sites increases to promote a higher growth rate. Furthermore, once the composite nodules form on the surface of

the SiC particles, metal channels are formed in a shorter time for the smaller particles due to the smaller effective pore radius,  $r_h$ , which can be calculated according to:<sup>87</sup>

$$r_h = \frac{d_p \phi}{6(1 - \phi)} \quad (6.11)$$

where  $d_p$  is the SiC particle diameter and  $\phi$  is the void volume fraction. The calculated pore sizes for the different SiC particles are shown in APPENDIX I. So as the particle size increases, the effective pore radius increases. The metal channels are formed once the already nucleated composite nodules on the exposed surface of the preform particles start to coalesce. This reinforces our belief that the growth of the composites in the presence of SiC preforms is largely dependent on the state of the preform surface where nucleation takes place.

# 7. CONCLUSIONS AND RECOMMENDATIONS

## 7.1 CONCLUSIONS

Ceramic metal composites were produced by the oxidation of various molten aluminum-magnesium-silicon alloys into four types of SiC powder: 240-, 320-, 400-, and 600-grit at temperatures ranging from 1150-1350°C.

1. It has been shown that  $\text{Al}_2\text{O}_3$  matrix composites containing SiC particles and an interpenetrating network of metal can be grown by directed oxidation of Al-Mg and Al-Mg-Si alloys at temperatures ranging from 1150-1350°C. The presence of the SiC preform disrupted the columnar growth of the  $\text{Al}_2\text{O}_3$  matrix, but it still remains three dimensionally interconnected.
2. In the SiC-free composites, the initial oxidation event corresponds to the formation of  $\text{MgAl}_2\text{O}_4$  spinel, followed by the evolution of the MgO on the outer surface during the incubation period. Initially the  $\text{MgAl}_2\text{O}_4$  and MgO layers thicken continuously with time. However, at 1150°C, the MgO layer becomes thinner toward the end of the incubation period. Melt wicking via the metal channels created in the spinel layer increases at the end of the incubation period where the melt comes into direct contact and reacts with the MgO layer, setting the stage for the formation of  $\text{Al}_2\text{O}_3/\text{Al}$  nodules.

3. The previous observations are similar in both Al-Mg and Al-Mg-Si alloys, but the process is accelerated in the latter alloy. This is because the addition of Si to the Al-Mg alloy decreases the viscosity of the latter which, in turn, increases the rate of metal supply to the reaction front. Therefore Si additions shorten the length of the incubation period as well as increase the rate of composite growth in the unreinforced composites.
4. The oxidation rates of the cast alloys were comparable to those reported for other commercial alloys under similar processing conditions. It was found that the growth rate is enhanced by the presence of a SiC preform. The growth rate also increases with decreasing particle size. The growth mechanism in the presence of a SiC preform involves an extended oxidation front, originating from the wetting of the preform particles by the molten alloy and nucleation of  $\text{Al}_2\text{O}_3$  nodules on the surface of the preform particles. The SiC particles act in two manners: they provide sites to disrupt the initial surface oxide layer, therefore exposing the underlying metal to the oxygen and supplying the metal to the reaction front through the  $\text{MgAl}_2\text{O}_4/\text{MgO}$  layer. The SiC particles also provide nucleation sites for composite nodule formation ahead of the alloy surface and thereby increase the rate of growth.
5. The  $\text{SiO}_2$  layer on the SiC particles plays two key roles in the composite formation process: it drastically shortens the length of the incubation period through its reaction with the Al-Mg alloy to form  $\text{MgAl}_2\text{O}_4$  and it increases the rate of composite growth by its reaction with the Al-Mg alloy to form  $\text{Al}_2\text{O}_3$ .

6. The overall linear bulk growth process is thermally activated and the growth rate for all the alloys increased with temperature in the range 1100-1300°C with an activation energy of  $E_a \approx 224$  kJ/mol for the SiC-reinforced composites.

## **7.2 RECOMMENDATIONS FOR FURTHER WORK**

Although there is a fair amount of literature regarding the processing of these composites, most of the research has focused on the mechanism by which these composites form in the absence of a reinforcing material. However, there still exist many discrepancies in the data and results of the different studies. Some of the points that need to be investigated further are:

1. Microstructural evolution in the presence of different types of reinforcing material, such as oxides and other carbide systems.
2. Microstructural evolution of the composites in other oxidizing atmospheres, such as nitrogen.
3. Effects of the processing parameters on the mechanical properties of the composites. In particular, how changing the preform size, the initial alloy composition and the processing temperature would affect the mechanical properties.
4. Elevated temperature property testing, to explore the potential for the use of the composites in higher temperature environments, e.g. mechanical and corrosion properties.

# 8. CONTRIBUTIONS TO ORIGINAL KNOWLEDGE

This thesis has been the first work to investigate both the microstructural evolution and the oxidation kinetics of the DIMOX<sup>TM</sup> composite system in the presence of a reinforcing material. The existing literature on reinforced composites includes only an examination of the microstructure of the composites and some mechanical investigations.

The study of the directed oxidation of Al-Mg-Si alloys into SiC preforms is considered to be a major contribution, not only because it is the first time that oxidation kinetics into SiC preforms were investigated, but also because it provided important information on the role of the SiO<sub>2</sub> layer that forms on the SiC particles. Therefore, the role of Si in the alloy was clarified in relation to the shortening of the incubation period and relative increase in the growth rate.

The kinetic studies of the present work were performed on large samples compared to TGA experiments conducted by previous workers who used samples weighing less than a gram. In this manner, the results are more consistent and are representative of the bulk composite growth process.

# APPENDIX I

## CALCULATION OF THE PORE VOLUME FRACTION

Values for the void fraction, effective particle diameter, and the effective pore radius are required in order to establish a relationship for the growth rate as a function of the particle size. The void fraction can be determined by adding water to the silicon carbide powder compacts. The specimens were weighed before and after all the voids were filled with water. The open void volume fraction was then calculated using the weight of the water added using a volumetric cylinder.

The total cross-sectional area of the pores,  $A_v$ , can be related to the area of the compact,  $A_c$ , by the void fraction:

$$A_v = \phi A_c \quad (\text{AI.1})$$

$\phi$  can be derived knowing the tapped density of the powder and the density of the SiC;

$$\rho_{\text{Tapped}} = \frac{m_{\text{SiC}}}{V_{\text{SiC}} + V_{\text{Pores}}} \quad (\text{AI.2})$$

where  $m_{\text{SiC}}$  is the mass of the SiC and,

$$\phi = \frac{V_{\text{Pores}}}{V_{\text{Pores}} + V_{\text{SiC}}} \quad (\text{AI.3})$$

and,

$$V_{\text{Pores}} = \phi(V_{\text{Pores}} + V_{\text{SiC}}) = \frac{m_{\text{SiC}}}{\rho_{\text{Tapped}}} - V_{\text{SiC}} = \frac{V_{\text{SiC}} \cdot \rho_{\text{SiC}}}{\rho_{\text{Tapped}}} - V_{\text{SiC}} \quad (\text{AI.4})$$

Solving for  $\phi$  yields:

$$\phi = 1 - \frac{\rho_{Tapped}}{\rho_{SiC}} \quad (AI.5)$$

The pore volume fractions for the four different SiC particle sizes can be calculated knowing the density of SiC ( $\rho_{SiC}=3.217\text{g/cm}^3$ ) and are presented in the following table:

Table AI.1: Calculated Pore Volume Fraction for the Four Different SiC Powders

SiC-Grit Size	$D_{50\%}$ ( $\mu\text{m}$ )	$\rho_{Tapped}$ ( $\text{g/cm}^3$ )	$\phi$	Surface Area $\text{m}^2/\text{g}$	Effective Pore Radius ( $\mu\text{m}$ )
240	44.5	1.84	0.428	0.127	5.55
320	29.2	1.78	0.447	0.214	3.93
400	17.3	1.76	0.453	0.386	2.39
600	9.3	1.67	0.481	0.691	1.44

# APPENDIX II

## THE COMPUTATION OF THE RATE OF OXIDATION FOR PURE LIQUID ALUMINUM

The slope of the oxidation rate was estimated by first establishing the parabolic constant, according to the equation:

$$w^2 = K \cdot t \quad (\text{AII.1})$$

Therefore, by plotting the square of the weight of oxidation versus time, the parabolic constant,  $K$ , can be computed from the slope of the straight line by performing regression analysis. Such plots are shown in Fig. AII.1.

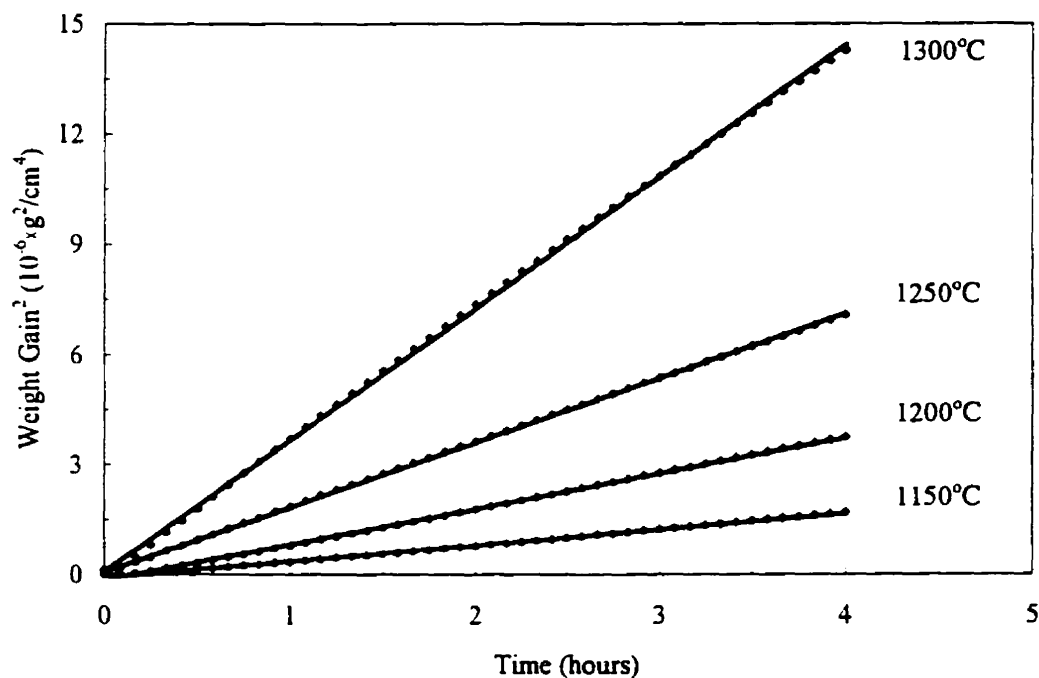


Fig. AII.1: Parabolic plots of oxidation data for pure aluminum.

Table AII.1: Computed Values from the Graph in Fig. AII.1

Temp. °C	$K$ $\text{g}^2/\text{cm}^4 \cdot \text{sec}$	$A$ $\text{g}^2/\text{cm}^4 \cdot \text{sec}$	$E_a$ J/mol
1150	$1.21 \times 10^{-10}$	0.36	257,860
1200	$2.69 \times 10^{-10}$		
1250	$4.90 \times 10^{-10}$		
1300	$9.97 \times 10^{-10}$		

Since the parabolic rate constant of oxidation increases with temperature ( $T$ ), it is possible to perform an Arrhenius analysis on these curves, hence establishing an activation energy,  $E_a$ , according to the equation:

$$K = A \cdot \exp\left(-\frac{E_a}{RT}\right) \quad (\text{AII.2})$$

where  $A$  is a constant,  $R$  is the Universal Gas constant, and  $T$  is the absolute temperature. The log of the parabolic rate constants were then plotted against the reciprocal of the oxidation temperature, in Kelvin. The resulting points were fitted with a straight, giving the Arrhenius plot shown in Fig. AII.2. The slope of this curve translates into an activation energy of 258 kJ/mol.

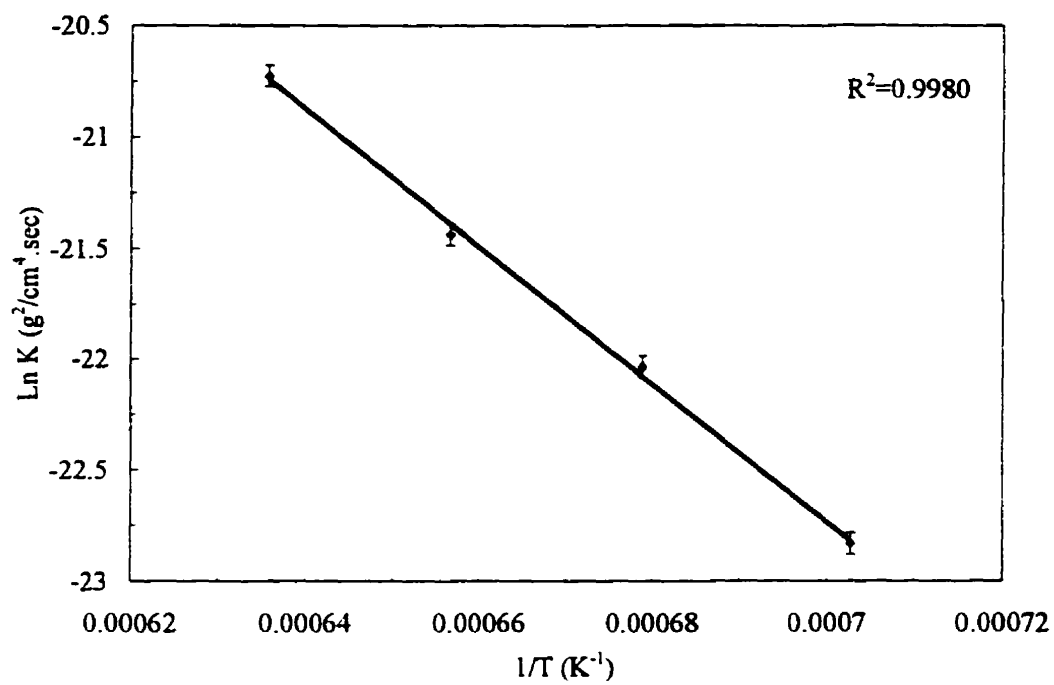


Fig. AII.2: Arrhenius plot of parabolic rate constant for pure aluminum.

# REFERENCES

- <sup>1</sup> R.A. Signorelli and J.A. DiCarlo, "High-Temperature Metal and Ceramic Composites," *Journal of Metals*, [6], 41-43 (1985).
- <sup>2</sup> D. Hull, in *An Introduction to Composite Materials*, Cambridge University Press, Co., Cambridge, Great Britain (1981).
- <sup>3</sup> A.G. Evans, "Prospective on the Development of High-Toughness Ceramics," *Journal of the American Ceramic Society*, **73** [2], 187-206 (1990).
- <sup>4</sup> G.H. Campbell, M. Rühle, B.J. Dalgleish, and A.G. Evans, "Whisker Toughening: A Comparison Between Aluminum Oxide and Silicon Nitride Toughened With Silicon Carbide," *Journal of the American Ceramic Society*, **73** [3], 521-530 (1990).
- <sup>5</sup> Y.M. Chiang, J.S. Haggerty, R.P. Messner, and C. Demetry, "Reaction-Based Processing Methods for Ceramic-Matrix Composites," *American Ceramic Society Bulletin*, **68** [2], 420-428 (1989).
- <sup>6</sup> K.K. Chawla, in *Ceramic Matrix Composites*, Published by Chapman & Hall, 2-6 Boundary Row, London SE1 8HN, First Edition, 127 (1993).
- <sup>7</sup> R. Ray and R.K. Bordia, "Sintering Behavior of Bi-Modal Powder Compacts," *Acta Metallurgica*, **32** [7]1003-1019 (1984).
- <sup>8</sup> B.J. Kellett and F.F. Lange, "Thermodynamics of Densification: I, Sintering of Simple Particle Arrays, Equilibrium Configurations, Pore Stability, and Shrinkage," *Journal of the American Ceramic Society*, **72** [5], 725-734 (1989).

- <sup>9</sup> M.D. Sacks, H.-W. Lee, and O.E. Rojas, "Suspension Processing of Al<sub>2</sub>O<sub>3</sub>/SiC Whisker Composites," *Journal of the American Ceramic Society*, **71** [5], 370-379 (1988).
- <sup>10</sup> M.N. Rahaman and L.C. De Jonghe, "Effect of Rigid Inclusions on the Sintering of Glass Powder Compacts," *Journal of the American Ceramic Society*, **70** [12], C348-C351 (1987).
- <sup>11</sup> J.A. Cornie, Y.M. Chiang, D.R. Uhlmann, A. Mortensen, and J.M. Collins, "Processing of Metal and Ceramic Matrix Composites," *American Ceramic Society Bulletin*, **65** [2], 293 (1986).
- <sup>12</sup> K.M. Prewo and J.J. Brennan, "High-Strength Silicon Carbide Fibre-Reinforced Glass-Matrix Composites," *Journal of Materials Science*, **15**, 463 (1980).
- <sup>13</sup> J.J. Brennan and K.M. Prewo, "Silicon Carbide Fibre Reinforced Glass-Ceramic Matrix Composites Exhibiting High Strength and Toughness," *Journal of Materials Science*, **17**, 2371 (1982).
- <sup>14</sup> L.M. Sheppard, "Progress in Composites Processing," *American Ceramic Society Bulletin*, **69** [4], 666-673 (1990)
- <sup>15</sup> D. Muscat, "Titanium Carbide/Aluminum Composites by Melt Infiltration," Ph.D. Thesis, McGill University (1993)
- <sup>16</sup> K. Shanker, L.T. Mavropoulos, R.A.L. Drew and P.G. Tsantrizos, "Properties of TaC-Based Metal-Matrix Composites Produced by Melt Infiltration," *Composites*, **23** [1], 47-53 (1992).
- <sup>17</sup> W.B. Hillig, "Melt Infiltration Approach to Ceramic Matrix Composites," *Journal of the American Ceramic Society*, **71** [2], C96-C99 (1988).

- <sup>18</sup> C. Williams and K.M. Fisher, "Solidification Technology in the Foundry and Casthouse," *Metals Society*, 137 (1983).
- <sup>19</sup> A. Mortensen, M.N. Gungor, J.A. Cornie, and M.C. Flemings, "Alloy Microstructures in Cast Metal Matrix Composites," *Journal of Metals*, **38** [3], 30-35 (1986).
- <sup>20</sup> A. Mortensen, J.A. Cornie, and M.C. Flemings, "Columnar Dendritic Solidification in a Metal-Matrix Composite," *Metallurgical Transactions A*, **19A**, 709-721 (1988).
- <sup>21</sup> K. Ohori, H. Watanabe, and Y. Takeuchi, "Silicon Carbide Whisker Reinforced Aluminum Composites- Fabrication and Properties," *Materials Science and Technology*, **3** [1], 57-60 (1987).
- <sup>22</sup> Y.L. Klipfel, M.Y. He, R.M. McMeeking, A.G. Evans, and R. Mehrabian, "The Processing and Mechanical Behavior of an Aluminum Matrix Composite Reinforced with Short Fibers," *Acta Metallurgica. Materiala*, **38** [6], 1063-1074 (1990).
- <sup>23</sup> T.W. Clyne, M.G. Bader, G.R. Cappleman, and P.A. Hubert, "The Use of a  $\delta$ -Alumina Fibre for Metal-Matrix Composites," *Journal of Materials Science*, **20**, 85-96 (1985).
- <sup>24</sup> H. Matsubara, Y. Nishida, M. Yamada, I. Shirayanagi, and T. Imai, " $\text{Si}_3\text{N}_4$  Whisker-Reinforced Aluminum Alloy Composite," *Journal of Materials Science Letters*, **6**, 1313-1315 (1987)
- <sup>25</sup> H. Fukunaga and K. Goda, "Fabrication of Fiber Reinforced Metal by Squeeze Casting," *Bulletin of the Japan Society of Mechanical Engineering*, **27** [228], 1245-1250 (1984).

- <sup>26</sup> M.S. Newkirk, H.R. Zwicker and A.W. Urquhart, "Composite Ceramic Articles and Methods of Making the Same," *European Patent Application No. 86300739.9*, Publ. No. 0193292, Filed 04.02.86.
- <sup>27</sup> M.S. Newkirk, A.W. Urquhart, H.R. Zwicker, and E. Breval, "Formation of Lanxide™ Ceramic Composite Materials," *Journal of Materials Research*, 1 [1], 81-89 (1986).
- <sup>28</sup> M.S. Newkirk, H.D. Lesher, D.R. White, C.R. Kennedy, A.W. Urquhart, and T.D. Claar, "Preparation of Lanxide™ Ceramic Matrix Composites: Matrix Formation by the Directed Oxidation of Molten Metals," *Ceramic Engineering and Science Proceedings*, 8 [7-8], 879-885 (1987).
- <sup>29</sup> A.J. Moulson, "Review: Reaction-Bonded Silicon Nitride: Its Formation and Properties," *Journal of Materials Science*, 14, 1017-1051 (1979).
- <sup>30</sup> S. Lee and D.K. Kim, "The Effect of Oxide Additives in Filler Materials During Directed Melt Oxidation Process," *Ceramic Engineering and Science Proceedings*, 11 [7-8], 795-805 (1990).
- <sup>31</sup> E. Breval, "Structure of Aluminum Nitride/Aluminum and Aluminum Oxide/Aluminum Composites Produced by the Directed Oxidation of Aluminum," *Journal of the American Ceramic Society*, 76 [7], 1865-1886 (1993).
- <sup>32</sup> D. K. Creber, S.D. Poste, M.K. Aghajanian, and T.D. Claar, "AlN Composite Growth by Nitridation of Aluminum Alloys," *Ceramic Engineering and Science Proceedings*, 9 [7-8], 975-983 (1988).
- <sup>33</sup> H. LeHuY and S. Dallaire, "Effects of Si and Mg Dopants on the Kinetics of Aluminum Growth by Nitridation," 302-311 in *Proceedings of the International Symposium on*

- Ceramics and Metal Matrix Composites*, CIM, Vol. 17, Edited by H. Mostaghaci. Pergamon Press, New York (1989).
- <sup>34</sup> H. Scholz and P. Greil, "Nitridation Reactions of Molten Al-(Mg,Si) Alloys," *Journal of Materials Science*, **26**, 669-677 (1991).
- <sup>35</sup> F.K. Ko, "Architecture for Ceramic-Matrix Composites," *American Ceramic Society Bulletin*, **68** [2], 401-414 (1989).
- <sup>36</sup> D.W. Richerson, in *Modern Ceramic Engineering*, Second Edition, Marcel Dekker, Inc. (1992).
- <sup>37</sup> R.N. Singh and A.R. Gaddipati, "Mechanical Properties of a Uniaxially Reinforced Mullite-Silicon Carbide Composite," *Journal of the American Ceramic Society*, **71** [2], C100-C103 (1988).
- <sup>38</sup> F.F. Lange, "Effect of Microstructure on Strength of Si<sub>3</sub>N<sub>4</sub>-SiC Composite System," *Journal of the American Ceramic Society*, **56** [9], 445-450 (1973).
- <sup>39</sup> E. Breval, M.K. Aghajanian, and S.J. Luszcz, "Microstructure and Composition of Alumina/Aluminum Composites Made by Directed Oxidation of Aluminum," *Journal of the American Ceramic Society*, **73** [9], 2610-2614 (1990).
- <sup>40</sup> C.A. Andersson and M.K. Aghajanian, "The Fracture Toughening Mechanism of Ceramic Composites Containing Adherent Ductile Metal Phase,"
- <sup>41</sup> C.A. Andersson, P.B. Antolin, A.S. Fareed, and G.H. Schiroky, "Properties of Fiber-Reinforced Lanxide™ Alumina Matrix Composites," *Proceedings of the International Conference on Whisker- and Fiber-Toughened Ceramics*, ASM International, Metals Park, OH, 209-215 (1988).

- <sup>42</sup> M.K. Aghajanian, N.H. MacMillan, C.R. Kennedy, S.J. Luszcz, and R. Roy, "Properties and Microstructures of Lanxide™ Al<sub>2</sub>O<sub>3</sub>-Al Ceramic Composite Materials," *Journal of Materials Science*, **24** [2], 658-670 (1989).
- <sup>43</sup> A.S. Nagelberg, A.S. Fareed, and D.J. Landini, "Production of Ceramic Matrix Composites for Elevated Temperature Applications using the DIMOX™ Directed Metal Oxidation Process," *Processing and Fabrication of Advanced Materials for High Temperature Applications*. Edited by V.A. Ravi and T.S. Srivatsan, The Minerals, Metals & Materials Society, 128-142 (1992).
- <sup>44</sup> A.S. Fareed, B.Sonuparlak, C.T. Lee, A.J. Fortini, and G.H. Schiroky, "Mechanical Properties of 2-D Nicalon™ Fiber-Reinforced LANXIDE™ Aluminum Oxide and Aluminum Nitride Matrix Composites," *Ceramic Engineering and Science Proceedings*, **11** [7-8], 782-794 (1990).
- <sup>45</sup> O. Kubaschewski, A. Cibula and D.C. Moore, in *Gases and Metals*, New York, American Elsevier Publishing Company, Inc. (1970).
- <sup>46</sup> C.N. Cochran and W.C. Sleppy, "Oxidation of High-Purity Aluminum and 5052 Aluminum-Magnesium Alloy at Elevated Temperatures," *Journal of the Electrochemical Society*, **108** [4], 322-327 (1961).
- <sup>47</sup> M.J. Dignam, "Oxide Films on Aluminum," *Journal of the Electrochemical Society*, **109** [3], 184-191 (1962).
- <sup>48</sup> P.E. Doherty and R.S. Davis, "Direct Observation of the Oxidation of Aluminum Single-Crystal Surfaces," *Journal of Applied Physics*, **34** [3], 619-628 (1963).

- <sup>49</sup> M.R. Deakin and O.R. Melroy, "Monitoring the Growth of an Oxide Film on Aluminum *In Situ* with the Quartz Crystal Microbalance," *Journal of the Electrochemical Society*, **136** [2], 349-352 (1989).
- <sup>50</sup> M.J. Dignam, W.R. Fawcett, and H. Böhni, "The Kinetics and Mechanism of Oxidation of Superpurity Aluminum in Dry Oxygen," *Journal of the Electrochemical Society*, **113** [7], 656-662 (1966).
- <sup>51</sup> F. Stucki, M. Erbudak, and G. Kostorz, "The Initial Oxidation of Solid and Liquid Aluminum," *Applied Surface Science*, **27**, 393-400 (1987).
- <sup>52</sup> W.W. Smeltzer, "Oxidation of Aluminum in the Temperature Range 400°-600°C," *Journal of the Electrochemical Society*, **103** [4], 209-214 (1956).
- <sup>53</sup> N. Cabrera and N.F. Mott, *Repts. Progr. Phys.*, **12**, 163 (1949).
- <sup>54</sup> O. Kubaschewski and B.E. Hopkins, in *Oxidation of Metals and Alloys*, Second Edition, London Butterworths, page 33 (1962).
- <sup>55</sup> S.J. Gregg and W.B. Jepson, *ibid.*, **87**, 187, (1959).
- <sup>56</sup> C. Jardin and D. Robert, *Applied Surface Science*, **35**, 495 (1988).
- <sup>57</sup> N.F. Mott, *Transactions of the Faraday Society*, **43**, 429 (1949).
- <sup>58</sup> R.D. Guminski and F.M.P. Meredith, *J. Oil and Colour Chemists' Assoc.*, **44**, 93 (1961).
- <sup>59</sup> R.A. Hine and R.D. Guminski, "High-Temperature Oxidation of Aluminum-Magnesium Alloys in Various Gaseous Atmospheres," *Journal of the Institute of Metals*, **89**, 417-422 (1961).
- <sup>60</sup> L. de Brouckère, *ibid.*, **71**, 131 (1945).

- <sup>61</sup> W.W. Smeltzer, "Oxidation of An Aluminum-3 Per Cent Magnesium Alloy in the Temperature Range 200°-550°C," *Journal of the Electrochemical Society*, **105** [2], 67-71 (1958).
- <sup>62</sup> M.H. Zayan, O.M. Jamjoom, and N.A. Razik, "High-Temperature Oxidation of Al-Mg Alloys," *Oxidation of Metals*, **34** [3-4], 323-333 (1990).
- <sup>63</sup> I.M. Ritchie, I.V. Sanders, and P.L. Weickhardt, "Oxidation of a Dilute Aluminum Magnesium Alloy," *Oxidation of Metals*, **3** [1], 91-101 (1971).
- <sup>64</sup> B. Goldstein and J.Dresner, "Growth of MgO Films with High Secondary Electron Emission on Al-Mg Alloys," *Surface Science*, **71**, 15-26 (1978).
- <sup>65</sup> C. Lea and C. Molinari, "Magnesium Diffusion, Surface Segregation and Oxidation in Al-Mg Alloys," *Journal of Materials Science*, **19**, 2336-2352 (1984).
- <sup>66</sup> G.R. Wallwork and A.Z. Hed, "Some Limiting Factors in the Use of Alloys at High Temperatures," *Oxidation of Metals*, **3** [2], 171-184 (1971).
- <sup>67</sup> M. Bishop and K.E. Fletcher, "Diffusion in Aluminum," *International Metallurgical Reviews*, **17**, 203-225 (1972)
- <sup>68</sup> M.H. Zayan, "Model for Nonprotective Oxidation of Al-Mg Alloys," *Oxidation of Metals* **34** [5-6], 465-472 (1990)
- <sup>69</sup> D.J. Field, G.M. Scamans, and E.P. Butler, "The High Temperature Oxidation of Al-4.2 Wt Pct Mg Alloys," *Metallurgical Transactions A*, **18A** [3], 463-472 (1987).
- <sup>70</sup> G.M. Scamans and E.P. Butler, "In Situ Observations of Crystalline Oxide Formation During Aluminum and Aluminum Alloy Oxidation," *Metallurgical Transactions A*, **6A** [11], 2055-2063 (1975).

- <sup>71</sup> W. Thiele, *Aluminium*, **38**, 780-786 (1962).
- <sup>72</sup> C.N. Cochran, D.L. Belitskus, and D.L. Kinosz, "Oxidation of Aluminum-Magnesium Melts in Air, Oxygen, Flue Gas, and Carbon Dioxide," *Metallurgical Transactions B*, **8B** [6], 323-332 (1977).
- <sup>73</sup> A. Mortenson and T. Wong, "Infiltration of Fibrous Preforms by a Pure Metal: Part III. Capillary Phenomena," *Metallurgical Transactions A*, **21A**, 2257-2263 (1990).
- <sup>74</sup> L.J. Mansur, A. Mortenson, J.A. Cornie, and M.C. Flemings, "Infiltration of Fibrous Preforms by Pure Metal: Part II. Experiment," *Metallurgical Transactions A*, **20A**, 2549 (1989).
- <sup>75</sup> H. Fukunaga, in *Cast Reinforced Metal Composites*, edited by S.G. Fishman and A.K. Dhingra, American Society for Metals International, Metals Park, Ohio, 101 (1988).
- <sup>76</sup> G.R. Cappleman, J.F. Watts, and T.W. Clyne, "The Interface Region in Squeeze-Infiltrated Composites Containing  $\delta$ -Alumina Fiber in an Aluminum Matrix," *Journal of Materials Science*, **20**, 2159-2168 (1985).
- <sup>77</sup> S.-Y. Oh, J.A. Cornie, and K.C. Russell, "Wetting of Ceramic Particulates with Liquid Aluminum Alloys Part II. Study of Wettability," *Metallurgical Transactions A*, **20A**, 533-541 (1989)
- <sup>78</sup> C.G. Goetzl, in *Cermets*, edited by Tinkelpaugh and Crandall, Reinhold, 73 (1976).
- <sup>79</sup> J.W. Gibbs, in *Thermodynamics*. The collected Works of J. Willard Gibbs **Volume I**, New Haven, Yale University Press, 219-229 (1928).
- <sup>80</sup> P.C. Carman, "Capillary Rise and Capillary Movement of Moisture in Fine Sands," *Soil Science*, **52**, 1-14 (1941).

- <sup>81</sup> L.W. White, "Capillary Rise in Powders," *Journal of Colloidal Interface Science*, **90** [2], 536-538 (1982).
- <sup>82</sup> C. Decharme, *Ann. Chim. Phys.*, **23**, 228-242 (1872).
- <sup>83</sup> E.W. Washburn, "The Dynamics of Capillary Flow," *The Physical Review*, **17** [3], 273-283 (1921).
- <sup>84</sup> R. Von Mises and K.O. Fredricks, in *Fluid Dynamics*, Brown University (1941).
- <sup>85</sup> P.C. Hiemenz, in *Principles of Colloid and Surface Chemistry*, 2<sup>nd</sup> Edition, Marcel Dekker Inc. (1986).
- <sup>86</sup> D. Muscat and R.A.L. Drew, "Modeling the Infiltration Kinetics of Molten Aluminum into Porous Titanium Carbide," *Metallurgical and Materials Transactions A*, **25A** [11], 2357-2370 (1994).
- <sup>87</sup> P.B. Maxwell, G.P. Martins, D.L. Olson, and G.R. Edwards, "The Infiltration of Aluminum into Silicon Carbide Compacts," *Metallurgical Transactions B*, **21B** [6], 475-485 (1990).
- <sup>88</sup> K.A. Semlak and Rhines, "The Rate of Infiltration of Metals," *Transactions of the Metallurgical Society of AIME*, [6], 325-331 (1958).
- <sup>89</sup> C. Toy and W.D. Scott, "Ceramic-Metal Composite Produced by Melt Infiltration," *Journal of the American Ceramic Society*, **73** [1], 97-101 (1990).
- <sup>90</sup> R. Asthana and P.K. Rohatgi, "Observations on Infiltration of Silicon Carbide Compacts with an Aluminum Alloy," *Journal of Materials Science Letters*, **11**, 1278-1281 (1992).

- <sup>91</sup> J. Frydrych, J. Lezanski, and W. Rutkowski, in *Modern Developments in Powder Metallurgy*, Plenum Press, NY, 69-79 (1966).
- <sup>92</sup> Z. Xia, Y. Zhou, Z. Mao, and B. Shang, "Fabrication of Fiber-Reinforced Metal-Matrix Composites by Variable Pressure Infiltration," *Metallurgical Transactions B*, **23B** [6], 295-302 (1992).
- <sup>93</sup> A. Alonso, A. Pamies, J. Narciso, C. Garcia-Cordovilla, and E. Louis, "Evaluation of the Wettability of Liquid Aluminum with Ceramic Particulates (SiC, TiC, Al<sub>2</sub>O<sub>3</sub>) by Means of Pressure Infiltration," *Metallurgical Transactions A*, **24A**, 1423-1432 (1993).
- <sup>94</sup> D. Muscat and R.A.L. Drew, "A Method of Measuring Metal Infiltration Rates in Porous Preforms at High Temperatures," *Journal of Materials Science Letters*, **12**, 1567-1569 (1993).
- <sup>95</sup> T.S. Srivatsan, I.A. Ibrahim, F.A. Mohamed, and E.J. Lavernia, "Processing Techniques for Particulate-Reinforced Metal Aluminum Matrix Composites," *Journal of Materials Science*, **26**, 5965-5978 (1991).
- <sup>96</sup> V. Laurent, D. Chatain, and N. Eustathopoulos, "Wettability of SiC by Aluminum and Al-Si Alloys," *Journal of Materials Science*, **22**, 244-250 (1987).
- <sup>97</sup> A. Mortensen, L.J. Mansur, J.A. Cornie, and M.C. Flemings, "Infiltration of Fibrous Preforms by a Pure Metal: Part I. Theory," *Metallurgical Transactions A*, **20A** [11], 2535-2547 (1989).
- <sup>98</sup> S. Schamm, R. Fedou, J.P. Rocher, J.M. Quenisset, and R. Naslain, "The K<sub>2</sub>ZrF<sub>6</sub> Wetting Process: Effect of Surface Chemistry on the Ability of a SiC-Fiber Preform to

- be Impregnated by Aluminum," *Metallurgical Transactions A*, **22A** [9], 2133-2139 (1991).
- <sup>99</sup> D.J. Lloyd, in *Advanced Structural Materials*, D.S. Wilkinson, ed., Pergamon Press, NY, 1 (1989).
- <sup>100</sup> T. Young, *Phil. Trans. R. Soc.*, **95**, 65-87 (1805).
- <sup>101</sup> A. Dupré, in *Theorie Mecanique de la Chaleur*, Gauthier Villars, Paris (1869).
- <sup>102</sup> V. Laurent, D. Chatain, and N. Eustathopoulos, "Wettability of SiO<sub>2</sub> and Oxidized SiC by Aluminum," *Materials Science and Engineering*, **A135**, 89-94 (1991).
- <sup>103</sup> J. Goicoechea, C. Garcia-Cordovilla, E. Louis, and A. Pamies, "Surface Tension of Binary and Ternary Aluminum Alloys of the Systems Al-Si-Mg and Al-Zn-Mg," *Journal of Materials Science*, **27**, 5247-5252 (1992).
- <sup>104</sup> T. Choh and T. Oki, "Wettability of SiC to Aluminum and Aluminum Alloys," *The Institute of Metals*, 378-385 (1987).
- <sup>105</sup> R. D. Carnahan, T.L. Johnston, and C.H. Li, "Some Observation on the Wetting of Al<sub>2</sub>O<sub>3</sub> by Aluminum," *Journal of the American Ceramic Society*, **41** [9], 343-347 (1958).
- <sup>106</sup> S.M. Wolf, A.P. Levitt, and J. Brown, "Whisker-Metal Matrix Bonding," *Chemical Engineering Progress*, **62** [3], 74-78 (1966).
- <sup>107</sup> J.A. Champion, B.J. Keene, and J.M. Sillwood, "Wetting of Aluminum Oxide by Molten Aluminum and Other Metals," *Journal of Materials Science*, **4**, 39-49 (1969).

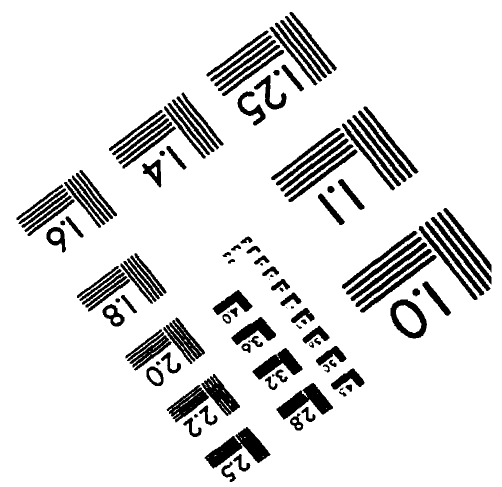
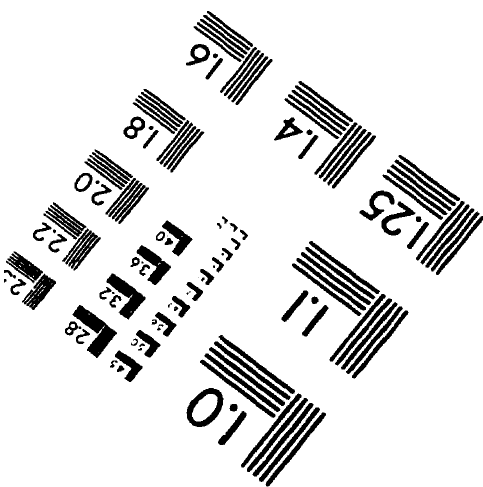
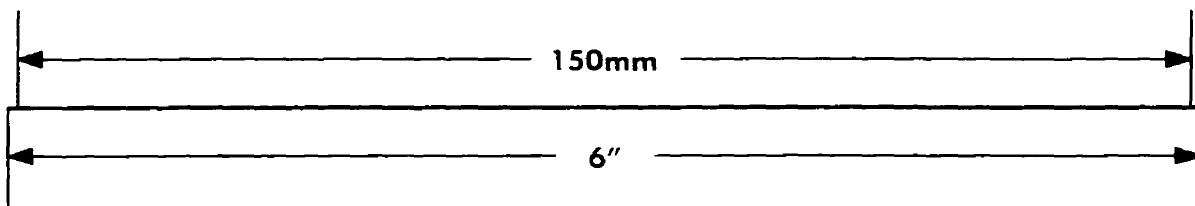
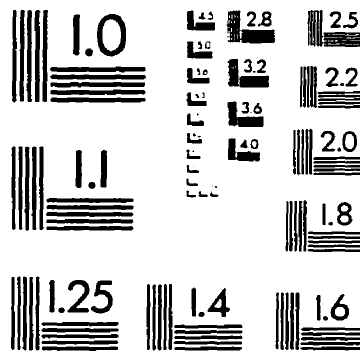
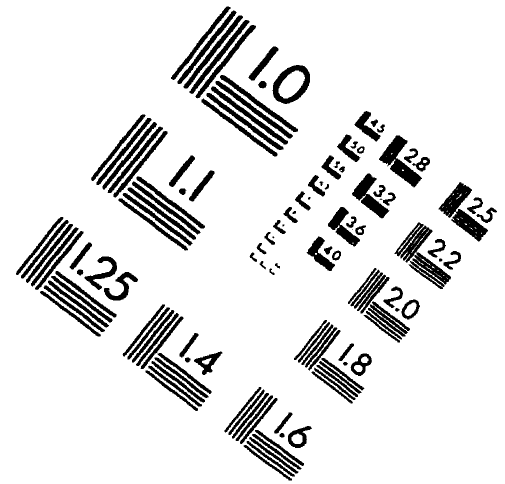
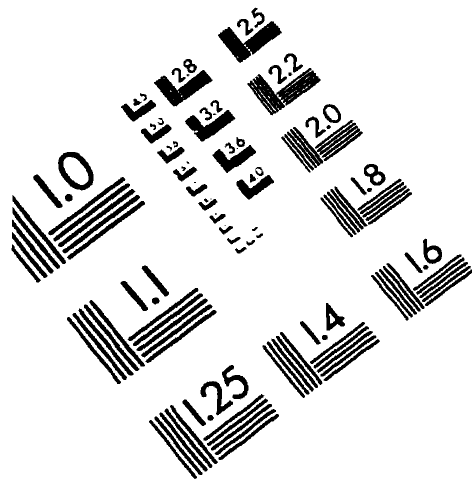
- <sup>108</sup> R. Asthana and S.N. Tewari, "Interfacial and Capillary Phenomena in Solidification Processing of Metal-Matrix Composites," *Composites Manufacturing*, 4 [1], 3-25 (1993).
- <sup>109</sup> S Lowell and J.E. Shields, in *Powder Surface Area and Porosity*, Chapman & Hall Ltd., Third Edition, 31 (1991).
- <sup>110</sup> S. Antolin, A.S. Nagelberg, and D.K. Creber, "Formation of Al<sub>2</sub>O<sub>3</sub>/Metal Composites by the Directed Oxidation of Molten Al-Mg-Si Alloys: Part I, Microstructural Development," *Journal of the American Ceramic Society*, 75 [2], 447-454 (1992).
- <sup>111</sup> D.-J. Lee, M.D. Vaudin, C.A. Handwerker, and U.R. Kattner, "Phase Stability and Interface Reactions in the Al-SiC System," *Materials Research Society Symposium Proceedings*, 120, 357-365 (1988).
- <sup>112</sup> E. Manor, H. Ni, C.G. Levi, and R. Mehrabian, "Microstructure Evolution of SiC/Al<sub>2</sub>O<sub>3</sub>/Al-Alloy Composites Produced by Melt Oxidation," *Journal of the American Ceramic Society*, 76 [7], 1777-1787 (1993).
- <sup>113</sup> O. Salas, H. Ni, V. Jayaram, K.C. Vlach, C.G. Levi, and R. Mehrabian, "Nucleation and Growth of Al<sub>2</sub>O<sub>3</sub>/Metal Composites by Oxidation of Aluminum Alloys," *Journal of Materials Research*, 6 [9], 1964-1981 (1991).
- <sup>114</sup> K.C. Vlach, O. Salas, H. Ni, V. Jayaram, C.G. Levi and R. Mehrabian, "A Thermogravimetric Study of the Oxidative Growth of Al<sub>2</sub>O<sub>3</sub>/Al Alloy Composites," *Journal of Materials Res.*, 6 [9], 1982-1995 (1991).
- <sup>115</sup> A.S. Nagelberg, "Effect of Alloy Composition on the Growth rate of Al<sub>2</sub>O<sub>3</sub>/Al Composites," *Solid State Ionics*, 32-33, 783-788 (1989).

- <sup>116</sup> R. Asthana, P.K. Rohatgi, and S.N. Tewari, "Infiltration Processing of Metal-Matrix Composites: A Review," *Processing of Advanced Materials*, **2**, 1-17 (1992).
- <sup>117</sup> A.Ya. Radin, *Svoistva Rasplavl. Met., Tr. Soveshch. Teor. Liteinykh Protessov*, "Oxidation of Molten Metals," 16th, 116-122 (1972); *Chemical Abstracts*, **82**, 90567 (1975).
- <sup>118</sup> D.L. Belitskus, "Effect of  $H_3BO_3$ ,  $BCl_3$ , and  $BF_3$  Pretreatments on Oxidation of Molten Al-Mg Alloys in Air," *Oxidation of Metals*, **8** [5], 303-307 (1974).
- <sup>119</sup> D.L. Belitskus, "Oxidation of Molten Al-Mg Alloy in Air, Air- $SO_2$ , and Air- $H_2S$  Atmospheres," *Oxidation of Metals*, **3** [4], 313-317 (1971).
- <sup>120</sup> M. Richard and R. Emery, "Liquid Aluminum Alloys: Oxidation and Reactivity with Refractories," *Fonderies*, [373], 389-396 (1977).
- <sup>121</sup> A.S. Nagelberg, "Observations on the Role of Mg and Si in the Directed Oxidation of Al-Mg-Si Alloys," *Journal of Materials Research*, **7** [2], 265-268 (1992).
- <sup>122</sup> T.P. Yao and V. Kondic, "The Viscosity of Molten Tin, Lead, Zinc, Aluminum, and Some of their Alloys," *Journal of the Institute of Metals*, **81**, 17-24 (1952-1953).
- <sup>123</sup> W.R.D. Jones and W.L. Bartlett, "The Viscosity of Aluminum and Binary Aluminum Alloys," *Journal of the Institute of Metals*, **81**, 145-152 (1952-1953).
- <sup>124</sup> O. Salas, V. Jayaram, K.C. Vlach, C.G. Levi, and R. Mehrabian, "Early Stages of Composite Formation by Oxidation of Liquid Aluminum Alloys," *Journal of the American Ceramic Society*, **78** [3], 609-622 (1995).
- <sup>125</sup> H.A. Wriedt, "The Al-O (Aluminum-Oxygen) System," *Bulletin of Alloy Phase Diagrams*, **6** [6], 548-553, 567-568 (1985).

- <sup>126</sup> D.A. Weirauch and G.E. Graddy, Jr., "Wetting and Corrosion in the Al-Mg-Si-O System," 251-266 in *Proceedings of the International Symposium on Advances in Refractories for the Metallurgical Industries* (Winnipeg, Canada, August 1987). Edited by M.A.J. Rigaud, Pergamon Press, New York (1988).
- <sup>127</sup> K.C. Vlach, C.G. Levi and R. Mehrabian, "On the Kinetics of the Oxidative Growth of Alumina-Metal Composites," *Processing and Manufacturing of Advanced Materials for High-Temperature Applications*. Edited by V.A. Ravi and T.S. Srivatsan, The Minerals, Metals and Materials Society, Warrendale, PA, 157-171 (1992).
- <sup>128</sup> R. Warren and C.H. Anderson, "Silicon Carbide Fibres and Their Potential for Use in Composite Materials. Part II," *Composites*, **15** [2], 101-111 (1984).
- <sup>129</sup> R.Y. Lin and K. Kannikeswaran, in *Interfaces in Metal-Ceramic Composites*, Edited by R.Y. Lin et al. page 153, TMS (1989).
- <sup>130</sup> J.C. Viala, P. Fortier and J. Bouix, "Stable and Metastable Phase Equilibria in the Chemical Interaction Between Aluminum and Silicon Carbide," *Journal of Materials Science*, **25**, 1842-1850 (1990).
- <sup>131</sup> A.E. Hughes, M.M. Hedges and B.A. Sextron, "Reactions at the Al/SiO<sub>2</sub>/SiC Layered Interface," *Journal of Materials Science*, **25**, 4856-4865 (1990).
- <sup>132</sup> S.D. Peteves, P. Tambuyser, P. Helbach, M. Audier, V. Laurent and D. Chatain, "Microstructure and Microchemistry of the Al/SiC Interface," *Journal of Materials Science*, **25**, 3765-3772 (1990)
- <sup>133</sup> T. Iseki, T. Kameda and T. Maruyama, "Interfacial Reactions Between SiC and Aluminum During Joining," *Journal of Materials Science*, **19**, 1692-1698 (1984).

- <sup>134</sup> O. Salas, V. Jayaram, K.C. Vlach, C.G. Levi, and R. Mehrabian, "Banded Microstructures in Al<sub>2</sub>O<sub>3</sub>/Al Composites Produced by Oxidation of Molten Al-Mg Alloys," *Processing and Manufacturing of Advanced Materials for High-Temperature Applications*. Edited by V.A. Ravi and T.S. Srivatsan, The Minerals, Metals and Materials Society, Warrendale, PA, 143-156 (1992).

# IMAGE EVALUATION TEST TARGET (QA-3)



**APPLIED IMAGE, Inc**  
1653 East Main Street  
Rochester, NY 14609 USA  
Phone: 716/482-0300  
Fax: 716/288-5989

© 1993, Applied Image, Inc., All Rights Reserved